Technical Report
TR-16-02
May 2016

Long-term safety of a planned geological repository for spent nuclear fuel in Forsmark, Sweden and Olkiluoto, Finland

Phase 2: impact of ice sheet dynamics, climate forcing and multi-variate sensitivity analysis on maximum ice sheet thickness

Aurélien Quiquet
Florence Colleoni
Simona Masina

SVENSK KÄRNBRÄNSLEHANTERING AB

SWEDISH NUCLEAR FUEL
AND WASTE MANAGEMENT CO

Box 250, SE-101 24 Stockholm
Phone +46 8 459 84 00
skb.se

SVENSK KÄRNBRÄNSLEHANTERING

ISSN 1404-0344
SKB TR-16-02
ID 1525326

May 2016
Updated 2016-09

Long-term safety of a planned geological repository for spent nuclear fuel in Forsmark, Sweden and Olkiluoto, Finland

Phase 2: impact of ice sheet dynamics, climate forcing and multi-variate sensitivity analysis on maximum ice sheet thickness

Aurélien Quiquet, Florence Colleoni
Centro Euro- Mediterraneo sui i Cambiamenti Climatici

Simona Masina
Centro Euro-Mediterraneo sui i Cambiamenti Climatici and
Istituto Nazionale di Geofisica e Vulcanologia

Update notice

The original report, dated May 2016, was found to contain factual errors which have been corrected in this updated version. The corrected factual errors are presented below.

Updated 2016-09

Location	Original text	Corrected text
Page 3	Summary	New Preface inserted
Page 4	Blank page	Summary

Preface

The following report constitutes a second and final phase of a study reconstructing the Eurasian ice sheet during the peak Saalian glaciation, 140 000 years ago, by climate- and ice sheet model simulations. The study was initiated and managed by Prof. Jens-Ove Näslund (SKB) and Dr. Florence Colleoni (Centro Euro-Mediterraneano sui Cambiamenti Climatici, CMCC). The project steering group consisted of Dr. Florence Colleoni (CMCC), Dr. Aurélien Quiquet (CMCC), Prof. Jens-Ove Näslund (SKB), Dr. Anne Kontula (Posiva), Dr. Lasse Koskinen (Posiva), and Dr. Simona Masina (CMCC).

The results will be used, together with the results of the first phase of the study (SKB report TR-14-21) and with other published scientific information, for constructing future scenarios with large ice sheet configurations for assessing the long-term safety of the planned repository for spent nuclear fuel in Forsmark, Sweden.

The report manuscript was reviewed by Prof. Philippe Huybrechts (Vrije Universiteit Brussel), Prof. Ralf Greve (Hokkaido University), Dr. Patrick Applegate (Pennsylvania State University), and Dr. Allan Hedin (SKB).

Stockholm, May 2016

Jens-Ove Näslund
Research coordinator Climate Programme SKB

Summary

This study is the second and final phase of a study aiming at simulating the impact of a past extensive glaciation over Forsmark, southeastern Sweden, and Olkiluoto, southwestern Finland. To this end, the Late Saalian glaciation (~192–135 kyrs BP), which is known to be the most extensive glaciation that occurred over Eurasia during the last 400 kyrs, was used as case study. In fact, some recent reconstructions suggest that during the peak of this glaciation, the area of the Eurasian ice sheet was at least twice as large as during the Last Glacial Maximum (LGM, ~21 kyrs BP). In the first phase of the study, we used a coupled Atmosphere-Ocean-Sea-Ice-Land model, set up and integrated with constant-in-time forcing Late Saalian conditions to simulate the Late Saalian glacial maximum climate at ~140 kyrs BP (i.e. the MIS 6 period). A set of two climate simulations were performed since the extent of the Laurentide ice sheet during this glaciation is uncertain: one including the LGM Laurentide ice sheet topography (B140_Topo1) and one including a smaller Laurentide ice sheet topography (B140_Topo2) (Colleoni et al. 2014b, 2016a, b). In both simulations, the prescribed Eurasian ice sheet was based on a previous ice sheet model simulation for the Late Saalian glacial maximum. Secondly, the simulated climates were, in the first phase of the study, used as initial condition to carry out two sets of 70 univariate simulations with an ice sheet model (Colleoni et al. 2014b, 2016b, Wekerle et al. 2016). In the complete set of sensitivity experiments, the ice sheet thickness in the Forsmark region ranged from 2991 (2650) metres to 3472 (3195) metres when using the B140_Topo1 (B140_Topo2) climate forcing. The corresponding bedrock depression increased from 707 (632) metres to 822 (760) metres. In the Olkiluoto region, the ice thicknesses ranged from 3109 (2791) metres to 3551 (3138) metres when using B140_Topo1 (B140_Topo2) climate forcing, which induced a bedrock depression ranging from −735 (−663) to −846 (−790) metres over the site.

In the second phase of this study, described in the present report, remaining issues identified in the previous study are investigated: i) the impact of different ice dynamics by means of ice sheet modeling, ii) the effect of different surface mass balance parametrisations, iii) the sensitivity of the ice sheet to different climate forcing, and iv) the impact of multi-variate sensitivity experiments on the Late Saalian Eurasian ice sheet topography. In addition, a second ice sheet model, with a different treatment of the ice temperature, but lacking activation of fast flow areas, is used to assess the impact of thermodynamics on the results presented in this study. The results show that the activation of fast-flowing areas in the ice sheet models is the process that most affects the ice thickness. Simulating the LGM Eurasian ice sheet or the last deglaciation (using six different simulated LGM climates from the PMIP3 project) does not help to further constrain those basal ice sheet processes for the Late Saalian. All together, the impact of the Surface Mass Balance (SMB) parametrisations does not induce large variations in ice thickness compared to the reference simulations over the two sites. Conversely, the use of various reconstructed numerical Late Saalian climates, based on six AOGCMs from the PMIP3 project, has a larger influence on the simulated Late Saalian than the SMB parametrisations.

Finally, multi-variate sensitivity experiments are carried out with the Latin Hypercube Sampling method (LHS). Parameters related to SMB and to ice sheet dynamics are sampled evenly, and two sets of 100 multi-variate experiments are carried out. The resulting averaged ice volumes are of about 58 m SLE using B140_Topo1 and about 56 m SLE when using B140_Topo2. This is slightly more than the averaged peak Saalian ice volumes obtained during the first phase of the study (by about 2 to 3 m SLE). The averaged ice thickness at Forsmark, from all simulations, ranges from 3128 to 3460 m. This leads to an averaged bedrock depression of −736 to −822 m. Over Olkiluoto, as already observed in the results of the first phase of the study, the averaged ice thickness is slightly larger. The thickness ranges from 3318 to 3585 m, associated with an averaged bedrock depression of −784 to −856 m. If we consider that the ensemble mean has more meaning than the members presenting the extreme values, the ice thickness obtained in response to changes in the climate forcing is the largest of this study. The maximum simulated steady-state ice thickness over both sites reaches around 4000 metres. If taking into consideration the global ice volume estimate for this time period, even though geological evidence supports a Laurentide ice sheet smaller than during the Last Glacial Maximum, this maximum ice thickness over Forsmark and Olkiluoto is likely to be an overestimation.

Contents

1 Overall framework of the project 7
1.1 Introduction 7
1.2 Overall objectives and methods 9
1.2.1 Work plan 9
1.2.2 Numerical methods 10

2 Implementation of new parametrisations for surface mass balance computations 13
2.1 Description of the new surface mass balance parametrisations 14
2.1.1 Melt coefficients dependency on surface air temperature 14
2.1.2 Temperature variability for PDD calculation 16
2.1.3 Snow and rain partitioning 16
2.1.4 Refreezing 19
2.1.5 Summary: impact of the new parametrisations on surface mass balance 19
2.2 Consequence of updated parametrisations on long-term ice sheet topography 21
2.2.1 Impact on individual parametrisations 21
2.2.2 Impact of combined parametrisations 23
2.3 Impact of the new surface mass balance parametrisations: summary of main results 27

3 Sensitivity to ice sheet model formulation and basal processes 29
3.1 SICOPOLIS ice sheet model experiments 29
3.1.1 Differences in model physics between SICOPOLIS and GRISLI 29
3.1.2 Reference simulations using the SICOPOLIS ice sheet model 31
3.2 Importance of spatial model resolution 36
3.3 The importance of an ice stream restriction in GRISLI 37
3.4 Discussion and summary of section 40

4 Evolution of Eurasian ice streams during the Weichselian deglaciation 43
4.1 Last Glacial Maximum climate forcing 43
4.2 Comparison of pre-industrial and LGM climates in six PMIP AOGCMs 44
4.2.1 Pre-industrial climates 44
4.2.2 Last glacial maximum climates 46
4.3 Last deglaciation experiments 49
4.3.1 Steady-state LGM experiments 50
4.3.2 Transient experiments over the last deglaciation (21–0 kyrs BP) 52
4.4 Discussion and summary of section 62

5 Sensitivity of the Late Saalian ice sheet to climate forcing 63
5.1 Late Saalian surface mass balance using the PMIP3 multi-model simulations 63
5.2 Impact on the simulated Late Saalian ice sheet topography 64
5.3 Discussion and summary of section 65

6 Latin Hypercube Sampling of ice sheet model parameters 67
6.1 Methodology and parameters tested 67
6.1.1 Latin Hypercube Sampling methodology 67
6.1.2 Model formulation used for the ensemble 67
6.1.3 Tested ice sheet model parameters 68
6.2 Results of the LHS simulations 71
6.2.1 Ice sheet volume 71
6.2.2 Ice thickness and bedrock depression at the repository sites 73
6.2.3 The sensitivity of the western part of the Eurasian ice sheet 76
6.3 Discussion and summary of section 79

7 Discussion 81
7.1 Basal drag 81

7.2 Steady-state versus transient ice sheet simulations 84
7.3 Model formulation 85
7.3.1 The choice of climate model 86
7.3.2 The choice of ice sheet model 87
7.4 Laurentide and Eurasian ice sheet extents 87

8 Conclusions 89

Acknowledgements 95

References 97

Appendix 1 105

1 Overall framework of the project

1.1 Introduction

The Swedish Nuclear Fuel and Waste Management Company (SKB) and Posiva Oy (Posiva) are responsible for the management of spent nuclear fuel and radioactive waste generated within the Swedish and Finnish nuclear power program respectively. After feasibility studies and sites investigations, license applications for geological repositories for spent nuclear fuel have been filed for the Forsmark site, southeastern Sweden and Olkiluoto, southwestern Finland, with the aim to construct the repositories within the next decades. The general safety objective of such a repository is to protect human health and the environment on short and long timescales. The geological repository shall keep radiotoxic material separated from man and environment for extended periods of time, up to 1 million years. The repository performance is dependent on e.g. isostatic pressure (attributed to lithosphere load, potential ice sheet load, and pressures generated within the repository itself), the risk for freezing, and changes in groundwater composition. These factors are in turn controlled by e.g. the presence of ice sheets, permafrost and variations in sea level. Thus, to assess long-term repository safety, knowledge of both past and future evolution of Earth's climate is of primary importance.

On timescales of the order of several hundreds of thousands of years, Sweden and Finland have been subjected to regular extensive glaciations. The most extensive glaciation recorded in dated geological proxies occurred over Eurasia around 140,000 years ago (Marine Isotope Stage 6, MIS 6), during the penultimate glacial cycle known as the Late Saalian (Svendsen et al. 2004). Recent numerical reconstructions of the Late Saalian Eurasian ice sheet lead to an ice volume between 60 metres Sea Level Equivalents (m SLE, Lambeck et al. 2006) and 70 m SLE (Peyaud 2006). For comparison, the reconstruction of the Last Glacial Maximum Eurasian ice sheet ICE-5G (Peltier 2004) amounts to about 22 m SLE and is by far less extensive over Siberia (Figure 1-1). In that context, SKB and Posiva asked for expertise of the Euro-Mediterranean Center on Climate Change (CMCC) in long timescale climate processes to simulate the most extensive glaciation that occurred over Eurasia during the last 400 kyrs at the Forsmark and Olkiluoto sites. The present study is a continuation of the analysis carried out by Colleoni et al. (2014b, 2016a, b). The detailed bibliography and the discussion about the Late Saalian glacial maximum global ice volume and topography is found in Colleoni et al. (2014b, 2016a, b), and are therefore not repeated here.

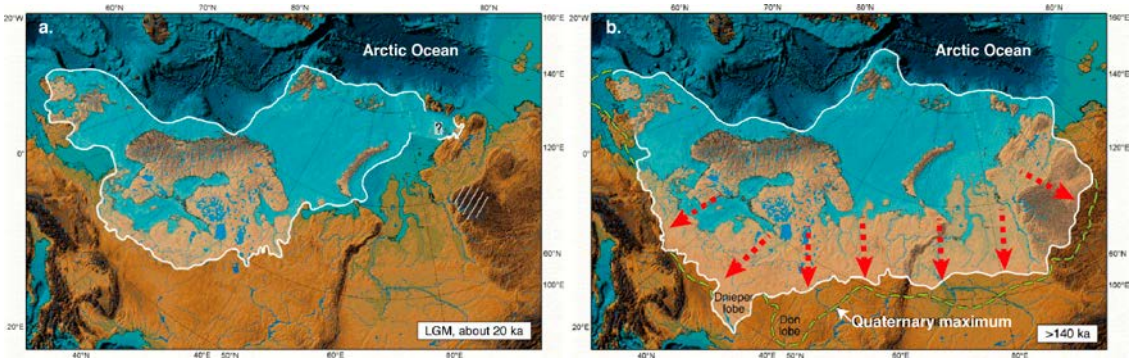

Figure 1-1. *Comparison of the Eurasian ice sheet extent between a. the Last Glacial Maximum (~21 kyrs BP) and b. the Late Saalian glacial maximum (~140 kyrs BP) after Svendsen et al. (2004). Compared to the LGM Eurasian ice sheet extent, the Late Saalian ice sheet expands further South and East (b, red arrows). The LGM Eurasian ice sheet reconstruction (ICE-5G, Peltier 2004) corresponds to an ice volume of ≈ 22 m SLE, which is about three times smaller than the Late Saalian Eurasian ice volume (≈ 70 m to 60 m SLE) simulated by Peyaud (2006) and Lambeck et al. (2006).*

In the first phase of the study, Colleoni et al. (2014b, 2016a, b) simulated the equilibrium Late Saalian climate by means of the NCAR coupled Atmosphere-Ocean-Sea-Ice Community Earth System Model (Gent et al. 2011). Two Late Saalian glacial maximum climate simulations, namely B140_Topo1 and B140_Topo2, including the Late Saalian Eurasian ice sheet from Peyaud (2006) and Svendsen et al. (2004) but differing in the prescribed North American ice sheet topographies were carried out (Colleoni et al. 2014b, 2016a, b). Those simulated climates, and in particular, surface air temperatures and precipitations were used to force the 3D thermo-mechanical ice sheet model GRISLI (Ritz et al. 2001) in order to perform steady-state simulations of roughly 200,000 years on a 20 km horizontal grid resolution. Based on a reference ice sheet simulation, physical parameters affecting the total mass balance of the ice sheet were subsequently varied in univariate sensitivity simulations to obtain an ensemble of possible ice thicknesses over the Forsmark and Olkiluoto sites. Those experiments were repeated for both climate simulations. In total, 70 univariate simulations were performed by Colleoni et al. (2014b, 2016b), including the reference experiments. The physical parameters related to the following five categories were investigated: climate downscaling, surface mass balance, basal drag, ice shelves and the solid Earth.

The difference in ice volume resulting from the use of B140_Topo1 (larger Laurentide ice sheet) and B140_Topo2 (smaller Laurentide ice sheet) was about 2 (m SLE), mostly due to geographical compensations between surface air temperature and precipitation differences (Figure 1-2). The largest ice sheet sensitivity was simulated for the surface mass balance parameters and basal drag parameter categories (Figure 1-2). The basal drag parameters provided the upper and lower bound in ice thickness over Forsmark in all the set of experiments, leading to an increase by up to 7 % with large basal drag and decrease up to 7 % with larger fast flow areas relative to the reference simulations. In those two cases, the resulting ice thicknesses over Forsmark ranged from 2991(2650) metres to 3472 (3195) metres when using B140_Topo1 (B140_Topo2) climate forcing (Figure 1-2). The bedrock depression corresponding to these two extreme cases increased from −707 (−632) metres to −822 (−760) metres over Forsmark. The Olkiluoto site showed a comparable sensitivity to model parameters. Therefore, the upper and lower bound of ice thicknesses at Olkiluoto were also obtained with the experiments testing the impact of the basal drag coefficient. The simulated upper and lower bound for ice thicknesses ranged from 3109 (2791) metres to 3551 (3138) metres when using B140_Topo1 (B140_Topo2) climate forcing. Those simulations induced a bedrock depression ranging from −735 (−663) to −846 (−790) metres over Olkiluoto (Figure 1-2).

In the analysis performed by Colleoni et al. (2014b) (see also Colleoni et al. 2016b and Wekerle et al. 2016), it was shown that several aspects of the ice dynamics could be improved to better constrain the range of realistic ice thicknesses attributed to the Late Saalian glaciation:

(1) Improve and constrain surface mass balance. Using a standard deviation of air surface temperature dependent on elevation changes (Fausto et al. 2009), Positive Degree Day melting coefficients C_{snow} and C_{ice} expressed as a function of temperature (Tarasov and Peltier 2002) instead of using fixed values, a partitioning between rain and snow fraction (Marsiat 1994) and a physically-based refreezing scheme (Janssens and Huybrechts 2000).

(2) Constrain the ice stream areas. Focus on the Weichselian glaciation (Last Glacial Maximum, LGM) to better constrain the extent of ice-stream areas, potentially validated by geomorphological evidence from this specific glaciation.

(3) Use a different ice sheet model. For example use the SICOPOLIS ice sheet model (Greve 2005) to test the impact of a polythermal ice sheet model on the geometry of the Late Saalian Eurasian ice sheet.

(4) Use different climate forcing. Different ice modeling studies report discrepancies in ice geometry obtained using different climate forcing (e.g. Charbit et al. 2007, Kirchner et al. 2011). Since Colleoni et al. (2014b, 2016a, b) are the only studies dealing with the Late Saalian climate with coupled Atmosphere-Ocean General Circulation Models (AOGCM), it was suggested to use a perturbed approach similarly to Quiquet et al. (2013). This method implies that the Late Saalian climate anomaly relative to pre-industrial is superimposed on top of simulated pre-industrial climates obtained from different AOGCMs participating to the PMIP3 project.

(5) Perform multi-parameter simulation ensembles. In the first phase of the study, univariate experiments were performed. Following Stone et al. (2010) and Applegate et al. (2012), it was decided to use the Latin Hypercube Method in order to test simultaneous changes of the ice sheet related parameters to increase the robustness of the sensitivity simulation ensemble.

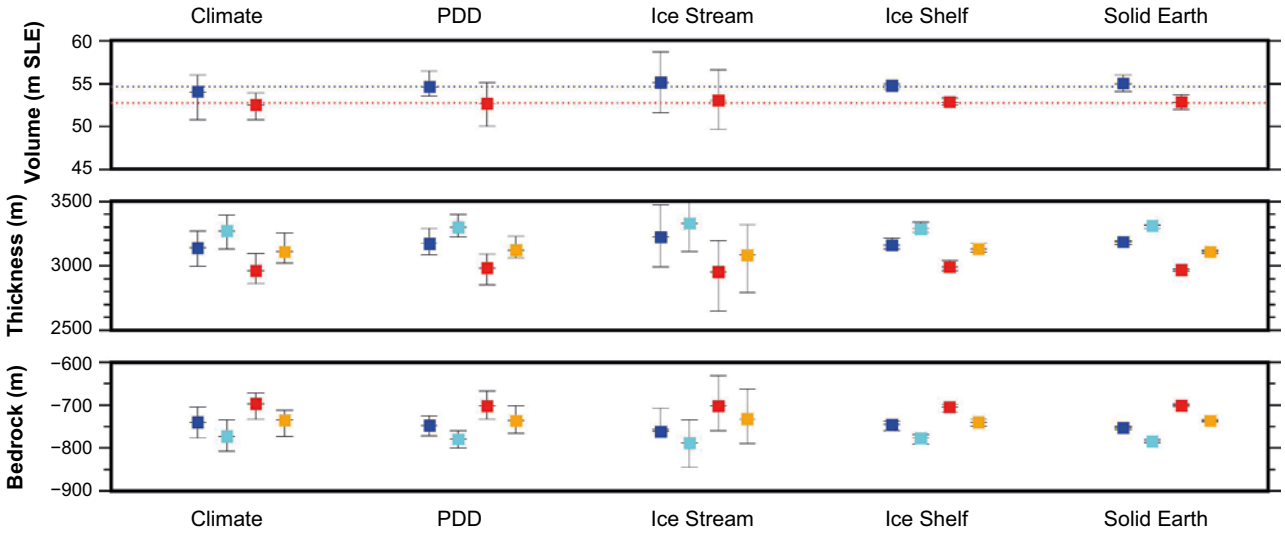

Figure 1-2. *Summary of the main results from Colleoni et al. (2014b, 2016b). Simulated Eurasian total ice volumes (m SLE) using B140_Topo1 (blue. Larger Laurentide ice sheet) and B140_Topo2 (red. Smaller Laurentide ice sheet), ice thickness (meters) and bedrock elevation (meters) for both topographies at Forsmark (blue and red) and at Olkiluoto (cyan and orange) sites. Values are categorised into five groups including the ice sheet model parameters that were varied in the simulations: i) Climate (lapse rate and precipitation factor), ii) Positive Degree Day (PDD, melting coefficients and standard deviation of temperature), iii) Ice Stream (dragging coefficient and sediment thickness), iv) Ice Shelves (calving and basal melting) and v) Solid Earth (geothermal heat flux and relaxation time of astenosphere-listosphere). Error bars indicate the maximum and minimum values obtained in each of the categories considered in the plot.*

1.2 Overall objectives and methods

1.2.1 Work plan

In this second phase of the study, we follow the suggestions that arose from the first phase of the assessment to obtain a more robust estimate of the range of ice thicknesses over Forsmark and Olkiluoto. The investigations are divided in four main steps, also displayed in Figure 1-3.

1. Investigating the impact of horizontal grid resolution and the ice sheet model physics. In addition to GRISLI, we use the SICOPOLIS ice sheet model (Greve 2005) since it considers a polythermal ice layer. Moreover, SICOPOLIS does not include any specific treatment for ice streams, which potentially induces large discrepancies in the simulated ice sheet geometry compared with GRISLI. SICOPOLIS is a state-of-the-art ice sheet model and has been used e.g. in various previous assessments conducted by POSIVA. In addition, SICOPOLIS actively participates in the ongoing SeaRISE project (Levermann et al. 2014) as well as PLIOMIP (de Boer et al. 2015). In the present study, three different horizontal grid resolutions are tested in both GRISLI and SICOPOLIS, 40 km, 20 km and 10 km.
2. Testing the impact of different surface mass balance formulations. In this part, different refreezing and melting parametrisations are implemented and tested with GRISLI. In addition, we also tested the late Saalian ice sheet sensitivity to climate forcing. For that, an anomaly method is used to derive new Late Saalian climates based on outputs from different coupled climate models of the PMIP3 intercomparison project.
3. Elaborate constraints on the Shallow Shelf Approximation (SSA). GRISLI treats large areas with the SSA. As a consequence, the basal velocities are larger over wider areas than when using the Shallow Ice Approximation (SIA) and the areas considered as ice streams might be overestimated. To investigate these mechanisms, a topographic criterion is used to restrict areas where the SSA is applied in GRISLI. We use outputs from the PMIP intercomparison project to construct LGM climate forcings. LGM steady-state and transient simulations are carried out to provide some constraints on this criterion.

4. Multi-variate sensitivity simulations by means of the Latin Hypercube method. During the first phase of the study we only varied one parameter for each simulation. Therefore, to get a more statistically robust simulation ensemble, the parameter space of the ice sheet model is sampled and a grid of 100 multi-parameter combinations is defined (See Chapter 5). We selected a set of ten parameters that includes ice dynamics and surface mass balance parameters. Within this framework, we do not assess the importance of model formulation listed in the previous point but we test the impact of changing the parameter values for a specific model configuration. However, the range of parameter values covers the uncertainties related to surface mass balance formulations and ice mechanics. This Latin Hypercube method is applied to GRISLI results only, i.e. not to SICOPOLIS results, and it is repeated for each of the two Late Saalian climate simulations performed in the first phase of the study.

1.2.2 Numerical methods

In this second phase, no climate simulations are performed. Instead, the Late Saalian climate forcing corresponds to the two Late Saalian climates, B140_Topo1 and B140_Topo2, computed during the first phase of the study (Colleoni et al. 2014b, 2016b) using the CESM 1.0.5 (Gent et al. 2011). For the present report, we however display the air surface temperature and precipitation fields from the pre-industrial simulation, and the comparison with the two Late Saalian simulations in Figure 1-4. For further details about the climate simulations, see Chapter 3 in Colleoni et al. (2014b, 2016b). Furthermore, in this second phase, we consider several simulated LGM climates, obtained by means of AOGCM, from the PMIP3 inter-comparison project publicly available on the main CMIP5 data portals. See Chapter 4 for a detailed analysis of these climates.

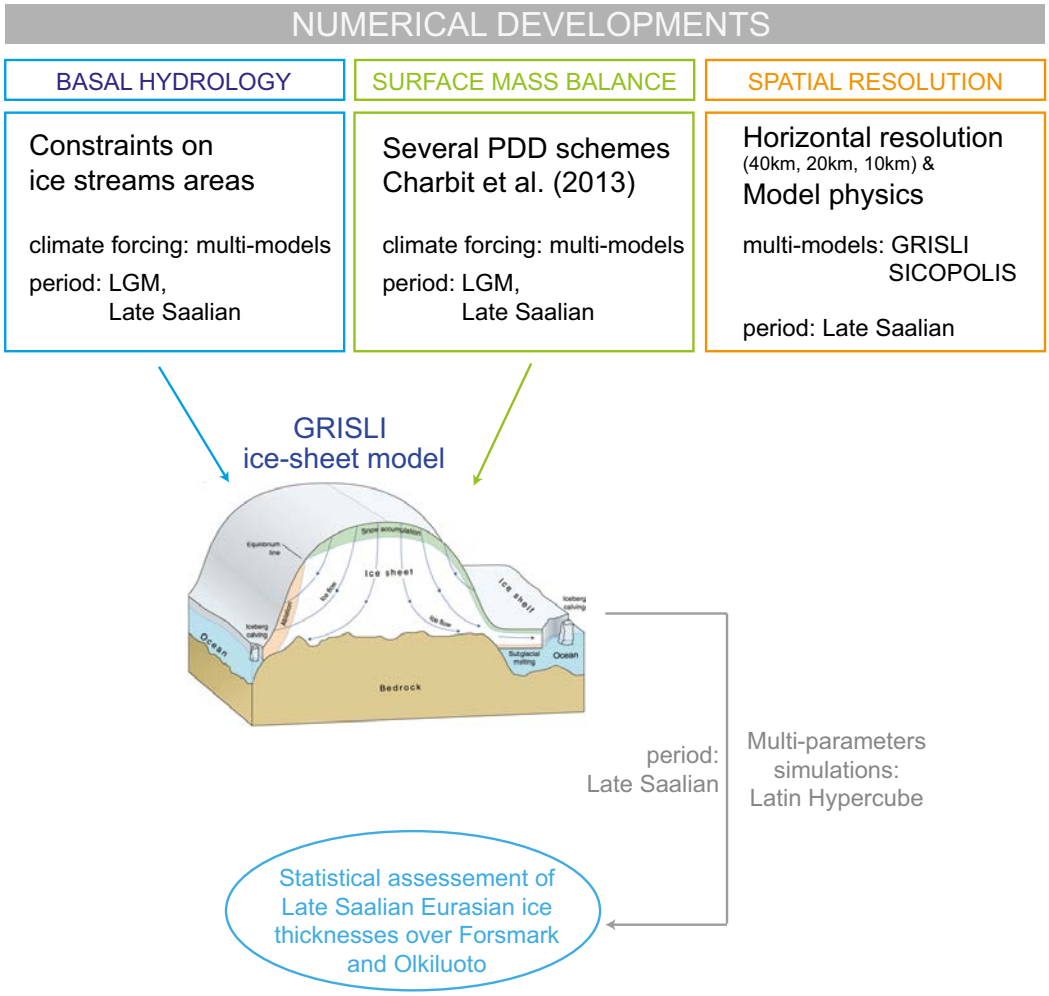

Figure 1-3. *Scheme of the work packages that were investigated in the present study. Source for the ice sheet transect: http://www.lima.nasa.gov/antarctica.*

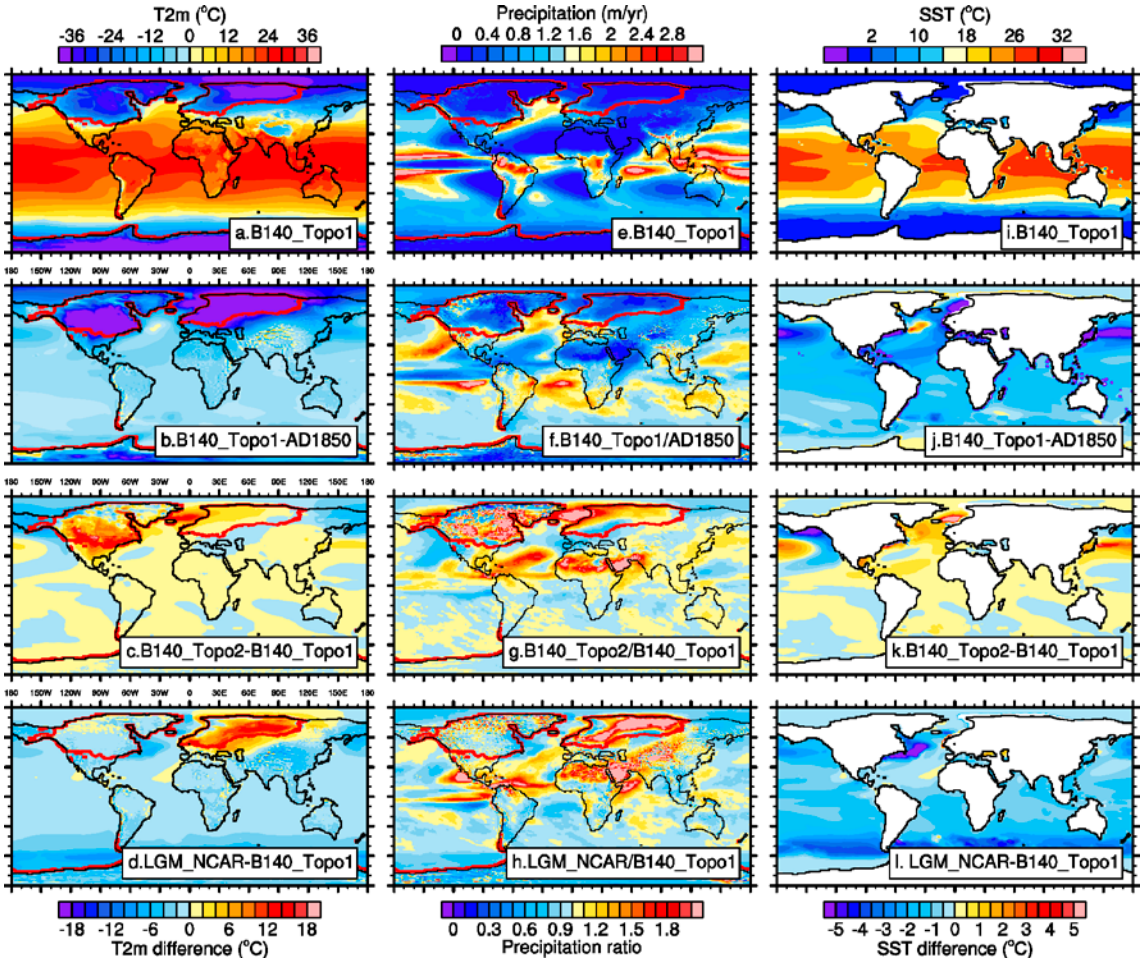

Figure 1-4. *Simulated annual mean surface temperature at 2 meters, precipitation and sea surface temperatures (SST): a) B140 Topo1 annual mean air surface temperature (°C). Note that the scale minimum is saturated. Annual mean air surface temperature difference (°C): b) between B140 Topo1 and pre-industrial simulation (hereafter AD1850); c) between B140 Topo1 and B140 Topo2; d) between LGM NCAR and B140 Topo1. e) B140 Topo1 annual mean precipitation (m/yr). Annual mean precipitation changes (ratio, dimensionless): f) between B140 Topo1 and AD1850; g) between B140 Topo1 and B140 Topo2; h) between LGM NCAR and B140 Topo1. i) B140 Topo1 annual mean sea surface temperature (°C, SST). Annual mean SST difference (°C): j) between B140 Topo1 and AD1850; k) between B140 Topo1 and B140 Topo2; l) between LGM NCAR and B140 Topo1. Red contours correspond to B140 Topo1 ice sheet topography.*

The ice sheet simulations are carried out using the GRISLI and the SICOPOLIS ice sheet models. An exhaustive description of the physics of GRISLI is provided in Chapter 4 in Colleoni et al. (2014b, 2016b), whereas the main physical differences between GRISLI and SICOPOLIS are reported in Chapter 3 of the present report. Similarly to the ice sheet simulations performed in the first phase of the study, the ice sheet simulations are forced with steady-state climate forcing and run for 200,000 model-years over a 20 km horizontal resolution grid of the Eurasian domain (Figure 1-5). All the simulations in the present report are branched from the two reference simulations REF_Topo1 and REF_Topo2 carried out in the previous phase of the study (Figure 1-5, Colleoni et al. 2014b, 2016b). As such, the different simulations are consistent and have the same spin-up state. However, it should be noted that the reference simulations REF_Topo1 and REF_Topo2 in the present report differs slightly from the ones in Colleoni et al. (2014b, 2016b) as they have been prolonged for 200 kyrs. The adjusted reference simulation ice sheet values are found in Table 1-1. This was made in order to bring the Topo2 simulations to complete equilibrium, since in phase one, a few of those simulations were not totally spin-up. However, this small adjustment does not affect the conclusions in Colleoni et al. (2014b, 2016b). Several parametrisations related to the surface mass balance processes are implemented and tested in phase two of the study. The conclusive part of phase two consists of two ensembles of 100 multi-variate sensitivity simulations, in which GRISLI space parameters are sampled by means of the Latin Hypercube method.

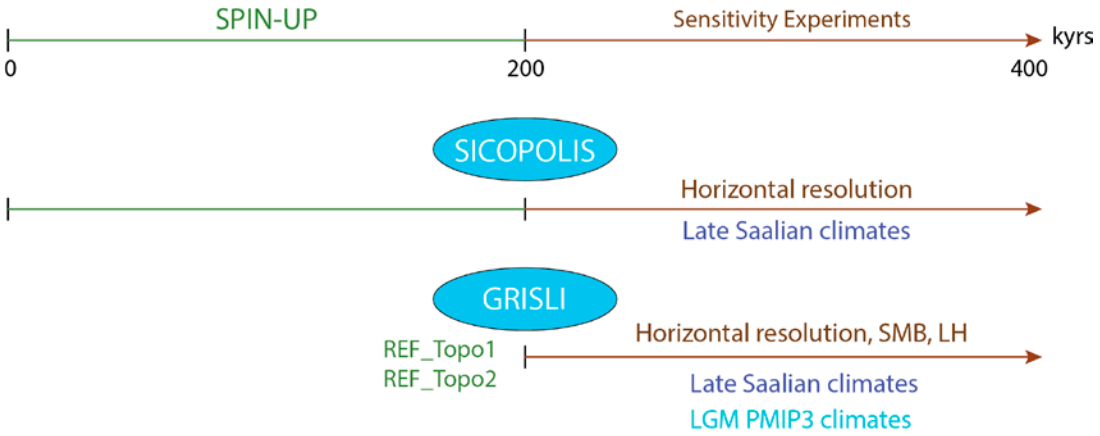

Figure 1-5. *Numerical scheme of the ice sheet simulations performed in both phase one and two of the study. Two ice sheet models are considered, GRISLI (Ritz et al. 2001) and SICOPOLIS (Greve 2005). For each model, two different spin-up simulations of 200 kyrs years are computed, forced with B140_Topo1 and B140_Topo2 Late Saalian climate forcing (Colleoni et al. 2014b, 2016a, b). In the case of GRISLI, the spin-up corresponds to the reference simulations carried out during the first phase of the study, namely REF_Topo1 and REF_Topo2 (Colleoni et al. 2014b, 2016b). In this second phase, the impact of horizontal resolution (up to 10 km), various surface mass balance-related parametrisations (SMB) and various climate forcings for the last two glaciations is investigated. The conclusive part of the second phase consists of computing two ensembles of 100 simulations following the Latin Hypercube method (LH).*

The new implementations or physical methods used to investigate each of the work packages reported in Figure 1-3 are described at the beginning of each corresponding section of the present report.

Table 1-1. Simulated ice volume, ice thickness and bedrock depression for the two reference simulations REF_Topo1 (B140_Topo1 climate forcing) and REF_Topo2 (B140_Topo2 climate forcing) performed in phase two of the study. The changes relative to the reference simulations in phase 1 of the study are small (here expressed in percent). The numbers reported in this table have been obtained with the same GRISLI ice sheet model setup as in Colleoni et al. (2014b, 2016b).

Reference simulation	Eurasian ice sheet volume		Ice thickness				Bedrock depression			
			Forsmark		Olkiluoto		Forsmark		Olkiluoto	
	m SLE	%	m	%	m	%	m	%	m	%
REF_Topo1	53.27	−2.8	3101.4	−3.0	3229.6	−2.8	−731.3	−2.8	−763.3	−2.6
REF_Topo2	51.51	−2.6	2914.8	−1.8	3062.5	−1.7	−684.7	−2.2	−720.5	−2.1

2 Implementation of new parametrisations for surface mass balance computations

In our modelling framework we use a thermo-mechanical ice sheet model to compute the evolution of the ice geometry and vertical properties. Because the ice sheet model used is not coupled to a climate model, we use outputs from previous climate model simulations as climate forcing. From these variables, namely near surface air temperature and total precipitation, we compute the surface mass balance (SMB) with a positive degree day (PDD) model (Reeh 1989). This method is commonly used in the paleoclimate community but has recently been criticised for its application to ice sheet simulations under warm climate conditions (e.g. Van der Berg et al. 2011). Robinson et al. (2010) compared the use of the PDD method with another alternative parametrisation based on radiation changes due to albedo and insolation (ITM method). The simulations carried out over Greenland show that both the PDD and the ITM method produce similar results. The ITM method, however, leads to melt rates slightly closer to observations than the PDD method because the former model accounts for radiative changes, which is not the case with the PDD method. Contrary to the PDD method, the ITM method requires input of daily atmosphere energy balance data. Such daily data were not saved during the climate simulations performed in the first phase of the study (Colleoni et al. 2014b, 2016a, b). Therefore we employed the PDD method. Because we do not compute the climate ice sheet feedbacks during runtime (such as the impact of ice sheet surface changes on atmospheric circulation), we refer to this kind of experiments as *steady state* experiments. One should keep in mind, however, that the climate forcings (surface air temperature and total precipitation) are corrected during runtime in the ice sheet simulations to account for the impact of ice sheet surface elevation changes on temperature by means of an atmospheric lapse rate (λ). Subsequently, the total precipitations are corrected using a ratio of precipitation change (γ) proportional to the surface air temperature evolution during the ice sheet simulations. The full description of the surface mass balance parametrisation can be found in the report from the first phase of the study (Section 4.1.7 in Colleoni et al. 2014b, 2016b).

During the first phase of the study, we highlighted the strong sensitivity of the simulated Late Saalian Eurasian ice sheet to climate corrections and surface mass balance parametrisations. As a consequence, we decided to implement some literature-based modifications to the standard original PDD parameters in this second phase. In the following section, we describe, quantify and discuss the impact of various parametrisations of individual processes such as ice and snow melt, partitioning between rain and snow, refreezing, and air surface temperature variability on the simulated Eurasian ice sheet topographies. The main equations of the PDD model are provided below in order to illustrate the changes that were introduced in the SMB computation method, but the reader might want to refer to Colleoni et al. (2014b, 2016b) for a full description of formalism and terminology.

The ice sheet surface mass balance is the difference between the accumulation and the ablation. The accumulation is deduced from the precipitation (solid and/or liquid) and eventually refreezing of meltwater. The ablation is described by a PDD model based on an empirical relationship between the number of positive degree days and the snow and ice melting rates. The number of positive degree days (PDD) integrated over one year (between t=1 and t=365 days) is given by:

$$PDD = \frac{1}{\sigma\sqrt{2\pi}} \int_{t=1}^{365} \int_{T'=0}^{\infty} \exp\left(\frac{-\left(T' - T_d\right)^2}{2\sigma^2}\right) dt dT' \qquad \text{(Equation 2-1)}$$

Where T_d is the daily temperature and σ is the standard deviation of the daily temperature. The daily temperature is computed from the July and the mean annual near-surface air temperature, assuming temperature follows a sinusoidal cycle:

$$T_d(t) = T_{ann} + (T_{july} - T_{ann}) \cos\left(\frac{2\pi t}{365}\right) \qquad \text{(Equation 2-2)}$$

The computed PDDs are preferentially used to melt the fresh snow (from the annual accumulation), at a linear rate of C_{snow} . Once the fresh snow is melted, the remaining PDDs are used to melt any existing superimposed ice formed by refreezing, at a rate of C_{ice}. Finally, if all fresh snow and eventual superimposed ice are melted, the remaining PDDs are used to melt the glacier ice at a rate of C_{ice}.

The PDD model is empirical and several improvements from the original model of Reeh (1989) are available in the literature. We test some of them in this section. In total, we perform eight simulations testing the separate or combined effect of those processes on the SMB and on the resulting ice sheet thickness. All the simulations are branched on the Ref_Topo1 spin-up ice topography and forced by the simulated Late Saalian climate B140_Topo1 from the first phase of the study. Subsequently, we perform the same set of simulations a second time but branched on the REF_Topo2 spin-up ice topography and forced by the B140_Topo2 climate. We carry out the simulations for 200 kyrs under stead-state climate forcing (details and references are reported in Table 2-1). The values of the physical parameters that are not under investigation here are similar to those of the REF_Topo1 simulations and are reported in Appendix 1 (Table A1-1).

Table 2-1. Summary of simulations testing parametrisations of various SMB-related processes in GRISLI: the relationship of melt coefficients C_{ice} and C_{snow} upon surface air temperature (Tarasov and Peltier 2002), the relationship of the daily surface air temperature variability upon elevation (Fausto et al. 2009), the partioning between rain and snow (Marsiat 1994; and an *ad hoc* temperature threshold) and the refreezing of the rain fraction at the surface of the ice sheet (Janssens and Huybrechts 2000). Note that in the reference simulation REF_Topo1 and REF_Topo2, all those parameter values are prescribed following Table A1.

Simulation ID	Tested PPD and accumulation parametrisations
SMB1	Melt coefficients (Tarasov and Peltier 2002)
SMB2	Temperature variability (Fausto et al. 2009)
SMB3	Rain fraction (p_{solid} temperature threshold)
SMB4	Rain fraction (Marsiat 1994)
SMB5	Refreezing (Janssens and Huybrechts 2000)
SMB6	Rain fraction (Marsiat 1994) + refreezing (Janssens and Huybrechts 2000)
SMB7	Melt coefficients (Tarasov and Peltier 2002) + rain fraction (Marsiat 1994) + refreezing (Janssens and Huybrechts 2000)
SMB8	Melt coefficients (Tarasov and Peltier 2002) + temperature variability (Fausto et al. 2009) + rain fraction (Marsiat 1994) + refreezing (Janssens and Huybrechts 2000)

2.1 Description of the new surface mass balance parametrisations

2.1.1 Melt coefficients dependency on surface air temperature

In the PDD model, melt is linearly related to the number of PDDs through the melt coefficients, C_{snow} and C_{ice}. In the original model of Reeh (1989) (hereafter denoted RE1989), the melt coefficients are prescribed constant in time and spatially homogeneous with typical values of 3 and 8 mm d^{-1} $°C^{-1}$ for C_{snow} and C_{ice}, respectively. However, observations on present-day glaciers and ice caps have revealed that this assumption is a crude approximation as melt coefficients are highly variable (Braithwaite 1995, Hagen et al. 1999, Braithwaite and Zhang 2000). To account for this variability in our large scale ice sheet model, and in order to reproduce results obtained with surface energy balance models, Tarasov and Peltier (2002) (hereafter denoted TP2002) suggested a surface air temperature dependency for the two melt coefficients:

$$C_{ice} = \begin{cases} C_{ice}^{c} & T < T^{c} \\ \frac{C_{ice}^{c} - C_{ice}^{w}}{(T^{w} - T^{c})^{3}} \; (T^{w} - T_{jja})^{3} + C_{ice}^{w} & T^{c} \leq T < T^{w} \\ C_{ice}^{w} & T \geq T^{w} \end{cases}$$

$$C_{snow} = \begin{cases} C_{snow}^{c} & T < T^{c} \\ \frac{C_{snow}^{c} - C_{snow}^{w}}{T^{w} - T^{c}} \; T_{jja} + C_{snow}^{c} & T^{c} \leq T < T^{w} \\ C_{snow}^{w} & T \geq T^{w} \end{cases}$$

(Equation 2-3)

Where T^{c} (resp. T^{w}) are the transition temperatures for cold (resp. warm) melt coefficient C^{c} (resp. C^{w}).

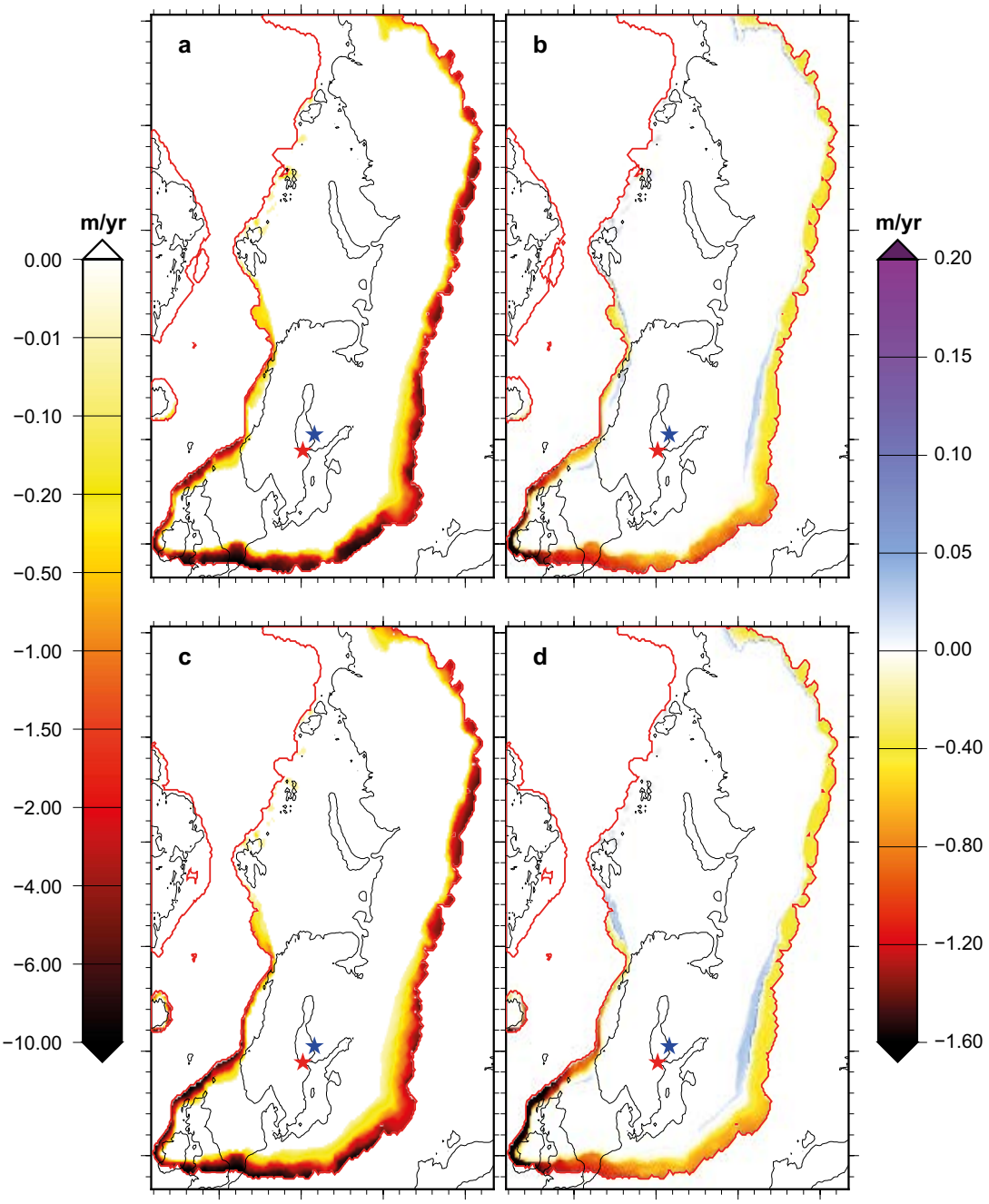

Figure 2-1. *The melt coefficients dependency on surface air temperature (simulation SMB1, Table 1-1). (a) Annual mean ablation rates (m/yr), under B140_Topo1 climate forcing and branched on REF_Topo1 spin-up ice topography, obtained with the reference PDD parametrisation RE1989. (b) The difference with the TP2002 PDD parametrisation (RE1989 -TP2002). Similarly, (c) shows the ablation rates derived using B140_Topo2 climate forcing and branched from REF_Topo2 spin-up ice topography when using the reference PDD parametrisation RE1989, whereas (d) shows the corresponding differences with the TP2002 parametrisation (RE1989 -TP2002). Note that by convention, in GRISLI, the absolute ablation field has a negative sign. Also note that the red contour corresponds to the extent of the ice sheet at the end of each SMB simulation and not to the reference simulations.*

The TP2002 model allows for spatially variable melt coefficients following the surface air temperature pattern. Also, because the temperature is evolving due to surface elevation changes during the simulation runtime, as previously mentioned, melt coefficients in the TP2002 model are not constant in time.

The values used in the TP2002 model are: $T_c = -1$ °C, $T_w = 10$ °C, $C^c_{ice} = 17.22$ mm d^{-1} °C^{-1}, $C^w_{ice} = 8.3$ mm d^{-1} °C^{-1}, $C^c_{snow} = 2.65$ mm d^{-1} °C^{-1}, $C^w_{snow} = 4.3$ mm d^{-1} °C^{-1}. Thus, for the same amount of PDDs, ice melt is more efficient at low temperature than at high temperature. The opposite is true for snow melt. Also, in the TP2002 model, C_{ice} is systematically higher than in RE1989.

Because of the warmer climate conditions at the ice sheet margins, the melt coefficient for snow, C_{snow}, in TP2002 is higher than the one in RE1989. As a consequence, in the TP2002 model, the margin experiences at least a 0.4 m yr^{-1} additional melting compared to the RE1989 (Figure 2-1b). The differences are even more pronounced at the westernmost tip of the ice sheet where the difference reaches more than 1.5 m in ice melt. Conversely, the TP2002 model produces a thin band of lower melt in the highest regions of the ablation area, due to lower air temperature (and subsequent lower C_{snow}) than in the RE1989 model. However, this decrease in melt is very limited (one order of magnitude smaller) compared to the general increase in melt in the ablation areas. These results are comparable with the ones obtained when using the B140_Topo2 climate forcing (Figure 2-1d). When using the B140_Topo2 climate forcing, the increase in melt is slightly enhanced compared with the simulations using B140_Topo1, because the former air temperatures are warmer on the western part of the ice sheet by about 4 °C (see Figure 3-4 in Colleoni et al. 2014b, 2016b).

2.1.2 Temperature variability for PDD calculation

The PDD calculation in the RE1989 model accounts for the daily surface air temperature variability using the standard deviation, σ. This number is usually considered constant in time and homogeneous in space. It is usually chosen around 5 °C, as representative of a mean value for all automatic weather stations available on the Greenland ice sheet. In the reference simulations of phase one, it was set to 5 °C. However, Fausto et al. (2009) have shown that the standard deviation of Greenland surface air temperature is highly variable from one station to another. In particular, there is a strong positive correlation of the standard deviation with altitude. To account for that, and following Charbit et al. (2013), we implement the relationship between the standard deviation, σ and the surface elevation, S, suggested by Fausto et al. (2009):

$$\sigma(x,y,t) = 1.574\ ^{\circ}C + 1.2224\ ^{\circ}C\ km^{-1} \times S(x,y,t) \qquad \text{(Equation 2-4)}$$

In this parametrisation, the standard deviation reaches 5 °C only above 2800 m a.s.l. This means that at low elevation, the standard deviation is much lower in the Fausto et al. (2009) relationship than the constant default value of 5 °C used in the reference simulations and in most of the simulations in the first phase of the study. This has a strong impact on the simulated ablation as shown in Figure 2-2. The entire ablation area experiences a decrease in ablation of around 0.6 m yr^{-1} (Figure 2-2b). At the westernmost tip of the ice sheet the local decrease in ablation can be higher than 1.5 m yr^{-1}. As in the case of the melt coefficients, the ablation obtained when using B140_Topo2 climate affects a slightly larger area than when using B140_Topo1 climate (Figure 2-2d).

2.1.3 Snow and rain partitioning

Along with surface air temperature, total precipitation simulated by a climate model is the second climate forcing generally used in ice sheet models. In the simplest approach, the total precipitation (P) is entirely converted into snow accumulation (*Acc*) over the ice sheet using the mean ice density. This was the approach followed for most of the simulations during the first phase of the study (Colleoni et al. 2014b, 2016b). In more sophisticated approaches, a partitioning parametrisation (P) is used to separate snow and rain fractions (e.g. Huybrechts 2002, Greve 2005).

In GRISLI, two major simple partitioning methods have been considered. The first model defines a daily surface air temperature threshold (p_{solid}) below which all precipitation (P) is turned into snow (P_s, Equation 2-5). Above this threshold, the precipitation is considered as rainfall and does not accumulate.

$$\frac{P_s}{P} = \begin{cases} 0\ , & T \geq p_{solid} \\ 1\ , & p_{solid} > T \end{cases} \qquad \text{(Equation 2-5)}$$

Note that T corresponds to the daily temperature calculated by means of the PDD equation. Instead of this abrupt temperature threshold, a refinement of this method has been proposed by Marsiat (1994) considering a linear transition between solid precipitation only to liquid precipitation only according to:

$$\frac{P_s}{P} = \begin{cases} 0 \ , & T \geq 7°C \\ (7°C - T)/17°C \ , & 7°C \geq T \geq -10°C \\ 1 \ , & -10°C \geq T \end{cases} \qquad \text{(Equation 2-6)}$$

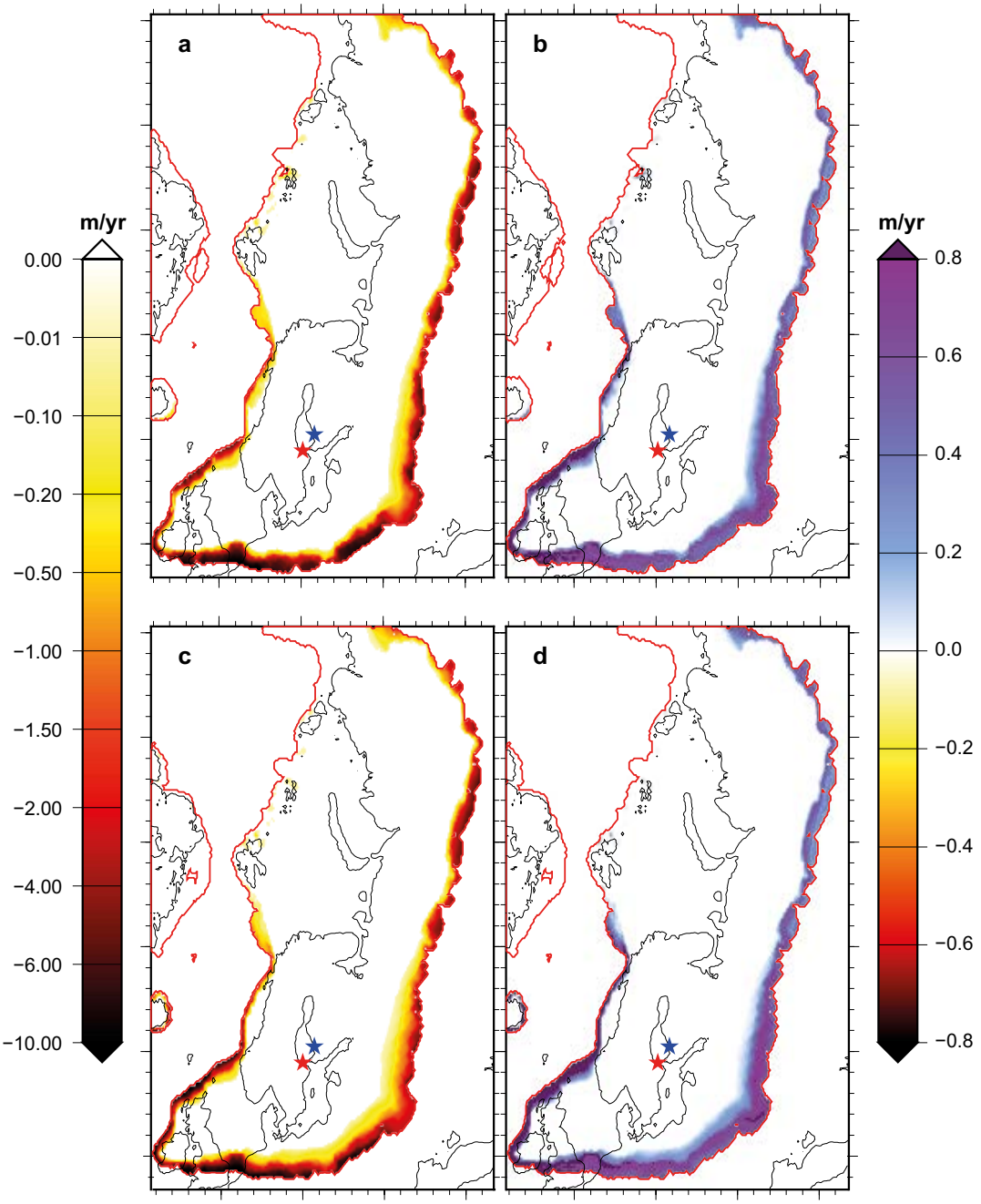

Figure 2-2. *Temperature variability for PDD calculations. (a) Annual mean ablation rates (m/yr) computed under B140_Topo1 climate forcing and branched on REF_Topo1 spin-up ice topography obtained with the reference parametrisation RE1989. (b) The difference with the Fausto et al. (2009) parametrisation (RE1989 – Fausto, simulation SMB2). Similarly, (c) shows the same ablation rates derived with the B140_Topo2 climate forcing and from the spin-up ice topography REF_Topo2, along with the differences with the Fausto et al. (2009) parametrisation shown in (d). Note that by convention, in GRISLI, the absolute ablation field has a negative sign. Also note that the red contour corresponds to the extent of the ice sheet at the end of each SMB simulation and not to the reference simulations.*

Note that contrary to the default GRISLI fractioning based on the p_{solid} threshold, the Marsiat (1994) method uses monthly temperatures and precipitations. The Marsiat (1994) model largely reduces the accumulation in the western part of the ice sheet, whereas the threshold is widespread to a narrow band along the southern margins (Figure 2-3b). Because of the large range of temperature over which the rain fraction is computed, the Marsiat (1994) model reduces the accumulation also at relatively high elevations. When the rain fraction is taken into account, accumulation is reduced by 0.1 to 0.5 m/yr when accounting for the prescribed temperature threshold p_{solid} (Figure 2-3c) ,whereas when using the parametrisation from Marsiat (1994), the reduction in accumulation is larger, ranging from 0.4 to more than 1.5 m/yr (Figure 2-3b).

Note that in the reference PDD scheme of Reeh (1989), the rain does not contribute to the accumulation. Therefore, the SMB obtained with p_{solid} or with the Marsiat (1994) model is lower than when converting all precipitation into snow. The combination of a more sophisticated rain fraction parametrisation together with a scheme that allows for rain refreezing at the surface of the ice sheet would compensate for the decrease in accumulation resulting from the use of a method partitioning the rain and the snow fractions. In the next section, we discuss the impact of a more physically-based refreezing scheme on the computation of the annual super-imposed ice layer due to refreezing of the rain fraction.

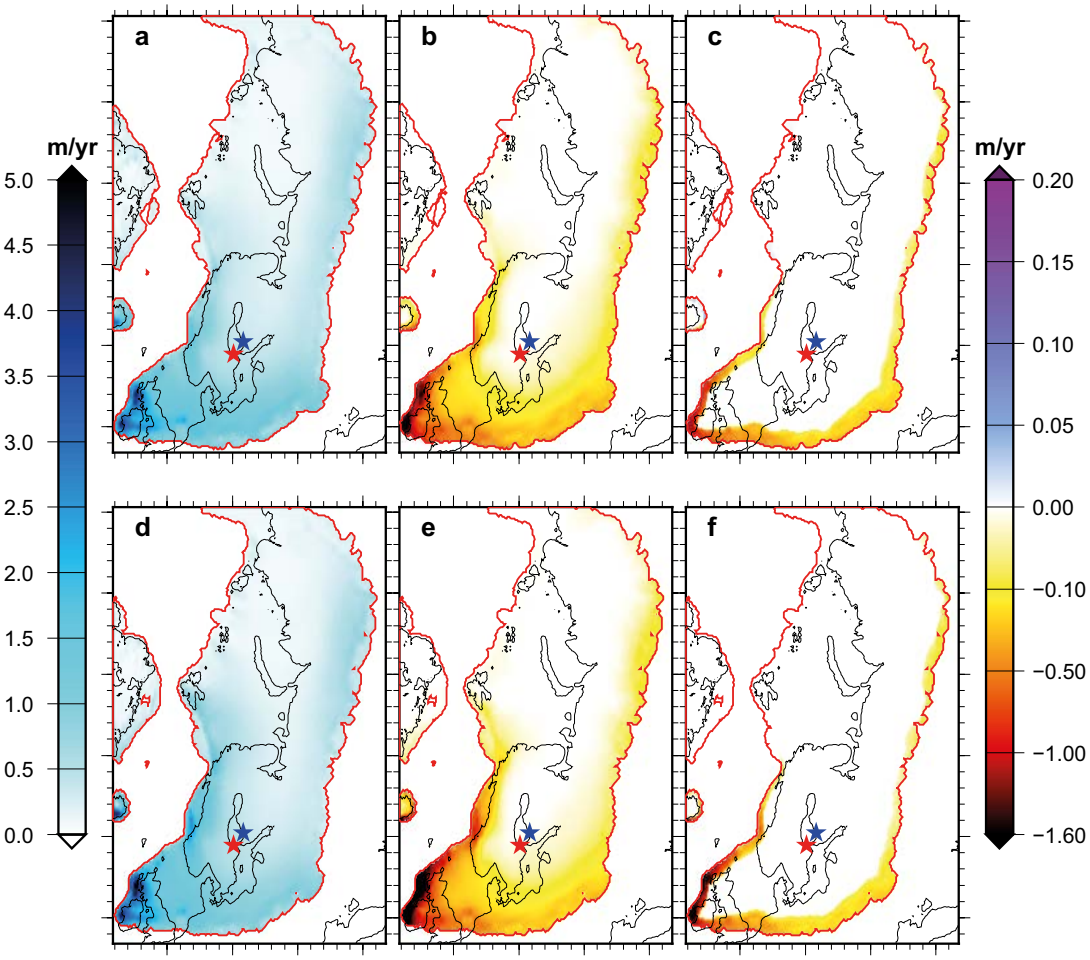

Figure 2-3. *(a): Annual mean accumulation rates (m/yr) computed under B140_Topo1 climate forcing and branched from the REF_Topo1 spin-up ice topography. The reference ice topography from REF_Topo1 is shown in (a) while the difference in mean accumulation (new-reference) are shown in: (b) when using Marsiat (1994) partitioning (SMB4), (c) using the temperature threshold p_{solid} for partitioning (SMB3), (d), (e) and (f) are similar to (a), (b) and (c) but simulations are branched from REF_Topo2 spin-up ice topography and use B140_Topo2 climate forcing. Note that the red contour corresponds to the extent of the ice sheet at the end of each SMB simulation and not to the reference simulations.*

2.1.4 Refreezing

In the RE1989 model, if the surface temperature is low enough, part of the melt will refreeze, forming a super-imposed layer of ice on top of the glacial ice. The maximum amount of refreezing, *csi*, allowed with this model is set arbitrarily to 60 % of the accumulation. The refreezing in RE1989 is largely empirical and does not account for the rain falling over the ice sheet.

More recently, physically-based refreezing methods have been developed and incorporated successfully into large scale ice sheet models. The most commonly used is the one of Janssens and Huybrechts (2000), hereafter denoted JH2000, based on the original formulation of Pfeffer et al. (1991). The JH2000 formulation relies on a strict thermodynamical consideration assuming that the amount of refreezing is proportional to the heat needed to warm the thermo-active layer up to the melting point:

$$SIF = \begin{cases} min(\ P_r + M\ ,\ f_{cap}(P_s - M) - \frac{d \times c_l}{L}\ min(T_{ann}, 0)), & P_s \geq M \\ min(\ P_r + M\ ,\ -\frac{d \times c_l}{L}\ min(T_{ann}, 0)), & M > P_s \end{cases} \quad \text{(Equation 2-7)}$$

where: d is the thickness of thermoactive layer (assumed to be 1 m), f_{cap} is a capillarity factor (with a value of 2.2), L is the latent heat of fusion (3.35×10^5 J kg^{-1}), c_l the ice specific heat capacity (depends on the ice temperature). P_r and P_s are the rain and snow derived from the total precipitation and M is the snowmelt. Note that Equation 2-7 here has been modified from JH2000 following TP2002.

As shown in Figure 2-4b, the JH2000 model reduces the amount of refreezing where the temperature and precipitation are highest, i.e. along the southern margins of the ice sheet. Hence, the westernmost part of the ice sheet shows a mean annual reduction of more than 0.8 m of refrozen water. However, over some areas of the ice sheet where the accumulation is low (easternmost areas for example) or under cold surface air temperature conditions (upper part of the ablation zone), the JH2000 model simulates slightly more refreezing than RE1989 (Figure 2-4b). However, in the simulations presented in Figure 2-4, we changed the refreezing scheme but converted all the precipitation into snow (assuming no rain), as in the reference simulation. The response of JH2000 would be different if we combined it to a rain and snow partitioning model, such as the method from Marsiat (1994) described in the previous sub-section. The impact of the combination of these new parametrisations on the surface mass balance and ultimately on the surface topography of the Eurasian ice sheet is further investigated in Section 2.2.

2.1.5 Summary: impact of the new parametrisations on surface mass balance

In the previous sections, we described the new parametrisations that were embedded into GRISLI to improve the computation of some of the aspects of the surface mass balance: the ice and snow melt, the refreezing of melt water and of rainfall and the rain and snow partitioning. In this section, we discuss the changes in SMB that these new parametrisations induces. The resulting SMBs are presented in Figure 2-5 (resp. Figure 2-6) when using B140_Topo1 (resp. B140_Topo2) as climate forcing.

As expected from the discussion in the previous sections, most of the new parametrisations imply a decrease in SMB relative to the reference simulation for both climates. The only exception is the use of Fausto et al. (2009) elevation dependency of the standard deviation of surface air temperature, which drastically increases the SMB by about 0.5 m/yr at the southern margins of the ice sheet (Figure 2-5c and 2-6c). The largest reduction in SMB is obtained when using partitioning between rain and snow, especially with the Marsiat (1994) model. However, the various processes have an impact on SMB of the same order of magnitude. Note that the SMB is positive over the entire ice sheet in all these simulations except along the southern margins (Figure 2-5a and 2-6a).

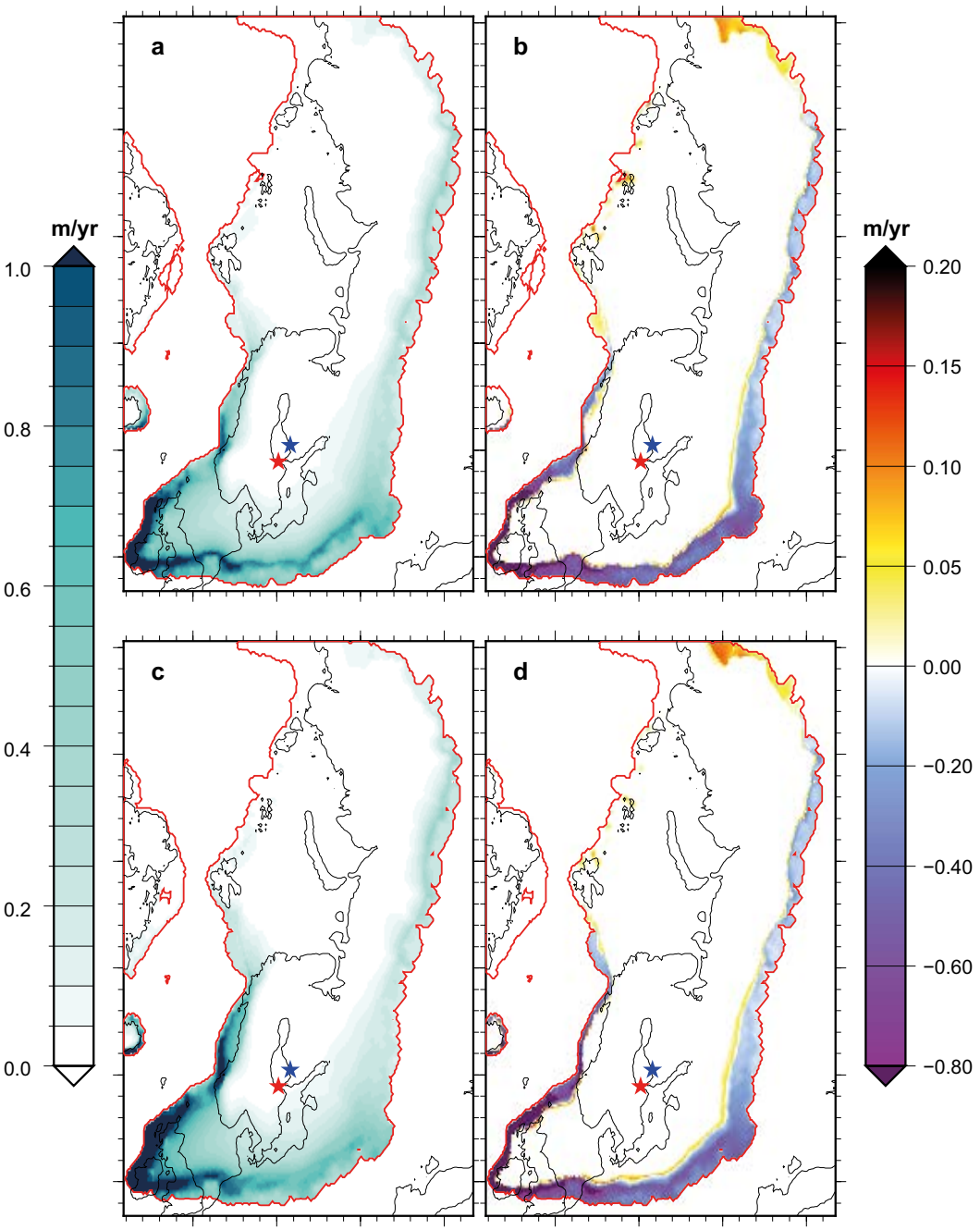

Figure 2-4. *Annual mean superimposed ice accumulation rates (m/yr) due to refreezing: (a) in RE1989 continued from REF_Topo1 topography using B140_Topo1 climate; and (b) difference with JA2000 model (RE1989 – JA2000, SMB5). (c) and (d) are similar to (a), and (b) but for climate B140_Topo2 over REF_Topo2. Note that the red contour corresponds to the extent of the ice sheet at the end of each SMB simulation and not to the reference simulations.*

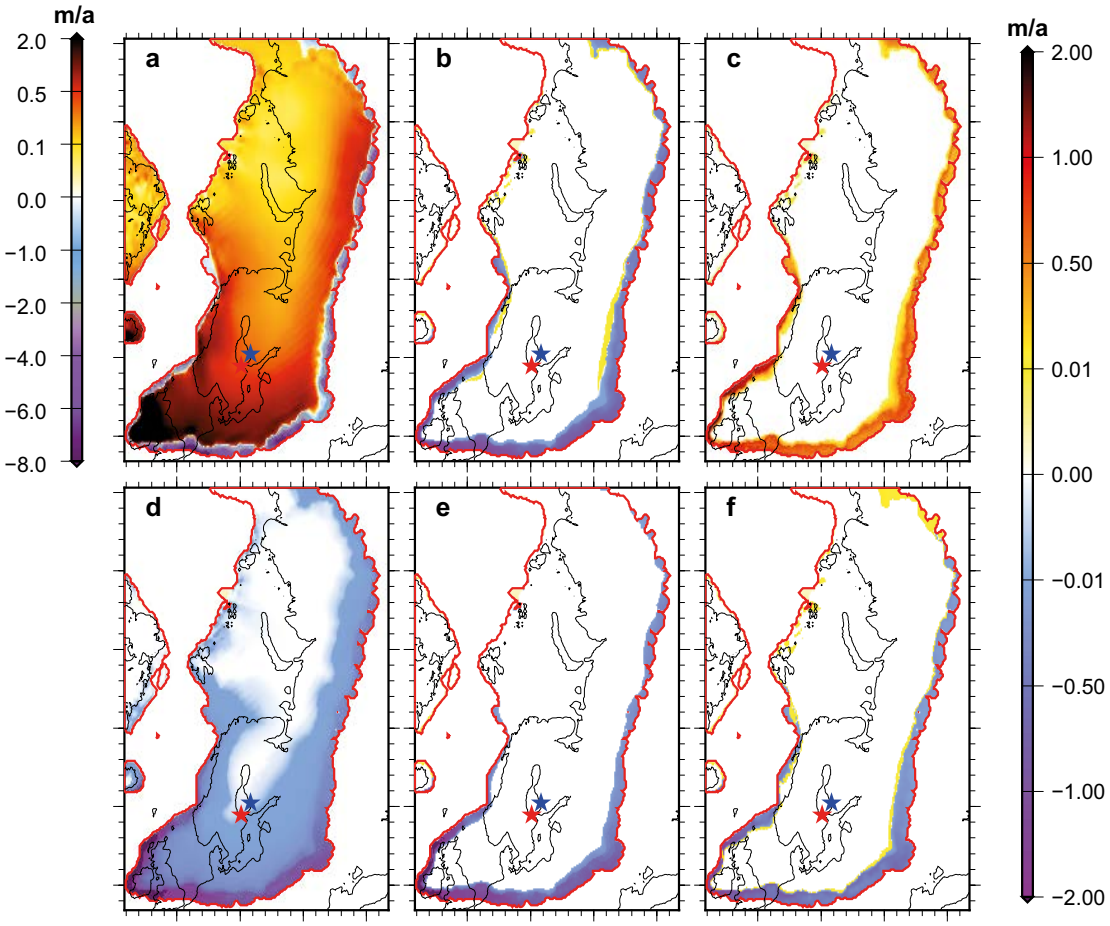

Figure 2-5. *Simulated SMB (m/yr) after 200 kyrs of simulation under the B140_Topo1 climate forcing, branched from the REF_Topo1 spin-up ice topography. The reference simulation REF_Topo1 is shown in (a) and the difference (new-reference) induced by the new parametrisations are shown in: (b) SMB1: Tarasov and Peltier (2002) melt coefficient, (c) SMB2: Fausto et al. (2009) elevation dependency of the temperature standard deviation, (d) SMB4: rain fraction from Marsiat (1994), (e) SMB3: rain fraction from a constant threshold p_{solid} of 2 °C, (f) SMB5: refreezing scheme from Janssens and Huybrechts (2000). Note that the red contour corresponds to the extent of the ice sheet at the end of each SMB simulation and not to the reference simulations.*

2.2 Consequence of updated parametrisations on long-term ice sheet topography

Based on the new implementations described above, long-term ice sheet simulations of 200 kyrs, branched on the reference simulations REF_Topo1 and REF_Topo2, have been performed. They test the impact of the individual and combined SMB-related parametrisations on the Late Saalian Eurasian ice sheet topography and ice thickness.

2.2.1 Impact on individual parametrisations

The impact of the new surface mass balance parametrisations on the Eurasian ice sheet extent and thickness after a 200 kyr simulation is depicted in Figure 2-7 (resp. 2-8) when using B140_Topo1 (resp. B140_Topo2) as climate forcing. While the Eurasian ice sheet extent is almost identical in all the simulations, the simulated ice thickness, on the contrary, exhibits larger differences compared with the reference simulations. The order of magnitude of the changes in thickness is similar for all the parametrisations. In the western part, ice thickness decreases up to 150 metres with respect to REF_Topo1 and REF_Topo2, whereas in the eastern part, ice thickness increases up to 150 metres. However, when testing the temperature standard deviation relationship from Fausto et al. (2009), the ice thickness increases homogeneously by about 200 metres over the entire ice sheet (Figure 2-7c

and 2-8c). The other parametrisations all lead to a decrease in ice thickness in the western part of the Eurasian ice sheet and induce an increase in ice thickness in the central to eastern areas. The simulation accounting for the rain and snow partitioning from Marsiat (1994) exhibits the strongest ice thickness reduction (about 500 m) in the western part (Figure 2-7d and 2-8d). In the other parametrisations, the maximum decrease in ice thickness occurs in the southwestern lobe (~200 m). This lobe is the most sensitive feature of the Late Saalian ice sheet reconstruction by Svendsen et al. (2004) because it is, due to its location, exposed to warm climate during summer. In fact, when using the B140_Topo2 climate, this lobe almost disappears (Figure 2-8). The eastern part of the ice sheet, on the contrary, is always thicker compared with REF_Topo1 and REF_Topo2. This was not expected in the case of the two experiments with rain and snow partitioning (Figure 2-7d, e. and 2-8d, e.), as these parametrisations necessarily imply a decrease in accumulation, not compensated for by other processes.

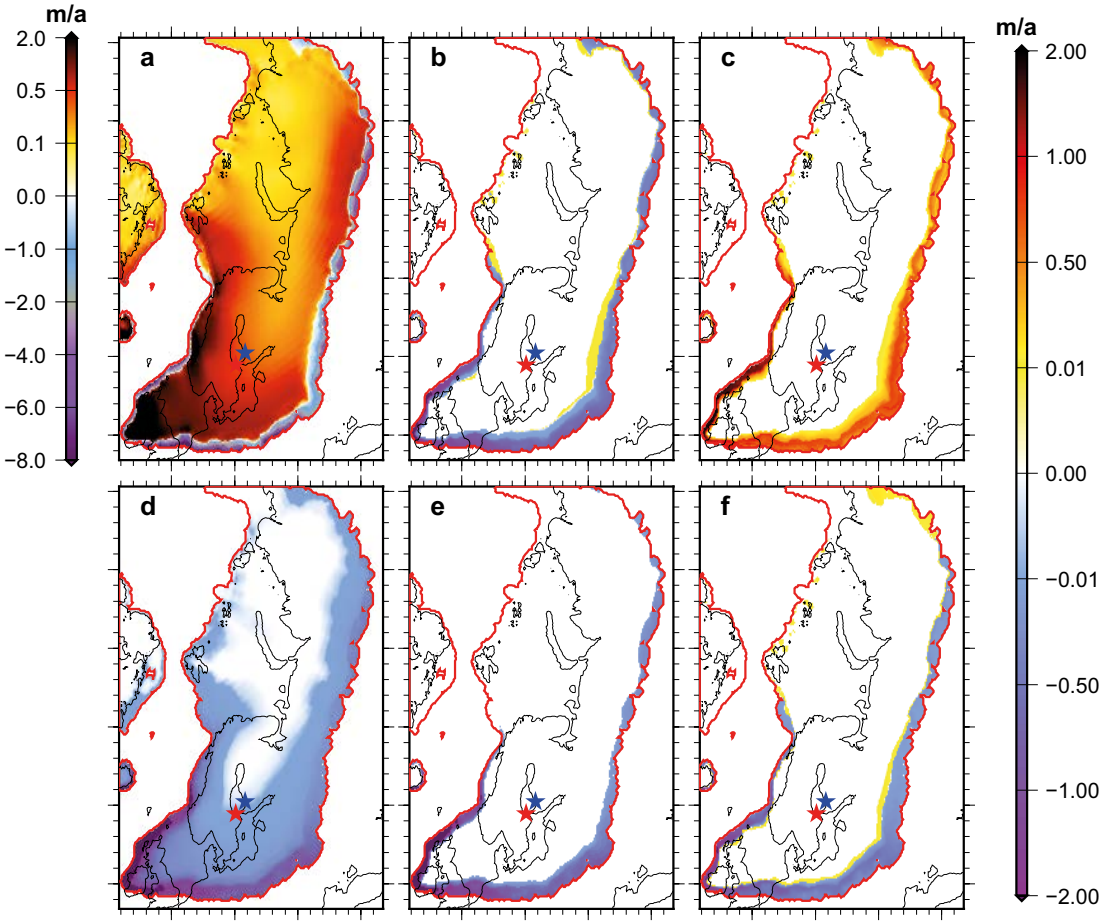

Figure 2-6. *Simulated SMB (m/yr) after 200 kyrs of simulations, under the B140_Topo2 climate forcing, branched from REF_Topo2 spin-up ice topography. The reference simulation REF_Topo2 is shown in (a) and the difference (new-reference) induced by the new parametrisations are shown in: (b) SMB1: Tarasov and Peltier (2002) melt coefficient, (c) SMB2: Fausto et al. (2009) elevation dependency of the temperature standard deviation, (d) SMB4: rain fraction from Marsiat (1994), (e) SMB3: rain fraction from a constant threshold p_{solid} of 2 °C, (f) SMB5: refreezing scheme from Janssens and Huybrechts (2000). Note that the red contour corresponds to the extent of the ice sheet at the end of each SMB simulation and not to the reference simulations.*

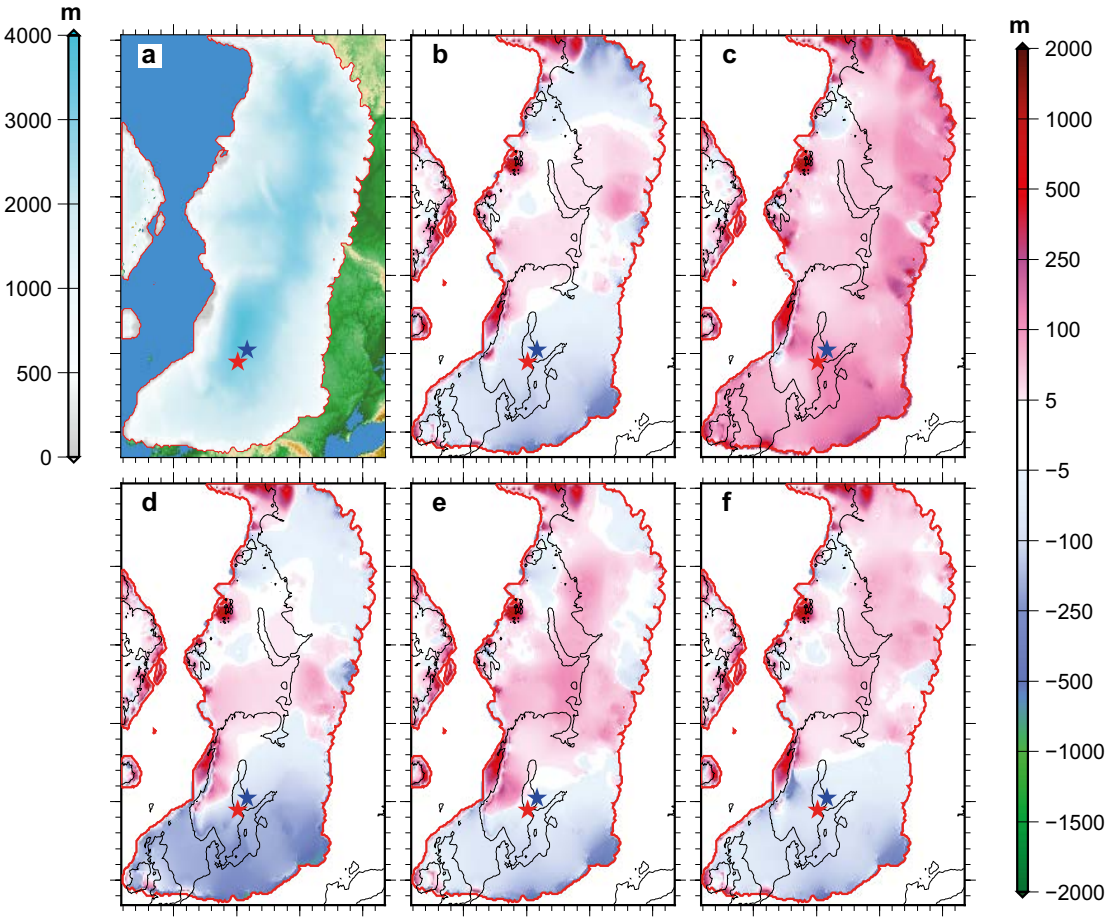

Figure 2-7. *Ice thickness after 200 kyrs of simulation using the B140_Topo1 climate forcing and branched on REF_Topo1 spin-up ice topography. For the need of comparison, the REF_Topo1 ice topography is shown in (a). The differences (new-reference) induced by the new parametrisations are shown in: (b) SMB1: Tarasov and Peltier (2002) melt coefficients, (c) SMB2: Fausto et al. (2009) elevation dependency of the temperature standard deviation, (d) SMB4: rain fraction from Marsiat (1994), (e) SMB3: rain fraction from a constant threshold p_{solid} of 2 °C, (f) SMB5: refreezing of Janssens and Huybrechts (2000). Note that the red contour corresponds to the extent of the ice sheet at the end of each SMB simulation and not to the reference simulations.*

2.2.2 Impact of combined parametrisations

So far, we have investigated the individual long-term effects of the new SMB-related parametrisations. Because most of the parametrisations individually suggest a decrease in the SMB and ice thickness, it is important to quantify those changes also when some or all those parametrisations are combined.

As previously mentioned, the new refreezing scheme has the ability to use the rain fraction of total precipitation as a component of the SMB. For this reason we combined the partitioning model of Marsiat (1994) with the new refreezing scheme from Janssens and Huybrechts (2000). While the use of the rain fraction of Marsiat (1994) leads to negative anomalies of SMB at high elevation in the western part of the Eurasian ice sheet (Figure 2-5d and 2-6d), this is no longer the case when we account for the refreezing of rainfall (Figure 2-9a and 2-10a). Along the southern margins, however, the use of this combination still induces higher ablation rates compared to the reference simulations REF_Topo1 and REF_Topo2, leading to an additional decrease in SMB of up to 2 m yr^{-1}.

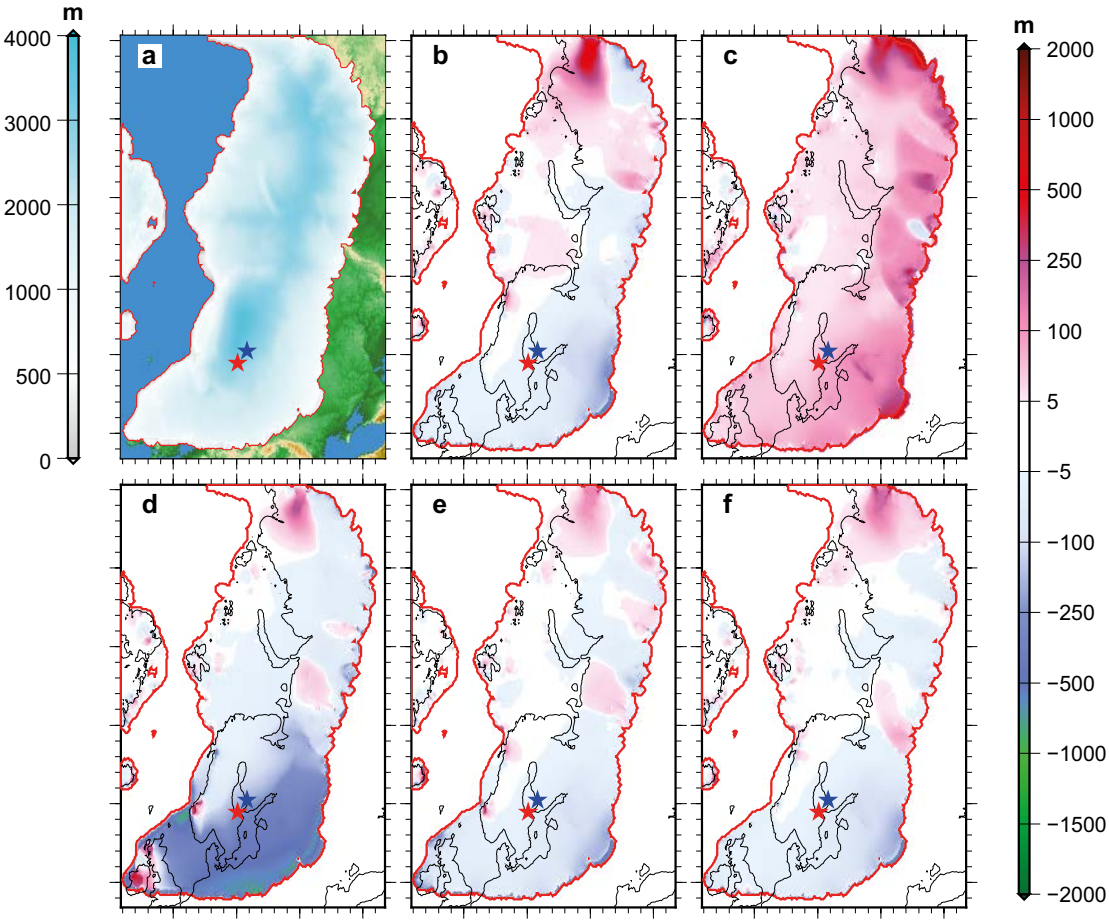

Figure 2-8. *Ice thickness after 200 kyrs of simulation, using the B140_Topo2 climate forcing and branched on REF_Topo2 spin-up ice topography. For the need of comparison, the REF_Topo2 ice topography is shown in (a). The differences (new-reference) induced by the new parametrisations are shown in: (b) SMB1: Tarasov and Peltier (2002) melt coefficients, (c) SMB2: Fausto et al. (2009) elevation dependency of the temperature standard deviation, (d) SMB4: rain fraction from Marsiat (1994), (e) SMB3: rain fraction from a constant threshold p_{solid} of 2 °C, (f) SMB5: refreezing of Janssens and Huybrechts (2000). Note that the red contour corresponds to the extent of the ice sheet at the end of each SMB simulation and not to the reference simulations.*

Another interesting combination is to use all the new parametrisations producing a lower SMB than in the reference simulations, i.e. rain/snow partitioning from Marsiat (1994), refreezing of rainfall from Janssens and Huybrechts (2000) and melt coefficient parametrisation from Tarasov and Peltier (2002), but excluding the temperature standard deviation parametrisation from Fausto et al. (2009). In this case the ablation rate is much higher than in the reference simulation, which leads to a more pronounced decrease in SMB than when prescribing fixed values for the melt coefficient C_{ice} and C_{snow} (Figure 2-9b and 2-10b). A larger portion of the western tip of the ice sheet experiences a reduction up to 2 m/yr of its SMB compared with the previous combination.

Finally, accounting for all the new parametrisations together leads to more heterogeneous SMB differences compared to the reference simulations (Figure 2-9c and 2-10c). Contrary to the previous two combinations, a large part of the Eurasian ice sheet southern margins exhibits an increased SMB (about 0.2 m/yr). This positive SMB mainly results from a decrease in ablation induced by a lower temperature standard deviation of Fausto et al. (2009). The westernmost part, however, still experiences a pronounced decrease in SMB.

Interestingly, whereas the anomaly in SMB induced by the rain fraction combined with refreezing (SMB6) under both climate forcings is negative along the southern margins (Figure 2-9a and 2-10a), the ice sheet becomes thicker than REF_Topo2 at the end of the simulation over this area

(Figure 2-12a). In fact, the ice sheet evolution over the British Isles is highly sensitive to the climate conditions that are warmer in B140_Topo2 than in B140_Topo1. The simulated ice thickness is numerically unstable and exhibits large-scale oscillations, with a periodicity of around 10 thousand years (not shown). The simulated final ice thickness displayed in Figure 2-11a corresponds a numerical oscillation larger than the mean ice thickness of this simulation. Therefore, the final ice thickness shown in Figure2-12a is larger than in REF_Topo2. In this case, the surface elevation decreases, local temperatures increase (by means of the prescribed atmospheric lapse rate) and part of this area melts. However, despite the local warming, the temperature remains cold enough to increase the effective accumulation over the western part of the ice sheet. In this way there is a competing effect between the warming induced by the lowering of the ice surface and the increase in accumulation resulting from the wetter climate induced by this warming. This simulation illustrates the dynamical instability arising during model simulation as a result of compensating feedbacks. This unstable behaviour was described also by Calov et al. (2010). Since we are unable to provide a definite number for the ice thickness at either Forsmark or Olkiluoto in this simulation, we discard this particular simulation from the overall assessment of maximum ice thickness.

When the melt coefficient parametrisation from Tarasov and Peltier (2002) is accounted for, along with the rain/snow partitioning and the refreezing (SMB7), the Eurasian ice sheet becomes thinner by 500 metres on average over the western part compared with REF_Topo1 (Figure 2-11b) and retreats over this area under the B140_Topo2 climate conditions (Figure 2-12b, green area broadly) losing the connection with the British ice sheet. However, if we take into account the temperature standard deviation parametrisation from Fausto et al. (2009) along with the other processes (SMB8), the ice sheet becomes thicker over most of the eastern and central parts than in the reference simulations (Figure 2-11c and 2-12c). The western part remains thinner than in the reference simulations, but less thin than in the previous cases of SMB6 and SMB7. This means that the temperature variability in the PDD calculation has the largest impact on ice thickness when compared to the other processes that we investigated in this section, since it can compensate for the SMB reductions implied by the other parametrisations.

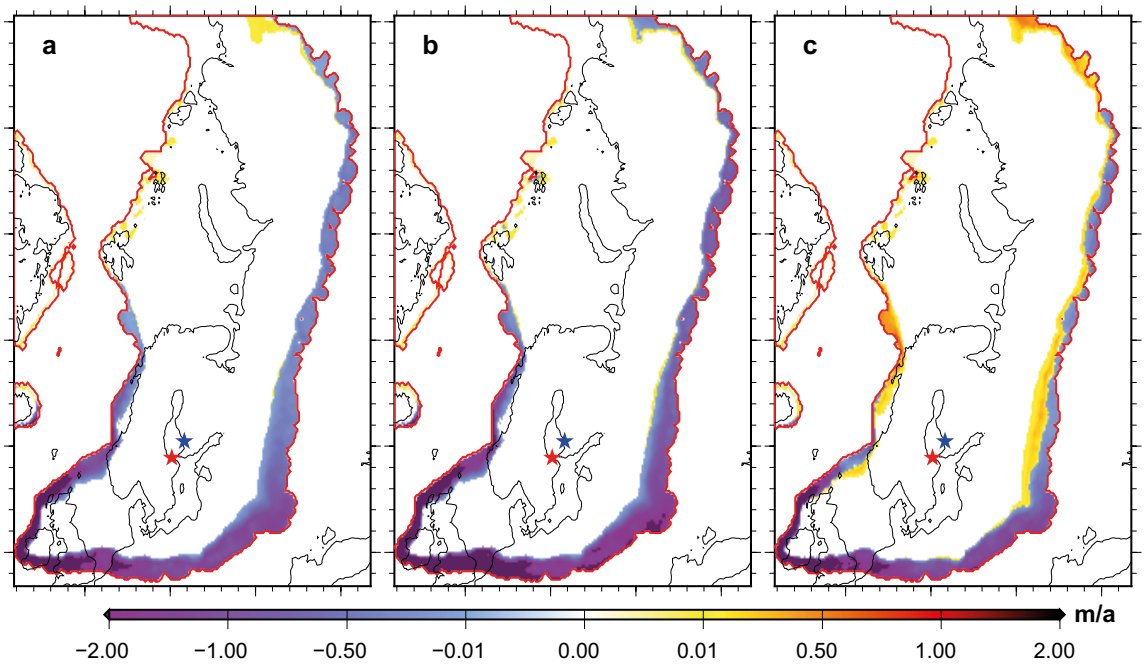

Figure 2-9. *Simulated SMB difference (m/yr) after 200 kyrs of simulation, between the reference simulation REF_Topo1 and the simulations forced by the B140_Topo1 climate and accounting for new parametrisations (new-reference): (a) SMB6: rain fraction from Marsiat (1994) together with the refreezing scheme of Janssens and Huybrechts (2000); (b) SMB7:same as for a. but using TP2002 melt coefficients parametrisation; (c) SMB8: same as for c. but accounting for the surface air temperature standard deviation from Fausto et al. (2009). Note that the red contour corresponds to the extent of the ice sheet at the end of each SMB simulation and not to the reference simulations.*

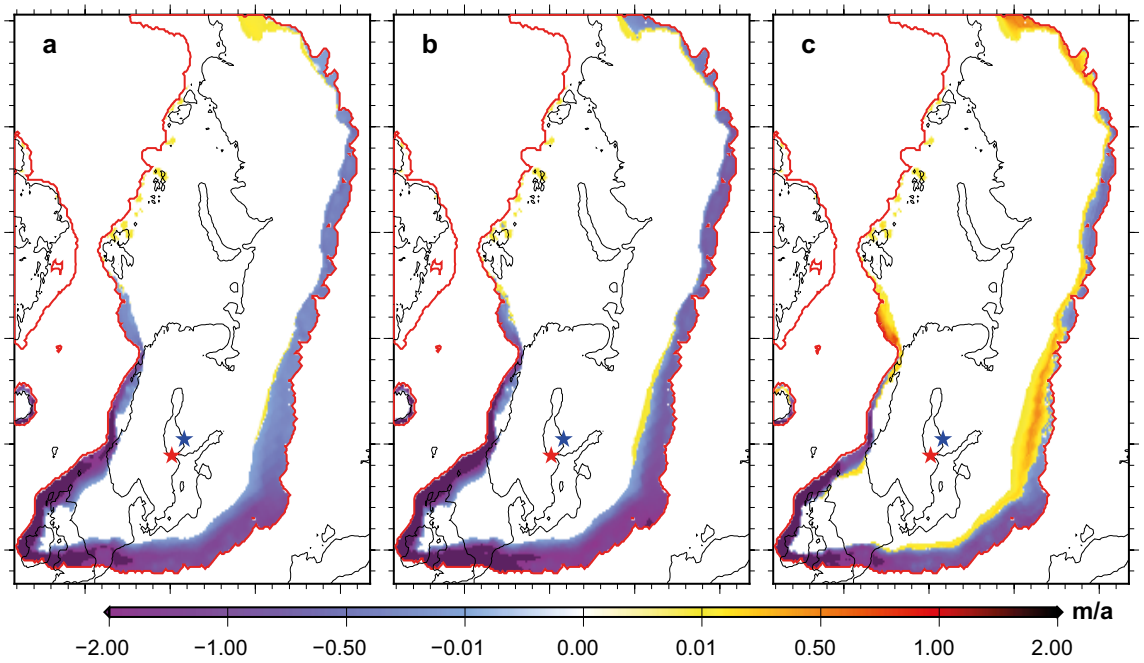

Figure 2-10. *Simulated SMB difference (m/yr) after 200 kyrs of simulation, between the reference simulation REF_Topo2 and the simulations forced by the B140_Topo2 climate and accounting for new parametrisations (new-reference): (a) SMB6: rain fraction from Marsiat (1994) together with the refreezing scheme of Janssens and Huybrechts (2000); (b) SMB7:same as for a. but using TP2002 melt coefficients parametrisation; (c) SMB8: same as for c. but accounting for the surface air temperature standard deviation from Fausto et al. (2009). Note that the red contour corresponds to the extent of the ice sheet at the end of each SMB simulation and not to the reference simulations.*

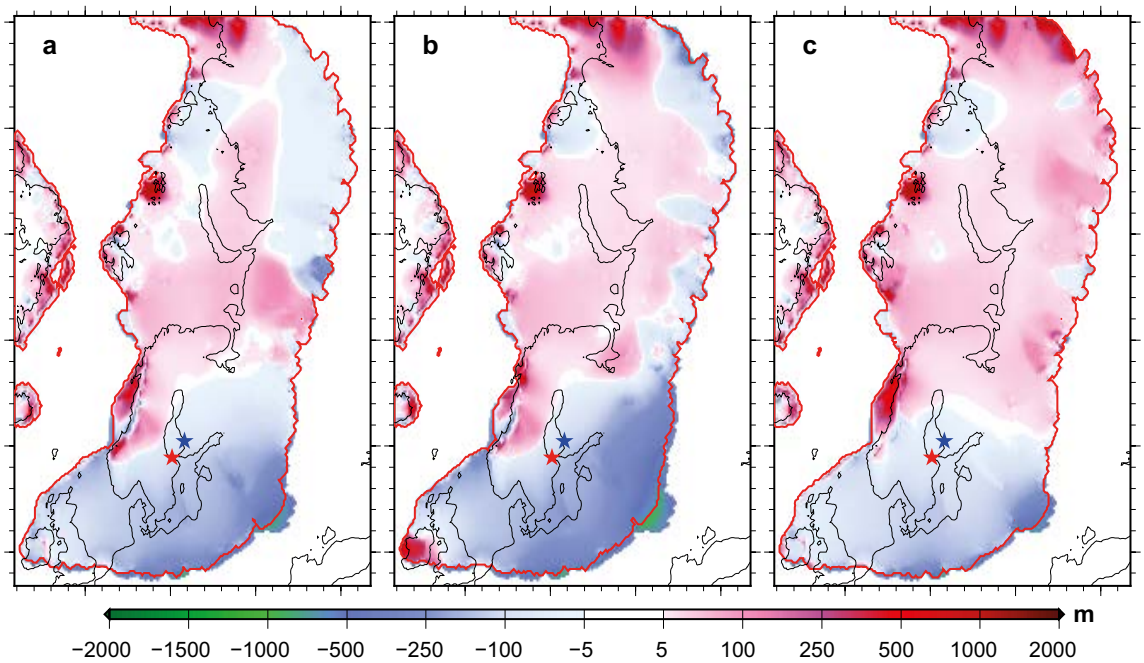

Figure 2-11. *Difference in ice thickness (m) between the reference simulation REF_Topo1 and the new parametrisations (new minus reference) after 200 kyrs of simulation. Simulations have been branched from REF_Topo1 spin-up ice topography and forced with the B140_Topo1 climate. Differences between REF_Topo1 and: (a) SMB6: rain fraction from Marsiat (1994) together with the refreezing scheme of Janssens and Huybrechts (2000); (b) SMB7: same as for (a) including Tarasov and Peltier (2002) melt coefficients parametrisation; (c) SMB8: same as for (b) but including the surface air temperature standard deviation parametrisation from Fausto et al. (2009). Note that the red contour corresponds to the extent of the ice sheet at the end of each SMB simulation and not to the reference simulations.*

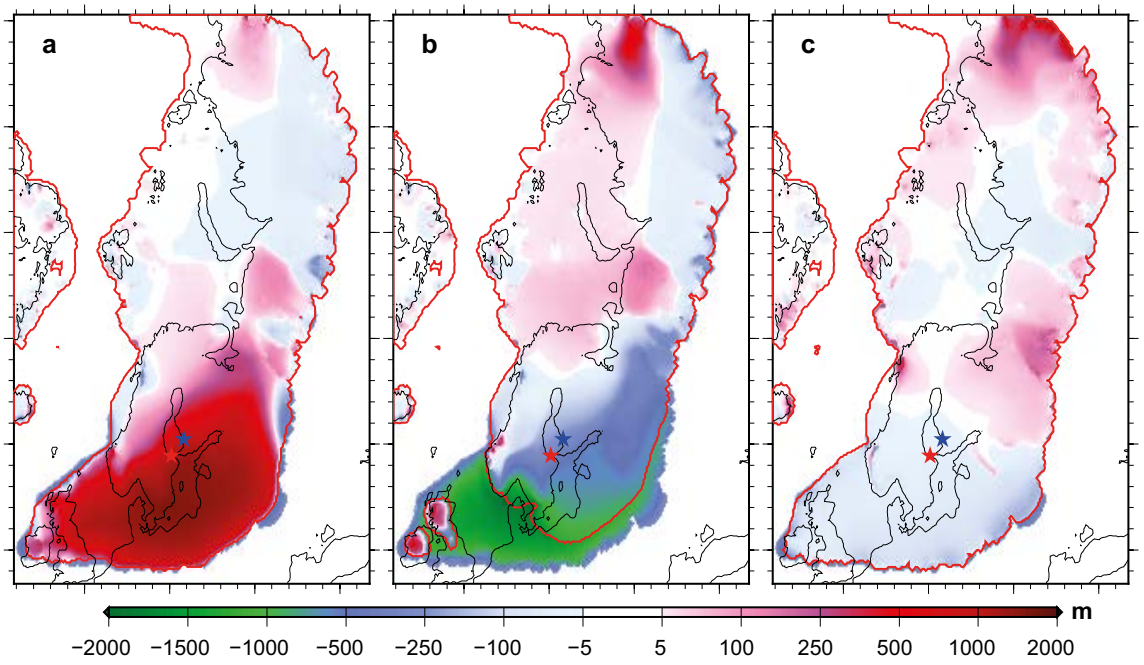

Figure 2-12. *Difference in ice thickness (m), between the reference simulation REF_Topo2 and the new parametrisations (new minus reference) after 200 kyrs of simulation. Simulations have been branched from REF_Topo2 spin-up ice topography and forced with the B140_Topo2 climate. Differences between REF_Topo1 and: (a) SMB6: rain fraction from Marsiat (1994) together with the refreezing scheme of Janssens and Huybrechts (2000); (b) SMB7: same as for (a) including Tarasov and Peltier (2002) melt coefficients parametrisation; (c) SMB8: same as for (b) but including the surface air temperature standard deviation parametrisation from Fausto et al. (2009). Note that the red contour corresponds to the extent of the ice sheet at the end of each SMB simulation and not to the reference simulations.*

2.3 Impact of the new surface mass balance parametrisations: summary of main results

We have implemented updated parametrisations affecting various aspects of the surface mass balance computation in the GRISLI ice sheet model. We tested their importance on the surface mass balance and on the ice thickness by means of steady-state experiments of 200 kyrs. The simulated ice volume, ice thickness and bedrock depression for each of the simulations in Table 2-1 are presented for the Forsmark and Olkiluoto sites in Table 2-2. The volume is systematically higher when using the B140_Topo1 climate forcing than when using the B140_Topo2, as in the first phase of the study (Colleoni et al. 2014b, 2016b). The minimum ice volume is obtained in the simulation accounting for all the new formulations, except the temperature standard deviation parametrisation (i.e. in the SMB7 simulation). The minimum ice sheet volume is 51.5 m SLE (resp. 44.5 m SLE) under the B140_Topo1 (resp. B140_Topo2) climate forcing, corresponding to a decrease of 3.4 % (resp. 13.7 %) of the reference volume. Conversely, the maximum ice volume is obtained in the simulation accounting for the temperature standard deviation parametrisation from Fausto et al. (2009) only (i.e. in the SMB2 simulation). The maximum ice volume value is 56.0 m SLE (resp. 53.7 m SLE) under the B140_Topo1 (resp. B140_Topo2) climate forcing, corresponding to an increase of 5.2 % (resp. 4.3 %) of the reference volume. The ice thicknesses and bedrock depressions at the two repository sites follow the same pattern as the volume. The ice thickness (resp. bedrock depression) ranges from 2577 to 3196 m (resp. −670 to −758 m) at Forsmark. Because of its position closer to the main dome, the ice thickness at Olkiluoto is systematically larger, ranging from 2787 to 3320 m (resp. −721 to −787 m).

Table 2-2. Simulated Late Saalian Eurasian ice sheet volume (meter Sea-Level Equivalent, m SLE), ice thickness (m) and bedrock depression elevation (m) at the end of the 200 kyrs simulation for the different experiments in Table 2-1 and testing the sensitivity of the ice sheet to various SMB-related formulations. For the ice thickness and bedrock depression data, Forsmark is identified by *F* and Olkiluoto by *O*. Changes, expressed in %, are computed relative to the reference simulations REF_Topo1 and REF_Topo2. The yellow marks highlight the maximum and minimum values for each metric. Note that the quantities are computed on a rectangular Cartesian grid using a Lambert Equal Area projection. To avoid distortion uncertainties, the values for Forsmark and Olkiluoto have been re-projected on a long-lat Mercator ellipsoidal grid to extract values for the correct positions.

	Eurasian ice sheet volume				Ice thickness					Bedrock depression				
	B140_Topo1		B140_Topo2		Site	B140_Topo1		B140_Topo2		Site	B140_Topo1		B140_Topo2	
ID	m SLE	%	m SLE	%		m	%	m	%		m	%	m	%
SMB1	52.2	−1.9	51.0	−0.9	*F*	3016	*−2.8*	2888	−0.9	*F*	−708	*−3.2*	−678	−1.0
					O	3157	*−2.3*	3035	−0.9	*O*	−743	*−2.7*	−712	−1.1
SMB2	56.0	5.2	53.7	4.3	*F*	3196	*3.1*	2966	1.7	*F*	−758	*3.6*	−699	2.1
					O	3320	*2.8*	3114	1.7	*O*	−787	*3.2*	−736	2.1
SMB3	53.3	−0.0	50.8	−1.4	*F*	3058	*−1.4*	2881	−1.2	*F*	−722	*−1.2*	−675	−1.4
					O	3211	*−0.6*	3030	−1.1	*O*	−757	*−0.8*	−711	−1.3
SMB4	51.6	−3.2	47.8	−7.3	*F*	2952	*−4.8*	2688	−7.8	*F*	−699	*−4.4*	−617	−9.9
					O	3118	*−3.4*	2866	−6.4	*O*	−736	*−3.6*	−661	−8.3
SMB5	53.9	1.1	51.0	−1.0	*F*	2948	*−5.0*	2882	−1.1	*F*	−693	*−5.2*	−676	−1.3
					O	3112	*−3.6*	3030	−1.1	*O*	−735	*−3.7*	−712	−1.2
SMB6	52.1	−2.3	–	–	*F*	3006	*−3.1*	–	–	*F*	−708	*−3.2*	–	–
					O	3149	*−2.5*	–	–	*O*	−742	*−2.7*	–	–
SMB7	51.5	−3.4	44.5	−13.7	*F*	2985	*−3.8*	2577	−11.6	*F*	−703	*−3.9*	−670	−2.1
					O	3119	*−3.4*	2787	−9.0	*O*	−734	*−3.9*	−721	−0.1
SMB8	53.3	0.0	51.5	−0.1	*F*	3038	*−2.1*	2887	−1.0	*F*	−714	*−2.4*	−677	−1.1
					O	3178	*−1.6*	3041	−0.7	*O*	−750	*−1.8*	−715	−0.7

Finally, we have shown that the SMB formulation has a strong impact on ice sheet topography, especially when the parametrisations are combined. Furthermore, because the B140_Topo2 climate forcing is much warmer than B140_Topo1, the changes related to surface mass balance and ice thickness are systematically larger, leading to a retreat of the ice sheet in some of the simulations using the B140_Topo2 climate forcing (SMB7).

However, all together the maximum and minimum ice thicknesses and bedrock depressions obtained with these new parametrisations fall within the range of those obtained during the phase one of the study when testing the impact of SMB related parameters in a more simplified analysis: 2991 (2650) metres to 3472 (3195) metres for ice thickness under B140_Topo1 and B140_topo2 climate forcing, and −707 (−632) metres to 822 (760) metres for bedrock depression. Hence, the set of parameters tested during phase one was covering almost completely the uncertainties in term of surface mass balance formulation explored in the present study. Nevertheless, it was necessary to explore different parametrisations to check if the ice thickness had a strong dependency on the chosen method. It is important to note that even if these new parametrisations rely on a more complex physics they are still subject to large uncertainties. In particular, all the analysed parametrisations have been calibrated to match present-day observations. In order to accurately use these parametrisations for other time periods, it would be necessary to determine a range of realistic values for those parameters for each time periods under investigation. However, there is no way to assess precisely the representativeness of those parameters for other time periods, as discussed by Charbit et al. (2013). Despite those uncertainties, the present investigations provide a useful picture of the sensitivity of the Eurasian ice sheet to different surface mass balance related parametrisations.

3 Sensitivity to ice sheet model formulation and basal processes

Phase one of the study concluded that basal processes were the major source of uncertainty when reconstructing the Late Saalian Eurasian ice sheet (Colleoni et al. 2014b, 2016b). Those processes include the basal hydrology, i.e. the determination of the amount of meltwater at the bed and its routing under the ice sheet, the basal sliding (and/or dragging) that depends mainly on the basal hydrology and the amount of sediments at the bed. In an ice sheet model, the basal processes regulate the ice velocities at the base of the ice sheet and impact the type of ice flow in specific areas, such as the presence of ice streams and the grounding zone. The type of flow, in turn, has a large impact on the simulated ice configuration and thickness. Basal processes are poorly constrained in ice sheet models because of a lack of observations and because of the poor representativeness of laboratory experiments aiming at investigating the rheological behavior of ice crystals.

In order to reduce the uncertainties related to ice flow dynamics we approach the problem in three different ways:

1. We use a second large-scale ice sheet model (SICOPOLIS) and examine the major differences with GRISLI.
2. We investigate the importance of model grid resolution to resolve ice streams areas.
3. We perform sensitivity experiments with GRISLI in which the large-scale ice stream flow is restricted.

In order to investigate the above issues, a set of four simulations is defined. Two simulations with the SICOPOLIS ice sheet model, one at 20 km and one at 40 km horizontal resolution (DYN1 and DYN2), in order to test the impact of the resolution on the model physics and on the resulting ice thicknesses, and two simulations with the GRISLI model at 20 km resolution, one with Shallow Ice Approximation (SIA) flow only (and no SSA) (DYN3), and one using both SIA and SSA but restricted by a topographic criterion (DYN4). Because we are interested in model formulation sensitivity, we set the model parameters for both models to reference values for SICOPOLIS (Eurasia configuration version 3.1, see Greve 2005) and GRISLI (REF_Topo1 and REF_Topo2). Note that SICOPOLIS uses the rain and snow partitioning from Marsiat (1994) whereas GRISLI considers the total precipitation as accumulation in these simulations. All simulations are run for both climate forcings. The simulations are summarised in Table 3-1.

Table 3-1. Summary of the experiments carried out to test the sensitivity to i) choice of ice sheet model, ii) ice flow formulations (SIA and SSA), and iii) horizontal grid resolution. The DYN1 simulation is considered as the reference simulation for the SICPOLIS ice sheet model whereas for GRISLI, the reference simulation is given by the SMB4 simulations described in Table 2-2.

Simulation ID	Ice sheet model	Grid resolution	Ice flow approximation
DYN1	SICOPOLIS	20 km	SIA
DYN2	SICOPOLIS	40 km	SIA
DYN3	GRISLI	20 km	SIA
DYN4	GRISLI	20 km	SIA + SSA + topo criterion

3.1 SICOPOLIS ice sheet model experiments

3.1.1 Differences in model physics between SICOPOLIS and GRISLI

We use SICOPOLIS v3.1 (hereafter SICOPOLIS, Greve 2005) as an alternative model to GRISLI for simulating the Late Saalian Eurasian ice sheet topography. In the same way as GRISLI, SICOPOLIS is a large-scale thermodynamical ice sheet model, and as such, most of the physics and the treatment of boundary conditions are identical between the models, with the following two major exceptions:

- SICOPOLIS only uses the Shallow Ice Approximation (SIA), whereas GRISLI is a hybrid model accounting for fast flowing ice streams by also applying the shallow shelf approximation, SSA.
- SICOPOLIS is a polythermal model that explicitly accounts for the possible presence of a temperate ice layer at the base of the ice sheet. GRISLI on the other hand only considers cold ice.

These differences are described in the following section.

a) Ice streams in GRISLI and SICOPOLIS

Due to a small vertical to horizontal aspect ratio , the SIA assumes that the vertical derivatives are greater than the horizontal derivatives (see the report by Colleoni et al. (2014b, 2016b) for a proper description of the SIA). As a consequence, the vertical velocity profile is parabolic, being minimum at the base and maximum at the surface. When the the ice sheet is cold-based, it is assumed that the basal velocity is zero, whereas when the ice temperature is at the pressure melting point, the basal velocity is equal to the sliding velocity. Both GRISLI and SICOPOLIS have a similar expression for the parametrisation of the sliding velocity (Weertman 1957).

The SIA is a good approximation for the ice flow over the major part of the ice sheet, i.e. when the ice velocity is low. However, specific parts of the current ice sheets, i.e. in Greenland and Antarctica, have an ice flow velocity significantly higher than the average ice sheet velocity. These areas are referred to as ice streams. In these areas, the ice is sliding over the bedrock, with a given basal drag, and the velocity profile is independent from depth. This vertical velocity distribution significantly differs from the one described by the SIA. From a mathematical point of view, the vertical derivatives in these cases are negligible compared to the horizontal ones. In this case, a different set of equations, referred as the Shallow Shelf Approximation (SSA) are used to compute the ice stream velocities.

Whilst SICOPOLIS only uses the SIA, GRISLI is a hybrid model which combines the two types of flow (SIA and SSA). The SSA is used when specific conditions are met. In particular, a thick sediment layer (at least 150 m in the reference simulation), saturated by meltwater to a certain extent (at least 100 m in the reference simulation) is required to trigger the SSA in GRISLI. In addition, narrow valleys (identified by local bedrock curvature) ending at the coast are also treated with the SSA.

From this point of view GRISLI differs from SICOPOLIS. However, GRISLI does not fully represent the state of present-day ice sheets. In particular, because of grid resolution limited by the use of the SIA, GRISLI is not able to resolve individual ice streams (typically a few km wide). Therefore, in GRISLI, in order to capture the potential “stream” areas, the SSA is applied to broad zones where the flow is consequently faster than in the part of the ice sheet treated with SIA. In this way, the criteria used to trigger the SSA rather than SIA are not very well constrained. For example, the importance of the thickness of the sediment layer under the present-day North East Greenland ice stream is unclear (Christianson et al. 2014, Vallelonga et al. 2014). In addition, it has been suggested than paleo-ice streams in the southwestern part of the Laurentide ice sheet during the LGM were not necessarily linked to bed topographic features (Margold et al. 2015).

Despite those limitations, GRISLI provides a correct representation of the past and present-day Greenland ice sheet (Quiquet et al. 2012, 2013) and is able to provide a correct representation of millennial scale variability and abrupt ice discharge that occurred during the last glacial cycle (Alvarez-Solas et al. 2011). In a recent contribution, a finely tuned version of SICOPOLIS was applied to the simulation of present-day Greenland ice streams. The results show that despite the tuning, the horizontal velocities in those fast-flowing areas were underestimated compared to observations, leading to an overestimation of ice elevation over Greenland (Greve and Herzfeld 2013).

b) Polythermal ice regime in GRISLI and SICOPOLIS

In both the GRISLI and the SICOPOLIS ice sheet models, the cold ice temperature at the surface is advected and diffused towards the bed. Both models also account for heat produced by ice deformation and friction at the base and for the warming at the base due to geothermal heat flux. Thus, under specific conditions, the basal ice can reach the pressure melting point temperature. In GRISLI, the basal ice layer is not allowed to contain water and the excess heat is used to compute basal melting

and basal meltwater production. Doing so, there is no temperate layer of ice in GRISLI. As a result, we might, under some circumstances, expect an underestimation of the deformation rate due to the absence of a temperate basal ice layer and perhaps to an overestimation of ice thickness. However, since GRISLI uses the SSA, this type of ice flow might compensate for the absence of temperate layer at the base.

Conversely, SICOPOLIS has the ability to include a temperate ice layer in which melt water coexists with ice. The coexistence of the two phases of water contributes to a modification of the ice viscosity and consequently of the deformation rate and ice velocity (Fowler 1984, Hutter 1982, 1993). The advection and diffusion of particles (liquid and ice) in the temperate layer are governed by the mixture theory (Fowler 1984). Contrary to what happens in GRISLI, in this case the temperature is not reset to the pressure melting point. Therefore, the temperate layer can expand from the base towards the surface. In order to represent the development of this temperate layer, SICOPOLIS has 81 vertical layers against 11 in GRISLI and 40 layers in the bedrock against five in GRISLI.

3.1.2 Reference simulations using the SICOPOLIS ice sheet model

In order to perform experiments similar to the ones performed with GRISLI, we created new grids over Eurasia and the North Hemisphere in SICOPOLIS, at 10, 20 and 40 km horisontal resolution, using the Lambert Equal Area projection. Initial Late Saalian bedrock, ice thickness and surface topographies, as well as climate forcing, are the same for both models.

To increase the robustness of the comparison, it would have been desirable to branch the simulations with SICOPOLIS on the reference simulations REF_Topo1 and REF_Topo2 carried out with GRISLI. Unfortunately, as mentioned above, the vertical discretisation of SICOPOLIS and GRISLI differs. Therefore, there is no simple way to use the GRISLI spun-up 3D fields, on e.g. vertical ice temperature and velocities, in order to initialise SICOPOLIS. In addition, the number of variables required by SICOPOLIS to restart from a previous ice sheet simulation is considerably larger than the variables required by GRISLI. Thus, we had to perform two new reference simulations, similar to REF_Topo1 and REF_Topo2 that were obtained from the first phase of the study, by starting from the initial MIS 6 topography from Colleoni et al. (2009). This topography includes the Laurentide, the Greenland and the Antarctic ice sheets from ICE-5G (Peltier 2004) and the MIS 6 Eurasian ice sheet from Peyaud (2006). The SICOPOLIS reference simulations used the DYN1 model setup (Table 3-1), and they are denoted SICO_Topo1 and SICO_Topo2. They are run for 360 kyrs using both Late Saalian climate forcings (B140_Topo1 and B140_Topo2) at a 20 km resolution over the Eurasian domain and a 40 km resolution over the remaining Northern Hemisphere grid. Due to numerical instabilities arising during runtime, we decided to run the first 160 kyrs in cold ice mode, i.e. not accounting for polythermal ice, and the last 200 kyrs with the polythermal mode until reaching a complete equilibrium in ice volume. The main ice sheet parameters were set identical to the GRISLI REF_Topo1 and REF_Topo2 parameters (reported in Table A1 in Appendix 1). Note that SICOPOLIS uses Marsiat (1994) rain fraction as a standard accumulation parametrisation. Thus, in order to compare the models, in the following we use the GRISLI SMB4 simulations that accounts for Marsiat (1994) partitioning (Table 2-1) as a reference for GRISLI. After spin-up, the ice sheets simulated with SICOPOLIS are in equilibrium, and thus comparable to the reference simulations carried out with GRISLI.

The spun-up ice topography SICO_Topo2 differs drastically from the corresponding SICO_Topo1 topography (Figure 3-1a and 3-1b). The simulated ice sheet in SICO_Topo1 is massive with very large ice thicknesses, but with a southern extent smaller than the one of Svendsen et al. (2004). The ice thicknesses for both sites are far above 4000 m (4422 m for Forsmark and 4453 m for Olkiluoto). It is interesting to note that if SICOPOLIS simulates very steep slopes at the margin, the inner region is relatively flat and the two sites have a similar ice thickness using the B140_Topo1 climate forcing (Figure 3-1a). Conversely, under the B140_Topo2 climate conditions, a large part of the south-western region retreats (Figure 3-1b). As a consequence, the resulting ice thickness is only 791 m at Forsmark. Because SICOPOLIS presents steep ice sheet margin gradients, and because Olkiluoto is located much closer to the western ice dome than Forsmark, the ice thickness over Olkiluoto remains quite large (about 1400 m). It is worth noting that even if the southwestern part of the ice sheet is retreating in SICO_Topo2, SICOPOLIS still predicts very thick ice elsewhere, with a morphology comparable to what is simulated in SICO_Topo1 (Figure 3-1a and 3-1b).

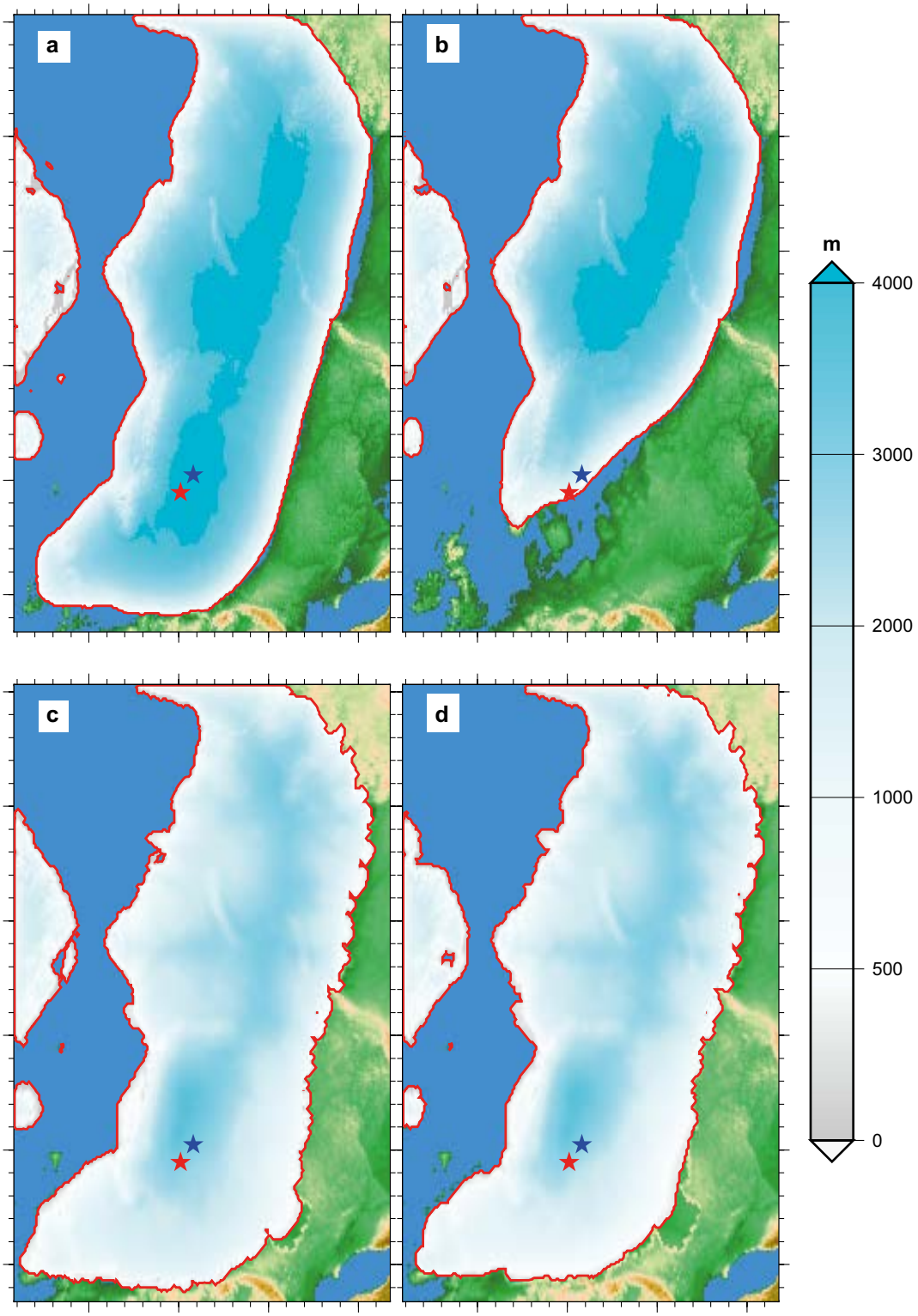

Figure 3-1. *Final ice thickness (m) simulated for the two reference runs by SICOPOLIS and GRISLI after 200 kyrs of simulation: (a) SICO_Topo1 using B140_Topo1 climate forcing , (b) SICO_Topo2 using B140_Topo2 climate forcing, (c) SMB4 (GRISLI, Table 2-1) using B140_Topo1 climate forcing and (d) SMB4 using B140_Topo2 climate forcing. However, note that ice thicknesses displayed in (a) is not compatible with global sea-level budgets for this period (Section 3.4), suggesting that this simulation overestimates ice volume and ice thicknesses.*

Compared with the GRISLI SMB4 simulations, the ice sheet extent in SICO_Topo1 and SICO_Topo2 is always smaller but the simulated ice thickness is systematically larger. Since the SMB computation relies on the PDD method in both models, the differences between GRISLI and SICOPOLIS only result from the treatment of the inner ice dynamics. The vertically integrated velocities in SICOPOLIS present a relatively smooth pattern, with higher values at the margins, decreasing almost homogeneously towards the inland areas (Figure 3-2a and 3-2b).GRISLI, on the other hand, exhibits a very heterogeneous velocity distribution, with major drainage areas with high velocities propagating inland (Figure 3-2c and 3-2d). These discrepancies explain the difference in ice thickness and ice extent between the two ice sheet models seen in Figure 3-1. The higher ice velocities in GRISLI bring more ice towards the ablation zone, compensating for the negative SMB along the southern margins and preventing the ice from retreating. It should be noted that the enhanced advection of ice towards the ablation zone in GRISLI does not always play in favor of large ice extent. If the ablation is strong enough, it can have the opposite effect and lead to the collapse of the ice sheet. This is in fact the case for a large number of experiments carried out with the Latin Hypercube methods presented in Chapter 6.

In order to further analyse the response of the SICOPOLIS ice sheet model, we perform two equilibrium experiments with GRISLI, denoted SIA_Topo1 and SIA_Topo2, in which we disable the use of the SSA equations (simulation DYN3 in Table 3-1). SIA_Topo1 and SIA_Topo2 have the same parameter values as the reference simulations (REF_Topo1 and REF_Topo2).

When the use of the SSA is disabled in GRISLI, the simulated ice sheet topographies show similar features to the ones obtained in SICO_Topo1 and SICO_Topo2 (Figure 3-3). Due to the much slower velocities compared to the reference simulations with SSA, the ice thickness increases by about 2000 metres along the margins and goes beyond 4000 metres along the ice divide (Figure 3-3a and 3-3b). Under climate B140_Topo2, the ice sheet in SIA_Topo2 does not retreat, in contrast to what happens in the SICO_Topo2 simulation (Figure 3-3b and 3-1b). This is probably due to internal differences in the code such as the inclusion of polythermal ice in SICOPOLIS. In particular, basal melting rates are much higher in SICOPOLIS than in GRISLI at the margins (Figure 3-4), which could explain the ice retreat in the SICO_Topo2 simulation.

The shape of the simulated Eurasian ice sheet in SIA_Topo1 and SIA_Topo2 is similar to the one in SICO_Topo1 and SICO_Topo2, with steep margins and a flat central part. However, because the margins in GRISLI are more stable than in SICOPOLIS, the ice volume in SIA_Topo1 (91.4 m SLE) and SIA_Topo2 (90.6 m SLE) is larger than in SICO_Topo1 (77.3 m SLE) and SICO_Topo2 (55.4 m SLE). The thickness at the two repository sites is also larger (about 5 % at Forsmark and 6 % at Olkiluoto when using B140_Topo1 climate forcing).

However, the experiments reported in this section should be interpreted with care for several reasons:

- First, when using the B140_Topo1 climate forcing, we already account for 74 m SLE in the Laurentide ice sheet. However, the simulated volumes in SICOPOLIS and in GRISLI with no SIA are always above 70 m SLE. Thus, in this scenario, the global ice volume goes beyond the upper limit of 150 m that the compilation of global sea level reconstructions Rabineau et al. (2006) indicates for the Late Saalian glacial maximum. This strongly suggests that these SICOPOLIS and GRISLI (without SIA) simulations overestimate the ice sheet volume and ice thicknesses (maximum over 4500 metres in both models).
- Second, the GRISLI simulations with only SIA limit the amount of ice streams developing during the simulations, whereas simulations accounting for the SSA might overestimate the areas treated as ice streams (see Section 3.1.1). Consequently, the simulations with SIA-only produces a larger ice volume and a thicker ice sheet, since the ice flow is slower, than the simulations accounting for SSA in the simulations. There is solid evidence of the presence of large ice streams for the Eurasian ice sheet during the past glaciations (Svendsen et al. 2004, Ottesen et al. 2005, Dowdeswell et al. 2006, Kleman and Glasser 2007). A good criterion for the choice of ice physics would be the performance in representing past MIS 6 ice streams matching such geological evidence.

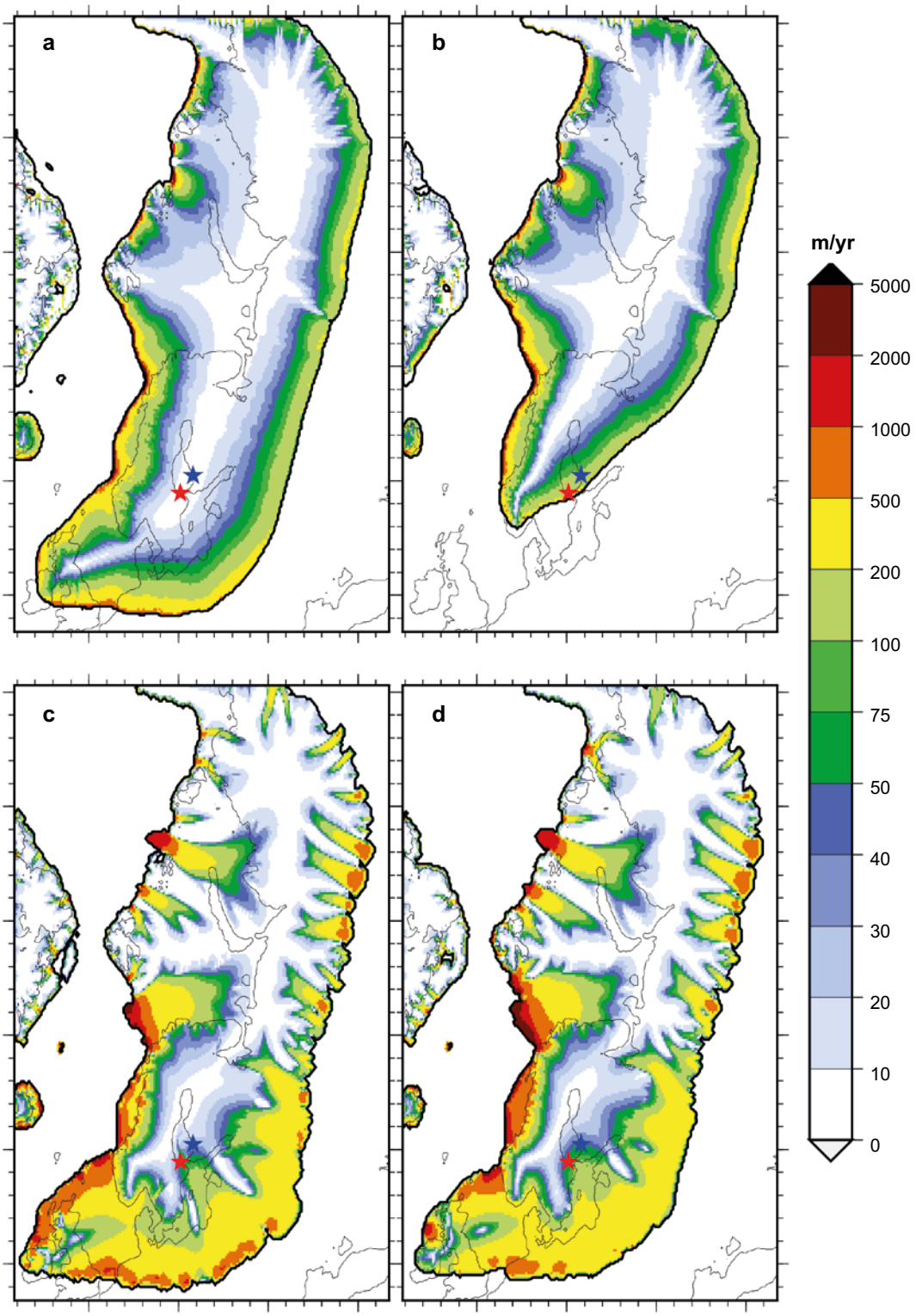

Figure 3-2. *Vertically integrated velocities (m/yr) for (a) SICO_Topo1, (b) SICO_Topo2, (c) SMB4 using GRISLI forced by B140_Topo1 climate forcing and (d) SMB4 using GRISLI forced by B140_Topo2.*

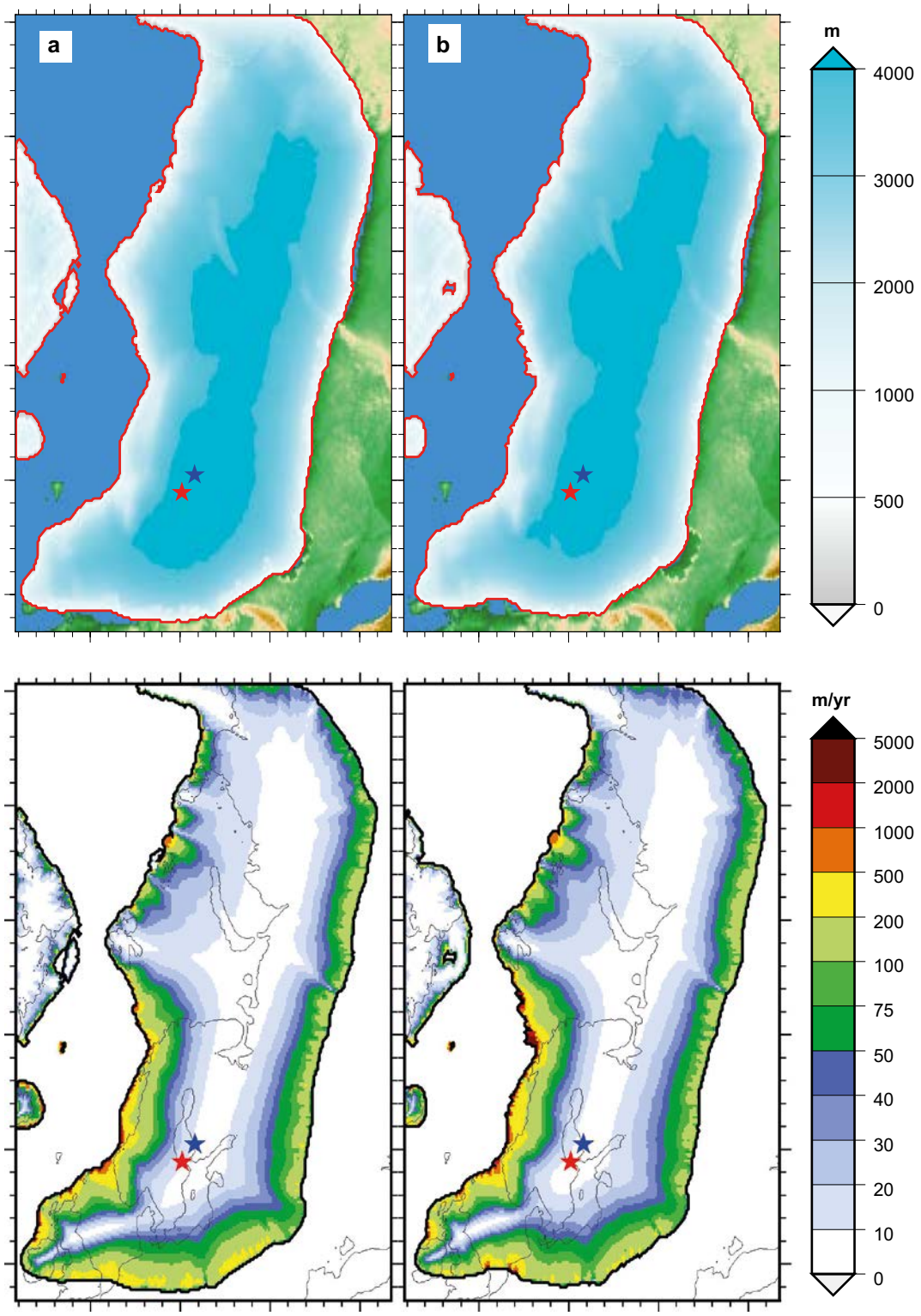

Figure 3-3. *Ice thickness (m) simulated by GRISLI with SIA only (DYN3): (a) SIA_Topo1 forced by the B140_Topo1 climate forcing (b) SIA_Topo2 forced by the B140_Topo2 climate forcing, and corresponding vertically integrated velocities (m/yr) for (c) SIA_Topo1 and (d) SIA_Topo2. Note that the black contour corresponds to the extent of the ice sheet at the end of each SMB simulation and not to the reference simulations. However, note that the ice thicknesses displayed in (a) and (b) are not compatible with global sea-level budgets for this period (Section 3.4), suggesting that these simulations overestimate ice sheet volumes and ice thicknesses.*

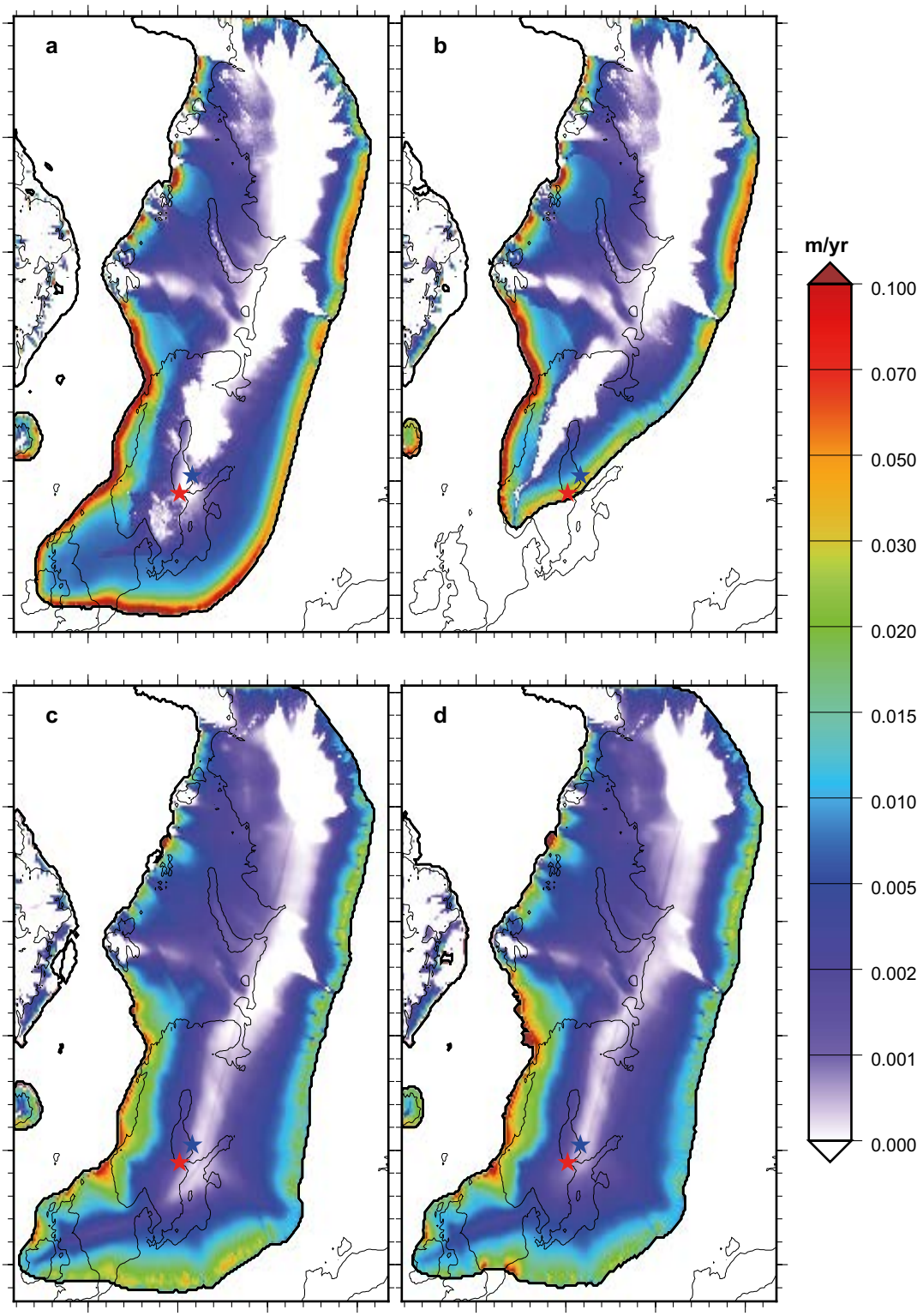

Figure 3-4. *Basal melting rates (m/yr) for (a) SICO_Topo1, (b) SICO_Topo2, (c) SIA_Topo1 and (d) SIA_Topo2. Note that the black contour corresponds to the extent of the ice sheet for the displayed simulations.*

3.2 Importance of spatial model resolution

During the first phase of the study (Colleoni et al. 2014b, 2016b), all simulations with GRISLI were performed at both 20 km and 40 km horizontal resolution. The sensitivity of GRISLI to model parameters has been shown to be the same for both resolutions, but with discrepancies in the amplitude of the ice sheet dimension-related quantities. The simulations performed on the 40 km

grid led to larger ice sheets with systematic differences in all the experiments compared with the results obtained on the 20 km grid. In term of ice volume, the coarse resolution led to an additional two to three m SLE (with about 200 m thicker ice above both repository sites). More details on those results are reported in Section 4.6 of Colleoni et al. (2014b, 2016b). The order of magnitude of this change motivated further investigations of the impact of model resolution.

For this reason, we here compare the previously performed GRISLI simulations with the results obtained with SICOPOLIS using the 20 km (DYN1) and 40 km grids (DYN2). Contrary to what has been simulated with GRISLI, there is no systematic change in ice volume when changing the horizontal grid resolution in SICOPOLIS. The final volume is larger by 1.3 % (+1 m SLE) when using the 20 km grid under B140_Topo1 climate forcing, but lower by about 0.8 % (−0.5 m SLE) under the B140_Topo2 climate forcing. Under B140_Topo1 climate conditions, the increase in resolution results in an increase in ice thickness at both sites of less than 100 m (Table 3-2). Under the B140_Topo2 climate conditions, the ice is retreating in the western part at both resolutions (e.g. Figure 3-1b), resulting in that the two sites are located closer to the ice sheet margin, especially the Forsmark site. When increasing the resolution from 40 km to 20 km under B140_Topo2 climate conditions, the ice thickness is reduced by more than 600 m at Forsmark (from 791 m to 124 m) and by about 450 m at Olkiluoto (from 1417 m to 957 m).

During the first phase of the study, the differences in topography between two resolutions in GRISLI were explained by the better representation of the complex topography of the Scandinavian mountain range with the 20 km grid resolution. It results in a better resolved velocity pattern in this area, increasing the flux of ice via narrow channels. Because SICOPOLIS use the SIA-only to represent ice streams, the velocity terms are less important than in GRISLI (see previous section), and, as a consequence, SICOPOLIS is less sensitive to horizontal resolution. However, the velocity is not the only variable affected by model resolution. A better resolved topography at the margins also allows for a better representation in surface mass balance. The potential effects of changes in grid resolution are not trivial.

We wanted to further explore the impact of model resolution by generating and implementing a new grid of 10 km resolution over Eurasia. Compared to the 20 km grid, the number of grid points is almost multiplied by a factor 4 (from 56,700 to 225,841). The time required to perform a simulation is thus drastically increased. As an example, we were only able to simulate 20 kyrs of ice sheet evolution in SICOPOLIS when running the model for 12 hours on our supercomputing platform. Also, the polythermal mode generated large numerical instabilities and had to be switched off. In addition, GRISLI was unfortunately not able to handle the size of the array and systematically crashed when trying to implement the 10 km resolution grid. For these reasons, we did not carry out additional 10 km grid resolution experiments.

3.3 The importance of an ice stream restriction in GRISLI

Due to the large difference in terms of ice flow between GRISLI and SICOPOLIS, it is interesting to investigate the impact of the distribution of SSA-treated zones on the ice extent and thickness. As described in Section 3.1.1, GRISLI triggers the SSA on broad areas and does not restrict the use of SSA to narrow valleys only. The criteria used to define the potential stream zones in GRISLI are partly empirical. Therefore, a more physical approach is used to limit the spatial application of the SSA. Most of the present-day observed ice streams in Greenland and Antarctica are well defined narrow features (Joughin et al. 2010, Rignot et al. 2011). It is suspected that most paleo ice streams presented the same characteristics (e.g. Stokes and Clark 1999) with width not greater than 250 km (Ottesen et al. 2005). However, a recent synthetic review of Margold et al. (2015) pointed out the existence of ice streams in the western part of the Laurentide ice sheet with no analogue to present-day ice streams and not primarily controlled by topography. In this area, streams were supposedly wide and short, with changing flow directions on short time scale. Margold et al. (2015) suggest that this was due specifically to the presence of thick deformable sediments under this part of the ice sheet.

In the GRISLI reference simulations REF_Topo1 and REF_Topo2, a large and widespread part of the ice sheet exhibits ice stream flow given the criteria described in Section 3.1.1, with almost 50 % of the ice sheet treated with the SSA (Figure 3-5). The flow in the western part of the ice sheet

strongly differs from the one in the eastern part. Due to its position relative to the North Atlantic storm tracks, the western region presents a warmer climate, with relatively high precipitation and temperatures (Figure 1-4). The high temperatures promote the presence of warm-based ice with high basal melting rates. As a consequence, GRISLI systematically predicts SSA conditions in this part of the ice sheet.

As previously mentioned, GRISLI relies on a saturated sediment thickness layer at the base of the ice sheet to trigger the SSA. However, this sediment criterion is not really restrictive in our simulations since, if we exclude continental Fennoscandia, the entire Eurasian grid domain is covered by a thick sediment layer, far above the imposed threshold for stream activation in GRISLI (see Figure 4-2 in Colleoni et al. 2014b, 2016b). As a consequence, for the purpose of the present study, GRISLI lacks a more physically-based condition to activate the SSA.

Most of present-day ice streams exhibit an imprint on the underlying bedrock. Thus, as exploratory tests, we restrain the SSA ice flow to the large-scale valleys in GRISLI. Following the methodology of Quiquet et al. (2013), we computed a large-scale topographic curvature map from the present-day topography in order to identify valleys. The curvature is calculated over a 5-degree radius (about 100 km at 80°N) from the 1 arc-minute global relief model ETOPO1 (Amante and Eakins 2009). The resulting mask for ice stream zones is shown in Figure 3-6.

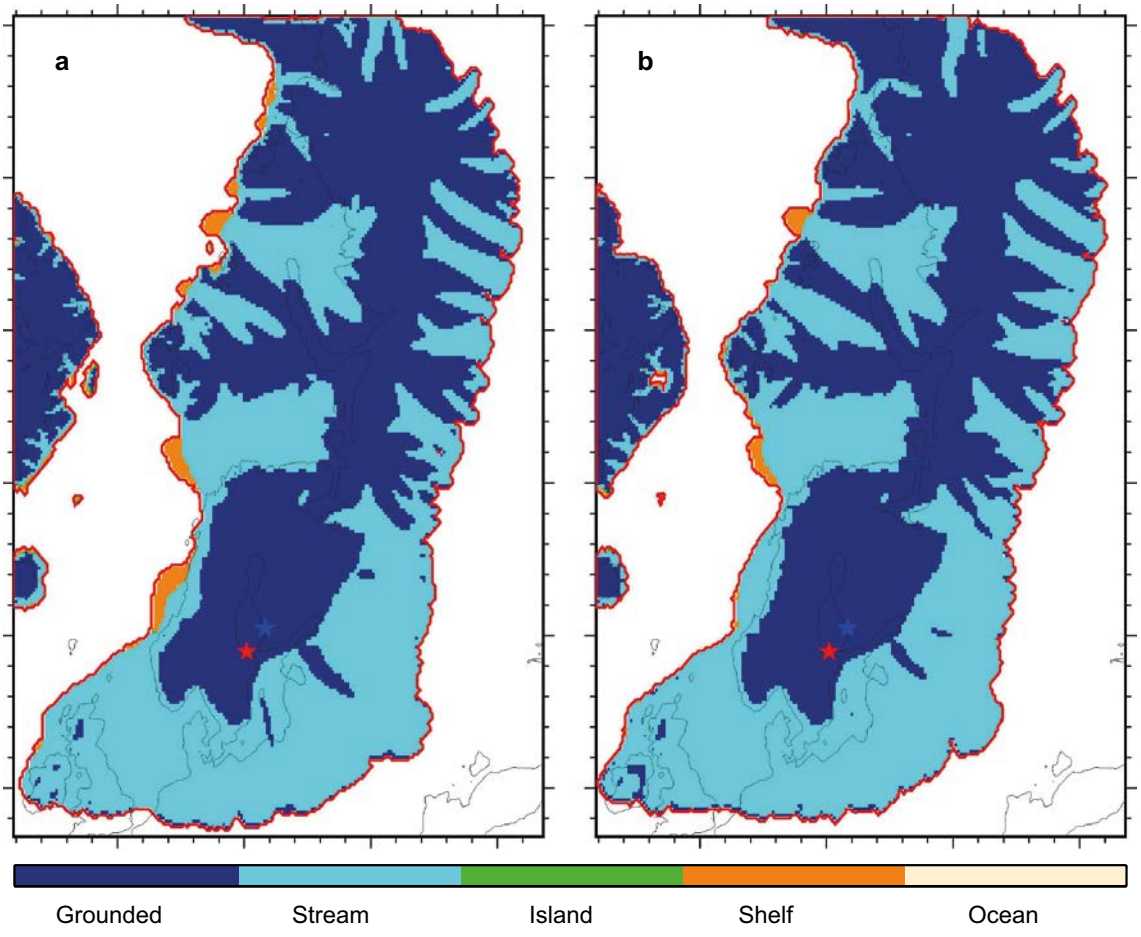

Figure 3-5. *Distribution of ice flow types in GRISLI for the reference simulations REF_Topo1 (a) and REF_Topo2 (b). A grid point in GRISLI can be either: i) grounded (grounded ice treated with the SIA), ii) stream (grounded ice treated with the SSA), iii) island (a grid point with no neighbor, treated with SIA and enhanced sliding), iv) ice shelf (floating ice treated with the SSA), or v) ocean, seas and lakes (no ice). The Forsmark location is shown with a red star and the Olkiluoto location with a blue star.*

As expected, the use of the restrictive mask drastically decreases the area treated with the SSA, in particular in the south-western part of the ice sheet (Figure 3-7b). The individual ice streams are well defined compared with the reference simulation. As a result, the simulated ice thickness ranges between that of the reference simulation and that of the simulation with SIA-only. Table 3-2 summarises the different performed experiments and the resulting ice volume and ice thicknesses at both repository sites.

With these exploratory experiments we have highlighted the importance of ice stream activations in GRISLI. However, the curvature criterion is somehow arbitrary as we need to define the scale of the valleys. In addition, bedrock topographic features are not the only driver for ice stream activation (e.g. Margold et al. 2015). Note that the simulations that we conducted to test the activation of the ice streams are idealised and therefore, the results should be interpreted with care.

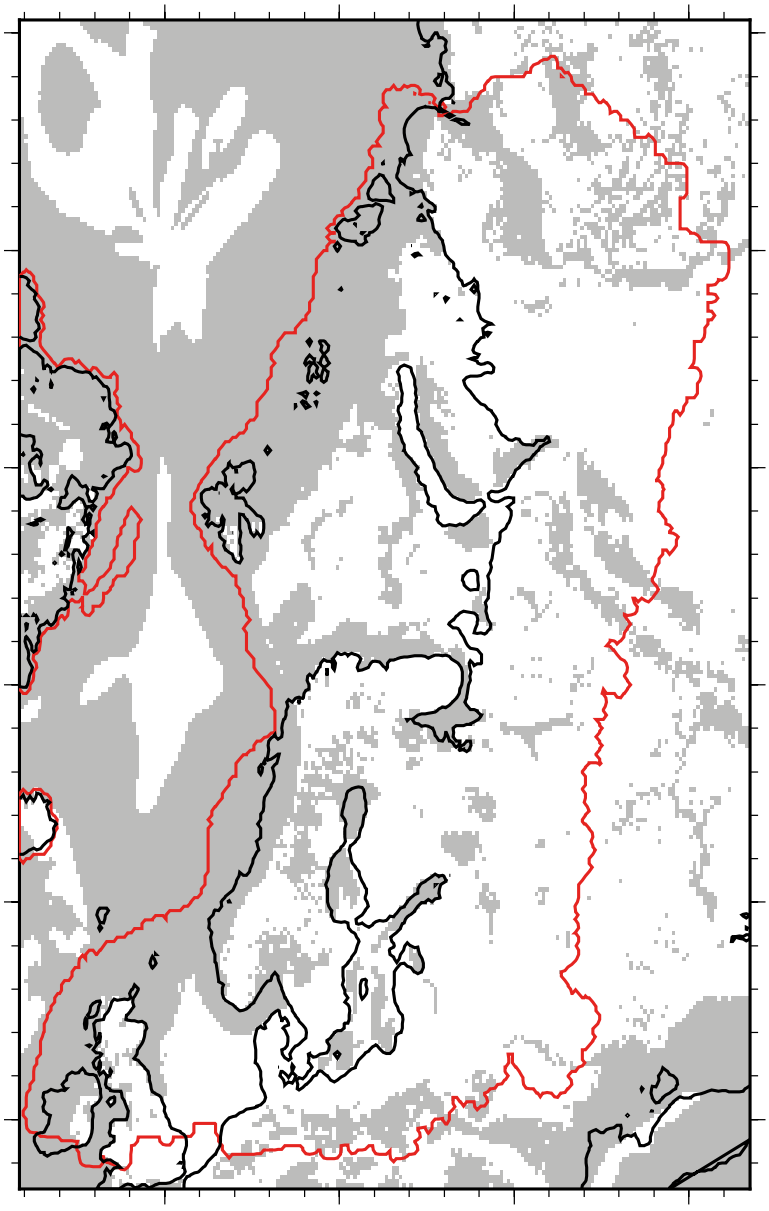

Figure 3-6. *Mask for allowed stream zones (in grey), computed from the 1 arc-minute global relief model ETOPO1 (Amante and Eakins 2009) over the Eurasian domain. The thick red line is the late Saalian ice extent of Peyaud (2006). The thick black line shows the present-day coast line.*

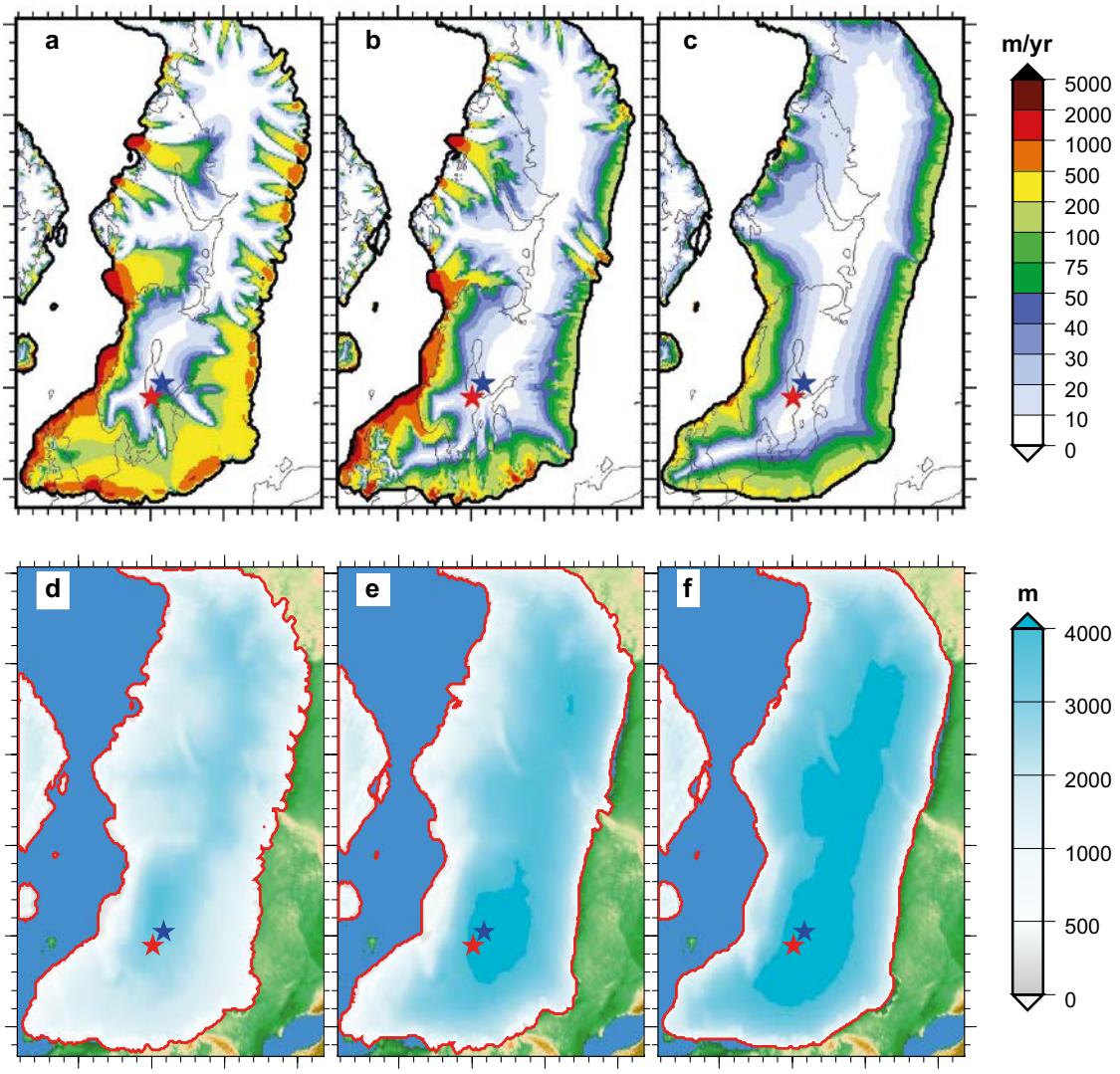

Figure 3-7. *Vertically averaged horizontal velocities (m/yr) simulated after 200 kyrs by GRISLI forced with B140_Topo1 climate forcing in (a) the reference simulation REF_Topo1, (b) using the mask presented in Figure 3-5 and (c) with SIA only and no mask (SIA_Topo1)(c). The corresponding ice thickness (m) is shown in (d), (e), and (f). Note that panels c) and f) are identical to Figure 3-3. They are repeated for the need of comparison with the other simulations. A red star denotes the Forsmark site and a blue star the Olkiluoto site. Note that the displayed ice thicknesses are not compatible with global sea-level budgets for this period (Section 3.4), suggesting that these simulations overestimate ice sheet volumes and ice thicknesses.*

3.4 Discussion and summary of section

In this section we have implemented new grids in the SICOPOLIS ice sheet model and performed experiments following the same methodology as previously made for GRISLI (Colleoni et al. 2014b, 2016b). The SICOPOLIS model presents important differences compared to GRISLI, since it is a poly-thermal SIA-only model. The use of a different ice sheet model has highlighted the major role of ice dynamics in explaining the Eurasian ice sheet volume and thickness. This is in line with the findings of the investigations conducted in the first phase of the study (Colleoni et al. 2014b, 2016b), suggesting that basal drag was the predominant factor determining ice thickness over the repository sites.

Table 3-2. Simulated Late Saalian ice volume (m SLE), ice thickness (m) and bedrock depression (m) at the end of the 200kyrs simulation for the different experiments testing the sensitivity to model formulation and resolution listed in Table 3-1. For ice thickness and bedrock depression, Forsmark is identified by an *F*, Olkiluoto by an *O*. Changes, expressed in %, are computed relative to the reference simulations REF_Topo1 and REF_Topo2. However, note that these results on ice volumes are not compatible with global sea-level budgets for this period (Section 3.4), suggesting that these simulations overestimate ice sheet volumes and ice thicknesses.

	Saalian ice sheet volume				Ice thickness					Bedrock depression				
	B140_Topo1		B140_Topo2		Site	B140_Topo1		B140_Topo2		Site	B140_Topo1		B140_Topo2	
ID	m SLE	%	m SLE	%		m	%	m	%		m	%	m	%
DYN1	77.34	45.2	55.44	7.63	*F*	4422	*42.6*	791	*−72.9*	*F*	−1183	*61.8*	−217	*−68.4*
					O	4453	*37.9*	1417	*−53.7*	*O*	−1210	*58.5*	−334	*−53.7*
DYN2	76.34	43.3	55.89	8.5	*F*	4358	*40.5*	124	*−95.7*	*F*	−1167	*59.6*	−158	*−76.9*
					O	4341	*34.4*	957	*−68.7*	*O*	−1183	*55.0*	−262	*−63.6*
DYN3	91.4	71.6	90.6	75.9	*F*	4664	*50.4*	4657	*59.8*	*F*	−1160	*58.6*	−1149	*67.8*
					O	4707	*45.7*	4712	*53.9*	*O*	−1174	*53.8*	−1167	*62.0*
DYN4	74.0	38.9	72.9	41.5	*F*	4238	*36.6*	4202	*44.2*	*F*	−1031	*41.0*	−1016	*48.4*
					O	4380	*35.6*	4359	*42.3*	*O*	−1079	*41.4*	−1066	*48.0*

When using the SIA-only model, the ice flow is considerably slower than when also using the SSA. As a result, the simulated ice topographies obtained in the simulations presented in this section are not considered realistic. This is also corroborated by the fact that, all the ice volumes obtained at the end of the simulations (Table 3-2) are beyond what is suggested by the global sea-level reconstructions (Rabineau et al. 2006). On the other hand, the reference simulations REF_Topo1 and REF_Topo2 are producing extensive ice streams areas, especially in the western part, where the velocities range between 200 m/yr and 500 m/yr, which have no equivalent in terms of width in present-day ice sheets. For this reason, we tested the impact of a topographic restriction criteria on the area treated with the SSA. This restriction leads to a decrease in ice flow and to an increase ice thickness but the robustness of such an approach is questionable since no clear geological evidence can be used to support the selection of the topographic restriction. In this section we have shown that the climate forcing has a strong impact on the ice stream activation and that a realistic calibration independent from climate forcing is difficult to obtain. However, the basal drag coefficient is a poorly constrained parameter that can mitigate the impact of the potential overestimation of ice stream areas.

Although the simulations in the present section are idealised and more of a theoretical construction, not possible to constrain by geological evidence, the value of total ice volume and ice thickness and bed depression for both repository sites, as simulated by GRISLI, are reported in Table 3-2. The ice volume obtained with this set of simulations varies between 74 and 91.4 m SLE. As stated in this section, if those numbers are considered in the global ice volume framework for the Late Saalian glacial maximum, those simulations goes beyond the upper bound suggested by sea-level reconstructions (Rabineau et al. 2006). The ice thickness ranges between 4238 m (124 m) to 4664 m (4657 m) at Forsmark under the B140_Topo1 (B140_Topo2) climate conditions. This corresponds to the bedrock depression varying from −1031 m (−158 m) to −1183 m (−1149 m). Over Olkiluoto, the ice thickness ranges from 4341 m (957 m) to 4707 m (4712 m) under the B140_Topo1 (B140_Topo2) climate forcing. The bedrock depression varies between −1079 m (−262 m) to −1210 m (−1167 m). It should however again be noted that these ice thickness vales are not considered realistic, both because of the ice sheet model formulations and because the resulting ice volumes exceed the global water budget for the investigated time period. The lowest values are obtained for the cases in which the ice partly retires over the western part of the ice sheet.

4 Evolution of Eurasian ice streams during the Weichselian deglaciation

In the previous section, the attempts to develop topographic criteria for the use of the SSA led to unconstrained simulations. Geomorphological evidence of the evolution of the Eurasian ice sheet flow is only available for the last glaciation, the Weichselian, and from that period mainly from the deglaciation (21 kyrs BP – 0 kyrs BP). Therefore, in this section, we perform steady-state simulations of the LGM and transient simulations covering the last 21 kyrs with the aim to better constrain the Eurasian ice sheet simulations for the Late Saalian. The advantage of the LGM and the last deglaciation is that it is considerably better documented than the Late Saalian. In addition, the LGM climate simulations outputs from the Paleoclimate Modelling Intercomparison Project phase 3 (PMIP3) are publicly available and can be used to force GRISLI.

4.1 Last Glacial Maximum climate forcing

The paleoclimate modelling intercomparison project (PMIP) is an international effort aiming for a better understanding of the mechanisms of past climate change. This is achieved via the coordination of climate model experiments, paleo-data syntheses and model-data comparisons. This project has now been running for more than 20 years and the fourth phase will be conducted under the CMIP6 models inter-comparison exercise. In this section, we will take advantage of the model outputs from PMIP3 to force GRISLI. In particular, complex and computationally expensive coupled atmosphere-ocean general circulation models (AOGCM) have been used to simulate the LGM and the pre-industrial (PI) climates. The participating modelling groups have performed steady-state time-slice experiments for which the boundary conditions (such as orbital forcing, ice sheets and GHGs) were kept constant.

From the various participating models in PMIP3, we have selected six AOGCMs for which both the LGM and the PI outputs were available:

- CNRM-CM5 (Voldoire et al. 2012), with an atmospheric resolution of 1.4°×1.4° (L 31).
- FGOALS-g2 (Li et al. 2013), with an atmospheric resolution of ~ 2.8°×2.8° (L 26).
- IPSL-CM5A-LR (Dufresne et al. 2013), with an atmospheric resolution of 3.75°×1.9° (L 39).
- MRI-CGCM3 (Yukimoto et al. 2012), with an atmospheric resolution of 1.125°×1.125° (L 48).
- MPI-ESM-P (Giorgetta et al. 2013), with an atmospheric resolution of ~ 1.9°×1.9° (L 47).
- MIROC-ESM (Watanabe et al. 2011), with an atmospheric resolution of ~ 2.8°×2.8° (L 81).

In our case, the variables of interest from these models are near-surface air temperature, total precipitation, and surface topography. We use the monthly climatological mean for surface air temperature and precipitation provided by the participating groups for both the LGM and PI simulations.

A climate model never perfectly represents the climate, and each climate model has its own physical or numerical biases that might substantially affect the ice dynamics in an ice sheet model (Pollard et al. 2000). One way to reduce the importance of these biases is to compute anomalies between the simulated climate and present-day observations as done for example by Charbit et al. (2007) or Quiquet et al. (2013). Those anomalies are an indication of the climate response to a change in the boundary or initial conditions, independently from the physical bias of the model. In the present study, the aim is not to correct those model biases, but to use the model diversity to obtain a perturbation of LGM climate relative to a chosen reference model. In the following, the terminology “anomaly” will refer to temperature ($T_{snap,anom}$) and precipitation ($P_{snap,anom}$) anomalies computed for a certain snapshot (LGM or Late Saalian) relative to the PI, such as:

$$\begin{cases} T^{GCM}_{snap,anom} = T^{GCM}_{snap} - T^{GCM}_{PI} \\ P^{GCM}_{snap,anom} = P^{GCM}_{snap} / P^{GCM}_{PI} \end{cases} \qquad \text{(Equation 4-1)}$$

For the precipitation, we compute a ratio instead of a difference to avoid negative precipitation rates (Charbit et al. 2007). The surface air temperature and precipitation anomalies are then added on top of a reference climatology, which in our case corresponds to the Pre-industrial simulation from the CESM model (Gent et al. 2011). This choice is motivated by the fact that our Late Saalian climates were simulated with CESM 1.0.5 (see Colleoni et al. 2014b, 2016a, and b):

$$\begin{cases} T_{snap}^{GCM} = T_{PI}^{CESM} + T_{snap,anom}^{GCM} \\ P_{snap}^{GCM} = P_{PI}^{CESM} \times P_{snap,anom}^{GCM} \end{cases} \quad \text{(Equation 4-2)}$$

Therefore, following this method, we obtain six LGM climates, all based on CESM pre-industrial simulations. We could have performed our LGM simulations by using the climate computed by the AOGCMs listed above without performing any additional transformations. However, the same method is also used to generate the anomalies, derived from each PMIP3 AOGCMs listed above, that are used in the transient simulations. More details on the transient experiments are provided in Section 4.5. To preserve the consistency between the steady-state and transient LGM simulations, the same method is applied to all LGM simulations. Note that all AOGCM climates were properly downscaled on the GRISLI 20 km grid using a lapse rate of 5 °C km^{-1} and a precipitation correction factor of 0.05 $°C^{-1}$ (same methodology used when creating the reference simulation REF_Topo1 and REF_Topo2, see Section 4.2.2 in Colleoni et al. 2014b, 2016b)

4.2 Comparison of pre-industrial and LGM climates in six PMIP AOGCMs

4.2.1 Pre-industrial climates

The climate over northern Eurasia is partly driven by the poleward atmospheric and oceanic heat transport. The atmospheric and oceanic heat transports can be influenced for example by the distribution of topography, bathymetry and surface albedo (vegetation, sea-ice cover). The six climate models mostly agree for the distribution of surface air temperature (Figure 4-1). Mean annual surface air temperature over the Arctic Ocean varies between −16 °C (MIROC-ESM) to −30 °C (FGOALS-g2). In all models, the Arctic Ocean is covered by a perennial sea-ice cover. However, the discrepancies in surface air temperature between the climate models could be due to differences in the amount of snow accumulation on the sea-ice and on different values prescribed for snow and ice albedo. Thus, the spatial distribution of the annual mean surface air temperature can be an indication of the strength of the Atlantic meridional overturning circulation (AMOC). The southward expansion of the sea-ice cover is also a good indicator of the strength of the deep water convection sites. In particular MIROC-ESM and MPI-ESM-P seem to have a stronger AMOC compared to the other models. In fact, the Norwegian Sea exhibits positive mean annual surface air temperatures in these models, which implies open ocean conditions during the summer (Figure 4-1). This also implies that the impact of the Gulf Stream on Western Europe and on Scandinavia is stronger in these two models. Conversely, FGOALS-g2 and IPSL-CM5A-LR are colder than the other models over the Norwegian Sea and exhibits negative mean annual temperatures (−4 °C to −2 °C). This implies that in this area, the sea-ice cover does not totally melt during summer and could prevent the North Atlantic intermediate warm waters from flowing in the Barents and Kara seas. Similar results are obtained when comparing the summer mean surface air temperature (not shown).

In Section 4.1, we described the methodology for the climate forcing at the LGM and in particular the use of the anomaly method. The base climate for the PI is, in our framework, the PI simulations from the CESM model (Gent et al. 2011). Figure 4-2 shows a comparison between the PMIP models and the CESM 1.0.5. CNRM-CM5 and FGOALS-g2 are systematically colder than CESM, whereas the other models seem to be slightly warmer in the eastern part of the domain.

In terms of precipitation, the maximum occurs in the North Atlantic stormtrack area. The northern expansion of the stormtrack area is determined by the extent of the sea-ice cover. This is why for example FGOALS-g2 and IPSL-CM5A-LR simulate large precipitation rates in the North Atlantic

(Figure 4-3). In addition, the models that have the lowest horizontal resolution tends to underestimate the precipitation maxima along the Norwegian coast (e.g. FGOALS-g2 and MIROC-ESM), whilst the models running on an intermediate resolution, around 1°, are able to capture the orographic precipitation maximum over the Scandinavian mountain range (MRI-CGCM3 and CNRM-CM5). The differences relative to CESM 1.0.5 are shown in Figure 4-4. Most of the AOGCMs present smaller amounts of precipitation over most of Eurasia, which could indicate a wet bias in CESM 1.0.5 during the PI in this region.

The discrepancies in the amplitude and distribution of surface air temperature and in precipitation between those models should have an important effect on the simulated Eurasian ice sheet geometry, as we will show in the following.

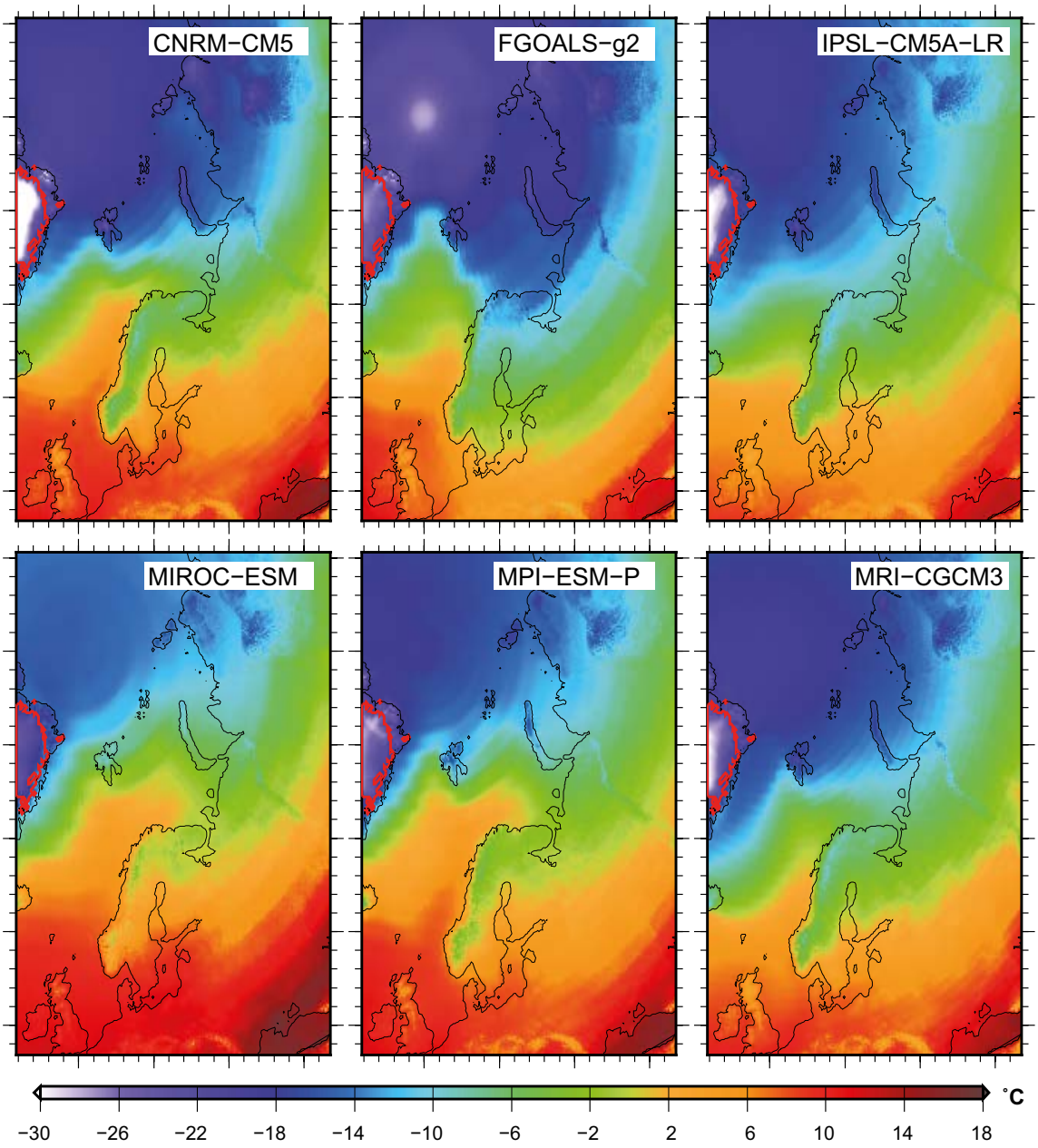

Figure 4-1. *Annual mean near-surface air temperature over Eurasia during the pre-industrial period as simulated by the six different AOGCMs.*

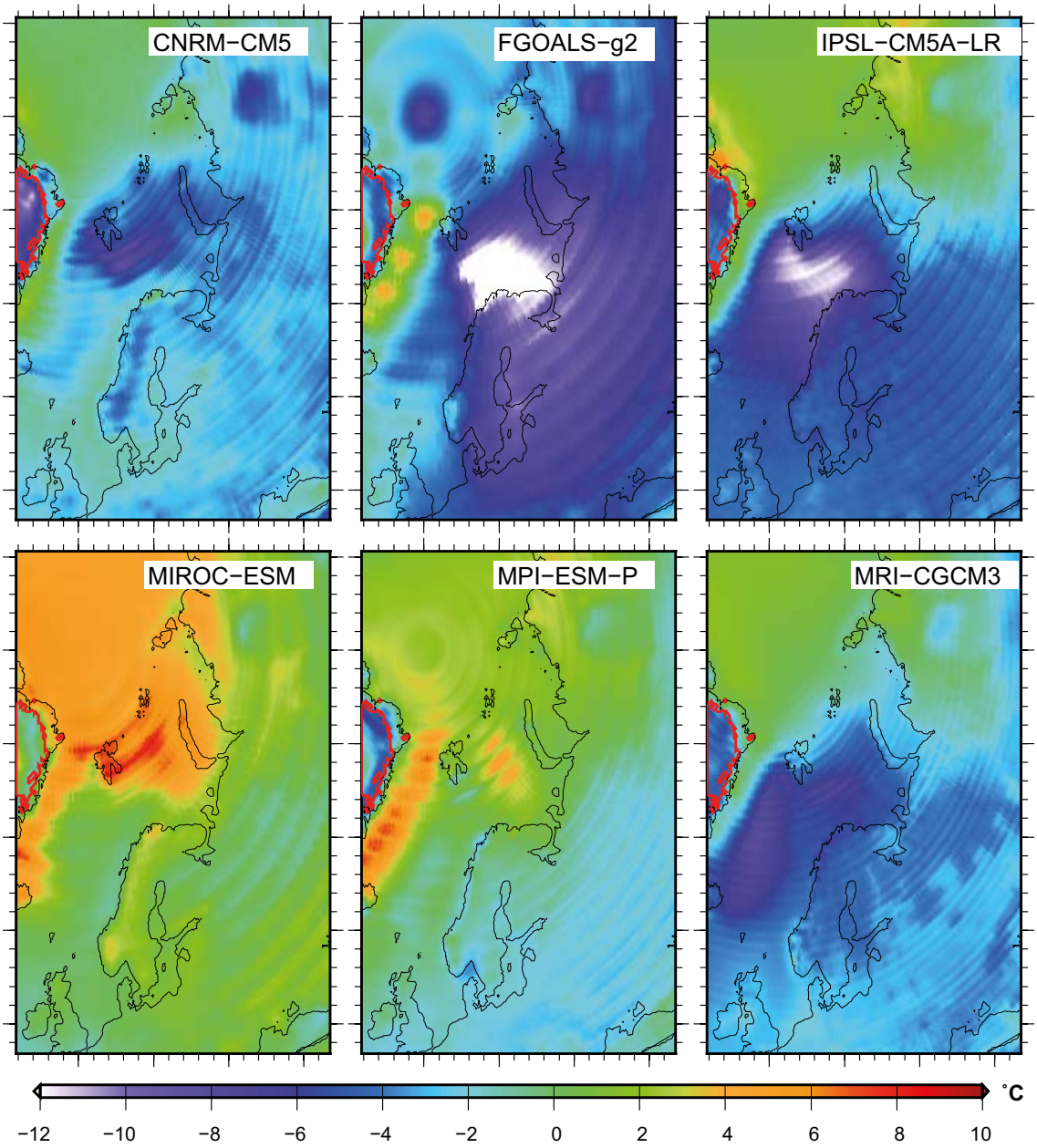

Figure 4-2. *Difference in annual mean near-surface air temperature over Eurasia during the pre-industrial period from the six AOGCMs relative to the CESM 1.0.5 (AOGCM – CESM). The radial pattern is due to the distortion induced by the projection and the interpolation from the coarse resolution of the climate model grid to the fine resolution of the ice sheet model grid.*

4.2.2 Last glacial maximum climates

Following the methodology presented in Section 4.1, we construct climate anomalies between the simulated LGM and the PI, from the six AOGCMs listed above, for the mean annual surface air temperature, the July surface air temperature and for the mean annual precipitation. Compared with their respective simulated pre-industrial climate, all the models simulate a negative annual mean temperature anomaly ranging from −2 °C over non-glaciated areas to −35 °C over the LGM Eurasian ice sheet and the North Atlantic sea-ice cover (Figure 4-5). Because of the high albedo and high elevation of the LGM ice sheet, all models clearly show the imprint of this ice sheet. However, the amplitude of the cooling differs to a large extent, from a relatively weak negative temperature anomaly in CNRM-CM5, IPSL-CM5A-LR and MRI-CGCM3 (−15 °C along the margins to −30 °C over the central area) to a very strong negative temperature anomaly (largely below −30 °C) in MPI-ESM-P and MIROC-ESM. Note that the cold temperature anomaly induced by the ice sheet implies the accumulation of a thick snow cover along the margins of the ice sheet. This snow cover induces, in turn, a local cooling, with an extent that differs considerably between the models (Figure 4-5).

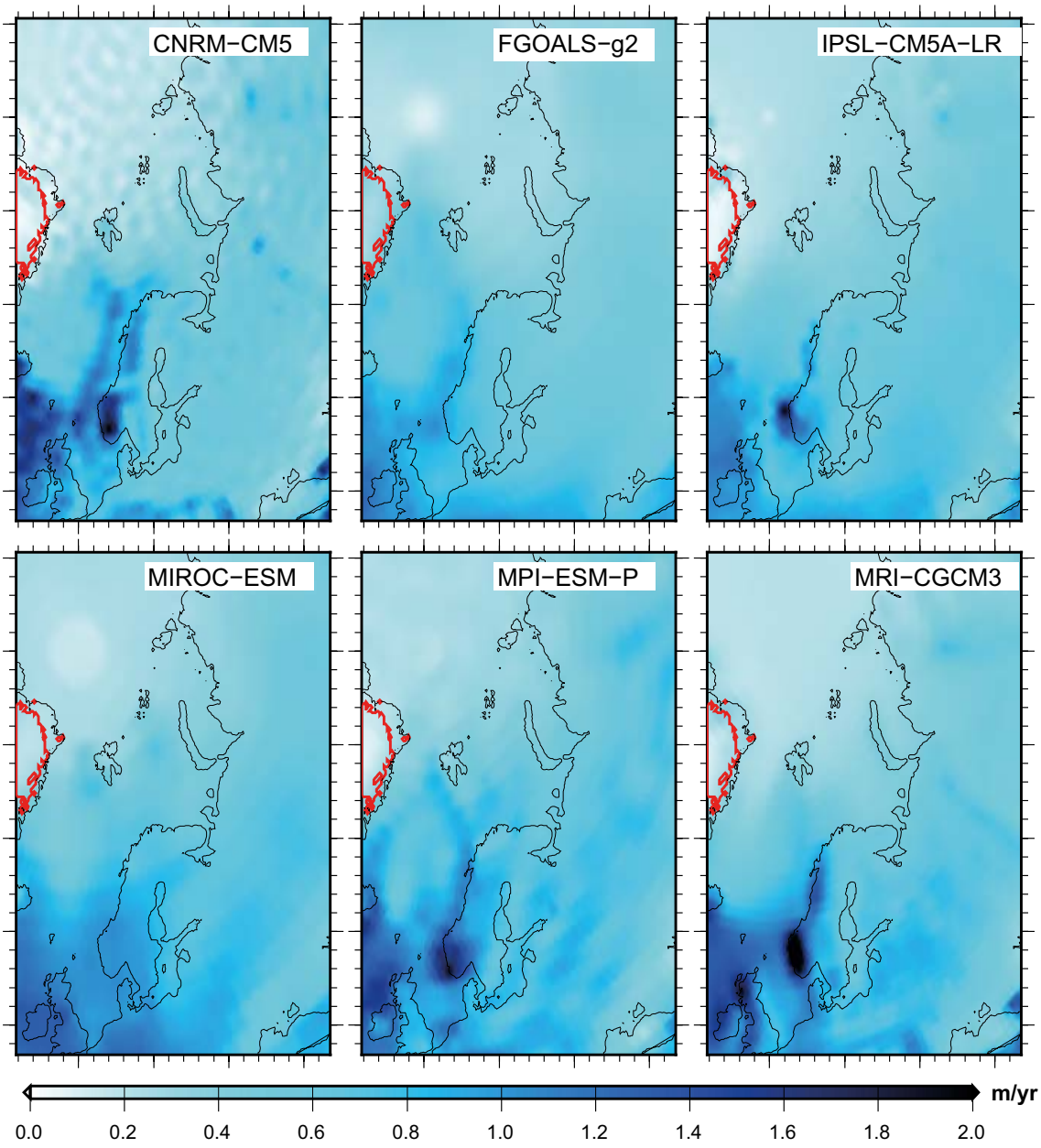

Figure 4-3. *Annual mean precipitation rate over Eurasia during the pre-industrial period as simulated by the six AOGCMs.*

Because ice sheet surface melt in GRISLI is driven by the July surface air temperature, we describe the relative surface air temperature anomaly in Figure 4-6. The variability among the models is much larger than for the annual mean. However, except for CNRM-CM5 and MRI-CGCM3, the anomaly remains negative over the non-glaciated areas in all the models. The CNRM-CM5 simulates a July warming of about 4 °C to 10 °C over the Russian plains and Siberia, which is by far too large compared to what the proxies suggest for the LGM over this area. With the exception of FGOALS-g2, all models simulate a slight warming of about 3 °C over East Siberia, which will prevent ice to grow over this area in our ice sheet simulations. MPI-ESM-P is the coldest model over the ice sheet, with a July temperature anomaly reaching −20 °C over the British Isles. Conversely, FGOALS-g2, IPSL-CM5A-LR and MIROC-ESM agree relatively well on the amplitude of the LGM summer cooling, with a cooling of about −15 °C over the Eastern part of the ice sheet and a cooling reaching −30 °C over the southwestern part of the ice sheet.

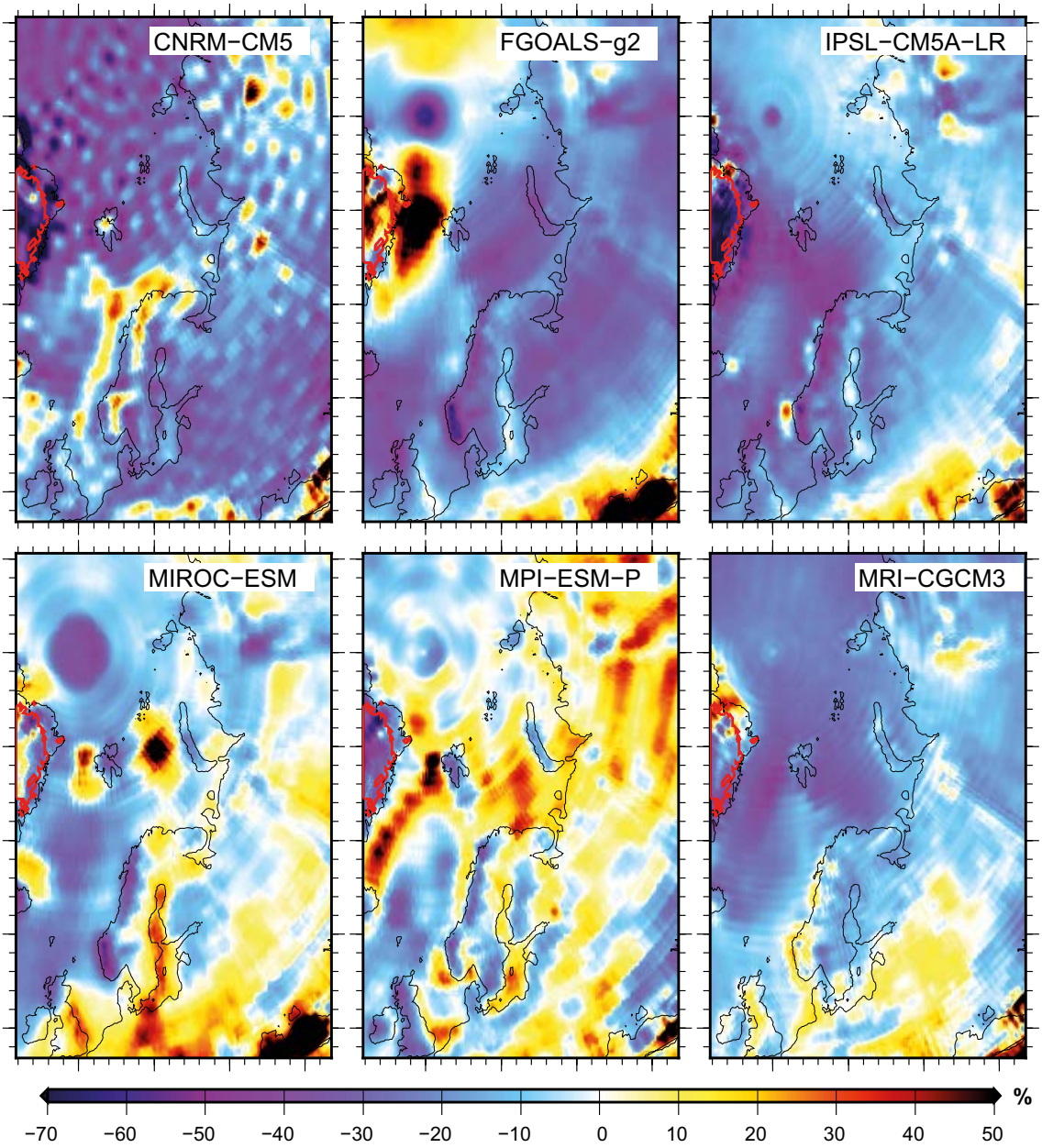

Figure 4-4. *Relative difference in annual mean precipitation rate over Eurasia during the pre-industrial period computed between the six AOGCMs and CESM 1.0.5 ((AOGCM-CESM)/CESM).*

The LGM cooling resulting from the orbital parameters, the atmospheric greenhouse gas (GHG) concentration and the prescribed ice sheet topography induces an overall drying of the Northern Hemisphere in all models (Figure 4-7). Over the Arctic, mean annual precipitation decreases by 30 % (IPSL-CM5A-LR) to 70 % (MIRCO-ESM) compared with PI. The precipitation also decreases by the same order along the eastern margins of the Eurasian ice sheet, and in some of the models also in the Russian plain. This is due to two main effects: (1) the precipitation is deviated southward during the LGM due to the presence of the Eurasian ice sheet since the ice sheet elevation blocks the atmospheric circulation over this area; (2) a snow cover develops along the ice sheet margins in all the models, except CNRM-CM5, which locally cools the temperature, which, in turn, reduces the precipitation over this area. Due to the high elevation of the Eurasian ice sheet, precipitation barely reaches the central parts of the ice sheet, and therefore precipitation decreases by almost 100 % compared with PI. Because the mean synoptic circulation is deviated southward due to the presence of a big Laurentide ice sheet over North America, precipitation rates increase at the southwestern margins of the Eurasian ice sheet in all the models. Due to its warm anomaly simulated at the LGM, the CNRM-CM5 model on average presents a moderate decrease in precipitation, and an increase of 20 % along the eastern margins. The latter feature, not produced by any of the other models, might result from the large positive summer anomaly shown in Figure 4-6.

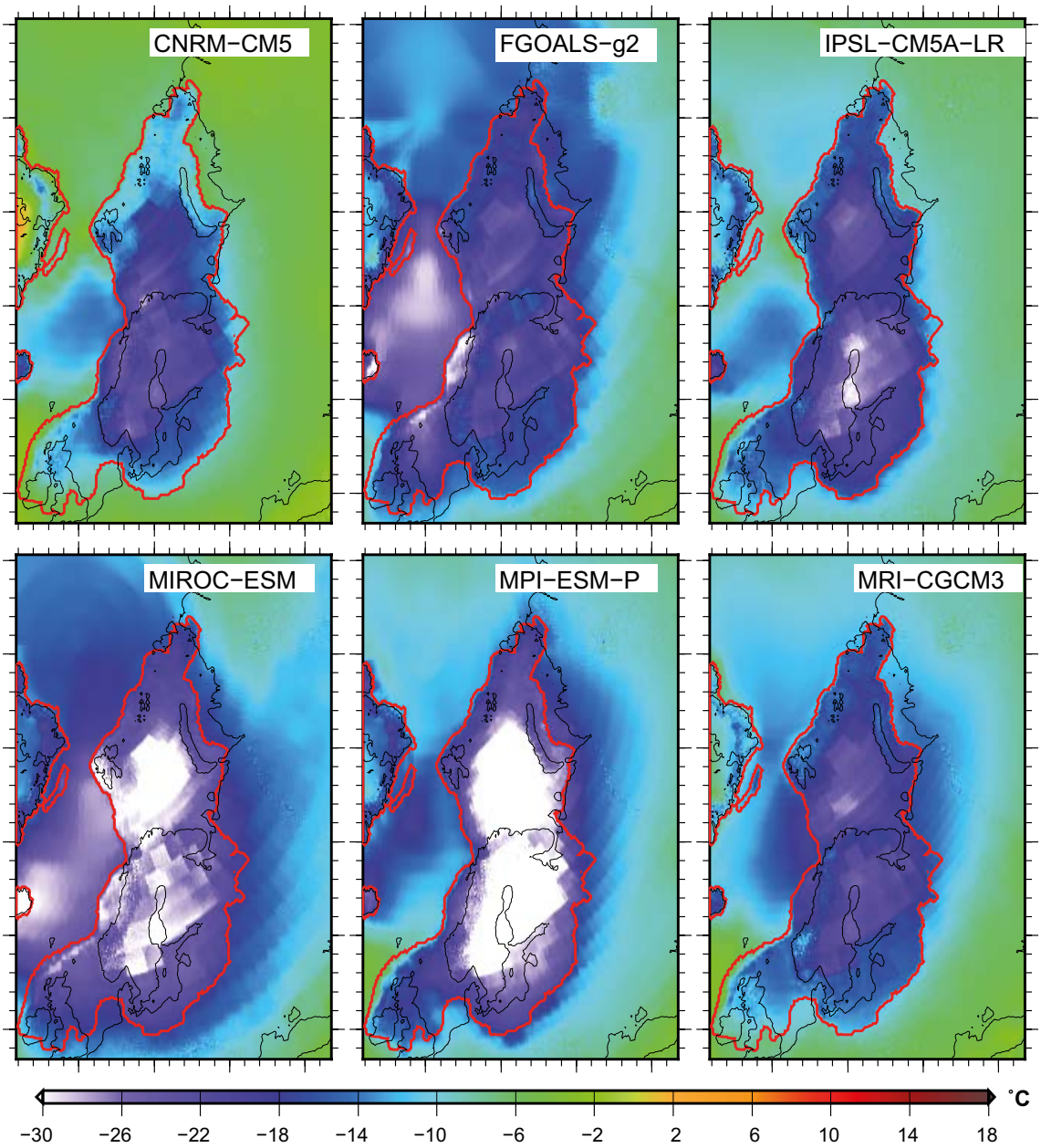

Figure 4-5. *Annual mean surface air temperature anomaly (°C) over Eurasia between the LGM and the PI (LGM-PI) as simulated by the six AOGCMs. The thick red line shows the ice sheet extent at the LGM from the ICE-5G reconstruction (Peltier 2004). This ice sheet extent was prescribed as boundary condition in the AOGCMs.*

4.3 Last deglaciation experiments

The last glacial-interglacial transition is considerably better documented than the previous deglaciation ending the Saalian glaciation. In particular, the evolution of the Northern Hemisphere ice sheets over the last deglaciation is now well dated (e.g. Peltier 2004, Svendsen et al. 2004, Stroeven et al. 2015). The aim of this section is to use this information to better constrain our model results for the Late Saalian. In particular we are interested in looking at the representation of ice streams in GRISLI during the deglaciation following the LGM and how well it compares with geomorphological reconstructions (e.g. Kleman and Glasser 2007).

For the consistency of our work, and because we have used the CESM 1.0.5 model for the Late Saalian climate simulations (climate B140_Topo1 and climate B140_Topo2), we chose the pre-industrial climate simulated by the NCAR-CESM model as reference. To construct LGM climates, we apply the LGM anomalies presented in Section 4.2 on top of this reference climate.

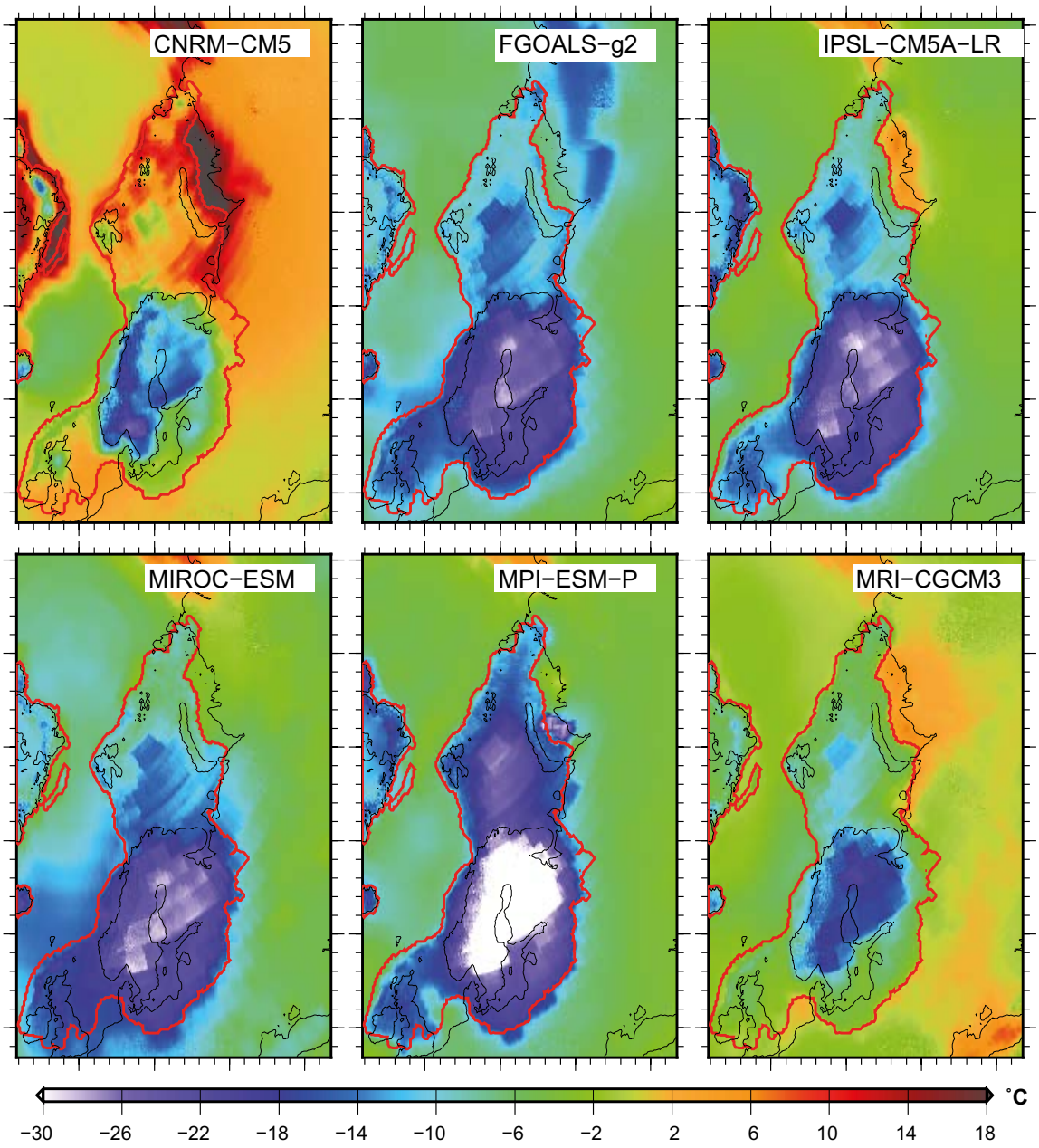

Figure 4-6. *July near-surface air temperature anomaly (°C) over Eurasia between the LGM and the pre-industrial (LGM-PI) as simulated by the six AOGCMs. The thick red line shows for the ice sheet ice extent at the LGM from the ICE-5G reconstruction (Peltier 2004). This ice sheet extent was prescribed as boundary conditions in the AOGCMs.*

4.3.1 Steady-state LGM experiments

In order to compare the LGM ice flow to that simulated in our steady-state Late Saalian simulations, we perform 200 kyrs steady-state LGM experiments with GRISLI forced by the LGM climates presented above. The model parameters for these LGM simulations follow those for the Late Saalian reference simulations REF_Topo1 and REF_Topo2 (Table A1). Because of the LGM summer warming relative to the PI (Figure 4-4), the CNRM-CM5 model is not able to maintain an ice sheet over Eurasia at the LGM. Therefore, we exclude this model from the following analysis. The simulated LGM ice sheet topographies (Figure 4-8) reflect the large variability in simulated LGM climate among the AOGCMs. The FGOALS-g2, MIROC-ESM and MPI-ESM-P climates lead to an ice sheet considerably larger than suggested by the reconstruction by e.g. Svendsen et al. (2004). On the contrary, The MRI-CGCM3 climate induces a moderate glaciation limited to the Kara-Barents archipelago and to the Scandinavian mountain range. The IPSL-CM5A-LR model produces an ice sheet very comparable in size to the one of Peltier (2004), which is also in close agreement with the extent reconstructed by Svendsen et al. (2004).

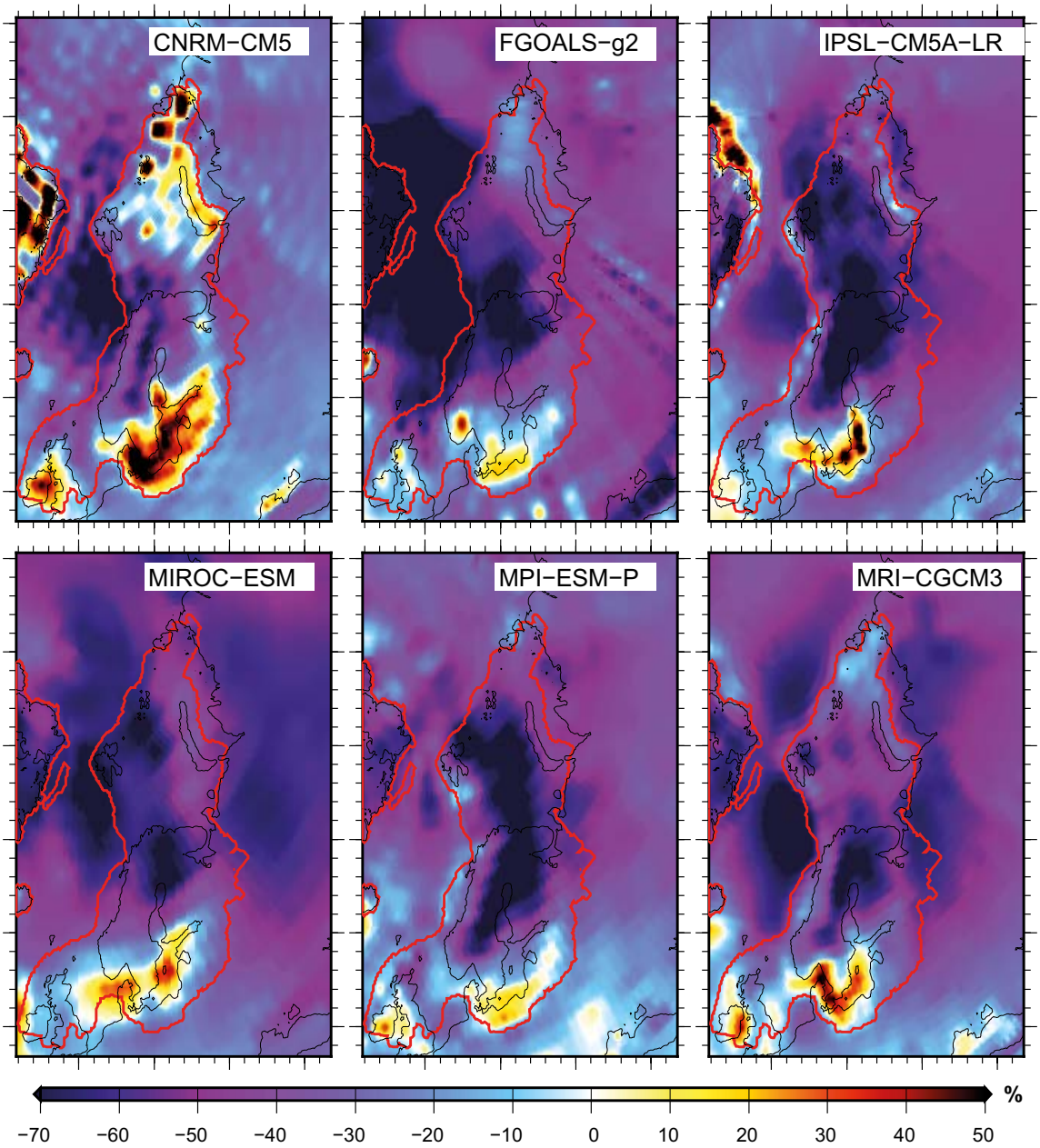

Figure 4-7. *Annual mean precipitation rate anomaly (% change) over Eurasia between the LGM and the PI ((LGM-PI)/PI) as simulated by the six AOGCMs. The thick red line shows for the ice sheet ice extent at the LGM from the ICE-5G reconstruction (Peltier 2004). This ice sheet extent was prescribed as boundary conditions in the AOGCMs.*

The type of GRISLI ice sheet flow for these different equilibrated ice sheets is shown in Figure 4-9. The western part of the ice sheet presents the same behaviour as for the Late Saalian, i.e. extended areas treated with the SSA. As for the late Saalian simulations, there are no ice streams over continental Fennoscandia. This is because the amount of sediment at the base of the ice sheet is very low in this area. Since the sediment threshold that determines the activation of ice streams is larger than the actual sediment thickness (Table A1), the SSA is not triggered here. In contrast to this, and also similar to our Late Saalian simulations, the eastern part of the ice sheet topography is similar amongst the different climate forcings, with more resolved ice streams than in the western part. This suggests that in this area, the ice streams are constrained more by the bedrock topography than by the presence of basal sediments. However, given the diversity of ice sheet topographies simulated, we are unable to better extract a criterion to limit the use of SSA over the western part in the LGM simulations. However, so far we performed steady-state LGM simulations, but the ice flow may evolve with the climate conditions and so may the ice streams areas. Thus, transient simulations over the last 21 kyrs BP are carried out in order to investigate the sensitivity of the ice stream evolution with GRISLI under time-varying climate forcing.

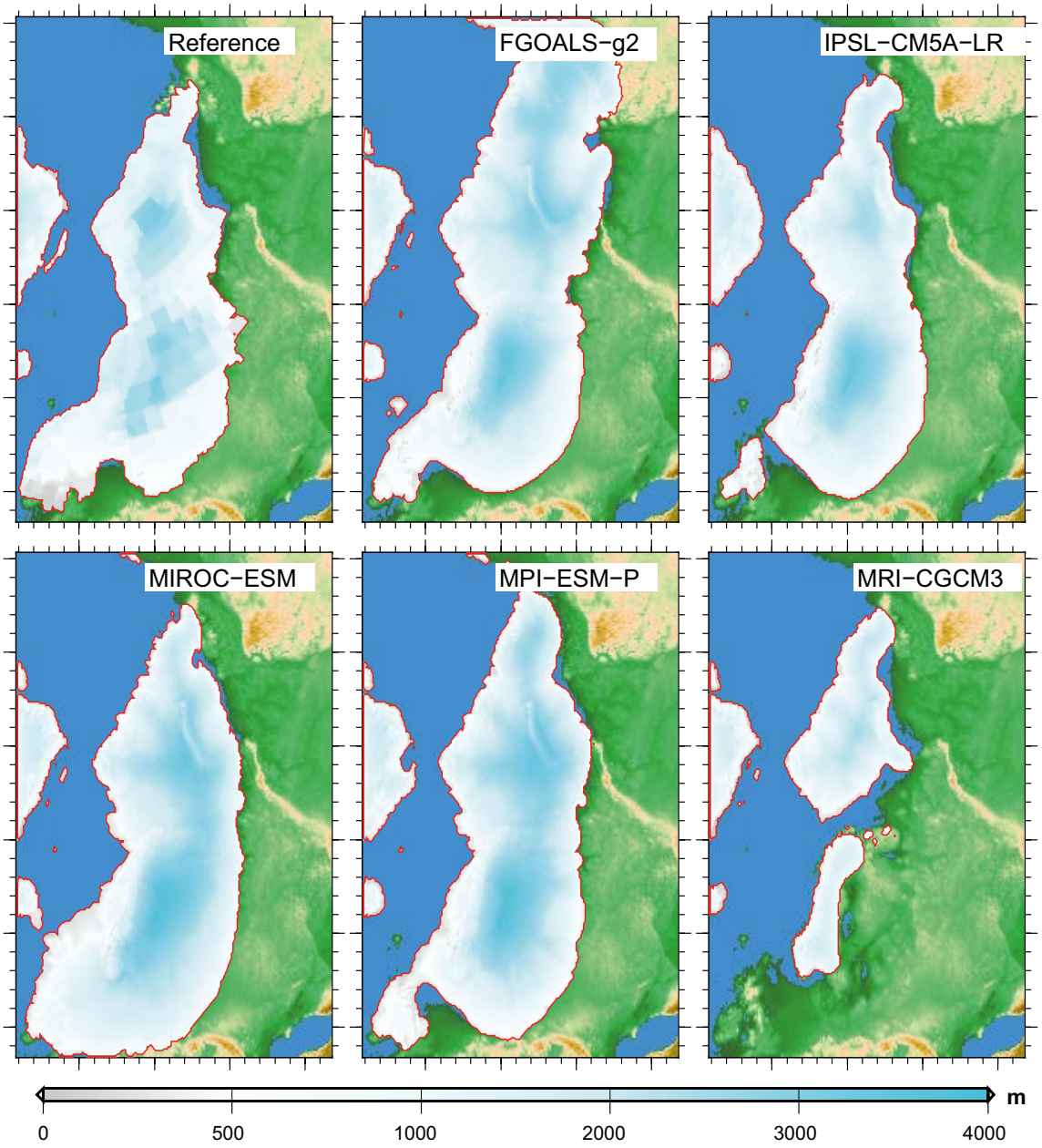

Figure 4-8. *Simulated ice thickness (m) after 200 kyrs under steady-state LGM climate forcing from the various AOGCMs (Figure 4-6 and 4-7). The reference ice thickness here is the ICE-5G reconstruction from Peltier (2004), i.e. the ice sheet reconstruction that was prescribed as boundary condition in the AOGCMs. The simulated ice sheet volumes are 33.9 m SLE (FGOALS-g2), 20.2m SLE (IPSL-CM5), 34.0 m SLE (MIROC-ESM), 31.6 m SLE (MPI-ESM-P) and 7.8 m SLE (MRI-CGCM3). The reference volume from Peltier (2004) is 20.9 m SLE.*

4.3.2 Transient experiments over the last deglaciation (21–0 kyrs BP)

In order to perform transient experiments we need to account for the climate evolution during the last deglaciation. Few transient coupled climate simulations have been performed so far and most of them were performed using Earth Models of Intermediate Complexity (EMIC, e.g. Abe-Ouchi et al. 2007, Bonelli et al. 2009, Ganopolski et al. 2010). A transient simulation of the last deglaciation was recently performed using the CCSM3 in its AOGCM version, varying the orbital parameters and the GHG concentrations and prescribing the ice evolution from the ICE-5G model (Peltier 2004).

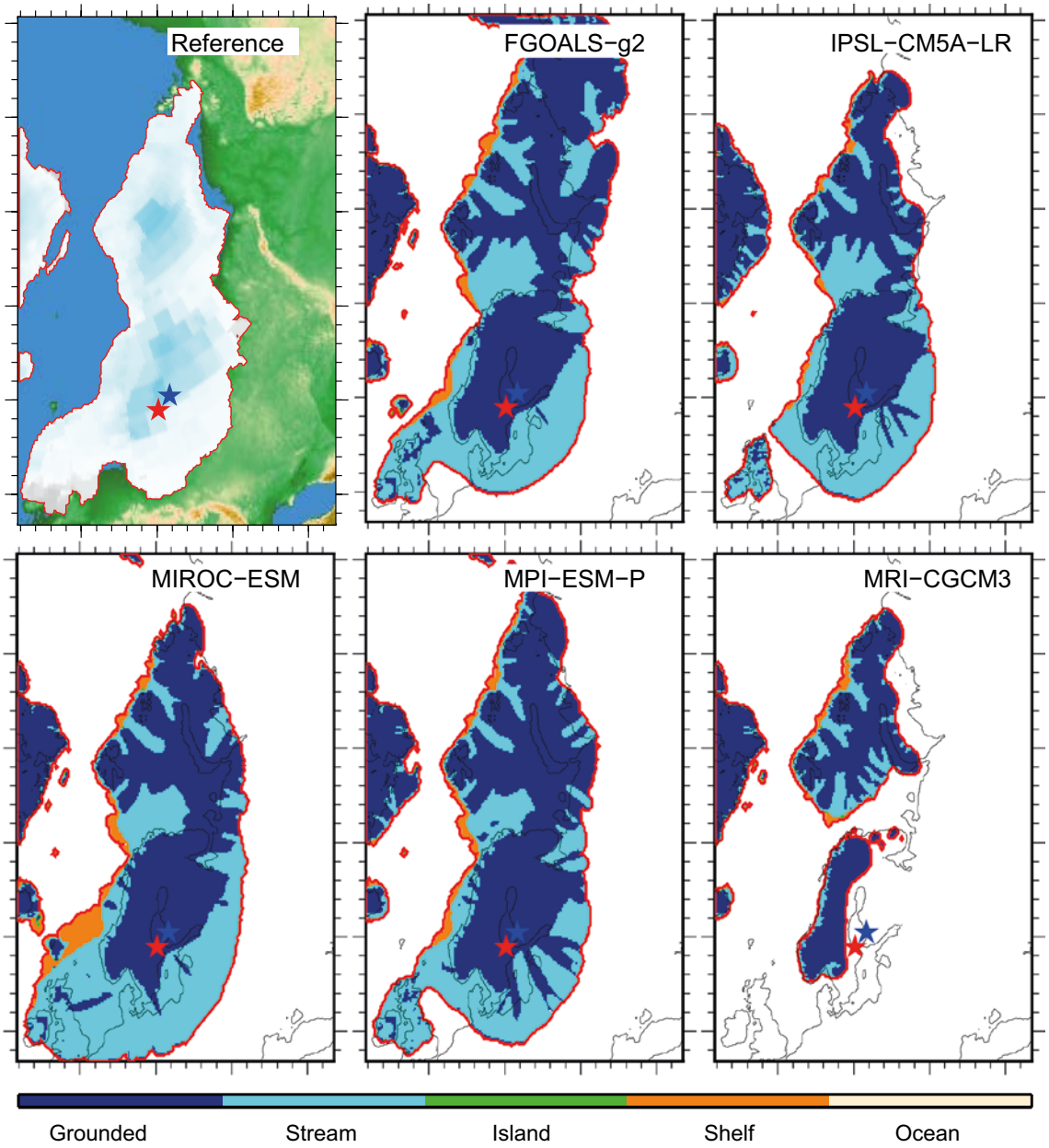

Figure 4-9. *Distribution of GRISLI ice flow types after 200 kyrs simulation under steady-state LGM climate forcing from the AOGCMs (Figure 4-6 and 4-7). The reference ice thickness is from Peltier (2004).*

However, the high climate variability during the last deglaciation reconstructed from the Greenland δ^{18}O record at North GRIP is poorly simulated by these climate models. For this reason, we use a method to interpolate the time evolution between two climate snapshots commonly used in the glaciological community, namely the index method. We use a climate index based on the Greenland δ^{18}O record at North GRIP (Andersen et al. 2004). The δ^{18}O is considered as a proxy for atmospheric temperature. The constructed index ($g(t)$) is scaled in order to have the value 1 at the LGM (21 kyrs BP) and 0 at the PI (Figure 4-10). This index is then used to modulate the climate forcing during the simulations according to:

$$\begin{cases} T(t) = g(t)\ T^{*}_{lgm,anom}(t) + T^{CESM}_{PI} \\ P(t) = g(t)\ P^{*}_{lgm,anom}(t) \times P^{CESM}_{PI} + P^{CESM}_{PI} \end{cases} \qquad \text{(Equation 4-3)}$$

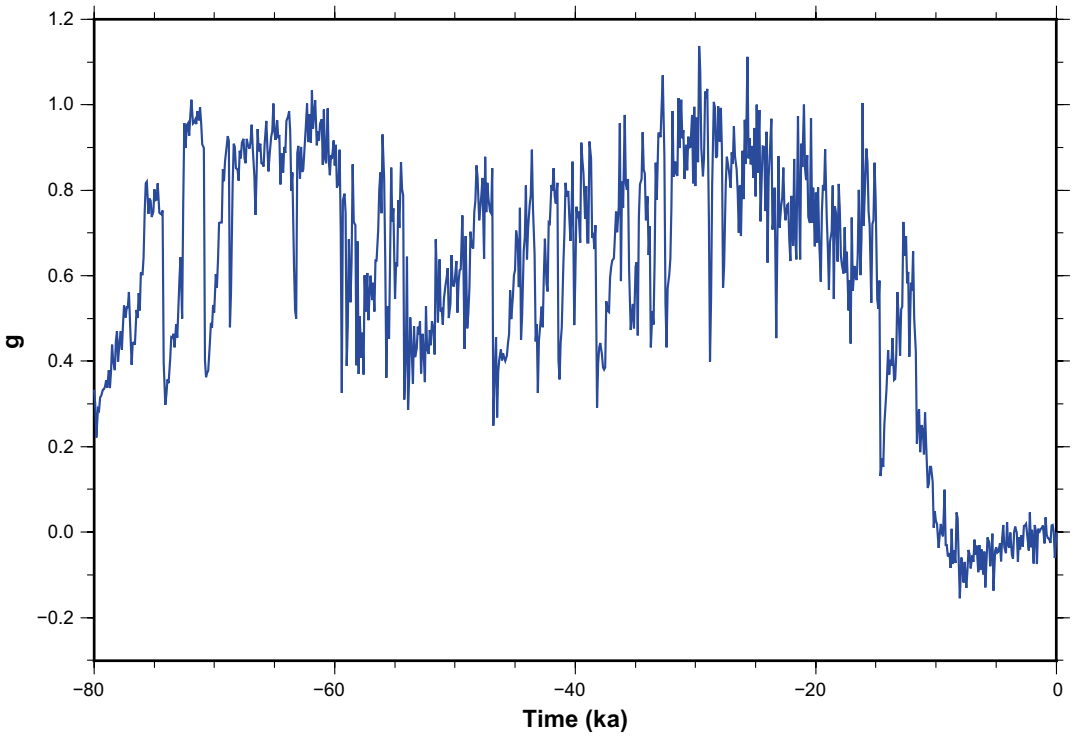

Figure 4-10. *Glacial index (g(t)) constructed from the $\delta^{18}O$ record of the North GRIP deep ice core from Greenland (Andersen et al. 2004).*

For a time period prior to, or at, the LGM, $T^*_{lgm,anom}$ and $P^*_{lgm,anom}$ are the climate anomalies presented in Section 4.2 (Equation 4-1) between the LGM and the PI simulations of each AOGCMs, and T_{PI}^{CESM} and P_{PI}^{CESM} are surface air temperature and precipitation from the CESM pre-industrial simulation (Colleoni et al. 2014b, 2016b). Otherwise, the anomalies are weighed with respect to their temporal distance from the PI:

$$\begin{cases} T^*_{lgm,anom}(t) = T_{lgm,anom} \times t/t_{lgm} \\ \\ P^*_{lgm,anom}(t) = P_{lgm,anom} \times t/t_{lgm} \end{cases} \qquad \text{(Equation 4-4)}$$

With t_{lgm} = 21 kyrs BP.

This method to force an ice sheet model has been extensively used in previous paleo-applications (e.g. Huybrechts 2002, Charbit et al. 2007, Kirchner et al. 2011, Quiquet et al. 2013, Colleoni et al. 2014a). Because it is based on paleo-observations, this method has the advantage of accounting for the high climate variability observed in paleo records, features that most AOGCMs are currently not capturing in a satisfactorily way. However, the climatic variability in Greenland is probably not representative of the variability over the entire Northern Hemisphere and in particular Eurasia.

In order to better capture the last termination, we start our simulations at 40 kyrs BP, from the equilibrated ice sheets simulated in the previous section (Section 4.4.1). Figure 4-11 presents the evolution of the Eurasian ice sheet volume for the last 40 kyrs using the AOGCMs climate forcing that led to the LGM Eurasian ice sheet topographies closest to the one of ICE-5G (Peltier 2004). The different models are relatively synchronous even if the maximum ice volume at the LGM is reached slightly later with the IPSL-CM5A-LR model. In the evolution of ice volume there is a local minimum around 35 kyrs BP due to the glacial variability presented in Figure 4-10. Also, it is important to note that the starting point of the simulations reflects the differences in LGM equilibrated ice sheets obtained in Section 4.4.1. MIROC-ESM and MPI-ESM-P start from a very similar initial Eurasian ice volume but they quickly diverge as the volume simulated with the MIROC-ESM decreases strongly and converge with the ice volume evolution simulated with the IPSL-CM5A-LR climate forcing. This illustrates the importance of the initial ice sheet geometry, not

only ice volume, i.e. the Eurasian ice sheets obtained using MIROC-ESM climate has a large flat ice topography in southwestern Europe (Figure 4-8). This part is consequently more sensitive to the climate fluctuations induced by the glacial index in our transient simulations. In contrast, the eastern part of the ice sheet is highly similar to the one obtained with the IPSL-CM5A-LR climate. Note that, because the simulations start from the LGM ice sheet topographies discussed in the previous section, and not from a realistic 40 kyrs BP ice sheet topography, the evolution of ice volume in our transient simulations between 40 kyrs and 21 kyrs is not realistic. For this reason, they are not further detailed and shown in the following.

The evolution of ice thickness for a selection of snapshots covering the last termination is presented in Figure 4-12 for the IPSL-CM5A-LR climate forcing, in Figure 4-13 for the MIROC-ESM climate forcing and in Figure 4-14 for the MPI-ESM-P climate forcing, respectively. Independently from the climate forcing, the eastern part of the ice sheet remains very stable between 22 kyrs BP and 12 kyrs BP (the retreat starts at 12 kyrs BP, Figure 4-11). The western part is more sensitive to surface melt induced by the index fluctuations and therefore reflects of the strong impact that climate forcing has on the geometry of the ice sheet.

For each of the snapshots and for each of the three climate forcings, the type of GRISLI ice flow is displayed in Figure 4-15 (IPSL-CM5A-LR), Figure 4-16 (MIROC-ESM) and Figure 4-17 (MPI-ESM-P). Here again, the evolution of the eastern part of the Eurasian ice sheet is relatively consistent amongst the climate forcings. The ice streams are well identified and remain at the same location from 22 kyrs BP to 12 kyrs BP (except in the simulations in which Fennoscandia is deglaciated before 12 kyrs BP). In the western part however, the entire continental Fennoscandia remains treated with the SIA, as in our Late Saalian experiments, with only few exceptions when the ice sheet has retreated enough (in particular with the IPSL-CM5A-LR model, Figure 4-15). As in the case of the steady-state experiments, it is difficult to observe a clear pattern emerging from the different ice sheet evolutions in this part of the ice sheet, as no permanent ice streams are observed. The only noticeable exceptions is the White Sea region, and the Baltic sea (Gulf of Finland and Gulf of Bothnia in particular), which are often treated with the SSA. This is related to the large amount of sediments in these areas, together with relatively high basal ice temperatures.

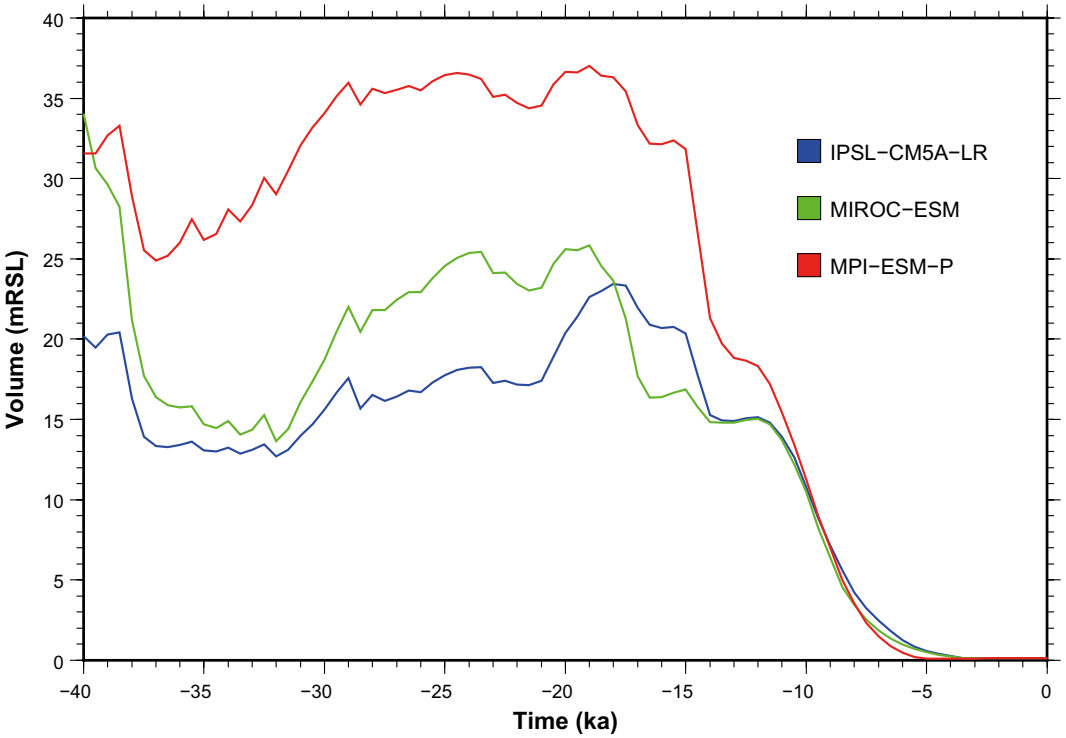

Figure 4-11. *Temporal evolution of the integrated last deglaciation Eurasian ice sheet volume for different AOGCMs from the PMIP3 database.*

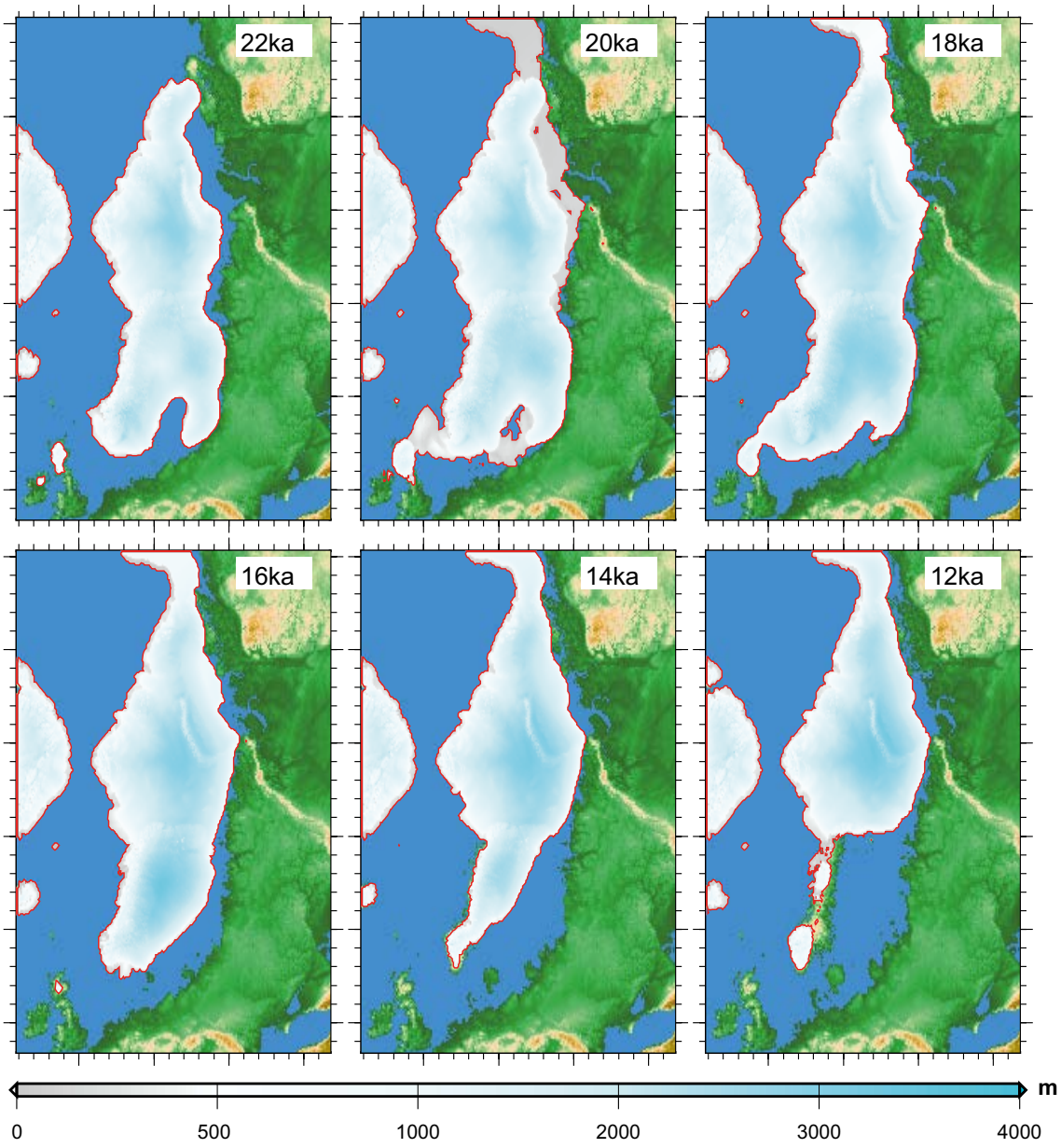

Figure 4-12. *A selection of snapshots of simulated ice sheet thickness covering the last termination using the IPSL-CM5A-LR climate forcing.*

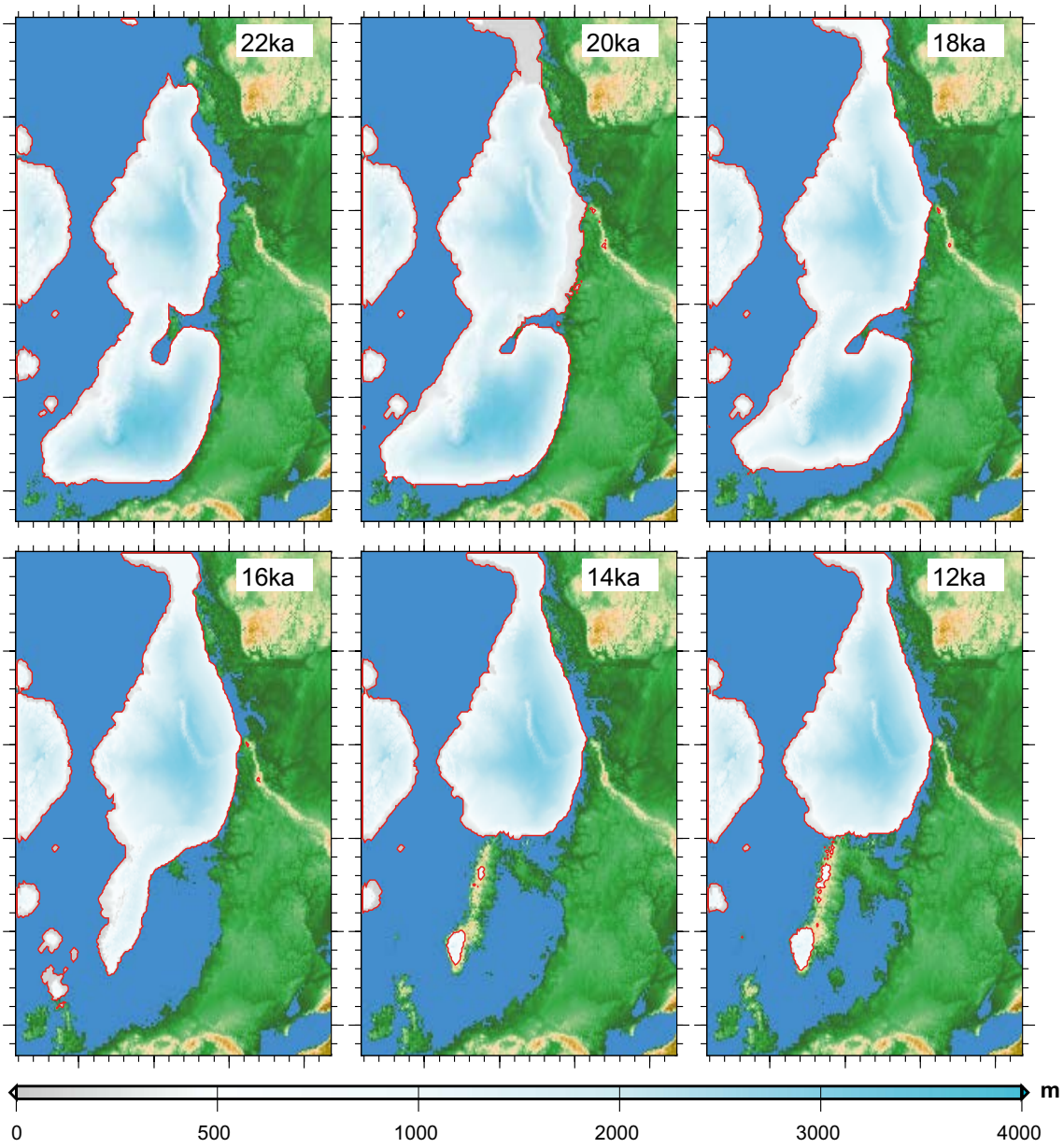

Figure 4-13. *A selection of snapshots of simulated ice sheet thickness covering the last termination using the MIROC-ESM climate forcing.*

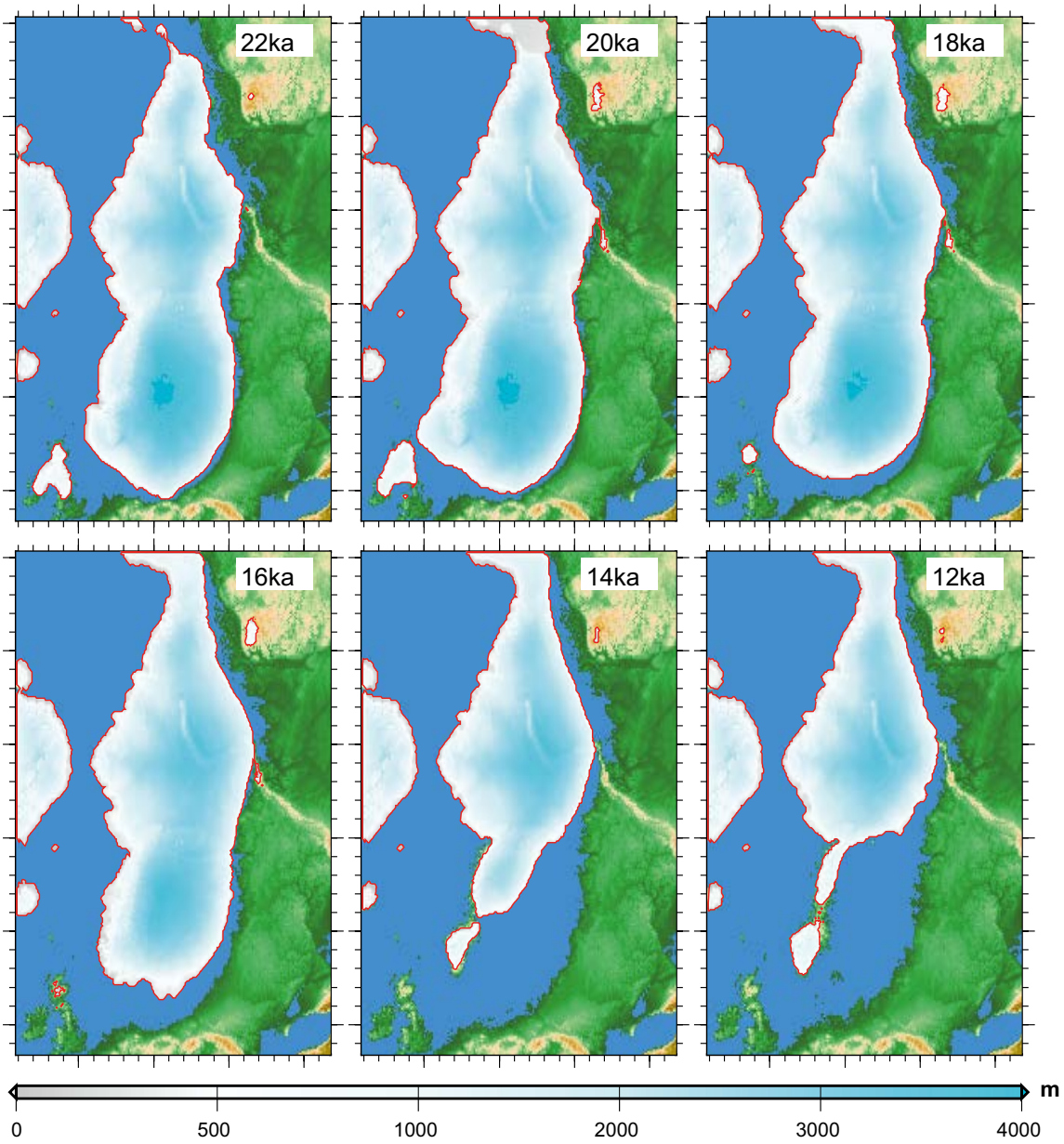

Figure 4-14. *A selection of snapshots of simulated ice sheet thickness covering the last termination using the MPI-ESM-P climate forcing.*

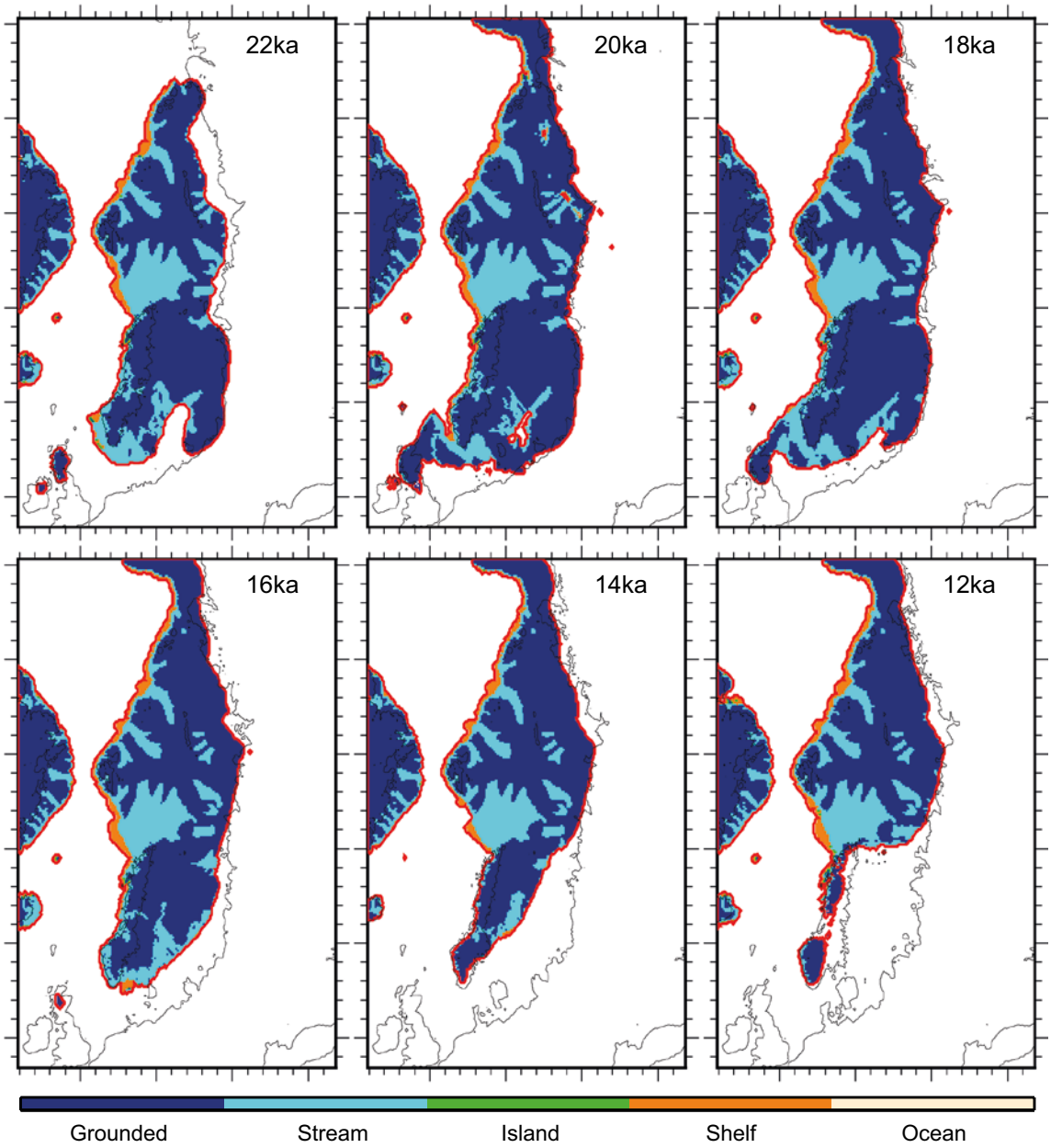

Figure 4-15. *A selection of snapshots of simulated GRISLI ice flow types covering the last termination using the IPSL-CM5A-LR climate forcing. The thick red line stands for the extent of the ice sheet.*

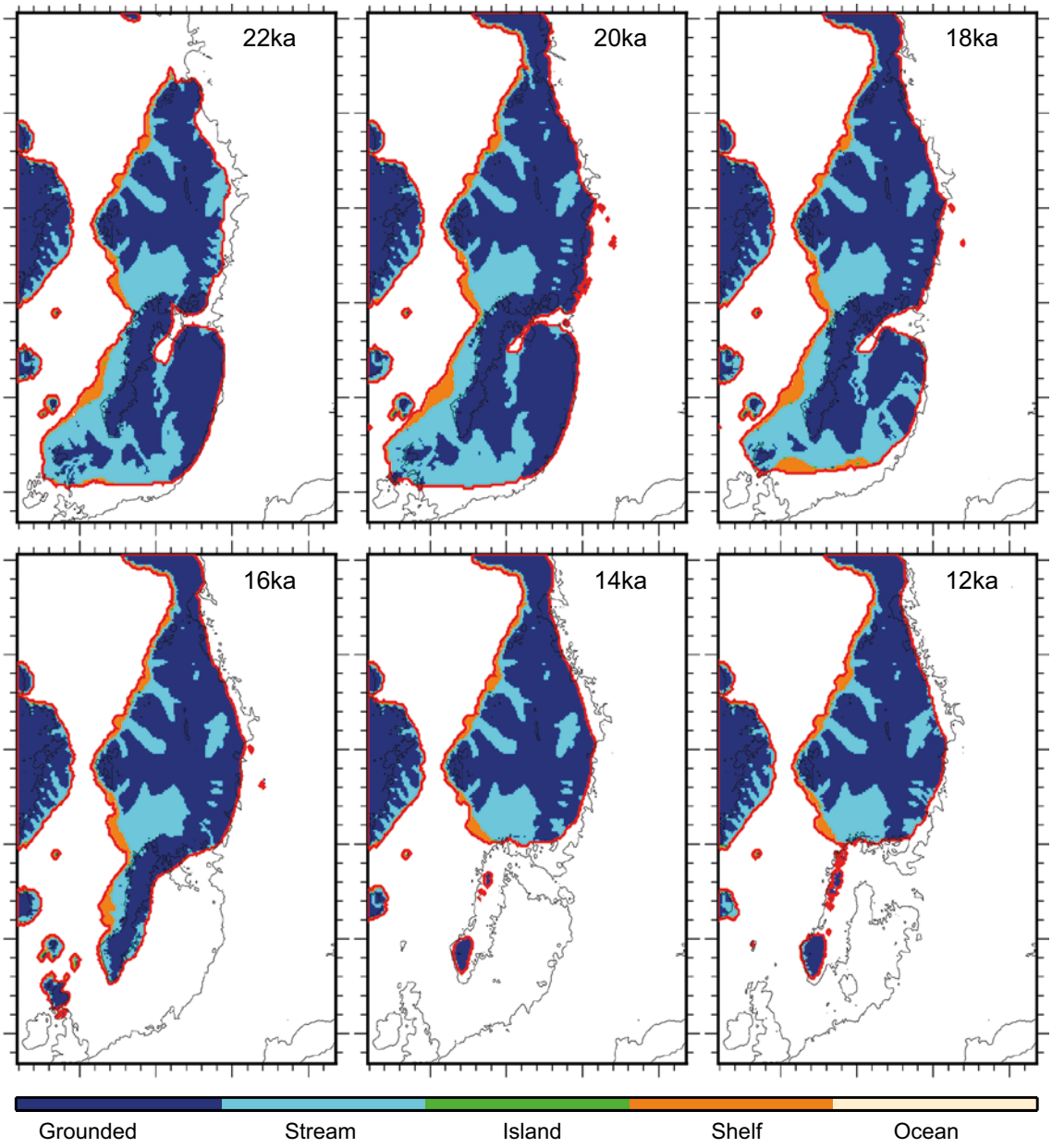

Figure 4-16. *A selection of snapshots of simulated GRISLI ice flow types covering the last termination using the MIROC-ESM climate forcing. The thick red line stands for the extent of the ice sheet.*

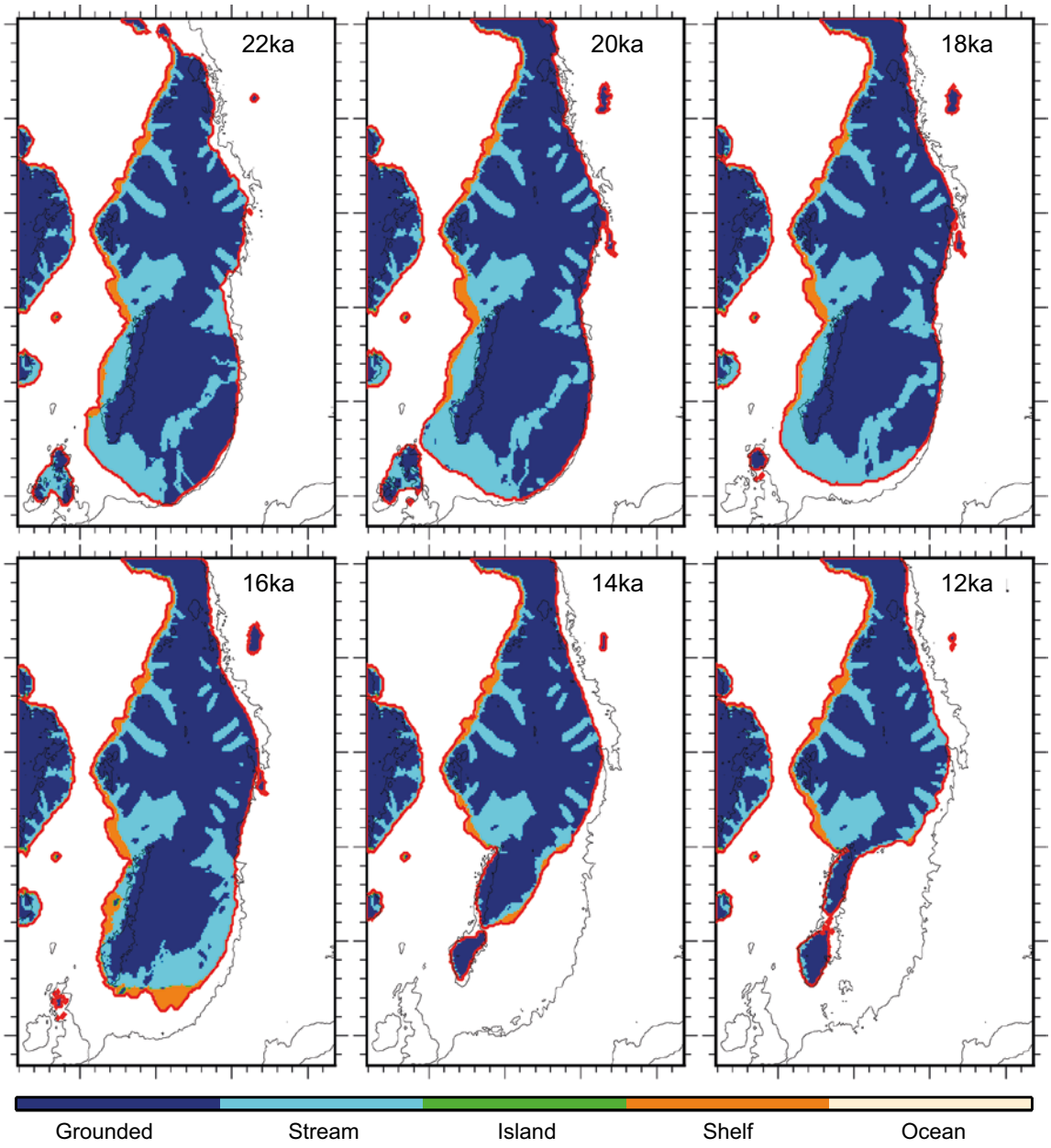

Figure 4-17. *A selection of snapshots of simulated GRISLI ice flow types covering the last termination using the MPI-ESM-P climate forcing. The thick red line stands for the extent of the ice sheet.*

4.4 Discussion and summary of section

In this section, we have used output from six different AOGCMs from the PMIP database for two different time periods, namely the pre-industrial and the LGM. With these, we carried out steady-state simulations of the LGM as well as transient simulations of the last termination. The aim was to quantify the ability of GRISLI to correctly simulate ice streams. As previously mentioned, the ice stream activation is triggered by surface and bedrock topography, sediment thickness and basal hydrology. However, climate forcing has an indirect effect since it impacts the ice sheet surface topography as well as the basal conditions and therefore also the ice sheet thickness and extent. In fact, we observed a very large sensitivity of ice stream activation to climate forcing. For this reason, the use of the Last Glacial Maximum does not help in giving more confidence in the ice stream representation in GRISLI and hence does not provide clues to constrain the use of the SSA in our Late Saalian ice sheet simulations. The LGM ice sheet topographies resulting from the different LGM climate forcings are so different that a proper tuning of the ice sheet model parameters is necessary to simulate a realistic ice sheet extent. As a consequence, a more thorough analysis for the LGM would be needed in order to increase the realism of the reconstructions. Such an analysis should include a parametric uncertainty analysis (involving basal drag) and climate sensitivity. Only then, the results could be compared with geomorphological evidences in order to include or exclude simulations and therefore constrain the range of the ice sheet model parameters values. In addition, the index method that was used here is oversimplified and might not be well suited for deglaciation experiments. This method has the advantage to preserve the temporal variability of climate evolution but not its spatial variability due to the changes in ice sheet elevation. In fact, the spatial distribution of precipitation and surface air temperature related to topographic changes is much more complex than a simple local lapse rate. The use of a coupled climate-ice sheet model would lead to a different spatial and temporal ice sheet evolution and might be more suited to simulate proper ice sheet inception and deglaciation processes.

Nevertheless, these exploratory results seem to suggest that continental Fennoscandia remains mostly cold-based (with no ice streams) in our simulation during the deglaciation, which is mostly in agreement with the reconstruction of Kleman and Glasser (2007). In addition, the broad zone considered as ice stream by GRISLI in the south-west could be similar to the low-gradient glaciers identified by Kaplan et al. (2001) for the Laurentide ice sheet and suggested by Kleman and Glasser (2007) for the southern part of the Eurasian ice sheet. The low-gradient glaciers are supposed to have similar characteristics as present-day West Antarctic ice sheet outlet glaciers.

In any case, if the ice sheet is big enough in the western part, independently from the climate forcing, GRISLI will treat the entire area, except the continental Fennoscandia with ice stream flow. This is consistent with what we simulated for the Late Saalian.

5 Sensitivity of the Late Saalian ice sheet to climate forcing

Several studies have reported a strong sensitivity of ice sheet reconstructions and projections to climate forcing (e.g. Charbit et al. 2007, Graversen et al. 2011, Quiquet et al. 2012, Fürst et al. 2015). Because the climate forcing that we used for the Late Saalian ice sheet simulations are the only one carried out with a coupled AOGCM and available in the literature, we are not able to directly assess the sensitivity of our Eurasian ice sheet numerical reconstructions to Late Saalian climate forcing.

Instead, in this section, we will use the outputs from the PMIP models presented in Section 4 in order to quantify the sensitivity of our Late Saalian reconstructions to climate forcing. Using Equation 4.1, we compute the two climate anomalies between B140_Topo1 and B140_Topo2 Late Saalian simulations and the pre-industrial simulation AD1850 (Figure 1-4) computed using the CESM 1.0.5. These two anomalies are then added on top of the pre-industrial climates simulated by the six AOGCMs presented in Section 4.2.:

$$\begin{cases} T_{140k}^{GCM} = T_{PI}^{GCM} + T_{140k,anom}^{CESM} \\ P_{140k}^{GCM} = P_{PI}^{GCM} \times P_{140k,anom}^{CESM} \end{cases} \quad \text{(Equation 5-1)}$$

Based on our two Late Saalian climate anomalies and our PMIP AOGCMs selection, we generate a set of two new forcing fields for our Late Saalian simulations, six for climate B140_Topo1 and six for climate B140_Topo2 (Table 5-1). Subsequently, twelve steady-state ice sheet simulations, forced with those climatologies are run for 200 kyrs, branched on the reference simulations REF_Topo1 and REF_Topo2.

Table 5-1. Simulation IDs for the different experiments testing the sensitivity of the Late Saalian ice sheet to climate forcing.

Simulation ID	Process tested
CLI1	140k climate anomaly on top of CNRM-CM5
CLI2	140k climate anomaly on top of FGOALS-g2
CLI3	140k climate anomaly on top of IPSL-CM5A-LR
CLI4	140k climate anomaly on top of MIROC-ESM
CLI5	140k climate anomaly on top of MPI-ESM-P
CLI6	140k climate anomaly on top of MRI-CGCM3

5.1 Late Saalian surface mass balance using the PMIP3 multi-model simulations

The change in Surface Mass Balance (SMB) over the Eurasian ice sheet compared to the reference simulation for the six new climate forcings using climate B140_Topo1 is depicted in Figure 5-1. Because we compute differences between the SMB based on Equation 5-1 and the SMB from the reference simulations REF_Topo1 and REF_Topo2, Figure 5-1 is mostly representative of the discrepancy between the PI climate computed with CESM 1.0.5 and the PMIP3 AOGCMs. For most of the climate forcing, there is an increase in surface mass balance at the ice sheet margins. This difference is explained by the fact that the PMIP3 AOGCMs PI simulations are colder than those simulated by CESM 1.0.5 in the Eurasian region, as shown in Figure 4-2. Therefore, the melting occurring along the margins in the reference simulations is reduced, which leads to a more positive SMB when using the other AOGCMs. The results obtained using the B140_Topo2 climate forcing are almost identical to the ones when using B140_Topo1. Here again, this is because we compute the differences relative to the reference simulation REF_Topo2, so the results mostly represent the impact of using a different PI base climate (from the PMIP3 database). In the following, we analyse the impact of these differences in SMB on the simulated Late Saalian ice thickness.

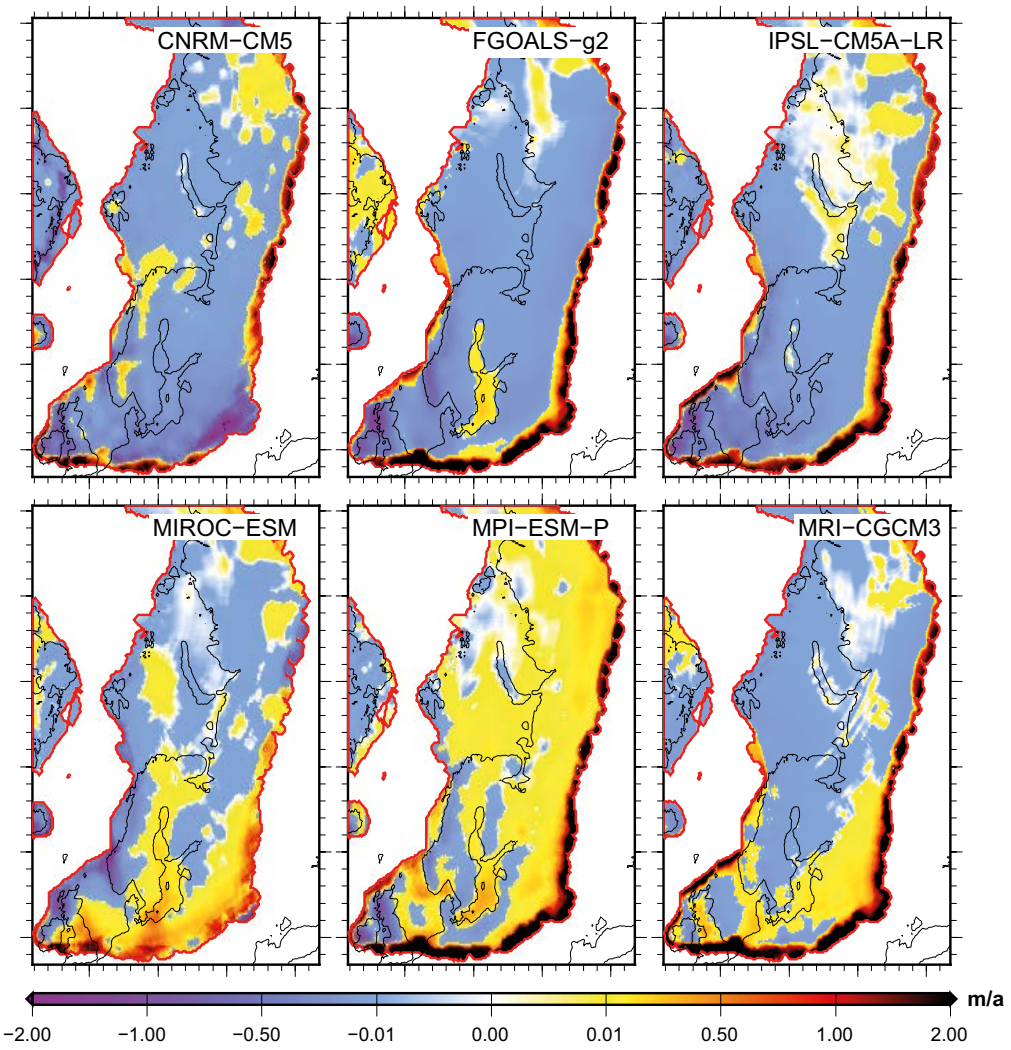

Figure 5-1. *Differences in surface mass balance (m/yr) between the reference simulation REF_Topo1 and the simulations using the climates generated from PMIP3 AOGCMs pre-industrial simulations and B140_Topo1.*

5.2 Impact on the simulated Late Saalian ice sheet topography

The thickness differences between the reference simulation and the six new simulations CLIM1 to CLI6 (Table 5-1) is shown in Figure 5-2a. Because of the more positive surface mass balance at the margins induced by the PMIP3 climates, the Eurasian ice sheet is expanding slightly more southward under most of the new climatic forcings compared with the REF_Topo1. As a result, the thickness is increased in the southern part of the ice sheet by 500 to 1000 m when using the Late Saalian climate forcing based on the FGOALS-g2, IPSL-CM5A-LR, MPI-ESM-P and MRI-CGCM3 models. The use of the CNRM-CM5 climate, the warmest AOGCM from the whole PMIP3 project (Figure 4-5), leads to a decrease in ice thickness in the western part of the ice sheet, but an increase in the south-eastern part. All six simulated ice sheet topographies are close to the initial one of Peyaud (2006) (Figure 5-2b).The simulation using the MIROC-ESM climate (CLI4) is the closest to the reference simulation with only minimal changes of about 150 metres compared with REF_Topo1.

The total Eurasian ice sheet volume and the ice thickness at the two repository sites are reported in Table 5-2. Compared to REF_Topo1 (REF_Topo2), the lowest ice volume, 52.21 m SLE (49.69 m SLE), is obtained by CLI4 (MIROC-ESM climate) with a decrease of 2.0 % (resp. 3.5 %).

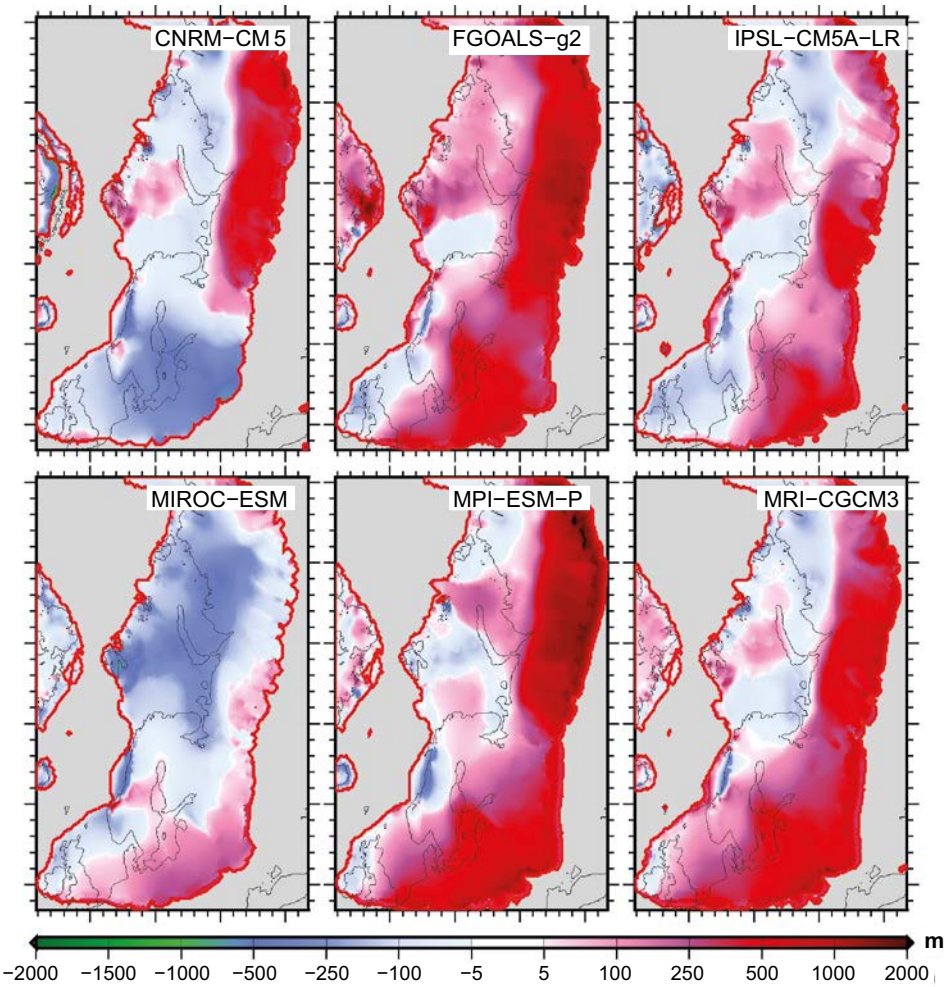

Figure 5-2a. *Differences in ice thickness (m) between the simulations CLI1 to CLI6 (Table 5-1) and REF_Topo1 after 200 kyrs of simulation.*

However, the lowest ice thickness (below 3000 m) is obtained in CLI1 (CNRM-CM5 climate) with a reduction of around 8 to 9 % at both repository sites. The maximum volume, 65.79 m SLE (63.88 m SLE), is obtained in CLI2 (FGOALS-g2) with a large increase of 23.5 % (resp. 24.0 %) compared to the reference simulation REF_Topo1 (resp. REF_Topo2). The FGOALS-g2-based Late Saalian climate forcing also corresponds to the maximum ice thickness over both Forsmark and Olkiluoto, more than 3700 m in the case of B140_Topo1 and more than 3400 m in the case of B140_Topo2. This corresponds to ~17 to 19 % increase in ice thickness, or ~550 m, compared to the reference simulations.

5.3 Discussion and summary of section

In this section, we have used the outputs from six different AOGCMs pre-industrial simulations from the PMIP3 database to generate new Late Saalian climate forcing fields for our Late Saalian simulations. The results show that the Late Saalian ice sheet shows a large sensitivity to climate forcing as the volume changes from −3.5 % to +24 % relatively to the reference simulations, depending on the AOGCM used. However, with our methodology we can only quantify the sensitivity to uncertainties related to the simulated pre-industrial climates. Those uncertainties are supposed to be lower than for other (older) time periods because the changes in external forcings (orbital parameters and GHG concentrations) relative to present-day are lower, which limits model divergence. Unfortunately, because no other AOGCM climate simulations are available for the Late Saalian at present, this is the only way to assess the sensitivity of the Eurasian ice sheet to climate forcing for this glaciation. Given the results obtained in this section, and in order to reduce the uncertainty on the upper and lower bound of ice thickness over both sites, the Late Saalian climate could be simulated by additional climate models to the one used in this study.

Table 5-2. Simulated total Late Saalian Eurasian ice sheet volume (m SLE), ice thickness (m) and bedrock depression (m) at the end of the simulations for testing the sensitivity of the Late Saalian ice sheet to climate forcing (Table 5-1). For ice thickness and bedrock depression Forsmark is identified by *F*, Olkiluoto by *O*. Changes are computed relative to the reference simulations REF_Topo1 and REF_Topo2 from which they are branched.

	Volume				Ice thickness					Bedrock depression				
	B140_Topo1		B140_Topo2		Site	B140_Topo1		B140_Topo2		Site	B140_Topo1		B140_Topo2	
ID	m SLE	%	m SLE	%		m	%	m	%		m	%	m	%
CLI1	55.53	4.3	53.23	3.3	*F*	2834.6	*−8.6*	2619.1	*−10.1*	*F*	−664.4	*−9.1*	−599.4	*−12.5*
					O	2983.5	*−7.6*	2799.8	*−8.6*	*O*	−701.8	*−8.1*	−644.0	*−10.6*
CLI2	65.79	23.5	63.88	24.0	*F*	3701.8	*19.4*	3417.0	*17.2*	*F*	−865.6	*18.4*	−803.4	*17.3*
					O	3791.1	*17.4*	3538.6	*15.5*	*O*	−897.9	*17.6*	−845.7	*17.4*
CLI3	59.44	11.58	55.80	8.3	*F*	3322.8	*7.1*	3069.4	*5.3*	*F*	−778.8	*6.5*	−720.6	*5.2*
					O	3450.4	*6.8*	3229.6	*5.5*	*O*	−817.4	*7.1*	−765.0	*6.2*
CLI4	52.21	−2.0	49.69	−3.5	*F*	3217.8	*3.8*	2975.9	*2.1*	*F*	−758.4	*3.7*	−696.6	*1.7*
					O	3318.5	*2.8*	3110.4	*1.6*	*O*	−784.6	*2.8*	−732.2	*1.6*
CLI5	62.21	16.8	60.87	18.2	*F*	3584.7	*15.6*	3381.4	*16.0*	*F*	−838.3	*14.6*	−799.1	*16.7*
					O	3639.6	*12.7*	3492.4	*14.0*	*O*	−862.5	*13.0*	−829.2	*15.1*
CLI6	61.85	16.1	60.02	16.5	*F*	3589.4	*15.7*	3322.1	*14.0*	*F*	−847.5	*15.9*	−787.9	*15.1*
					O	3686.2	*14.1*	3464.8	*13.1*	*O*	−876.2	*14.8*	−824.8	*14.5*

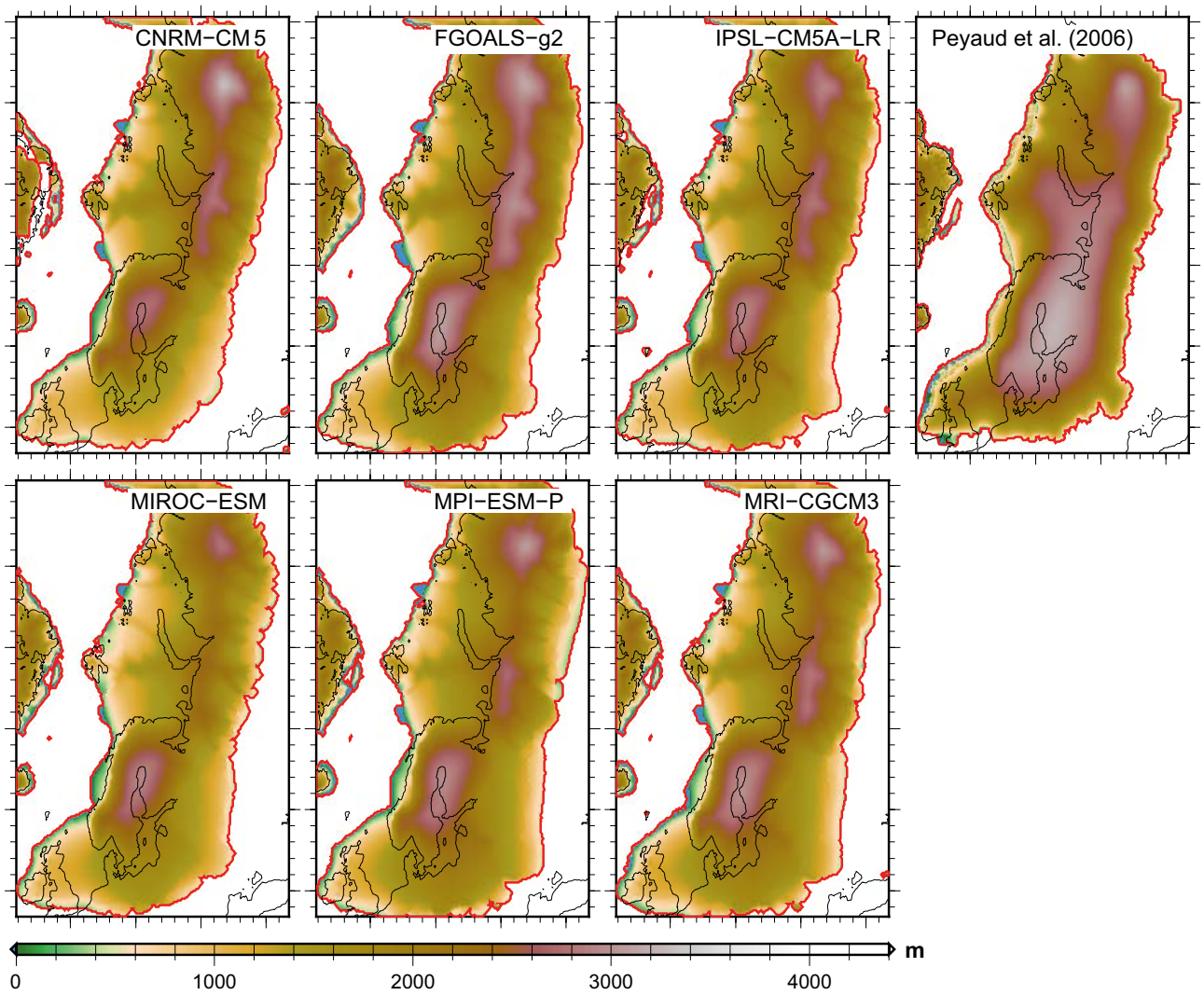

Figure 5-2b. *Surface elevation (m) for the simulations CLI1 to CLI6 (Table 5-1) after 200 kyrs of simulation. The Eurasian ice sheet elevation from Peyaud (2006) is displayed for comparison.*

6 Latin Hypercube Sampling of ice sheet model parameters

In the previous sections, we have explored the sensitivity of the Late Saalian Eurasian ice sheet to model formulation (surface mass balance and ice dynamics) as well as to climate forcing. Also, during the first phase of the study, some important ice sheet model parameters were systematically tested within a specific range in order to assess the parametric uncertainties. However, during the first phase of the study, in most of the sensitivity experiments, each parameter were only tested individually (univariate), not accounting for potential interactions between parameters. Therefore, in the following, we further explore the parametric uncertainties using an ensemble of model simulations and combinations of parameter changes.

6.1 Methodology and parameters tested

6.1.1 Latin Hypercube Sampling methodology

Due to the large number of parameters in the ice sheet model and their wide range of values, a systematic exploration of all possible combinations is computationally unrealistic. In geosciences, Monte-Carlo exploration is often used for various applications (e.g. Bamber and Aspinall 2013, Dahl-Jensen et al. 2003, Fischer et al. 2008, Shapiro and Ritzwoller 2004). In a Monte-Carlo sampling, each parameter range is randomly explored in order to generate the different parameter combinations. If the computational cost allows a large number of simulations (large number of experiments), then a sufficient exploration of the range of the different parameters may be possible with the Monte Carlo method. However, if, as in our case, the computational cost does not allow for a large number of simulations, the tails of the parameter distributions may not be sufficiently explored with the Monte Carlo method. The Latin Hypercube Sampling (LHS) is a refinement of the standard Monte-Carlo method, for which the whole range is systematically explored. For this purpose, we first define the k variables selected for the sensitivity analysis and their individual ranges. Each variable range is then divided equally into n bins, where n is the total number of experiments for the sensitivity analysis. A set of n input parameter samples is then defined such that each of the n bins for each of the k variables is used exactly once. As a result, compared to the standard Monte-Carlo exploration, the LHS has better space-filling quality.

Once defined, the LHS can eventually be reshaped if needed. For example, both the number of experiments (n) and the number of variables (k) can be increased, whilst keeping the properties of the initial definition.

For the present study, in order to explore the parametric uncertainties within GRISLI, we constructed a LHS with $k=10$ different parameters and $n=100$ experiments for the two different climate forcing at 140 kyrs BP (B140_Topo1 and B140_Topo2).

6.1.2 Model formulation used for the ensemble

The model formulation used for the LHS experiments mostly corresponds to the one used in the reference simulation. However, there are a few differences:

- We account for a physically based refreezing scheme (Janssens and Huybrechts 2000), see Section 2.2.4, instead of the empiric model of Reeh (1989) used in the reference simulation.
- We allow for a rain fraction from the total precipitation, using the temperature threshold presented in Section 2.1.3. This is motivated by results shown in Chapter 2 suggesting that the rain fraction could have an important impact when using a physically based refreezing scheme. The reference simulation, on the other hand, used the total precipitation as accumulation.
- The impact of ice anisotropy on the deformation has been slightly modified. Anisotropy tends to facilitate the ice deformation due to vertical shear (i.e. in the SIA part of the ice sheet), but reduces the deformation due to longitudinal stress (in SSA regions) (e.g. Gillet-Chaulet et al. 2006, Seddik et al. 2008). Studies suggest a ratio of enhancement factors (ESIA:ESSA) around 5:1 to

10:1 (Ma et al. 2010). In the reference simulation, this ratio was set to 33:1. In all the LHS experiments, we use a ratio of enhancement factors more in line with the literature, using 8:1 (e.g. Martin et al. 2011, Pollard and DeConto 2012). This new ratio, more in agreement with literature induces slightly slower velocities in the SIA part, but this does not change the behaviour of the model and does not impact on the conclusions of the study.

All the different members of the Latin hypercube ensemble are run for 100 kyrs, starting from the spun-up ice sheet topographies simulated by the reference simulations.

6.1.3 Tested ice sheet model parameters

Given the model formulation and the various parameters used in GRISLI, we selected 10 representative parameters for the sensitivity experiments. We chose to use a uniform distribution of the LHS parameters following Stone et al. (2010) and Applegate et al. (2012) and because the uncertainties regarding the selected parameters are large. The LHS simulations ensemble can be repeated with different statistical distributions to strengthen the conclusions drawn with a uniform statistical distribution of the ice sheet parameters values. For most of the parameters, the selected range reflects geographic variability observed for present-day ice sheet under present-day climate. There is no strong indication that these parameters have remained constant over several glaciations. Table 6-1 lists the different parameters and their associated tested range. The number of tested parameters is large compared to Stone et al. (2010) and Applegate et al. (2012) who tested five parameters.

1–2: Ablation coefficient for snow and ice

In the following, the ablation model is the one from Reeh (1989) and the same as in the reference simulation, Because of their importance for the SMB (see also Chapter 2), we include both the snow (C_{snow}) and ice (C_{ice}) ablation coefficients in the parameters of the LHS. The melt coefficients are often deduced from observation of melt rates for present-day glaciers and ice sheets combined with energy-balance modelling. The range for C_{ice} is very wide, ranging from about 5 to 20 mm w.e. d^{-1} $°C^{-1}$, whereas the range for C_{snow} is somewhat narrower, ranging from 2.8 to 5.5 mm w.e. d^{-1} $°C^{-1}$ (Braithwaite and Zhang 2000). Tarasov and Peltier (2002) and Greve (2005) used a temperature dependency for ablation coefficients which assumes a C_{ice} ranging from 7 to 15 mm w.e. d^{-1} $°C^{-1}$ and a C_{snow} from 2.3 and 3.7 mm w.e. d^{-1} $°C^{-1}$. For their LHS design, Stone et al. (2010) used the range of 8 to 20 mm w.e. d^{-1} $°C^{-1}$ for C_{ice}, and 3 to 5 mm w.e. d^{-1} $°C^{-1}$ for C_{snow} . Similarly, Applegate et al. (2012) explored a slightly wider range: 5 to 20 mm w.e. d^{-1} $°C^{-1}$ for C_{ice}, and 1 to 5 mm w.e. d^{-1} $°C^{-1}$ for C_{snow}. We have chosen to use a very similar range to the ones explored in the previous studies with a C_{ice} ranging from 6 to 20 mm w.e. d^{-1} $°C^{-1}$ and a C_{snow} ranging from 1 to 5 mm w.e. d^{-1} $°C^{-1}$.

3: Topographic lapse rate

The topographic lapse rate is used to take into account temperature changes related to ice sheet surface elevation changes. A single homogeneous value is used to warm (resp. cool) the near-surface air temperature as the ice elevation is decreasing (resp. increasing). It is important to note that this parameter is not an atmospheric lapse rate as observed from the climatological vertical air temperature profile over the ice sheet. Instead, this lapse rate represents an approximation of how much the near-surface air temperature changes from a given change in topography. Therefore, this parameter is not directly observable and it is only estimated by means of models. The topographic lapse rate should account for the complex reorganisation of local atmospheric circulation due to a local change in elevation. This is why this parameter is relatively poorly constrained in ice sheet models.

Most previous large-scale ice sheet modelling studies have used topographic lapse rates close to the moist or dry adiabatic atmospheric lapse rate, from about 6 to 8 °C km^{-1} (e.g. Marshall et al. 2000, Ritz et al. 2001, Huybrechts 2002; Tarasov and Peltier 2002, Zweck and Huybrechts 2005). Krinner and Genthon (1999) performed present-day atmospheric simulations modifying the ice elevation of Antarctica and Greenland. They found a relatively weak lapse rate of around 5 °C km^{-1} at the margins of the ice sheets, but much greater values further inland (about 10 °C km^{-1}). In a similar model framework, Abe-Ouchi et al. (2007) computed topographic lapse rates from an AOGCM at the LGM, using ice sheet topographies of LGM, 12 kyrs BP and present-day. They found weaker values than the one used by the ice sheet modelling community, with a lapse rate of around 4.1 °C km^{-1} for

the Fennoscandian ice sheet. Also, even if not directly comparable, Marshall et al. (2007) reported observations of a near-surface atmospheric lapse rate which match the values by Abe-Ouchi et al. (2007), 4.1 °C km^{-1}.

For the design of the LHS we decided to explore the range 4 to 8.2 °C km^{-1} since it covers the range of values found in literature. This is also the range explored in the LHS of Stone et al. (2010).

4: Daily near-surface air temperature standard deviation

The Reeh (1989) PDD model is forced by monthly mean near-surface air temperature. To account for the daily variability, we use a single parameter, the standard deviation (σ). As already mentioned in Chapter 2, the standard deviation is highly variable in space and time and considering a constant and homogeneous value for this parameter is a crude approximation. In Chapter 2, we highlighted the importance of this parameter for the simulated SMB when using parametrisation of Fausto et al. (2009).

For the LHS, we use a constant and homogeneous value for the standard deviation but we allow this parameter to take any value between the lower (1.57 °C) and upper (6.56 °C) bound from the parametrisation of Fausto et al. (2009). This range encompasses what has been used previously in the literature (about 5 °C).

5: Solid to liquid temperature threshold

Contrary to the reference simulation, for the LHS we use a partitioning model to distinguish the rain fraction from the total precipitation. This choice is motivated by the importance of rain contribution to accumulation when using a physically based refreezing scheme, as discussed in Chapter 2. Because it gives similar results compared to the model from Marsiat (1994), we select the most simple partitioning, i.e. the model based on a single threshold, in order to make the sensitivity analysis easier.

Whilst simple, a temperature threshold is nonetheless not far from what is used in sophisticated atmospheric models. For example, in the regional climate model RACMO2.1, all precipitation formed in a mixed phase cloud is solid if the temperature is below −1 °C (van Meijgaard et al. 2008). In order to account for the uncertainties related to this process, we have explored the range −2 to 2 °C for the temperature threshold.

6: Precipitation ratio

As in the reference simulation, in GRISLI, the total precipitation is allowed to change due to temperature change. A warming (resp. cooling) corresponds to an increase (resp. decrease) in precipitation. The ratio of precipitation change is exponentially related to the change in temperature, using a single parameter γ:

$$P/P_0 = exp\left(\gamma\left(T - T_0\right)\right) \qquad \text{(Equation 6-1)}$$

This exponential relationship approximates the saturation pressure of water vapour (Charbit et al. 2002) and is commonly used for reconstructions of past accumulation from ice core layer counting (e.g. Johnsen et al. 1989; Dahl-Jensen et al. 1993).

The value of γ is not well constrained as precipitation rate is much more complex than this simple formulation. In ice sheet modelling studies, this parameter has often been set in the range 0.03 °C^{-1} to 0.078 °C^{-1} (e.g. Charbit et al. 2002). However, in a climate modelling study looking at sea ice changes during glacial climates, Li et al. (2010) found that γ is highly variable in space and could be much higher (around 0.11 °C^{-1}). Using synthetic Greenland ice cores simulated by GRISLI, Quiquet et al. (2013) found that the use of 0.11 °C^{-1} was needed to reproduce observed ice cores. The need for higher values than the one of the model of Johnsen et al. (1989) was also suggested by Guillevic et al. (2013) in an isotopic study of air and water stable isotope measurements from the Greenland deep ice cores.

Given these uncertainties described above, the range 0.03 to 0.1 °C^{-1} has been included in the LHS.

7: Thermo-active layer thickness

Because we decided to use the physically based refreezing scheme of Janssens and Huybrechts (2000) instead of the simple parametrisation, we need to account for its uncertainties. There is no large ice sheet modelling that explicitly tested the sensitivity of refreezing using a physically based model. We decided to explore this sensitivity modifying the thickness of the thermo-active layer (*d* in Equation 2-5). This parameter is somehow arbitrarily set to 1m, but should be representative of the thickness of fresh snow (annual accumulation) (Pfeffer et al. 1991). For this reason, for the LHS, we select the range 0.4 to 2 m, representing typical values of annual accumulation at ice sheet margins.

8: Flow enhancement factor

As describe earlier in this section, anisotropy is not explicitly taken into account in ice sheet models. Instead, a factor is applied to increase deformations due to vertical shear stress in the SIA regions, and another factor is applied to reduce the longitudinal deformations in the SSA regions. Most of the time, the SSA factor is defined through a constant ratio relative to the SIA enhancement factor (5:1 to 10:1). In the following, we consider this ratio as fixed to 8:1.

In large-scale ice sheet modelling studies, the SIA enhancement factor has been set to values ranging from 1 to 5 (e.g. Ritz et al. 1996, Greve 1997, Huybrechts 2002). The SIA enhancement factor is not a quantity measurable in laboratory experiments. However, anisotropic full-Stokes models which explicitly account for the grain orientation (fabric) exist and have been applied to present-day ice sheet (e.g. Seddik et al. 2011). Ma et al. (2010) used this kind of model in order to provide a bound for enhancement factors of simpler models. They suggest a value of 5.6, which is slightly higher than what is typically used by the ice sheet modelling community.

In the LHS design, we explore the full range of values used in the literature, ranging from 1 to 5.6.

9: Geothermal heat flux

Geothermal heat flux may have important implications for basal temperatures and thus basal velocities. Given that we have both the reconstructions of Shapiro and Ritzwoller (2004) and Näslund et al. (2005), we can directly quantify the uncertainties over the Eurasian region. These uncertainties are generally around 20 %. For this reason, in the LHS we apply a constant geothermal heat flux modification γ_{GHF} to the reconstruction of Näslund et al. (2005), with γ_{GHF} ranging from 0.8 to 1.2.

10: Dragging coefficient

The basal drag is a resistive force that acts at the base of the ice sheet in regions treated with the SSA. The importance of this parameter has already been shown during the first phase of the study (Colleoni et al. 2014b, 2016b). In particular, the lower and upper bounds of the simulated ice sheet thickness over the repository sites were given when changing the parameter linked to this feature.

The expression of the basal drag in GRISLI is:

$$\tau_b = -\beta u_b \qquad \text{(Equation 6-2)}$$

Where β is a positive scalar and u_b is the basal velocity. In the version of GRISLI used in the present study, β is calculated from the effective water pressure (N_{eff}):

$$\beta = C_f N_{eff} \qquad \text{(Equation 6-3)}$$

The parameter C_f has no dimension and corresponds to the parameter tested in the sensitivity experiments during the first phase of the study (Colleoni et al. 2014b, 2016b). This parameter has been included in the Latin hypercube experiments.

The C_f parameter value was set to 2×10^{-5} in REF_Topo1 and REF_Topo2. In the first phase of the study, the lower bound of ice thickness was obtained with the value 1×10^{-5}, whereas the upper bound was obtained with the value 3×10^{-5} (Colleoni et al. 2014b, 2016b).

In early works with GRISLI, the value of C_f was set to 9×10^{-5} in order to match present day observed Antarctic ice velocities (Dumas 2002). However, Peyaud et al. (2007) used a lower value

of 1×10^{-5} to simulate the Eurasian ice sheet. On the other hand, in order to simulate the Northern Hemisphere ice sheets and investigate the role of Heinrich events, Alvarez-Solas et al. (2011) used considerably higher values ranging from 10×10^{-5} to 100×10^{-5}.

Based on the above values, the range chosen for the LHS was set to 1 to 10×10^{-5}.

Table 6-1. Parameters included in the Latin Hypercube ensemble. The range of the different parameters is associated with the references listed.

Parameters		Units	Min.	Max.	References
Ice ablation coefficient	C_{ice}	mm °C^{-1} d^{-1}	6	20	Applegate et al. (2012), Braithwaite and Zhang (2000), Stone et al. (2010)
Snow ablation coefficient	C_{snow}	mm °C^{-1} d^{-1}	1	5	
Topographic lapse rate	λ	°C km^{-1}	4	8.2	Abe-Ouchi et al. (2007), Marshall et al. (2007)
Daily temperature variability	σ	°C	1.57	6.46	Fausto et al. (2009)
Solid precipitation threshold	p_{solid}	°C	−2	2	van Meijgaard et al. (2008)
Accumulation ratio	γ	°C^{-1}	0.03	0.1	Li et al. (2010), Guillevic et al. (2013)
Thermoactive layer thickness	d	m	0.4	2.0	Pfeffer et al. (1991)
SIA Enhancement factor	E_{SIA}	–	1.0	5.6	Ma et al. (2010)
GHF modificator	γ_{GHF}	–	0.8	1.2	Näslund et al. (2005), Shapiro and Ritzwoller (2004)
Dragging coefficient	C_f	–	1×10^{-5}	10×10^{-5}	Alvarez-Solas et al. (2011), Peyaud et al. (2007)

6.2 Results of the LHS simulations

In the following, we present the results from the LHS ensemble simulations. We focus on the diagnostics of interest, namely ice volume, ice thickness and bedrock depression.

6.2.1 Ice sheet volume

Figure 6-1 and 6-2 presents the simulated ice volume using the B140_Topo1 and B140_Topo2 climates for each individual ensemble member as a function of parameters. Thanks to the LHS methodology, all the different ranges are evenly explored. The simulated ice sheet volumes range from almost no ice to around 70 m SLE. There is no clustering amongst the different parameters and, as a first approximation, for a given parameter, any value can produce any simulated ice volume. This indicates that no single parameter alone, within its tested interval, is drastically influencing the model response. However, there is a clustering of the simulated ice volumes, independently from the parameters, around three bands: around 15 m SLE, around 35 m SLE and around 60 m SLE. The models that fall in the upper category are the ones that maintain the initial ice extent of Svendsen et al. (2004). The middle category corresponds to the simulations that loose a fraction, or all, of the western part of the Eurasian ice sheet. This area is subjected to a warm climate and therefore sensitive to climate forcing whilst the bedrock is situated mostly below sea level leading to ice sheet instability. The eastern part of the ice sheet, on the contrary is subject to cold climate conditions and, as a result, is able to maintain, while the western part has collapsed (simulations presenting very low ice volume).

Given that virtually all volumes are simulated between 0 to 70 m SLE, we need to find constraints to assess the realism of certain combinations. However, only few constraints exist in order to restrict the range of possible reconstructions. One of them is the ice sheet extent, which is relatively well known (Svendsen et al. 2004). In particular, it is virtually certain than both the Olkiluoto and Forsmark repository sites where ice covered at 140 kyrs BP. For this reason, all simulations which present an ice thickness lower than 500 m at one of the sites are discarded (red stars in Figure 6-1 and 6-2). Those simulations do not agree with geological evidence and, as such, should be discarded from the analysis. Doing so, the lower bound is better constrained. It is important to note that the retreat of the ice sheet starts systematically in the western part of the Eurasian ice sheet (not shown), whereas the eastern part is more stable. The western part is indeed the most sensitive to SMB changes, see Chapter 2, and corresponds to the region with the highest ice velocities (Chapter 3).

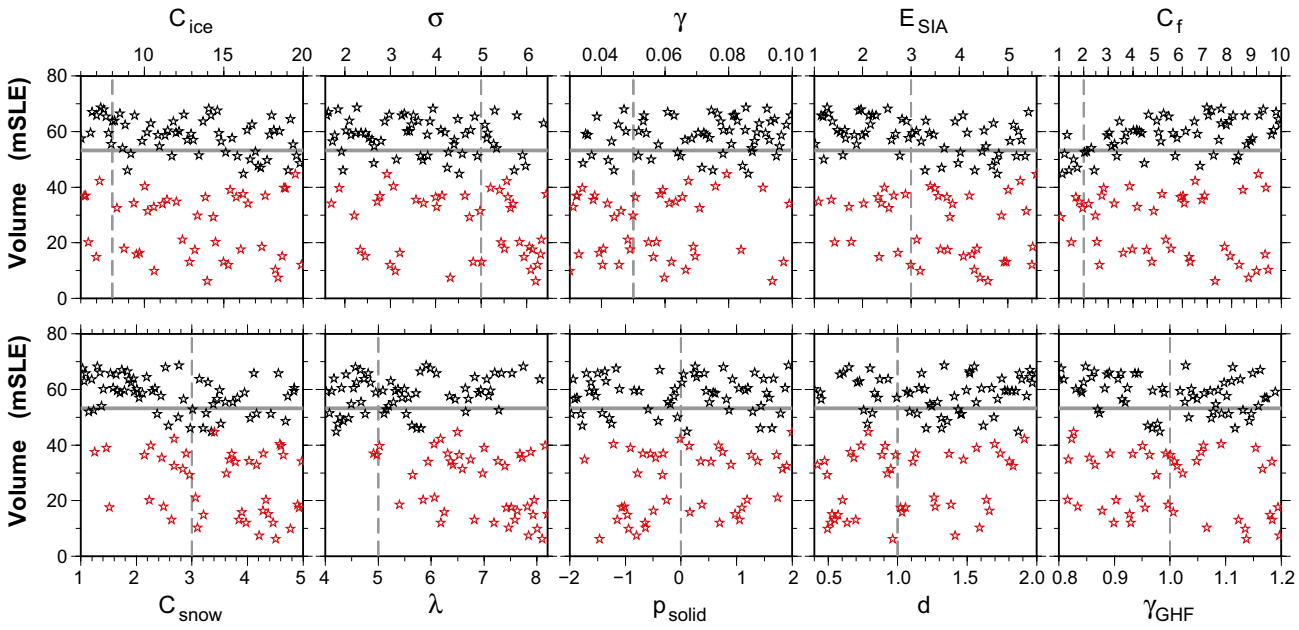

Figure 6-1. *Final Late Saalian ice sheet volumes simulated using B140_Topo1 climate forcing for each member of the Latin hypercube ensemble as a function of parameter values. Horizontal lines correspond to the volume simulated in the reference simulation during the first phase of the project (Colleoni et al. 2014b, 2016b). Vertical dashed lines correspond either to the parameter value used in the reference simulation (if this parameter was used), or to a standard value from literature. The red stars are the simulations that are discarded since they do not preserve ice (thickness less than 500 m) at the repository sites (i.e. an unrealistically large ice sheet retreat).*

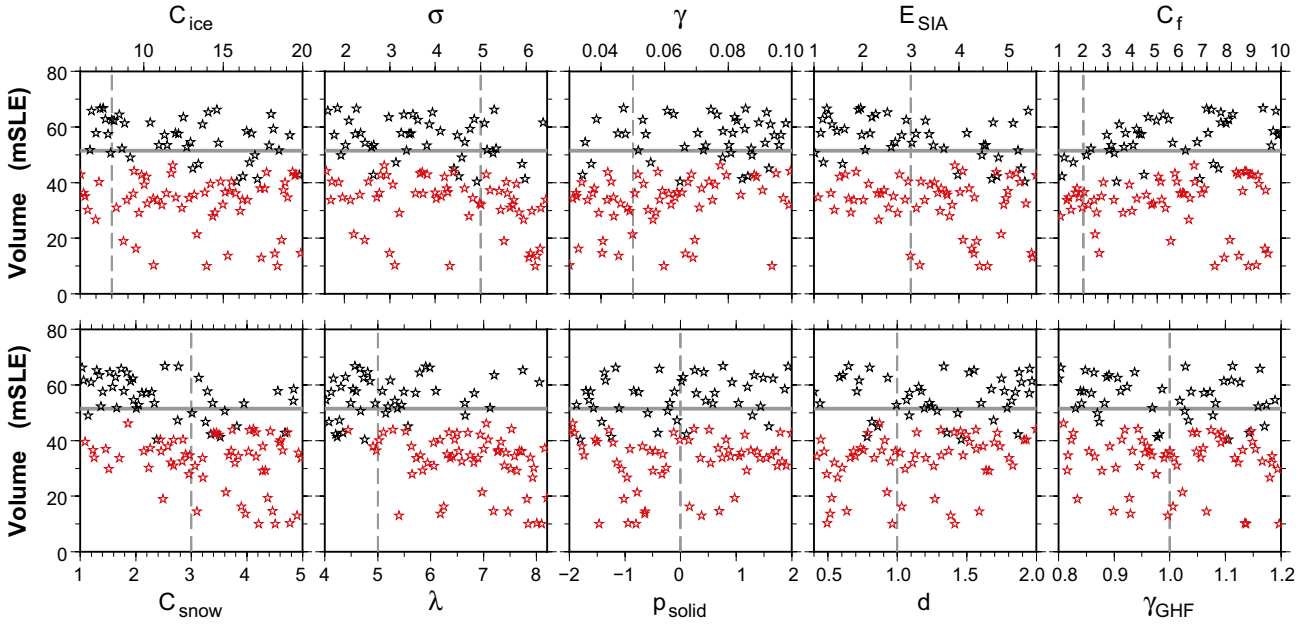

Figure 6-2. *Final Late Saalian ice sheet volumes simulated using B140_Topo2 climate forcing for each member of the Latin hypercube ensemble as a function of parameter values. Horizontal lines correspond to the volume simulated in the reference simulation during the first phase of the project (Colleoni et al. 2014b, 2016b). Vertical dashed lines correspond either to the parameter value used in the reference simulation (if this parameter was used), or to a standard value from literature. The red stars are the simulations that are discarded since they do not preserve ice (thickness less than 500 m) at the repository sites (i.e. an unrealistically large ice sheet retreat).*

On the other hand, ice volume itself can also be used as an additional potential constraint. Global sea-level reconstructions suggest a range of −92 to −150 m for the Late Saalian relative to present-day (Rabineau et al. 2006). The Late Saalian reconstruction of Lambeck et al. (2006) of 60 m SLE, but also the one of Peyaud (2006) of 70 m SLE, is in agreement with the range of sea level reconstructions. Because all our simulations suggest volumes lower than 70 m SLE, the upper bound in term of volume cannot be better constrained than this. In B140_Topo2, the Laurentide ice sheet accounts for 30 m SLE and the Antarctic ice sheet for 17 m SLE. Thus, in the case of B140_Topo2, the Eurasian ice sheet should not present a volume lower than ~40 m SLE in order to be in agreement with global sea-level reconstructions. In fact, in our set of experiments, the only simulations that have a lower volume than 40 m SLE also present no ice at the repository sites. As such, the ice thickness criterion (red stars on Figures) is always more restrictive than the ice volume criterion.

The remaining ice sheet simulations preserving both the ice extent (thickness at repository sites) and ice volume criteria correspond to the black stars in Figure 6-1 and 6-2. For some parameters there is no correlation between the parameter value and the simulated ice volume. This is the case for temperature threshold for the solid fraction of precipitation (p_{solid}) and the thickness of the thermo-active layer (d). For other parameters, a relatively strong correlation exist. This is the case for the dynamical parameters (enhancement factor, E_{SIA}) and basal drag coefficient (C_f). Also, for some parameters there is some kind of thresholds, which explain the retreat of the western part of the ice sheet. For example, a value higher than 3 mm $°C^{-1}$ d^{-1} for the snow ablation coefficient (C_{snow}) or, a value higher than 5 °C for the temperature standard deviation (σ), leads to the most unstable conditions under the B140_Topo2 climate (Figure 5-2). Furthermore, a topographic lapse rate lower than 5 $°C^{-1}$ km^{-1} guarantees the stability of the western part of the ice sheet (very few red stars).

The ice sheet volumes from the ensemble members are generally slightly higher than the volume of the reference simulation. The mean volume of the ensemble members that match both the extent and volume criteria (black stars on Figure 6-1 and 6-2) is 58.5 m SLE (B140_Topo1) and 55.9 m SLR (B140_Topo2), corresponding to an increase of 6 % (B140_Topo1) and 7 % (B140_Topo2) relative to the reference simulation. The minimum and maximum volumes are 44.8 and 68.7 m SLE using B140_Topo1 climate and 40.4 and 66.8 m SLE using B140_Topo2 climate.

As expected, the LHS experiments present a wider range of resulting ice thicknesses than the sensitivity experiments of the first phase of the study (volumes ranging from 49.7 to 58.7 m SLE, see Colleoni et al. 2014b, 2016b). This could be the result of various factors:

- The individual range of all the parameters tested is considerably larger than during the first phase of the study since they now cover the full range of literature values. As a consequence, a wider range of simulated volumes was expected from this sensitivity analysis.
- The sensitivity to dynamical parameters was only briefly explored during the first phase of the study, as only the dragging coefficient C_f was tested. This coefficient already gave the lower and the upper bound of all the sensitivity experiments during phase one, when only testing the range 1 to 3×10^{-5}. In the LHS, we test both this dragging coefficient (with a considerably wider range) and the SIA enhancement factor.
- Also, the ratio of enhancement factors for SIA and SSA has been slightly modified from Colleoni et al. (2014b, 2016b) study for the LHS and this could have some impact (supposedly lower than the impact of parameter changes).

6.2.2 Ice thickness and bedrock depression at the repository sites

Because the ice volume is an integrated variable over the entire ice sheet, part of the information is not shown by this parameter, for example the ice sheet conditions at the repository sites. The simulated ice thickness over the repository sites using the B140_Topo1 climate forcing for each members of the ensemble as function of parameter values is presented in Figure 6-3 (Forsmark) and Figure 6-4 (Olkiluoto). Figure 6-5 (Forsmark) and Figure 6-6 (Olkiluoto) present the corresponding results when using B140_Topo2 climate forcing. As already suspected from the results on ice volume, about 50 % of the simulations fail to preserve ice over the repository sites. This number is slightly higher when using the B140_Topo2 climate forcing compared to B140_Topo1. Also, the results are split between no ice and relatively thick ice. No experiments present moderate amounts of ice (i.e. ~2000 m of ice or less) over Forsmark and very few for Olkiluoto. Interestingly, this means that in order to have an

extended ice sheet under the Late Saalian with our methodology, the thickness has to be greater than 2500 m at the repository sites. A few simulations preserve just some ice at Olkiluoto because this site is closer to the eastern part of the Eurasian ice sheet. The eastern part is always more resilient because the climate there is drastically colder than in the west.

The ice sheet extent criterion discards the simulations that do not preserve ice at the repository locations. Only weak correlations between ice thickness and parameter values emerge from the sensitivity experiments. The lack of emerging relationships was already reported in Applegate et al. (2012) who used a Latin Hypercube ensemble to simulate the Greenland ice sheet with SICOPOLIS. However, we have two noticeable exceptions from this, as we observe a negative correlation between the ice thickness and the enhancement factor (E_{SIA}), and a positive correlation with the basal drag coefficient (C_f). This could suggest that those parameters, linked to internal ice sheet dynamics, are more important for the ice thickness than surface mass balance parameters. In particular, for an enhancement factor lower than 3, the simulated ice thickness is almost systematically larger than in REF_Topo1 and REF_Topo2, independently from the values of the other parameters. This is especially true in the case of the B140_Topo1 climate forcing, which preserve more ice in the western part of the Eurasian ice sheet. The same is true for the basal drag coefficient, where a value higher than 2 tends to generate thicknesses greater than in the reference simulation.

As already observed for ice volume, the mean ice thickness for the ensemble members that match both the extent and volume criteria (black stars in Figures 6-3, 6-4, 6-5 and 6-6) is 3578 m (resp. 3153 m) under B140_Topo1 (resp. B140_Topo2) climate at Forsmark and 3697 m (resp. 3352 m) under B140_Topo1 (resp. B140_Topo2) climate at Olkiluoto. This corresponds to an increase from the reference simulation of 15.4 % (resp. 8.2 %) under B140_Topo1 (resp. B140_Topo2) climate at Forsmark and 14.5 % (resp. 9.4 %) under B140_Topo1 (resp. B140_Topo2) climate at Olkiluoto. The minimum ice thickness (resp. bedrock depression) at Forsmark is 2707 m (resp. −629 m) using B140_Topo1 and 581 m (resp. −178 m) using B140_Topo2. At Olkiluoto, the minimum ice thickness (resp. bedrock depression) is 2872 m (resp. −669 m) using B140_Topo1 and 1518 m (resp. −237 m) using B140_Topo2. The maximum ice thickness (resp. bedrock depression) at Forsmark is 4150 m (resp. −1003 m) using B140_Topo1 and 3957 m (resp. −958 m) using B140_Topo2. At Olkiluoto, the maximum ice thickness (resp. bedrock depression) is 4190 m (resp. −1017 m) using B140_Topo1 and 4023 m (resp. −977 m) using B140_Topo2.

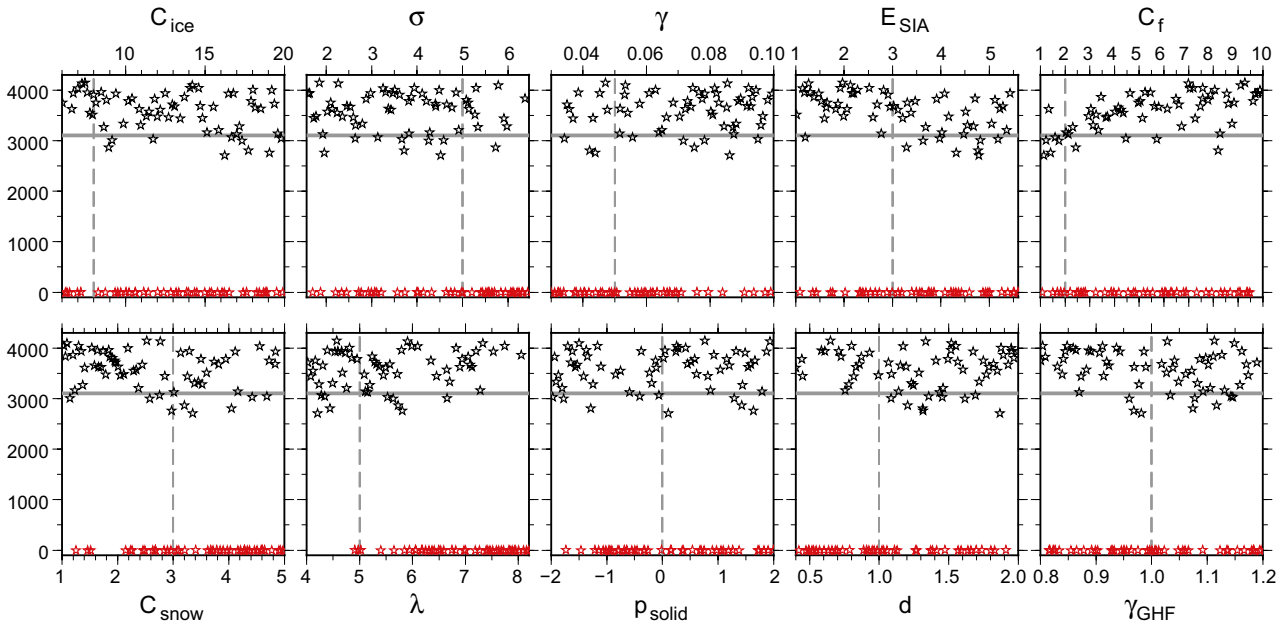

Figure 6-3. *Ice thickness over Forsmark using B140_Topo1 climate forcing for each member of the Latin hypercube ensemble as a function of parameter values. Horizontal lines correspond to the ice thickness simulated in the reference simulation during the first phase of the project (Colleoni et al. 2014b, 2016b). Vertical dashed lines correspond either to the parameter value used in the reference simulation (if this parameter was used), or to a standard value from literature. The red stars are the simulations that are discarded since they do not preserve ice (thickness less than 500 m) at the Forsmark site (i.e. an unrealistically large ice sheet retreat).*

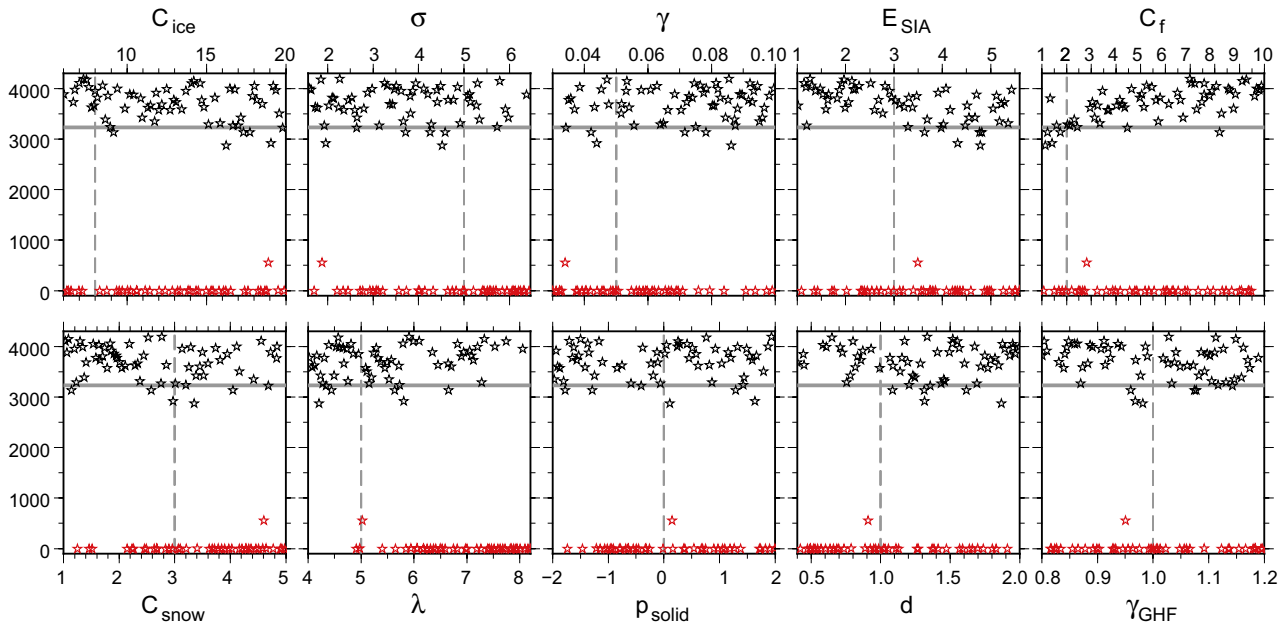

Figure 6-4. *Ice thickness over Olkiluoto using B140_Topo1 climate forcing for each member of the Latin hypercube ensemble as a function of parameter values. Horizontal lines correspond to the ice thickness simulated in the reference simulation during the first phase of the project (Colleoni et al. 2014b, 2016b). Vertical dashed lines correspond either to the parameter value used in the reference simulation (if this parameter was used), or to a standard value from literature. The red stars are the simulations that are discarded since they do not preserve ice (thickness less than 500 m) at the Olkiluoto (i.e. an unrealistically large ice sheet retreat).*

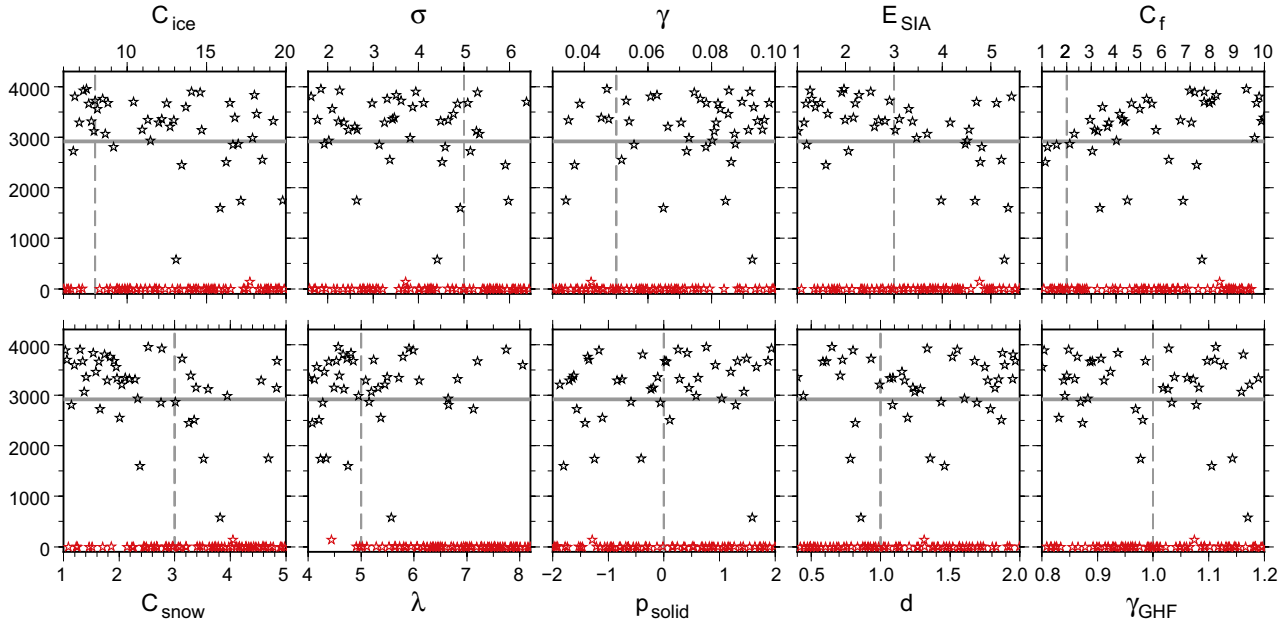

Figure 6-5. *Final ice thickness over Forsmark using B140_Topo2 climate forcing for each member of the Latin hypercube ensemble as a function of parameter values. Horizontal lines correspond to the ice thickness simulated in the reference simulation during the first phase of the project (Colleoni et al. 2014b, 2016b). Vertical dashed lines correspond either to the parameter value used in the reference simulation (if this parameter was used), or to a standard value from literature. The red stars are the simulations that are discarded since they do not preserve ice (thickness below 500 m) at the Forsmark (i.e. an unrealistically large ice sheet retreat).*

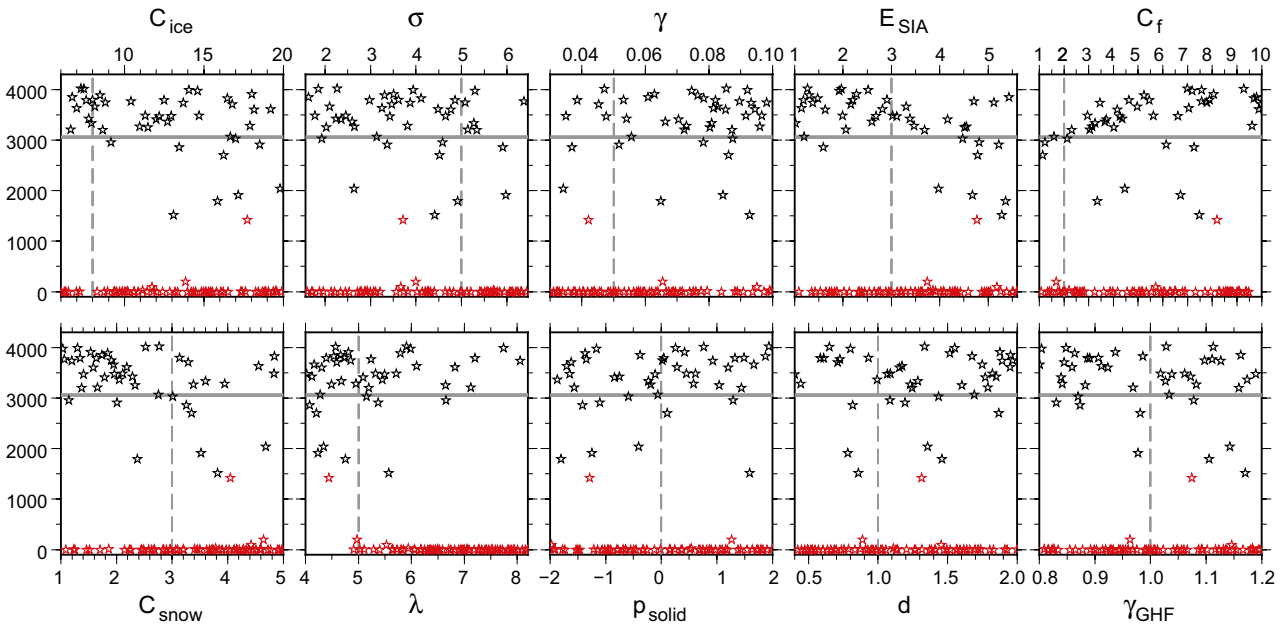

Figure 6-6. *Final ice thickness over Olkiluoto using B140_Topo2 climate forcing for each member of the Latin hypercube ensemble as a function of parameter values. Horizontal lines correspond to the ice thickness simulated in the reference simulation during the first phase of the project (Colleoni et al. 2014b, 2016b). Vertical dashed lines correspond either to the parameter value used in the reference simulation (if this parameter was used), or to a standard value from literature. The red stars are the simulations that are discarded since they do not preserve ice (thickness below 500 m) at the Olkiluoto (i.e. an unrealistically large ice sheet retreat).*

The bedrock depression mainly reflects what has already been described for the ice thickness. The relationships between parameter values and this variable remain the same as for ice thickness. Table 6-2 summarizes the result of the ensemble mean when considering the members that match the ice extent and volume criteria. The ensemble mean is higher than the reference simulations REF_Topo1 and REF_Topo2 but is well within the range of the different tested sensitivities. In particular, the climate forcing sensitivity described in Chapter 5 produced a thickness larger than 15 % compared to the reference simulations REF_Topo1 and REF_Topo2 when using FGOALS-g2 or MPI-ESM-P.

6.2.3 The sensitivity of the western part of the Eurasian ice sheet

As mentioned in the previous section, a large number of the ensemble members fail at preserving ice for the western part of the Eurasian ice sheet, especially when using B140_Topo2 climate forcing. Here we conduct an in-depth analysis in order to understand why the ice is unstable and retreats in this region.

Figure 6-7 and 6-8 presents the percentage of experiments that do not fulfill the ice extent (thickness greater than 500 m over both sites) and ice volume criteria when using the B140_Topo1 and B140_Topo2 climate forcings as a function of the parameter values. In these figures, we see clear relationships emerging. For example, when using the B140_Topo1 climate forcing, a value lower than five for the topographic lapse rate always preserve the ice at the repository locations, independently from the values of the other parameters. Also, some parameters present clear relationships: temperature variability, snow ablation coefficient, precipitation ratio and thickness of the thermoactive layer. On the contrary, other parameters do not present any relationship (ice ablation coefficient, basal drag coefficient or geothermal heat flux). This means that the parameters linked to surface mass balance are crucial for the ice extent (retreat), even though they are not directly correlated to the thickness over the repository sites (Section 6.2.2). Interestingly, the basal drag coefficient, that has been shown to be strongly correlated with ice thickness at the sites, is not responsible for high sensitivity (ice retreat) of the western part of the ice sheet.

Table 6-2. Simulated Late Saalian Eurasian ice sheet volume, ice thickness and bedrock depression for the ensemble mean considering the ensemble members that preserve ice (thickness greater than 500 m) at both repository sites. For ice thickness and bedrock depression Forsmark is identified by *F*, Olkiluoto by *O*. Changes are computed relative to the reference simulation under each climate forcing.

	Eurasian ice sheet volume						Ice thickness							Bedrock depression						
	B140_Topo1			B140_Topo2			Site	B140_Topo1			B140_Topo2			Site	B140_Topo1			B140_Topo2		
ID	m SLE	%	σ	m SLE	%	σ		m	%	σ	m	%	σ		m	%	σ	m	%	σ
LHS	58.46	*9.7*	6.4	55.94	*8.6*	*7.3*	*F*	3578	*15.4*	380.8	3153	*8.2*	*704.3*	*F*	−850	*16.3*	90.3	−737	*7.7*	*164.5*
							O	3697	*14.5*	328.9	3352	*9.4*	*809.5*	*O*	−885	*15.9*	78.5	−789	*9.5*	*173.6*

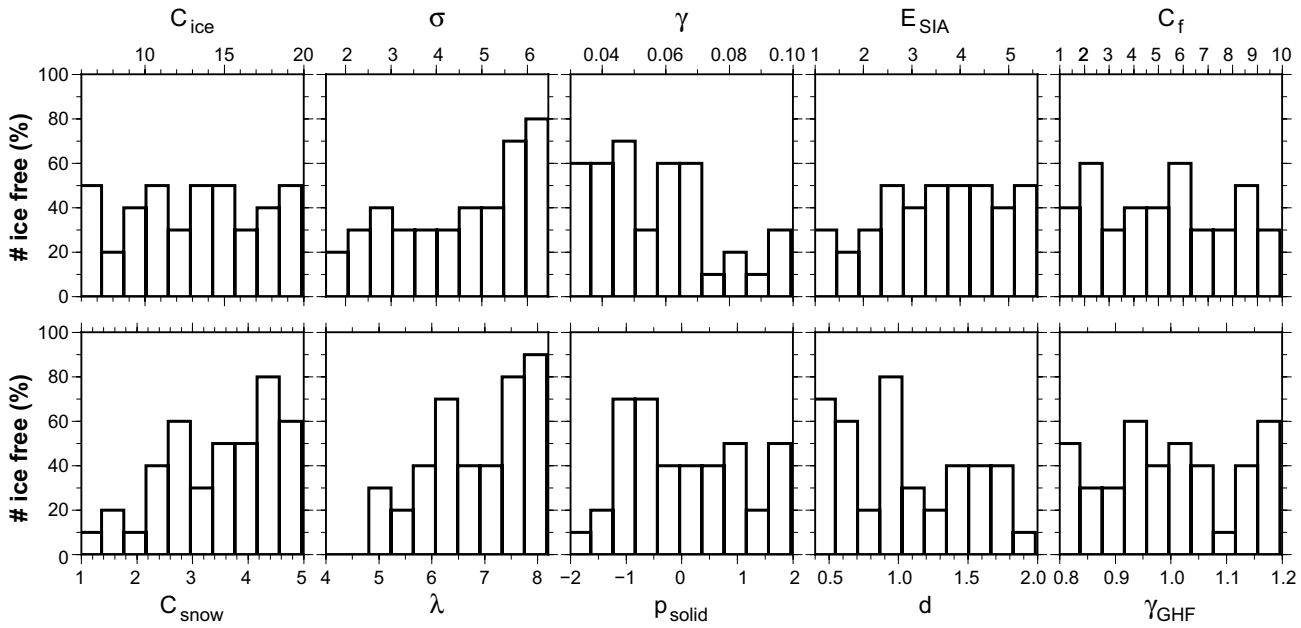

Figure 6-7. *Percentage of experiments that do not fulfil the ice extent (thickness greater than 500 m over both repository sites) and ice volume criteria when using the B140_Topo1 climate forcing. The parameter ranges are divided into ten classes of equal size (each class consists of 10 experiments).*

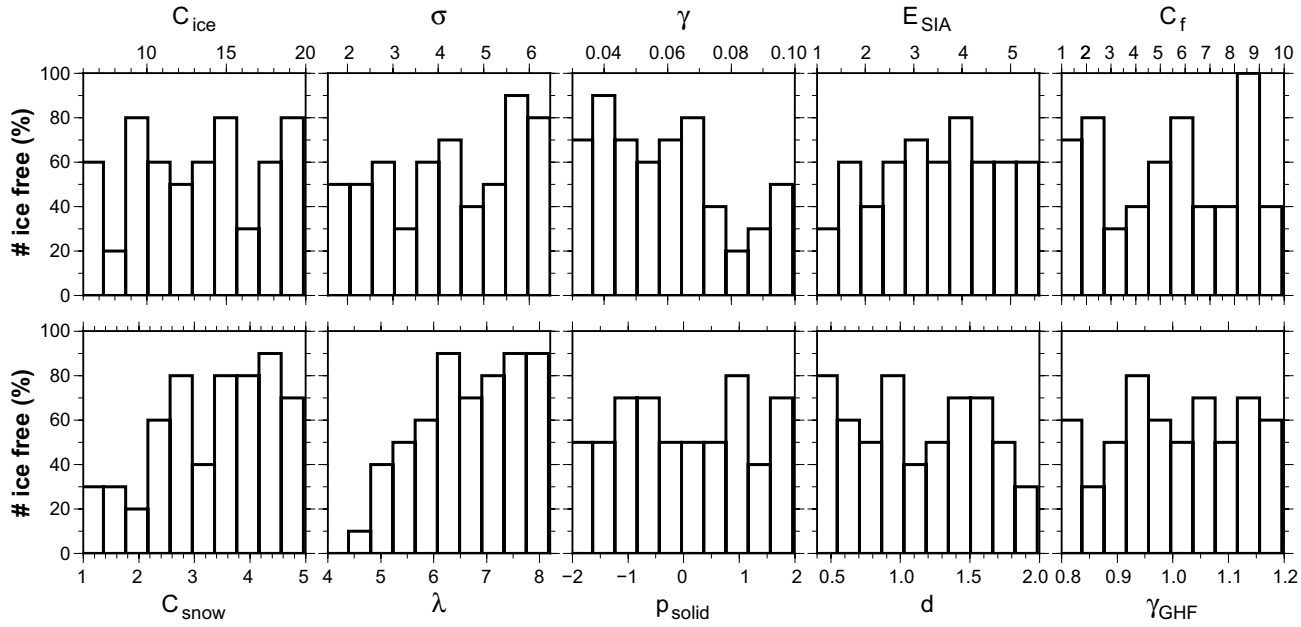

Figure 6-8. *Percentage of experiments that do not fulfil the ice extent (thickness greater than 500 m over both repository sites) and ice volume criteria when using the B140_Topo2 climate forcing. The parameter ranges are divided into ten classes of equal size (each class consists of 10 experiments).*

6.3 Discussion and summary of section

We have performed a detailed multi-variate parametric sensitivity analysis of the simulated Late Saalian ice sheet using a Latin hypercube sampling method. We tested ten different ice sheet model parameters covering the surface mass balance uncertainties as well as ice sheet dynamical uncertainties. The results showed a wide range of ice volumes, whereas the simulated thicknesses and bedrock depressions at the repository sites mostly fell into two categories (no ice or very thick ice sheet). The parameters linked to surface mass balance have the strongest impact on the stability of the western part of the Eurasian ice sheet but they only have a limited impact on the ice thickness and bedrock depression at the repository sites given relatively stable ice sheet conditions. The parameters linked to the internal ice dynamics have the opposite influence; they mostly impact the ice thickness and bedrock depression, but do not explain the retreat of the western part of the Eurasian ice sheet in many of the simulations.

The ensemble members predict generally more ice and greater bedrock depression than the reference simulation. This is probably due mostly to the fact that we use wider ranges for the tested parameters and in particular for the basal drag coefficient. With our range for the basal drag coefficient (1 to 10×10^{-5}), 90 % of the simulations have a greater value than the reference value (2×10^{-5}). Due to its importance for the ice thickness, it is therefore not surprising that most of the ensemble members are thicker than the reference simulation. This is further discussed in Chapter 7 below.

7 Discussion

The present study is the second and final phase of a study aiming at simulating the ice thickness over Forsmark (Eastern Sweden) and Olkiluoto (Western Finland) for the most extensive glaciation on record that occurred over Eurasia around 140 kyrs BP. The first phase was reported in Colleoni et al. (2014b, 2016b). In the first phase of the study, two Late Saalian climate simulations, named B140_Topo1 and B140_Topo2, were carried out using the CESM 1.0.5 model. They used prescribed topographies including the Late Saalian Eurasian ice sheet elevation from Peyaud (2006) and including two different ice sheet elevation reconstructions over North America. These climate simulations were subsequently used to perform about 140 univariate ice sheet simulations by means of the 3D thermomechanical ice sheet, ice-streams and ice-shelves model GRISLI. In the previous report (Colleoni et al. 2014b, 2016b), we studied many aspects dealing with:

- Uncertainties of the initial and boundary conditions of the climate simulations, i.e. the prescribed ice sheet topographies and vegetation cover in CESM. The reader is referred to the discussion in Colleoni et al. (2014b, 2016b) for further details.
- Uncertainties related to the ice sheet simulations: the impact of the initialisation of the ice sheet simulations, the advantages/disadvantages of steady-state simulations, the impact of the climate forcing related parameters (lapse rate, surface mass balance method) and the impact of the simple regional isostasy module embedded in the ice sheet model.

In the present study, the impact of surface mass balance formulation, ice dynamics formulation and climate forcing sensitivity have been further investigated. A large ensemble of multivariate ice sheet simulations has also been performed in order to thoroughly assess the parametric uncertainty. Results have shown the importance of ice dynamics for glaciological reconstructions of the Late Saalian Eurasian ice sheet. In the following, the use of the basal drag coefficient in SIA-SSA ice sheet simulations is discussed since it provides the upper bound for ice sheet thickness over the repository sites of the whole set of experiments carried out in the present study. The impact of the complexity of different numerical models is also discussed since each type of ice sheet model and climate model presents physical assumptions or drawback that potentially impacts on the geometry of the simulated ice sheets. Since all our experiments are equilibrium simulations run for at least 200,000 years, we discuss the differences in ice volume, extent and thickness that those steady-state simulations can generate compared with transient experiments.

7.1 Basal drag

In Chapter 6, we highlighted the major influence of the basal drag coefficient C_f on the simulated ice thickness. Larger values for C_f induce larger values for ice thickness, independently from the choice of the other parameters. In fact, the LHS methodology makes sure that the larger values of C_f are well distributed amongst the range of other parameters (Figure 7-1 and 7-2).

In Chapter 6 we presented the basal drag coefficient C_f used in GRISLI, which modulates the resistive force exerted by the bedrock at the base of the ice sheet in the regions treated with the SSA. A very large part of our reconstructed Late Saalian Eurasian ice sheet is warm based, in particular in the western part where the climate forcing is warmer than in the eastern part. For this reason, the use of the SSA is widespread and mainly limited by the sediment distribution. This explains why this parameter presents such a large influence on the ice sheet ice thickness. For illustrative purposes, in Figure 7-3, we present the basal temperature distribution simulated by GRISLI in the reference simulation (C_f=2×10^{-5}, Figure 7-3a), in one member of the LHS presenting a C_f towards the higher end (C_f=9.8×10^{-5}, Figure 7-3b) and for the experiment with no SSA presented in Chapter 3 (DYN3, Figure 7-3c). A larger C_f induces a thicker ice and results in warmer basal temperatures than in the reference simulation. The experiment with no SSA is even more extreme because of extremely thick ice.

The basal drag C_f is not an universal parameter because different ice sheet models have different expressions for β in Equation 6-3. Consequently we cannot compare the value of this parameter with other works in literature. However, β has a precise physical meaning and can be compared with the literature. Unfortunately, only few studies provide the value of this variable.

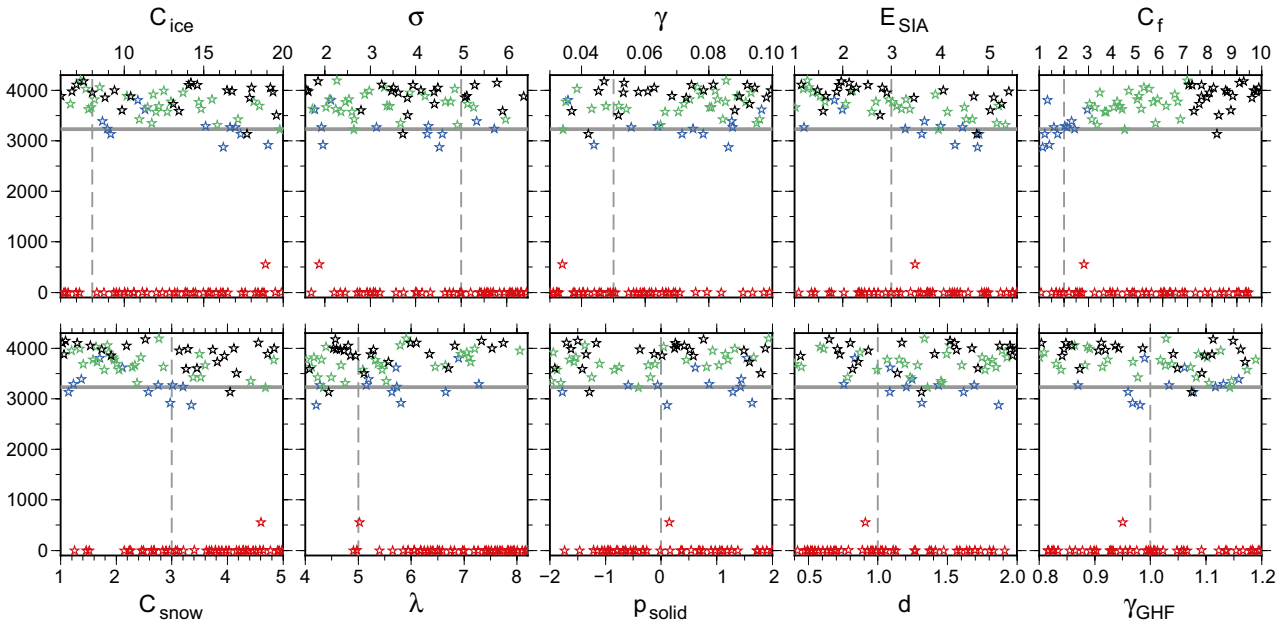

Figure 7-1. *Final ice thickness over Forsmark simulated using B140_Topo1 climate forcing for each member of the Latin hypercube ensemble as a function of the parameter values. Horizontal lines correspond to the thickness simulated in the reference simulation during the first phase of the project. Vertical dashed lines correspond either to the parameter value used in the reference simulation (if this parameter was used), or to a standard value from literature. The red stars are the simulations that do not preserve ice (thickness less than 500 m) at the repository sites (i.e. an unrealistically large ice sheet retreat). The light blue stars correspond to the experiments with a C_f value lower than 3×10^{-5} (maximum explored during phase one), green stars correspond to the experiments with a C_f value between 3 × 10-5 and 7×10^{-5} and the black stars correspond to the experiment with a C_f value greater than 7×10^{-5}.*

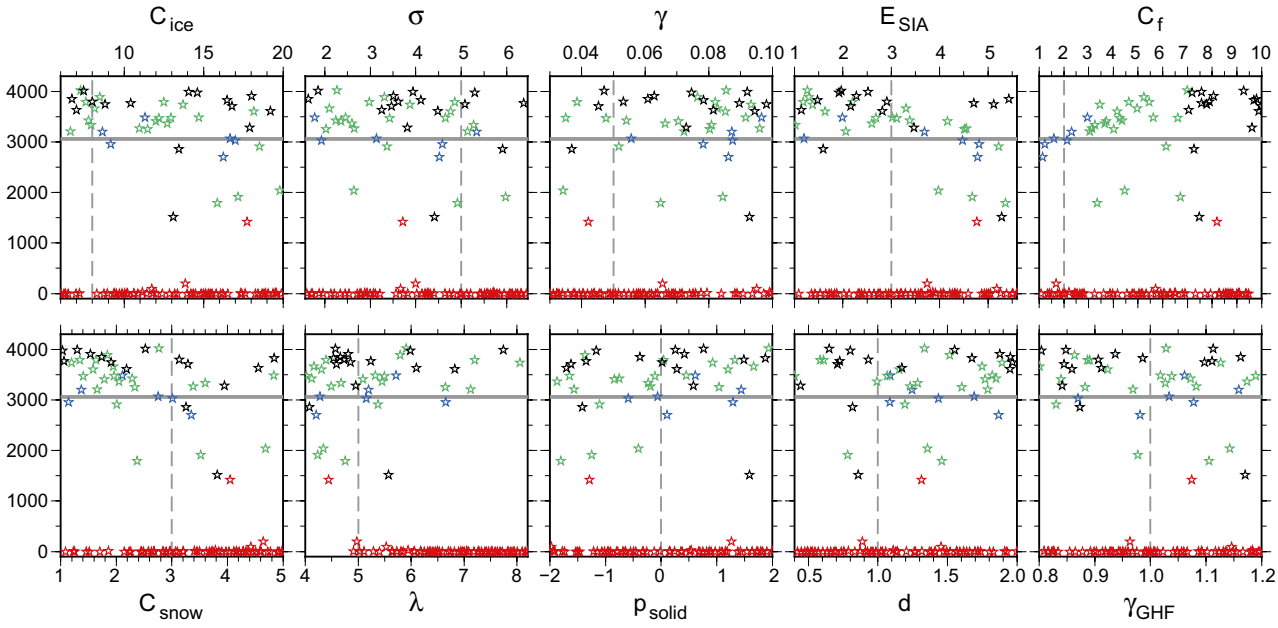

Figure 7-2. *Final ice thickness over Olkiluoto simulated using B140_Topo1 climate forcing for each member of the Latin hypercube ensemble as a function of the parameter values. Horizontal plain lines correspond to the thickness simulated in the reference simulation during the first phase of the project. Vertical dashed lines correspond either to the parameter value used in the reference simulation (if this parameter was used), or to a standard value from literature. The red stars are the simulations that do not preserve ice (thickness less than 500 m) at the repository sites (i.e. an unrealistically large ice sheet retreat). The light blue stars correspond to the experiments with a C_f value lower than 3×10^{-5} (maximum explored during phase one), green stars correspond to the experiments with a C_f value between 3×10^{-5} and 7×10^{-5} and the black stars correspond to the experiment with a C_f value greater than 7×10^{-5}.*

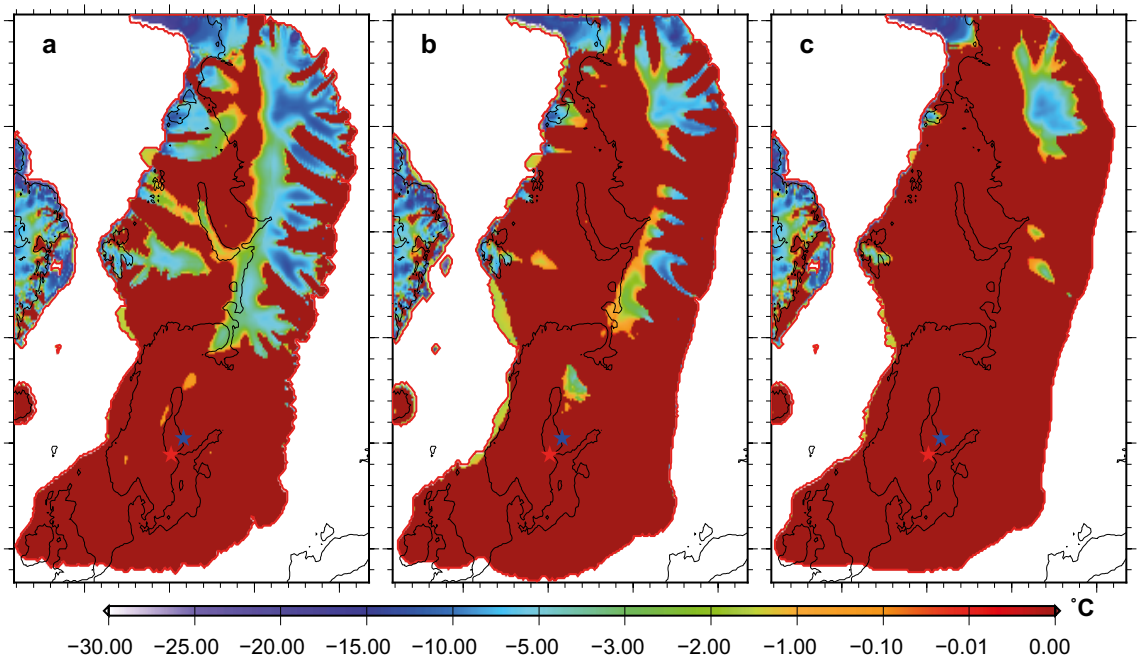

Figure 7-3. *Basal temperature distribution for (a) the reference simulation ($C_f = 2 \times 10^{-5}$) using B140_Topo1 climate forcing, (b) for one member from the Latin Hypercube ensemble presenting a high C_f value (9.8×10^{-5}) using the same climate forcing, and for (c) the experiment with no SSA (DYN3).*

As most other basal processes, basal drag is not a variable that is directly observable. Relatively recently, the use of radar interferometry from satellite measurements has allowed the construction of accurate surface velocity maps over both the Greenland and Antarctic ice sheets. From those maps, several inverse modelling studies have inferred the basal drag coefficient using an ice sheet model (Gillet-Chaulet et al. 2012, Morlighem et al. 2010, 2013). The results have shown that the β parameter is highly heterogeneous below the ice sheets. For example in Figure 5 in Morlighem et al. (2013), most of Antarctica presents a β higher than 2500 Pa yr m^{-1} (cyan color; $\alpha^2 = \beta$). However, below the main ice streams the values are generally around 150–200 Pa yr m^{-1}, even if they can be locally much smaller reaching a few Pa yr m^{-1}. Schäfer et al. (2012) list typical values for the basal drag coefficient for a Svalbard ice cap, which range from 100 to around 5000 Pa yr m^{-1}.

Figure 7-4 presents the value of the basal drag coefficient, β, as simulated by GRISLI under the B140_Topo1 climate in the reference simulation (Figure 7-4a) and in one member from the Latin hypercube ensemble presenting a C_f towards the higher end (C_f=9.8×10^{-5}, Figure 7-4b). As shown in Chapter 3, the Late Saalian Eurasian ice sheet simulated in GRISLI presents a large part treated with SSA and consequent having a low basal drag. In the reference simulation, around two thirds of the ice sheet presents a basal drag coefficient between 20 and 100 Pa yr m^{-1}. Due to the GRISLI model formulation, the C_f and β coefficients are linearly related. As a consequence, there is almost a factor 10 in β between the experiment using the largest C_f value and the reference simulation.

As a comparison, Figure 7-4c shows the β coefficient retrieved with GRISLI below the Greenland ice sheet in the context of the Ice2Sea project. Because of the highly mountainous region in the East and the wet bias in climate forcing (Ettema et al. 2009), simulated ice sheets are generally too thick in the eastern part of Greenland. The inferred basal drag coefficient reflects the need to compensate for this bias, strongly decreasing the basal drag in this area. The western and northeastern areas show more realism and correspond to the findings of Morlighem et al. (2013) over Antarctica. Even in the well identified large ice stream of the North East region, the basal drag coefficient presents a minimum value around 20 and 50 Pa yr m^{-1}, but it is systematically greater than 300 Pa yr m^{-1} inland. Thus, the numbers do not match our experiments of the late Saalian, as we always have lower values for the basal drag coefficients, even with a C_f at 9.8×10^{-5}. As a side note, Quiquet et al. (2013) used a homogeneous value of 1500 Pa yr m^{-1} for the Greenland ice sheet simulated with GRISLI over the last glacial-interglacial cycle.

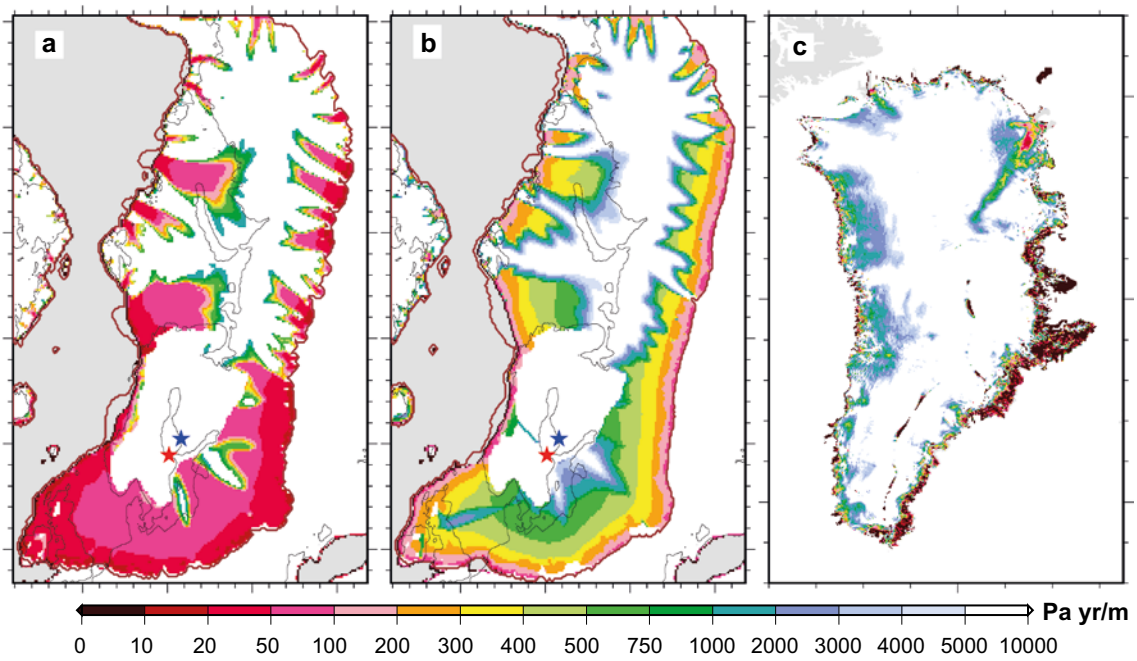

Figure 7-4. *Basal drag coefficient β, for (a) the reference simulation ($C_f = 2 \times 10^{-5}$) using the B140_Topo 1 climate forcing, and (b) for one member from the Latin Hypercube ensemble presenting a high C_f value (9.8×10^{-5}) using the same climate forcing. (c) shows the basal drag coefficient inferred under the Greenland ice sheet with GRISLI in the context of the Ice2Sea project (Edwards et al. 2014).*

Even if not necessarily comparable, results for Greenland and Antarctica suggest a strongly heterogeneous pattern for the basal drag coefficient. Present-day ice streams are well identified with local values around 150 Pa yr m^{-1}. This is in contrast to our simulations where the lack of spatial resolution combined with the lack of knowledge about the mechanisms of ice stream activation lead to broad zones of values below 100 Pa yr m^{-1}.

To conclude, at this stage it is difficult to better constrain the range of C_f used in the Latin hypercube analysis because no physical constrain nor observation play in favor of low values more than high values.

7.2 Steady-state versus transient ice sheet simulations

To provide estimates of ice thickness and bedrock depression at the repository sites for peak glacial conditions during the Late Saalian period, we performed long steady-state experiments under a constant glacial climate describing the situation at 140 kyrs BP in order to reach equilibrium conditions in terms of ice sheet volume. Of course, in the real world, the climate system is never in equilibrium and the steady-state assumption is a crude approximation when reconstructing ice sheets. Transient simulations present the advantage of updating the atmosphere and ocean circulation, as well as vegetation and terrestrial processes, with changes in surface topography. Only few numerical transient simulations covering the last 400,000 years has been performed, as for example Ganopolski and Calov (2012) and Abe-Ouchi et al. (2013). Other transient simulations have been performed for the last glacial cycle only, such as Bonelli et al. (2009) and Liu et al. (2009). In the case of Ganopolski and Calov (2012), Abe-Ouchi et al. (2013) and Bonelli et al. (2009), the numerical climate models are of intermediate complexity, which means that some of the processes are over-simplified and the horizontal resolution is extremely coarse. However, in these studies, the climate is coupled to either the SICOPOLIS or GRISLI ice sheet models. In the case of Liu et al. (2009), the climate model constitutes a full AOGCM with an increased horizontal grid resolution of T31 (96 longitudes × 31 latitudes grid points). However, the ice sheet evolution is not interactively computed by means of an ice sheet model but prescribed based on ICE-5G (Peltier 2004).

The above simulations all present limitations, for example the impact of a coarse spatial resolution on the ablation processes over glaciated areas. But on the other hand, the synoptic circulation can evolve with the changing surface topography in these simulations, which is not the case in our steady-state ice sheet simulations. In fact, our crude correction of surface temperature and precipitation due to elevation changes by means of a lapse rate and a precipitation factor does not capture the changes in regional circulation. In Section 4.3.2 we described the index method that allows for an interpolation of the climate between two snapshots by means of a glacial index. This method accounts, in a simple way, for changes in synoptic circulation. In Section 4.3, we constructed our index based on the $\delta^{18}O$ record of the North GRIP Greenland ice core, assuming this temperature proxy as representative for the Eurasian region. However, the Greenland ice cores do not go beyond the Last Interglacial (~125 kyrs BP) and this approach could thus not be followed for the Late Saalian.

In Section 4.3.2, we simulated the transient evolution of the LGM Eurasian ice sheet using different simulated LGM and Pre-industrial climate forcings. All the transient simulations started from an initial spun-up LGM Eurasian ice sheet topography that was carried out with steady-state LGM climate forcing for about 200,000 years. The initial Eurasian ice sheet ice volume obtained from those spin-up simulations is about 34 m SLE using the MIROC-ESM climate, about 32 m SLE using the MPI-ESM-P climate and 20 m SLE using the IPSL-CM5A-LR climate forcing (Figure 4-11). The initial LGM Eurasian ice sheet topography prescribed in those climate models was the numerical reconstruction from ICE-5G (Peltier 2004) that holds about 21 m SLE of ice volume. From the three different climate forcing used in Figure 4-11, the steady-state final equilibrium ice volume is well beyond the prescribed ICE-5G LGM ice volume, except in the case of the IPSL climate forcing. Therefore, performing a steady-state simulation in those cases leads to no excess in ice volume (leading to a slightly larger extent and to a larger ice thickness) compared with the initial ice sheet volume. In the case of the transient experiments, the LGM Eurasian ice volume obtained, after applying the index method to derive the climate forcing evolution, reaches 35 m SLE in the case of MPI-ESM-P, 23 m SLE in the case of MIROC-ESM and 18 m SLE in the case of IPSL-CM5-LR (Figure 4-11). Once again, depending on the climate forcing, the ice volume obtained from a transient evolution based on the index method forcing is either larger than the spun-up initial ice volume (MPI model), or lower (MIROC), or only slightly different (IPSL).

These results suggest that steady-state simulations, integrated until equilibrium for a long amount of model time can lead to an excessive ice volume compared to reconstructions based on proxy data. In a steady-state simulation performed with a glacial climate forcing, some compensation occurs between the lack of accumulation that the dry glacial climate implies and the long time of integration of the simulation. On the contrary, in a transient simulation, the peak glacial climate is not the dominant climate. Therefore, during the climate evolution, the averaged accumulation is larger than under the steady-state glacial climate forcing. However, the transient air temperature is also typically warmer than under a constant peak glacial climate forcing. Therefore, the ice volume might result as either larger or smaller. These results also suggest that depending on the climate forcing, steady-state or transient simulations can lead to either an excess or a shortfall in ice volume. As a consequence, because we could not apply transient simulations for the Late Saalian period, it is difficult to conclude whether or not a transient simulation would lead to a smaller Eurasian ice volume for a large ice sheet extent. However, the initial Late Saalian Eurasian ice sheet extent on which this study relies, Svendsen et al. (2004), is particularly large, which in general have led to massive ice volume reconstructions in ice sheet models. Since evidence suggests that part of the extent described by Svendsen et al. (2004) was reached earlier in the Saalian glacial cycle, the peak glacial ice sheet extent occurring at around 140 kyrs BP could have been smaller than the extent proposed by Svendsen et al. (2004).

7.3 Model formulation

For this assessment, we derived ice sheet thickness and bedrock depression from an ice sheet model forced by outputs from a climate model. We covered most of the range of uncertainties as we performed a large sensitivity analysis on the importance of model formulation, climate forcing sensitivity and parametric sensitivity. However, we simulated the Late Saalian climate using essentially one single climate model (to which we adapted the forcing of the PMIP AOGCM models) and we based our conclusions on the results from one ice sheet model. In the following we discuss the limitations related to this approach.

7.3.1 The choice of climate model

Ice sheet modelling exercises have shown the importance of climate forcing sensitivity on the resulting ice sheet properties (e.g. Charbit et al. 2007, Graversen et al. 2011, Quiquet et al. 2012). As mentioned in Chapter 5, there are no other available reconstructions of the Late Saalian climate except the one we simulated with the CESM 1.0.5 model. To account for the sensitivity to climate forcing, we performed two Late Saalian climate simulations (the B140_Topo1 and B140_Topo2 simulations, Colleoni et al. 2014b, 2016b). However, these simulations were performed with the same climate model and as such any systematic bias is expected to be conserved. Also, in Chapter 6, we generated new Late Saalian climate forcings from pre-industrial climates simulated for a set of PMIP3 participating models. We confirmed the strong sensitivity of the Late Saalian simulated ice sheets to climate forcing. However, as discussed in Chapter 6, we were only able to quantify the sensitivity to uncertainties in the pre-industrial climate simulations. For other (older) time periods than the pre-industrial, with larger changes in boundary conditions (atmospheric greenhouse gas concentrations and orbital forcings), we expect the discrepancies between climate models to be larger.

In Section 4.3 and 5 we saw that the climate forcing simulated by different AOGCMs have a large impact on the geometry of the Eurasian ice sheet. Figure 4-11 shows that the best representation of the LGM ice sheet is obtained using the LGM climate from the IPSL climate model and a worse case occurs when using the CNRM LGM climate simulation. Because paleoclimate simulations are an important test to validate the flexibility and ability of climate models, several inter-comparison projects have been developed over the last decades. One of the largest, Paleoclimate Modelling Intercomparison Project (PMIP), is still going on, now with its phase 4. That project aims at simulating past climate states, significantly different from, or close to, the present-day climate. To that end, the LGM, Last Interglacial (~125 kyrs BP), and Mid-Holocene (6 kyrs BP) periods are analysed. The project involves more than 30 AOGCMs and the complexity of the simulations evolves along the various phases of the project.

The results from the PMIP3 phase show that, on average, models can reproduce the averaged climate change implied by the boundary conditions of the LGM quite well. However, the models are still not good enough to simulate climate amplitudes in agreement with paleoproxy data (e.g. Braconnot et al. 2012). Moreover, while the global averaged climate are quite satisfying, the regional spatial patterns of the various climate quantities still differ significantly from what the climate proxies suggest (e.g. Harrison et al. 2014, 2015). According to the recent benchmark by Harrison et al. (2014), all climate models underestimate the LGM cooling by up to 3.5 °C (Figure 7-5).

From Figure 7-5, the best fit with climate proxy data comes from the CMIP5 simulations, i.e. the PMIP3 phase in which some of the carbon cycle processes have been accounted for (which is different from the previous phases of PMIP). However, the difference between the models and between their physical complexities is large and lead to different results for the LGM climate. Finally, even if the multi-model ensemble mean provides a satisfying performance representing the current climate, both in terms of spatial patterns and amplitude of the climate processes, this is not the case for the paleoclimate simulations (Braconnot et al. 2012, Harrison et al. 2014, 2015). The present study was conducted using a climate forcing based on two climate simulations performed in the first phase of this study (Colleoni et al. 2014b, 2016b) by means of the CESM 1.0.5 climate model (with CAM4 physics). In Harrison et al. (2014), the performance of this specific model, compared to the others involved in PMIP3 LGM simulations, is good. CCSM4 is second in rank and IPSL5 arrives fifth. However, as concluded in the benchmark studies, the simulation of regional climate patterns differ among the models and in our case, IPSL gives the better representation of the LGM Eurasian ice sheet (Figure 4-11).

To conclude, the present study is based on the CESM 1.0.5 climate model. As shown above and in Chapter 4 and 5, the Eurasian ice sheet is sensitive to the choice of the climate forcing. Therefore, it is probable that simulating the Late Saalian glacial maximum with a different climate model would lead to a different ice sheet topography. However, the results obtained in this study by means of a LHS ensemble allow us to put an upper bound on ice thicknesses over both sites. The ice thickness obtained by means of this method reaches the same upper bound than when changing the climate forcing. Therefore, the results obtained in the present study provide a valid estimate of the maximum ice thickness over both Forsmark and Olkiluoto. Note that given the idealised characteristics of the DYN experiments, the thickness obtained with those simulations should be considered with care.

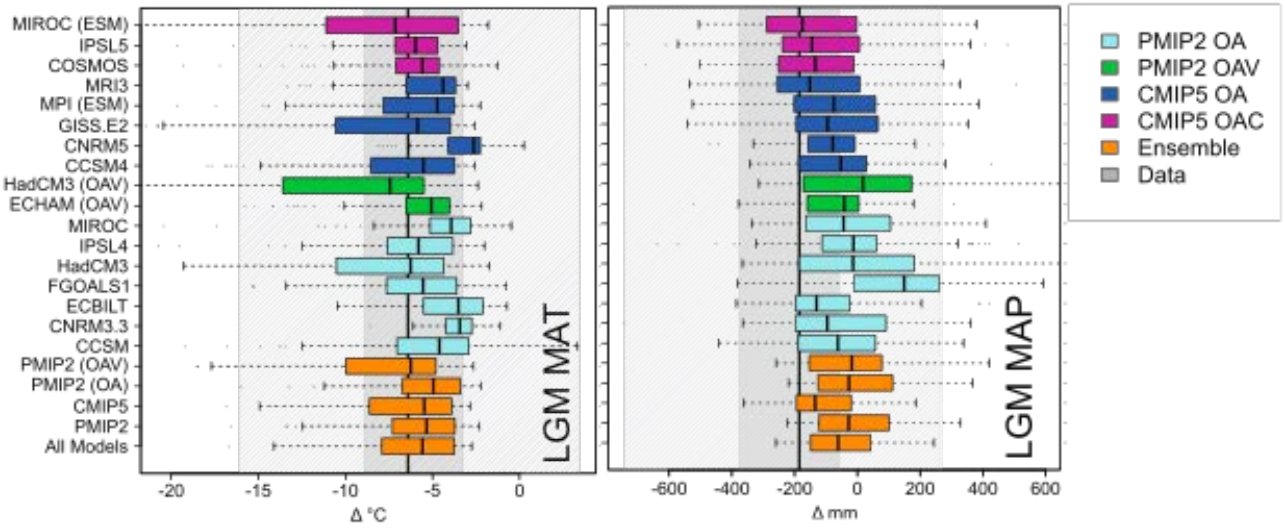

Figure 7-5. *Simulated LGM anomaly in global mean annual temperature (MAT, °C) and precipitation (MAP, mm) compared with Pre-industrial climate (after Harrison et al. 2014). OA stands for Ocean-Atmosphere coupled models, OAV is Ocean-Atmosphere-Vegetation models and OAC corresponds to Ocean-Atmosphere-Carbon-cycle models.*

7.3.2 The choice of ice sheet model

In the present study we have only briefly explored the sensitivity to ice model choice when we reconstructed the late Saalian ice sheet also with the SICOPOLIS model. We have shown that because of the lack of ice streams in SICOPOLIS, the simulated ice sheet is much thicker than its equivalent with GRISLI. Conversely, during the first phase of the study, we have shown that the results were insensitive to ice-shelf parameters, because the Late Saalian ice sheet is already mostly grounded in our simulations. These two observations suggest that, depending on the application, the ability of the models to deal with a particular feature is not necessarily always relevant. However, some ice sheet parameters account for unresolved processes. For example, the enhancement factors presented in Chapter 6 allow for a very simple representation of ice anisotropy. Also, we have shown with GRISLI, that by increasing the basal drag below the ice streams, we produce ice sheets closer to what a SIA-only model simulates (Figure 7-3). Similarly, even if the SICOPOLIS model does not explicitly accounts for fast flowing ice streams, using selected parametrisations of basal sliding velocity, this model has been shown to only coarsely reproduce Greenland fast flowing areas (Greve and Herzfeld 2013). Thus, this suggests that the ice thickness obtained with SICOPOLIS in this study might be overestimated and the interpretation of those simulations should be done with care.

7.4 Laurentide and Eurasian ice sheet extents

The Late Saalian glaciation over Eurasia is characterized by two major advances, at ~160 and ~140 kyrs BP, and a substantial retreat at ~150 kyrs BP (mainly due to the large summer insolation peak occurring at this time, Astakhov 2004, Svendsen et al. 2004). Colleoni et al. (2009) showed that even though the summer insolation at ~150 kyrs BP seems not favorable for maintaining an ice sheet over the Northern Hemisphere high latitudes at this time, the ablation occurring along the southern ice sheet margins is compensated for by an increased accumulation. In the Colleoni et al. (2009) experiments, the Late Saalian Eurasian ice sheet is able to survive this insolation peak. However, geological evidence shows that a major ice sheet retreat occurred at ~150 kyrs BP. If we consider that the Late Saalian extent from the QUEEN project corresponds to MIS 6 glacial maximum at ~140 kyrs BP, this leaves only 10 kyrs for the Eurasian ice sheet to regrow to this large extent. This short duration does not seem reasonable and suggests that the major extent could have been reached at different moments of the cycle rather than at the MIS 6 glacial maximum, towards 140 kyrs BP. This hypothesis appears to be reasonable also if compared to the last glacial cycle, which results in larger Eurasian ice sheet extents over Eastern Siberia at the beginning of the cycle, i.e. at ~85 and ~60 kyrs BP, rather than at the Last Glacial Maximum, where most of the Eurasian ice sheet developed over Western Europe.

The fact that only indirect evidence of glacial dynamics during the MIS 6 period exists for North America appears to be a strong limitation to computing a well-defined MIS 6 Northern Hemisphere climate. In the first phase of the study, we considered an extreme Late Saalian glaciation case for which the Northern Hemisphere ice topography is composed of the Eurasian ice sheet from Peyaud (2006) and the Laurentide ice sheet prescribed from LGM ICE-5G (Peltier 2004). Since no geological evidence supports this extreme MIS 6 Laurentide ice sheet configuration, we also chose to prescribe a smaller ice sheet over North America from Peltier (2004) to investigate the impact that the Laurentide ice sheet has on the Eurasian climate (Figure 3-1 in Colleoni et al. 2014b, 2016b). This topography, with a more restricted Laurentide ice sheet, appears to be more in line with paleoclimate proxies and is also less extreme than the first glacial topography that we used (Colleoni et al. 2016a). This is further supported by two main lines of evidence:

- Records of ice-rafted debris from the Hudson Bay area (de Abreu et al. 2003, Channell et al. 2012) reveal that the fluxes of icebergs from the Laurentide ice sheet during the MIS 6 glacial maximum were much lower than during the LGM. This is a clear indication that ice dynamics was reduced compared to those of the LGM, implying that the MIS 6 Laurentide ice sheet was smaller than at the LGM. This is further supported by recent evidence from Naafs et al. (2013) and the compilation of proxies linked with the Late Saalian glaciation from Obrochta et al. (2014).
- In our simulations, a restricted Laurentide ice sheet configuration induces the accumulation of a thick perennial snow cover over the East Siberian continental shelf, more extended than when using the LGM Laurentide topography. This result is supported by recent evidence for the existence of a thick ice cap over the Beringia area during the Pleistocene glaciations (Jakobsson et al. 2010, Niessen et al. 2013). However, no ice cap developed over Beringia during the LGM. This fact is particularly important since, at the LGM, the Eurasian ice sheet was smaller than at ~140 kyrs BP. All together, these facts suggest that to grow an ice cap over the East Siberian shelf, both a small Laurentide and a large Eurasian ice sheet (extending far to the East) are necessary.

The two climate simulations that we carried out are useful to constrain the Northern Hemisphere Late Saalian ice sheet topography. Given the lack of geological constraints, the southern extent of the Late Saalian Eurasian ice sheet reconstruction from Svendsen et al. (2004) might be more questionable, since it is highly sensitive to summer climate in our simulations. The two climate simulations B140_Topo1 and B140_Topo2 suggest that to stay in line with past sea-level reconstructions, ice-rafted debris reconstructions and Arctic ice sheets, the Laurentide ice sheet need to be substantially smaller than during the LGM. In Topo2, we used a Laurentide ice sheet reconstruction from Peltier (2004) of ~30 m SLE, i.e. corresponding to the ice volume during the deglaciation period at ~13 kyrs BP. It seems that, for the investigated MIS 6 period, this more restricted Laurentide ice sheet topography is more realistic than the LGM one. It could be useful to perform a transient climate-ice sheet simulation to grow a proper MIS 6 Laurentide ice sheet in order to investigate the ice elevation threshold over North America that would affect the circulation just enough to allow for the build-up of an ice cap over Beringia (Colleoni et al. 2016a).

Another alternative to this hypothesis would be that, as suggested by Huybers and Tziperman (2008), the presence of sediments at the ice sheet bed might yield large but thin ice sheets that are more sensitive to obliquity changes than to precession changes. This type of ice sheets would correspond to the glaciations that occurred before the Mid-Pleistocene transition (~1 Myrs BP). The MIS7 – MIS 6 glacial cycle presents some characteristics of those older cycles, as for example the very low CO_2 and CH_4 concentration and a peak interglacial of moderate intensity (Tzedakis et al. 2009). Based on the study by Huybers and Tziperman (2008), it could be that the Eurasian ice sheet was the most extensive glaciation during the Late Saalian glacial maximum but not necessarily the thickest one over the last 400 kyrs. But given the dimension of the Eurasian ice sheet reconstructed by Svendsen et al. (2004), it is highly likely that the ice sheet was thicker than during the LGM to remain dynamically stable. Therefore, in a framework of assessing the maximum ice thickness that can occur over both repository sites, the Late Saalian glaciation remains the best case to study.

8 Conclusions

This study was divided into a first phase, reported in Colleoni et al. (2014b, 2016b), and a second phase described in the present report. In this second phase, we have performed glaciological reconstructions of the Eurasian ice sheet for the Late Saalian glacial maximum (140 kyrs BP), for the Last Glacial Maximum (21 kyrs BP) and for the last deglaciation (21–0 kyrs BP). We made use of two different ice sheet models, namely GRISLI and SICOPOLIS, which we forced with climate forcing representatives of the Late Saalian glacial maximum and Last Glacial Maximum. We performed long steady-state simulations in order to test the Late Saalian Eurasian ice sheet sensitivity to: (1) boundary conditions (climate forcing), (2) model formulation (surface mass balance and ice dynamics), (3) model resolution and parameter values. Transient simulations of the last deglaciation were also carried out in order to better constrain our model results for the Late Saalian Eurasian ice sheet reconstructions. Figure 8-1 (Forsmark) and Figure 8-2 (Olkiluoto) present a summary of all the different experiments for the main variables of interest, namely the Eurasian ice volume and ice thickness and bedrock depression at the two repository sites. Finally, Figure 8-3 compares the results from phase one of the study with the main results of phase 2. The main conclusions from this second phase of the study are:

Sensitivity to surface mass balance formulation in the ice sheet model:

- Following Charbit et al. (2013), we implemented various surface mass balance (SMB) parametrisations in GRISLI: i) melt coefficients dependent on surface temperature (Tarasov and Peltier 2002), ii) a daily temperature standard deviation (Fausto et al. 2009), iii) rain and snow partitioning (Marsiat 1994) and iv) a physically based refreezing scheme (Janssens and Huybrechts 2000). Except for the temperature standard deviation, the new parametrisations lead to a decrease in SMB and therefore a decrease in ice thickness over both repository sites. While the use of the rain fraction of Marsiat (1994) leads to the strongest ice thickness reduction, the combination of the different parametrisations compensates for their individual impact, leading to an overall slight decrease in ice thickness relative to the reference simulations.
- All together, the ranges of ice thickness (2577 to 3320 m) and bedrock depression (−617 to −787 m) obtained with these new SMB parametrisations (Figure 8-3) are mostly in line with the ranges obtained for the sensitivity experiments during phase one of the study: 2650 metres to 3472 metres for ice thickness and −632 metres to −822 metres for bedrock depression accounting for both climate forcing range and both sites (Figure 8-3). The impacts of the uncertainties related to SMB are thus comparable to those of the lapse rate and precipitation correction factor tested in phase one.

Sensitivity to the thermo-mechanical formulation in the ice sheet models:

- We compared two different ice sheet models: GRISLI which is a hybrid model accounting for fast flowing ice (SSA) and the Shallow-Ice approximation (SIA), and SICOPOLIS which is a SIA-only model but accounting for polythermal ice. SIA-only reconstructions, both with SICOPOLIS and GRISLI present lower ice velocities and, as a consequence, thicker ice than when activating the SSA in GRISLI. The maximum simulated steady-state ice thickness over both sites reaches around 4000 metres. If taking into consideration the global ice volume estimate for this time period, even though geological evidence supports a Laurentide ice sheet smaller than during the Last Glacial Maximum, this maximum ice thickness over Forsmark and Olkiluoto is likely to be an overestimation. As a consequence, the Eurasian ice volumes obtained with those simulations, either accounting for a large or a small Laurentide ice volume in the calculations, goes beyond the upper bound of global sea-level reconstructions (Rabineau et al. 2006) and are therefore not realistic.
- We have shown that accounting for the SSA, responsible for the activation of ice stream areas in GRISLI, is important in order to produce an ice sheet geometry in agreement with existing ice sheets. However, in GRISLI the SSA is applied to large regions instead of narrow regions, which has no equivalent amongst modern ice sheets. An attempt to limit the spatial application of the

SSA to large topographic valleys, based on the bedrock curvature was performed. However, there is no geological evidence to constrain this criterion, which makes this approach problematic.

- These set of experiments, investigating the thermo-mechanical model formulations provide the thickest ice over both Forsmark and Olkiluoto in the present study, with both ice sheet models. However, due to the lack of physical and geological constraints on ice stream distribution during that MIS 6 glacial maximum, we consider the results from this set of simulations as unrealistic since it is highly likely that ice streams existed in the Eurasian ice sheet, as observed for example for present-day Greenland and Antarctic ice sheets.

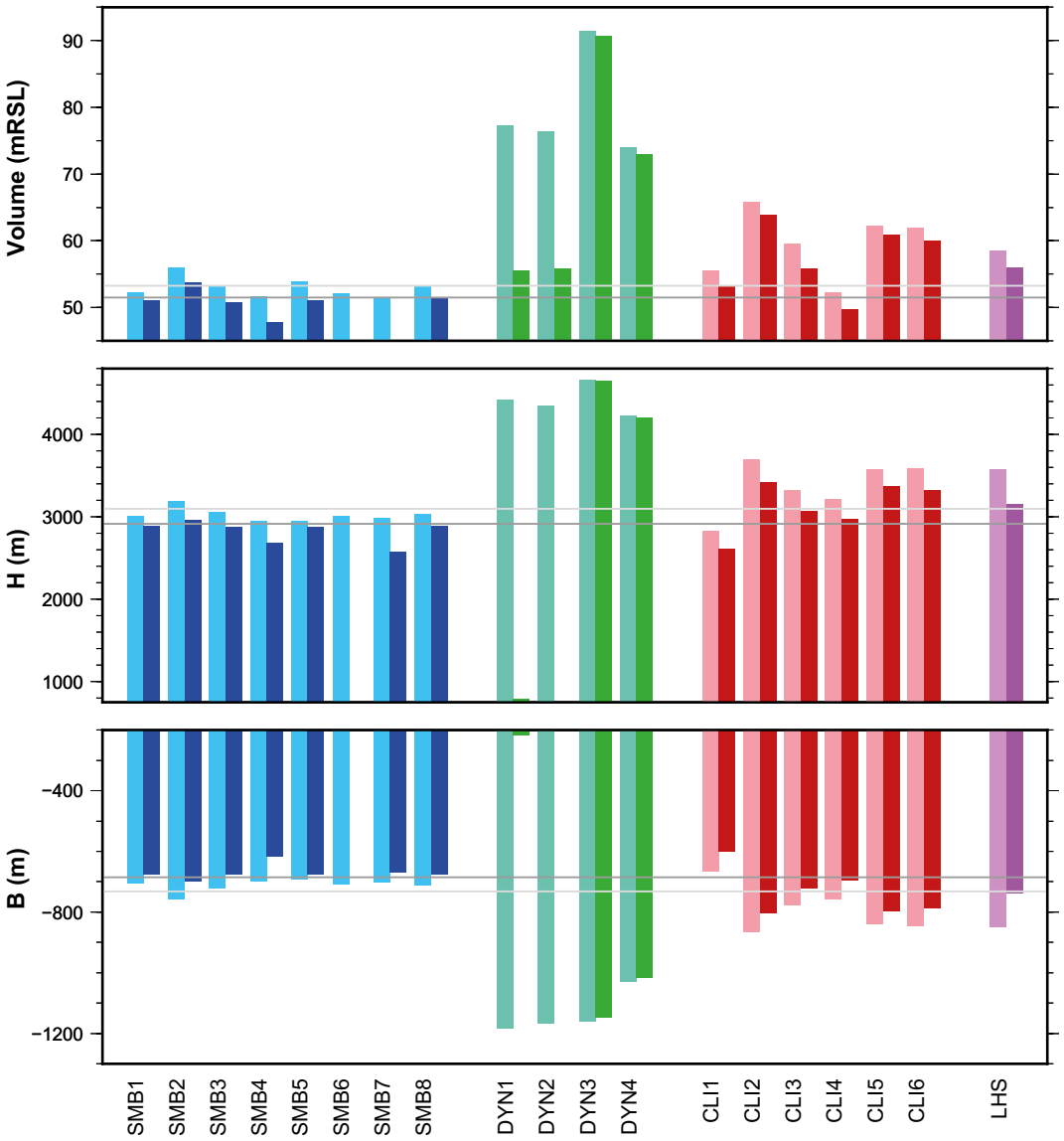

Figure 8-1. *Final Late Saalian total Eurasian ice sheet volume (top), ice thickness at Forsmark (middle) and bedrock elevation at Forsmark (bottom) using the B140_Topo1 climate forcing (light colors) and B140_Topo2 forcing (dark colors). The ice volume is expressed in m relative sea level change. The horisontal lines shows the values of the reference simulations REF_Topo1 (light grey) and REF_Topo2 (dark grey). The different categories (SMB, DYN, CLI and LHS) are described in the Chapter 2, 3, 5 and 6, respectively. As previously discussed (see Section 7.4), the Northern Hemisphere ice configuration and climate of B140_Topo2 is considered to be more realistic than that of B140_Topo1.*

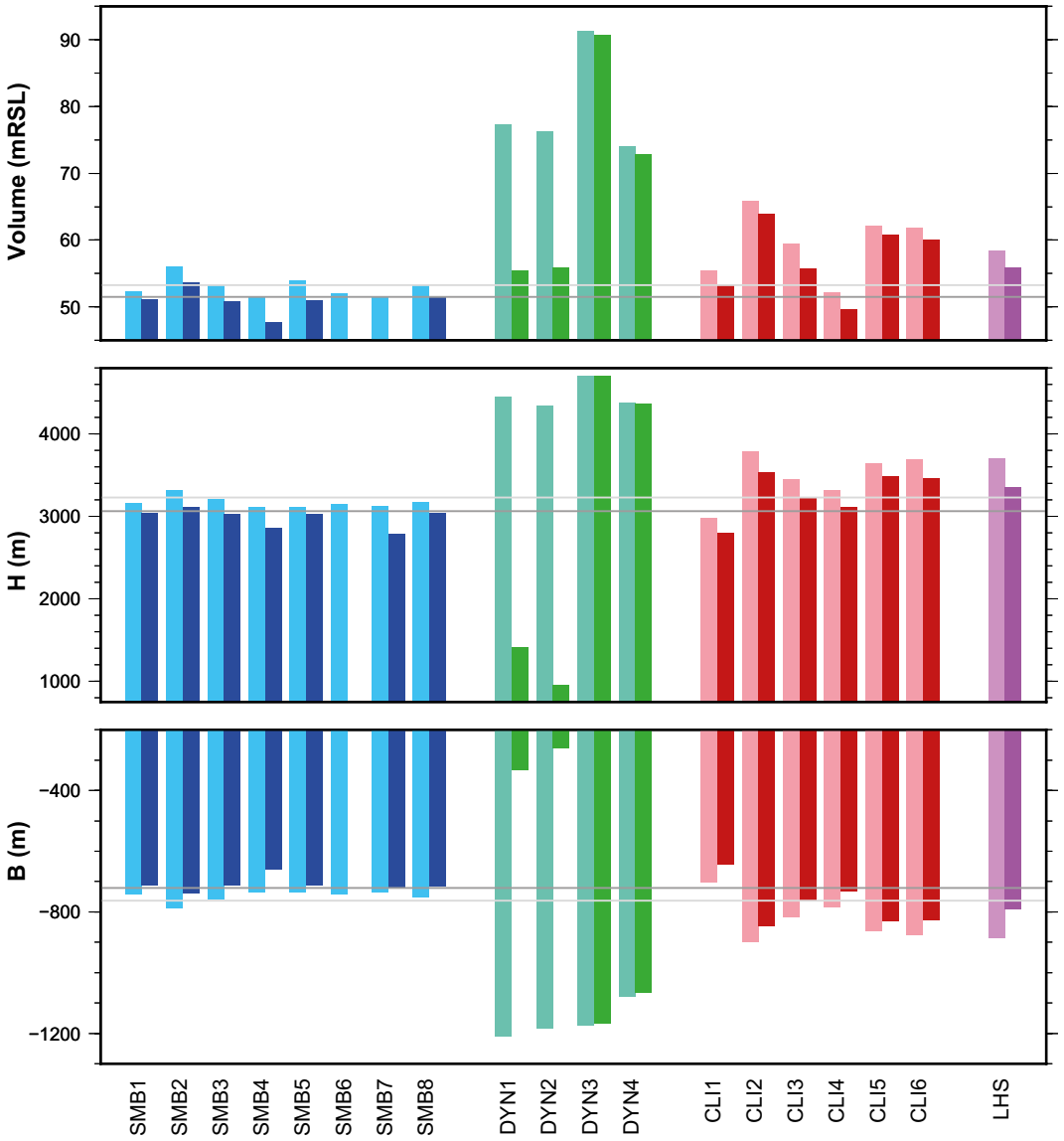

Figure 8-2. *Final total Late Saalian Eurasian ice sheet volume (top), ice thickness at Olkiluoto (middle) and bedrock elevation at Olkiluoto (bottom) using the B140_Topo1 climate forcing (light colors) and B140_Topo2 forcing (dark colors). The ice volume is expressed in m relative sea level change. The horisontal lines shows the values of the reference simulations REF_Topo1 (light grey) and REF_Topo2 (dark grey). The different categories (SMB, DYN, CLI and LHS) are described in the Chapter 2, 3, 5 and 6, respectively. As previously discussed (see Section 7.4), the Northern Hemisphere ice configuration and climate of B140_Topo2 is considered to be more realistic than that of B140_Topo1.*

Simulations of the Late Weichselian Eurasian ice sheet:

- To better constrain the Late Saalian ice sheets geometry, and in particular the application of the SSA, steady-state simulations of the Last Glacial Maximum (LGM) and transient simulations of the last deglaciation were carried out. To this end, GRISLI was forced with the output from six different AOGCMs from the PMIP3 database. Because of the very large sensitivity to this diversity in climate forcing, the resulting LGM Eurasian ice sheets topographies differ widely. Because of this, the ice stream extent remained poorly constrained.
- In both the LGM steady-state and the transient deglaciation simulations, the ice sheet over Fennoscandia remains mostly cold base (no ice streams). This is in good agreement with the reconstruction of Kleman and Glasser (2007).

- If the ice sheet is thick enough in the western part of Eurasia, GRISLI treats the entire area, except for the cold-based Fennoscandia, with the SSA, i.e. as having ice stream flow characteristics, independently from the climate forcing. This is consistent with what we simulate for the Late Saalian, the LGM and the last deglaciation.

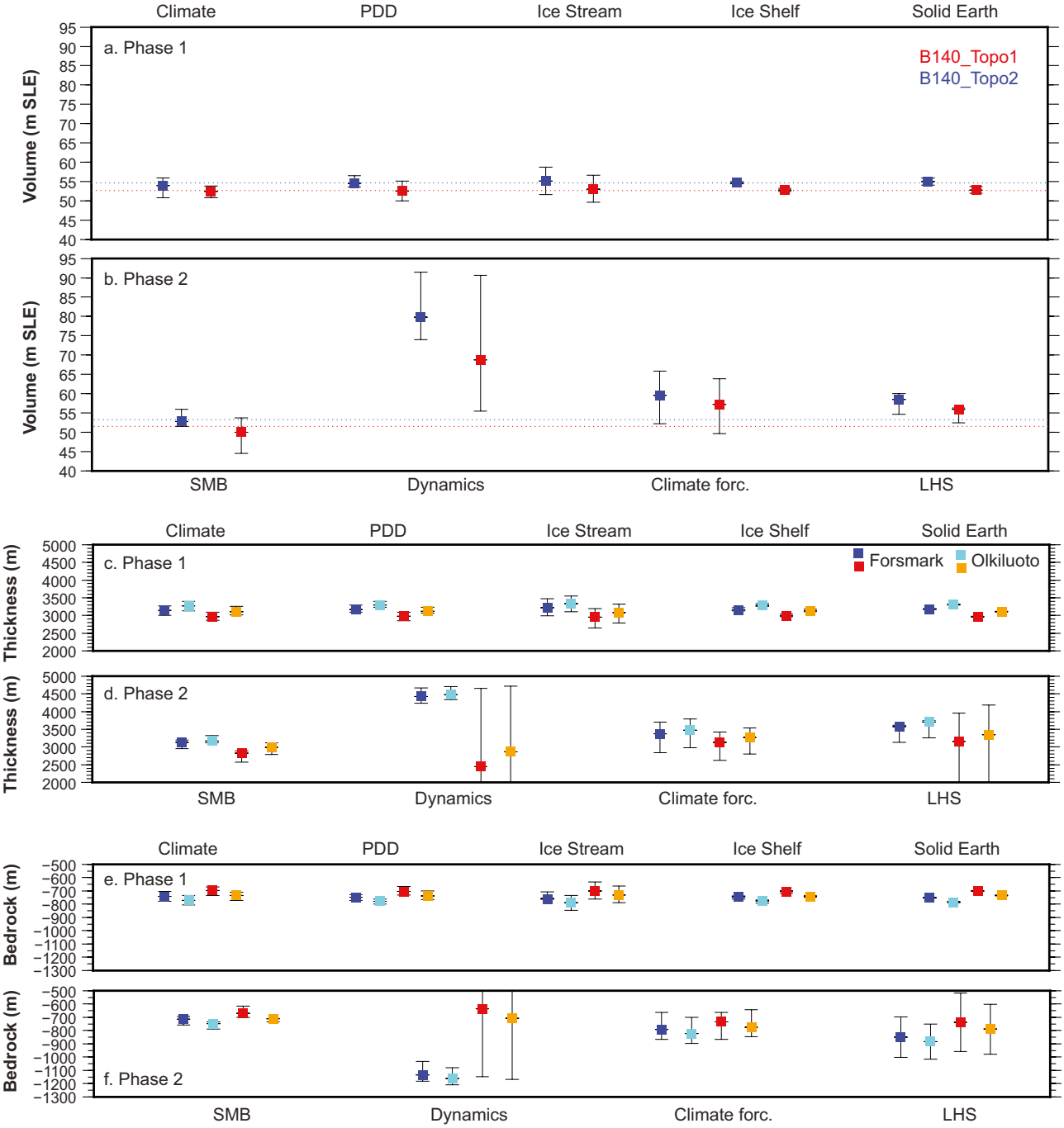

Figure 8-3. *Comparison between the ice sheet results from phase 1 (Colleoni et al. 2014b, 2016b) and phase 2 (present report): (a) and (b) show the mean simulated Late Saalian Eurasian ice sheet volume (m SLE) using the two simulated climates B140_Topo1 (blue) and B140_Topo2 (red). Error bars corresponds to the minimum and maximum values of each category (the values are reported in the tables in the various sections); (c) and (d) show the simulated ice thickness (m) over Forsmark (dark colors) and Olkiluoto (light colors) using both Late Saalian climates B140_topo1 (blue/cyan) and B140_Topo2 (red/orange); (e) and (f) show the corresponding bedrock depression to the cases in (c) and (d) at both sites (m).*

Late Saalian Eurasian ice sheet sensitivity to climate forcing:

- We used the pre-industrial simulations from the six AOGCMs of the PMIP3 database to generate new Late Saalian climate forcing fields. The Late Saalian ice sheet exhibits a very large sensitivity to climate forcing as the volume changes from −3.5 % to +24 % relative to the reference simulations, depending on the AOGCM used. This range of change is considerably greater than the one obtained for the sensitivity to SMB formulation. Once again, this highlights the fact that our results were obtained using one ice sheet model forced by the climate simulated by only one AOGCM, and therefore the interpretation of the results should be seen in this framework. The fact that we used only one combination of two models suggests that the range of ice volumes obtained in the present study could be larger if we used different AOGCMs and ice sheet models.

Ice sheet model parametric uncertainty:

- The Latin Hypercube Sampling (LHS) methodology is used to generate a grid combination of parameter values covering the surface mass balance uncertainties as well as ice sheet dynamical uncertainties. While we obtained a wide spread of ice volumes, ice thicknesses and bedrock depressions at both repository sites, the simulations mostly fell into two categories with either no ice over the sites or a large thickness with more than 3000 m of ice over the repository sites.
- The parameters linked to surface mass balance have the strongest impact on the stability of the western part of the Eurasian ice sheet, but they have a limited impact on the ice thickness and bedrock depression at the repository sites.
- The parameters linked to the internal ice dynamics mainly impact the ice thickness and bedrock depression at the repository sites, but they do not explain the retreat of the unstable western part of the Eurasian ice sheet.
- The largest ice thicknesses and bedrock depression are achieved with the largest basal drag coefficient values at both the Forsmark and Olkiluoto site.

The Latin Hypercube experiments yield the minimum and maximum values on ice thickness and bedrock depression if we do not take into account the idealised DYN sets of experiments (Chapter 3 and Table 3-1) addressing uncertainties in inner thermo-mechanical formulation. Thus:

- The minimum ice thickness (resp. bedrock depression) at Forsmark is 2707 m (resp. −629 m) using the B140_Topo1 climate and 581 m (resp. −178 m) using the B140_Topo2 climate. At Olkiluoto, the minimum ice thickness (resp. bedrock depression) is 2872 m (resp. −669 m) using the B140_Topo1 climate and 1518 m (resp. −237 m) using the B140_Topo2 climate. As previously discussed (see Section 7.4), the Northern Hemisphere ice configuration and climate of B140_Topo2 is considered to be more realistic than that of of B140_Topo1 (Colleoni et al. 2016a).
- The maximum ice thickness (resp. bedrock depression) at Forsmark is 4150 m (resp. −1003 m) using the B140_Topo1 climate and 3957 m (resp. −958 m) using the B140_Topo2 climate. At Olkiluoto, the maximum ice thickness (resp. bedrock depression) is 4190 m (resp. −1017 m) using B140_Topo1 and 4023 m (resp. −977 m) using B140_Topo. As previously discussed (see Section 7.4), the Northern Hemisphere ice configuration and climate of B140_Topo2 is considered to be more realistic than that of of B140_Topo1 (Colleoni et al. 2016a).
- Finally the ensemble mean of the LHS experiments gives an ice thickness (resp. bedrock depression) of 3153 metres (resp. –737 m) over Forsmark and 3351 metres over Olkiluoto (resp. –789 m).

Excluding the LHS results and the unrealistic DYN experiments, the minimum and the maximum values arise from the climate forcing sensitivity experiments:

- The Late Saalian climate forcing modified by the CNRM-CM5 climate provides the lower bound on ice thickness and bedrock depression. The minimum ice thickness (resp. bedrock depression) at Forsmark is 2835 m (resp. 664 m) using the modified B140_Topo1 climate forcing and 2619 m (resp. −599.4 m) using the modified B140_Topo2 climate forcing. At Olkiluoto, the minimum ice thickness (resp. bedrock depression) is 2984 m (resp. −702 m) using the modified B140_Topo1 climate forcing and 2800 m (resp. −644 m) using the modified B140_Topo2 climate forcing.

- The FGOALS-g2 climate forcing provides the upper bound. The maximum ice thickness (resp. bedrock depression) at Forsmark is 3702 m (resp. −866 m) using B140_Topo1 climate forcing and 3417 m (resp. −803 m) using B140_Topo2 climate forcing. At Olkiluoto, the maximum ice thickness (resp. bedrock depression) is 3791 m (resp. −898 m) using B140_Topo1 climate forcing and 3539 m (resp. −846 m) using B140_Topo2 climate forcing.

Three aspects potentially impacting the uncertainty of the upper bound of ice thickness were identified. First, the changes in climate forcing from the six PMIP AOGCMs lead to an upper bound of a similar magnitude as in the LHS analysis (Figure 8-3). However, the mean ice thickness obtained with a perturbation of the climate forcing is lower than the mean ice thickness simulated with the LHS method. This means that the LHS provides a good estimate of the upper bound, including the uncertainty related to climate forcing. Note however, that the method we used to perturb the B140_Topo1 and B140_Topo2 climate forcing is simple and might not reflect the atmospheric circulation as simulated with each of the AOGCM considered in the CLI experiments. Therefore, the interpretation of the results obtained within the CLI set of experiments has to be made with caution. Second, the LHS method follows statistical sampling of parameters of the most important processes in the ice sheet model. Therefore, the results from the LHS have a statistical meaning that the other sets of analyses do not have, which provide a clear strength to those results. Third, the choice of ice sheet model determines the impact of the results. As we show, when the dynamics linked with the fast flowing areas is treated with different criteria, the results might present substantial differences in the thickness. To reduce the overall uncertainty of the upper bound of ice thickness, this study could be repeated with different climate and ice sheet models and also by means of transient experiments. In Colleoni et al. (2014b, 2016b) and in the present study, we performed long steady-state simulations that might overestimate the simulated ice volume. However, depending on the climate preceding the glacial maximum and on the local feedback operating in the area of interest, transient simulations might lead to either an over- or underestimate of the ice volume. Finally, a very large number of parameters and aspects of the climate and ice sheet system have been tested in the first phase of the study and in the present study. The results provided by our simulations have been compared to available climate proxies (Colleoni et al. 2016a) and sea-level reconstruction in order to put some constraints on their interpretation. Every aspect has been investigated objectively and the limitations have been discussed carefully which provides solid basis for the conclusions that this study reaches about the maximum ice thickness over Forsmark and Olkiluoto.

Acknowledgements

We would like to thank Dr. Patrick Applegate (Penn State University), Dr. Allan Hedin (Swedish Nuclear Fuel and Waste Management Company, SKB), Prof. Philippe Huybrechts (Vrije Universiteit Brussel) and Prof. Ralf Greve (Hokkaido University) for providing constructive comments on the manuscript. We are grateful to Catherine Ritz for providing the GRISLI ice sheet model, to Ralph Greve for providing the SICOPOLIS ice sheet model and to the PMIP community for providing the simulated paleo-climate of the Last Glacial Maximum.

References

SKB's (Svensk Kärnbränslehantering AB) publications can be found at www.skb.com/publications.

Abe-Ouchi A, Segawa T, Saito F, 2007. Climatic conditions for modelling the Northern Hemisphere ice sheets throughout the ice age cycle. Available at: http://hal-insu.archives-ouvertes.fr/hal-00298083/ [25 january 2011].

Abe-Ouchi A, Saito F, Kawamura K, Raymo M E, Okuno J, Takahashi K, Blatter H, 2013. Insolation-driven 100,000-year glacial cycles and hysteresis of ice-sheet volume. Nature 500, 190–193.

Alvarez-Solas J, Charbit S, Ramstein G, Paillard D, Dumas C, Ritz C, Roche D M, 2011. Millennial-scale oscillations in the Southern Ocean in response to atmospheric CO_2 increase. Global and Planetary Change 76, 128–136.

Amante C, Eakins B W, 2009. ETOPO1 1 Arc-Minute Global Relief Model: procedures, data sources and analysis. NOAA Technical Memorandum NESDIS NGDC-24, National Geophysical Data Center, National Oceanic and Atmospheric Administration.

Andersen K K, Azuma N, Barnola J-M, Bigler M, Biscaye P, Caillon N, Chappellaz J, Clausen H B, Dahl-Jensen D, Fischer H, Flückiger J, Fritzsche D, Fujii Y, Goto-Azuma K, Grønvold K, Gundestrup N S, Hansson M, Huber C, Hvidberg C S, Johnsen S J, Jonsell U, Jouzel J, Kipfstuhl S, Landais A, Leuenberger M, Lorrain R, Masson-Delmotte V, Miller H, Motoyama H, Narita H, Popp T, Rasmussen S O, Raynaud D, Rothlisberger R, Ruth U, Samyn D, Schwander J, Shoji H, Siggard-Andersen M-L, Steffensen J P, Stocker T, Sveinbjörnsdóttir A E, Svensson A, Takata M, Tison J-L, Thorsteinsson T, Watanabe O, Wilhelms F, White J W C, 2004. High-resolution record of Northern Hemisphere climate extending into the last interglacial period. Nature 431, 147–151.

Applegate PJ, Kirchner N, Stone E J, Keller K, Greve R, 2012. An assessment of key model parametric uncertainties in projections of Greenland Ice Sheet behavior. The Cryosphere 6, 589–606.

Astakhov V, 2004. Middle Pleistocene glaciations of the Russian North. Quaternary Science Reviews, Quaternary Environments of the Eurasian North (QUEEN) 23,1285–1311.

Bamber J L, Aspinall W P, 2013. An expert judgement assessment of future sea level rise from the ice sheets. Nature Climate Change 3, 424–427.

Bonelli S, Charbit S, Kageyama M, Woillez M-N, Ramstein G, Dumas C, Quiquet A, 2009. Investigating the evolution of major Northern Hemisphere ice sheets during the last glacial-interglacial cycle. Climate of the Past 5, 329–345.

Braconnot P, Harrison S P, Kageyama M, Bartlein P J, Masson-Delmotte V, Abe-Ouchi A, Otto-Bliesner B, Zhao Y, 2012. Evaluation of climate models using palaeoclimatic data. Nature Climate Change 2, 417–424.

Braithwaite R J, 1995. Positive degree-day factors for ablation on the Greenland ice sheet studied by energy-balance modelling. Journal of Glaciology 41, 153–160.

Braithwaite R J, Zhang Y, 2000. Sensitivity of mass balance of five Swiss glaciers to temperature changes assessed by tuning a degree-day model. Journal of Glaciology 46, 7–14.

Calov R, Greve R, Abe-Ouchi A, Bueler E, Huybrechts P, Johnson J V, Pattyn F, Pollard D, Ritz C, Saito F, Tarasov L, 2010. Results from the Ice-Sheet Model Intercomparison Project – Heinrich Event IntercOmparison (ISMIP HEINO). Journal of Glaciology 56, 371–383.

Channell J E T, Hodell D A, Romero O, Hillaire-Marcel C, de Vernal A, Stoner J S, Mazaud A, Röhl U, 2012. A 750-kyr detrital-layer stratigraphy for the North Atlantic (IODP Sites U1302–U1303, Orphan Knoll, Labrador Sea). Earth and Planetary Science Letters 317–318, 218–230.

Charbit S, Ritz C, Ramstein G, 2002. Simulations of Northern Hemisphere ice-sheet retreat: : sensitivity to physical mechanisms involved during the Last Deglaciation. Quaternary Science Reviews 21, 243–265.

Charbit S, Ritz C, Philippon G, Peyaud V, Kageyama M, 2007. Numerical reconstructions of the Northern Hemisphere ice sheets through the last glacial-interglacial cycle. Climate of the Past 3, 15–37.

Charbit S, Dumas C, Kageyama M, Roche D M, Ritz C, 2013. Influence of ablation-related processes in the build-up of simulated Northern Hemisphere ice sheets during the last glacial cycle. The Cryosphere 7, 681–698.

Christianson K, Peters L E, Alley R B, Anandakrishnan S, Jacobel R W, Riverman K L, Muto A, Keisling B A, 2014. Dilatant till facilitates ice-stream flow in northeast Greenland. Earth and Planetary Science Letters 401, 57–69.

Colleoni F, Krinner G, Jakobsson M, Peyaud V, Ritz C, 2009. Influence of regional parameters on the surface mass balance of the Eurasian ice sheet during the peak Saalian (140 kya). Global and Planetary Change, The 2005 HOTRAX Expedition to the Arctic Ocean 68, 132–148.

Colleoni F, Masina S, Cherchi A, Navarra A, Ritz C, Peyaud V, Otto-Bliesner B, 2014a. Modeling Northern Hemisphere ice-sheet distribution during MIS 5 and MIS 7 glacial inceptions. Climate of the Past 10, 269–291.

Colleoni F, Wekerle C, Masina S, 2014b. Long-term safety of a planned geological repository for spent nuclear fuel in Forsmark – estimate of maximum ice sheet thicknesses. SKB TR-14-21, Svensk Kärnbränslehantering AB.

Colleoni F, Wekerle C, Näslund J O, Brandefelt J, Masina S, 2016a. Constraint on the penultimate glacial maximum Northern Hemisphere ice topography (~140 kyrs BP). Quaternary Science Reviews 137, 97–112.

Colleoni F, Wekerle C, Quiquet A, Masina S, 2016b. Long-term safety of a planned repository for spent nuclear fuel in Olkiluoto, Finland – Phase 1: estimate of maximum ice sheet thickness in Olkiluoto. Posiva Working Report 2015-33, Posiva Oy, Finland.

Dahl-Jensen D, Johnsen S J, Hammer C U, Clausen H B, Jouzel J, 1993. Past accumulation rates derived from observed annual layers in the GRIP ice core from Summit, Central Greenland. In Peltier W R (ed). Ice in the climate system. Berlin: Springer, 517–532.

Dahl-Jensen D, Gundestrup N, Gogineni S P, Miller H, 2003. Basal melt at NorthGRIP modeled from borehole, ice-core and radio-echo sounder observations. Annals of Glaciology 37, 207–212.

de Abreu L, Shackleton N J, Schönfeld J, Hall M, Chapman M, 2003. Millennial-scale oceanic climate variability off the Western Iberian margin during the last two glacial periods. Marine Geology 196, 1–20.

de Boer B, Dolan A M, Bernales J, Gasson E, Goelzer H, Golledge N R, Sutter J, Huybrechts P, Lohmann G, Rogozhina I, Abe-Ouchi A, Saito F, van de Wal R S W, 2015. Simulating the Antarctic ice sheet in the late-Pliocene warm period: PLISMIP-ANT, an ice-sheet model intercomparison project. The Cryosphere 9, 881–903.

Dowdeswell J A, Ottesen D, Rise L, 2006. Flow switching and large-scale deposition by ice streams draining former ice sheets. Geology 34, 313–316.

Dufresne J-L, Foujols M-A, Denvil S, Caubel A, Marti O, Aumont O, Balkanski Y, Bekki S, Bellenger H, Benshila R, Bony S, Bopp L, Braconnot P, Brockmann P, Cadule P, Cheruy F, Codron F, Cozic A, Cugnet D, Noblet N de Duvel J-P, Ethé C, Fairhead L, Fichefet T, Flavoni S, Friedlingstein P, Grandpeix J-Y, Guez L, Guilyardi E, Hauglustaine D, Hourdin F, Idelkadi A, Ghattas J, Joussaume S, Kageyama M, Krinner G, Labetoulle S, Lahellec A, Lefebvre M-P, Lefevre F, Levy C, Li Z X, Lloyd J, Lott F, Madec G, Mancip M, Marchand M, Masson S, Meurdesoif Y, Mignot J, Musat I, Parouty S, Polcher J, Rio C, Schulz M, Swingedouw D, Szopa S, Talandier C, Terray P, Viovy N, Vuichard N, 2013. Climate change projections using the IPSL-CM5 Earth System Model: from CMIP3 to CMIP5. Climate Dynamics 40, 2123–2165.

Dumas C, 2002. Modélisation de l'évolution de l'Antarctique depuis le dernier cycle glaciaire-interglaciaire jusqu'au futur : importance relative des différents processus physiques et rôle des données d'entrée. PhD thesis. Université Joseph-Fourier – Grenoble I.

Edwards T L, Fettweis X, Gagliardini O, Gillet-Chaulet F, Goelzer H, Gregory J M, Hoffman M, Huybrechts P, Payne A J, Perego M, Price S, Quiquet A, Ritz C, 2014. Effect of uncertainty in surface mass balance–elevation feedback on projections of the future sea level contribution of the Greenland ice sheet. The Cryosphere 8, 195–208.

Ettema J, van den Broeke M R, van Meijgaard E, van de Berg W J, Bamber J L, Box J E, Bales R C, 2009. Higher surface mass balance of the Greenland ice sheet revealed by high-resolution climate modeling. Geophysical Research Letters 36. doi : 10.1029/2009GL038110

Fausto R S, Ahlstrøm A P, van As D, Johnsen S J, Langen P L, Steffen K, 2009. Improving surface boundary conditions with focus on coupling snow densification and meltwater retention in large-scale ice-sheet models of Greenland. Journal of Glaciology 55, 869–878.

Fischer H, Behrens M, Bock M, Richter U, Schmitt J, Loulergue L, Chappellaz J, Spahni R, Blunier T, Leuenberger M, Stocker T F, 2008. Changing boreal methane sources and constant biomass burning during the last termination. Nature 452, 864–867.

Fowler A C, 1984. On the transport of moisture in polythermal glaciers. Geophysical & Astrophysical Fluid Dynamics 28, 99–140.

Fürst J J, Goelzer H, Huybrechts P, 2015. Ice-dynamic projections of the Greenland ice sheet in response to atmospheric and oceanic warming. The Cryosphere 9, 1039–1062.

Ganopolski A, Calov R, 2012. Simulation of glacial cycles with an earth system model. In Berger A, Mesinger F, Sijacki D (eds). Climate change: inferences from paleoclimate and regional aspects. Vienna: Springer, 49–55.

Ganopolski A, Calov R, Claussen M, 2010. Simulation of the last glacial cycle with a coupled climate ice-sheet model of intermediate complexity. Climate of the Past 6, 229–244.

Gent P R, Danabasoglu G, Donner L J, Holland M M, Hunke E C, Jayne S R, Lawrence D M, Neale RB, Rasch P J, Vertenstein M, Worley P H, Yang Z-L, Zhang M, 2011. The Community Climate System Model Version 4. Journal of Climate 24, 4973–4991.

Gillet-Chaulet F, Gagliardini O, Meyssonnier J, Zwinger T, Ruokolainen J, 2006. Flow-induced anisotropy in polar ice and related ice-sheet flow modelling. Journal of Non-Newtonian Fluid Mechanics 134, 33–43.

Gillet-Chaulet F, Gagliardini O, Seddik H, Nodet M, Durand G, Ritz C, Zwinger T, Greve R, Vaughan D G, 2012. Greenland ice sheet contribution to sea-level rise from a new-generation ice-sheet model. The Cryosphere 6, 1561–1576.

Giorgetta M A, Jungclaus J, Reick C H, Legutke S, Bader J, Böttinger M, Brovkin V, Crueger T, Esch M, Fieg K, Glushak K, Gayler V, Haak H, Hollweg H-D, Ilyina T, Kinne S, Kornblueh L, Matei D, Mauritsen T, Mikolajewicz U, Mueller W, Notz, D, Pithan F, Raddatz T, Rast S, Redler R, Roeckner E, Schmidt H, Schnur R, Segschneider J, Six K D, Stockhause M, Timmreck C, Wegner J, Widmann H, Wieners K-H, Claussen M, Marotzke J, Stevens B, 2013. Climate and carbon cycle changes from 1850 to 2100 in MPI-ESM simulations for the Coupled Model Intercomparison Project phase 5. Journal of Advances in Modeling Earth Systems 5, 572–597.

Graversen R G, Drijfhout S, Hazeleger W, van de Wal R, Bintanja R, Helsen M, 2011. Greenland's contribution to global sea-level rise by the end of the 21st century. Climate Dynamics 37, 1427–1442.

Greve R, 1997. Application of a polythermal three-dimensional ice sheet model to the Greenland ice sheet: response to steady-state and transient climate scenarios. Journal of Climate 10, 901–918.

Greve R, 2005. Relation of measured basal temperatures and the spatial distribution of the geothermal heat flux for the Greenland ice sheet. Annals of Glaciology 42, 424–432.

Greve R, Herzfeld U C, 2013. Resolution of ice streams and outlet glaciers in large-scale simulations of the Greenland ice sheet. Annals of Glaciology 54, 209–220.

Guillevic M, Bazin L, Landais A, Kindler P, Orsi A, Masson-Delmotte V, Blunier T, Buchardt S L, Capron E, Leuenberger M, Martinerie P, Prié F, Vinther B M, 2013. Spatial gradients of temperature, accumulation and δ^{18}O-ice in Greenland over a series of Dansgaard–Oeschger events. Climate of the Past 9, 1029–1051.

Hagen J O, Melvold K, Eiken T, Isaksson E, Lefauconnier B, 1999. Mass balance methods on Kongsvegen, Svalbard. Geografiska Annaler (Series Physical Geography) 81, 593–601.

Harrison S P, Bartlein P J, Brewer S, Prentice I C, Boyd M, Hessler I, Holmgren K, Izumi K, Willis K, 2014. Climate model benchmarking with glacial and mid-Holocene climates. Climate Dynamics 43, 671–688.

Harrison S P, Bartlein P J, Izumi K, Li G, Annan J, Hargreaves J, Braconnot P, Kageyama M, 2015. Evaluation of CMIP5 palaeo-simulations to improve climate projections. Nature Climate Change 5, 735–743.

Hutter K, 1982. A mathematical model of polythermal glaciers and ice sheets. Geophysical & Astrophysical Fluid Dynamics 21, 201–224.

Hutter K, 1993. Thermo-mechanically coupled ice-sheet response – cold, polythermal, temperate. Journal of Glaciology 39, 65–86.

Huybers P, Tziperman E, 2008. Integrated summer insolation forcing and 40,000 year glacial cycles: the perspective from an ice sheet/energy balance model. Paleoceanography 23, PA1208. doi:10.1029/2007PA001463

Huybrechts P, 2002. Sea-level changes at the LGM from ice-dynamic reconstructions of the Greenland and Antarctic ice sheets during the glacial cycles. Quaternary Science Reviews 21, 203–231.

Jakobsson M, Nilsson J, O'Regan M, Backman J, Löwemark L, Dowdeswell J A, Mayer L, Polyak L, Colleoni F, Anderson L G, Björk G, Darby D, Eriksson B, Hanslik D, Hell B, Marcussen C, Sellén E, Wallin Å, 2010. An Arctic Ocean ice shelf during MIS 6 constrained by new geophysical and geological data. Quaternary Science Reviews 29, 3505–3517.

Janssens I, Huybrechts P, 2000. The treatment of meltwater retardation in mass-balance parameterizations of the Greenland ice sheet. Annals of Glaciology 31, 133–140.

Johnsen S J, Dansgaard W, White J W C, 1989. The origin of Arctic precipitation under present and glacial conditions. Tellus B 41B, 452–468.

Joughin I, Smith B E, Howat I M, Scambos T, Moon T, 2010. Greenland flow variability from ice-sheet-wide velocity mapping. Journal of Glaciology 56, 415–430.

Kaplan M R, Miller G H, Steig E J, 2001. Low-gradient outlet glaciers (ice streams?) drained the Laurentide ice sheet. Geology 29, 343–346.

Kirchner N, Greve R, Stroeven A P, Heyman J, 2011. Paleoglaciological reconstructions for the Tibetan Plateau during the last glacial cycle: evaluating numerical ice sheet simulations driven by GCM-ensembles. Quaternary Science Reviews 30, 248–267.

Kleman J, Glasser N F, 2007. The subglacial thermal organisation (STO) of ice sheets. Quaternary Science Reviews 26, 585–597.

Krinner G, Genthon C, 1999. Altitude dependence of the ice sheet surface climate. Geophysical Research Letters 26, 2227–2230.

Lambeck K, Purcell A, Funder S, Kjær K H, Larsen E, Moller P, 2006. Constraints on the Late Saalian to early Middle Weichselian ice sheet of Eurasia from field data and rebound modelling. Boreas 35, 539–575.

Levermann A, Winkelmann R, Nowicki S, Fastook J L, Frieler K, Greve R, Hellmer H H, Martin M A, Meinshausen M, Mengel M, Payne A J, Pollard D, Sato T, Timmermann R, Wang W L, Bindschadler R A, 2014. Projecting Antarctic ice discharge using response functions from SeaRISE ice-sheet models. Earth System Dynamics 5, 271–293.

Li C, Battisti D S, Bitz C M, 2010. Can North Atlantic sea ice anomalies account for Dansgaard–Oeschger climate signals? Journal of Climate 23, 5457–5475.

Li L, Lin P, Yu Y, Wang B, Zhou T, Liu L, Liu J, Bao Q, Xu S, Huang W, Xia K, Pu Y, Dong L, Shen S, Liu Y, Hu N, Liu M, Sun W, Shi X, Zheng W, Wu B, Song M, Liu H, Zhang X, Wu G, Xue W, Huang X, Yang G, Song Z, Qiao F, 2013. The flexible global ocean–atmosphere–land system model, Grid-point Version 2: FGOALS-g2. Advances in Atmospheric Sciences 30, 543–560.

Liu Z, Otto-Bliesner B L, He F, Brady E C, Tomas R, Clark P U, Carlson A E, Lynch-Stieglitz J, Curry W, Brook E, Erickson D, Jacob R, Kutzbach J, Cheng J, 2009. Transient simulation of last deglaciation with a new mechanism for Bølling–Allerød warming. Science 325, 310–314.

Ma Y, Gagliardini O, Ritz C, Gillet-Chaulet F, Durand G, Montagnat M, 2010. Enhancement factors for grounded ice and ice shelves inferred from an anisotropic ice-flow model. Journal of Glaciology 56, 805–812.

Margold M, Stokes C R, Clark C D, 2015. Ice streams in the Laurentide Ice Sheet: identification, characteristics and comparison to modern ice sheets. Earth Science Reviews 143, 117–146.

Marshall S J, Tarasov L, Clarke G K, Peltier W R, 2000. Glaciological reconstruction of the Laurentide Ice Sheet: physical processes and modelling challenges. Canadian Journal of Earth Sciences 37, 769–793.

Marshall S J, Sharp M J, Burgess D O, Anslow F S, 2007. Near-surface-temperature lapse rates on the Prince of Wales Icefield, Ellesmere Island, Canada: implications for regional downscaling of temperature. International Journal of Climatology 27, 385–398.

Marsiat I, 1994. Simulation of the northern hemisphere continental ice sheets over the last glacial–interglacial cycle: experiments with a latitude-longitude vertically integrated ice sheet model coupled to zonally averaged climate model. Paleoclimates 1, 59–98.

Martin M A, Winkelmann R, Haseloff M, Albrecht T, Bueler E, Khroulev C, Levermann A, 2011. The Potsdam Parallel Ice Sheet Model (PISM-PIK) – Part 2: Dynamic equilibrium simulation of the Antarctic ice sheet. The Cryosphere 5, 727–740.

Morlighem M, Rignot E, Seroussi H, Larour E, Ben Dhia H, Aubry D, 2010. Spatial patterns of basal drag inferred using control methods from a full-Stokes and simpler models for Pine Island Glacier, West Antarctica. Geophysical Research Letters 37, L14502. doi:10.1029/2010GL043853

Morlighem M, Seroussi H, Larour E, Rignot E, 2013. Inversion of basal friction in Antarctica using exact and incomplete adjoints of a higher-order model. Journal of Geophysical Research, Earth Surface 118, 1746–1753.

Naafs B D A, Hefter J, Stein R, 2013. Millennial-scale ice rafting events and Hudson Strait Heinrich(-like) Events during the late Pliocene and Pleistocene: a review. Quaternary Science Reviews 80, 1–28.

Niessen F, Hong J K, Hegewald A, Matthiessen J, Stein R, Kim H, Kim S, Jensen L, Jokat W, Nam S-I, Kang S-H, 2013. Repeated Pleistocene glaciation of the East Siberian continental margin. Nature Geoscience 6, 842–846.

Näslund J-O, Jansson P, Fastook J L, Johnson J, Andersson L, 2005. Detailed spatially distributed geothermal heat-flow data for modeling of basal temperatures and meltwater production beneath the Fennoscandian ice sheet. Annals of Glaciology 40, 95–101.

Obrochta S P, Crowley T J, Channell J E T, Hodell D A, Baker P A, Seki A, Yokoyama Y, 2014. Climate variability and ice-sheet dynamics during the last three glaciations. Earth and Planetary Science Letters 406, 198–212.

Ottesen D, Dowdeswell J A, Rise L, 2005. Submarine landforms and the reconstruction of fast-flowing ice streams within a large Quaternary ice sheet: The 2500-km-long Norwegian-Svalbard margin (57°–80°N). Geological Society of America Bulletin 117, 1033–1050.

Peltier W R, 2004. Global Glacial Isostacy and the Surafce of the Ice-age Earth: The ICE-5G (VM2) Model and GRACE. Annual Review of Earth and Planetary Sciences 32, 111–149.

Peyaud V, 2006. Rôle de la dynamique des calottes glaciaires dans les grands changements climatiques des périodes glaciaires-interglaciaires. PhD thesis. Université Joseph-Fourier – Grenoble I.

Peyaud V, Ritz C, Krinner G, 2007. Modelling the Early Weichselian Eurasian ice sheets: role of ice shelves and influence of ice-dammed lakes. Available at: http://hal-sde.archives-ouvertes.fr/hal-00330759/ [2 February 2011].

Pfeffer W T, Meier M F, Illangasekare T H, 1991. Retention of Greenland runoff by refreezing: Implications for projected future sea level change. Journal of Geophysical Research, Oceans 96, 22117–22124.

Pollard D, DeConto R M, 2012. Description of a hybrid ice sheet-shelf model, and application to Antarctica. Geoscientific Model Development 5, 1273–1295.

Pollard D, PMIP Participating Group, 2000. Comparisons of ice-sheet surface mass budgets from Paleoclimate Modeling Intercomparison Project (PMIP) simulations. Global and Planetary Change 24, 79–106.

Quiquet A, Punge H J, Ritz C, Fettweis X, Gallée H, Kageyama M, Krinner G, Salas y Mélia D, Sjolte J, 2012. Sensitivity of a Greenland ice sheet model to atmospheric forcing fields. The Cryosphere 6, 999–1018.

Quiquet A, Ritz C, Punge H J, Salas y Mélia D, 2013. Greenland ice sheet contribution to sea level rise during the last interglacial period: a modelling study driven and constrained by ice core data. Climate of the Past 9, 353–366.

Rabineau M, Berné S, Olivet J-L, Aslanian D, Guillocheau F, Joseph P, 2006. Paleo sea levels reconsidered from direct observation of paleoshoreline position during Glacial Maxima (for the last 500,000 yr). Earth and Planetary Science Letters 252, 119–137.

Reeh N, 1989. Parameterization of melt rate and surface temperature on the Greenland ice sheet. Polarforschung 59, 113–128.

Rignot E, Mouginot J, Scheuchl B, 2011. Ice flow of the Antarctic ice sheet. Science 333, 1427–1430.

Ritz C, Fabre A, Letréguilly A, 1996. Sensitivity of a Greenland ice sheet model to ice flow and ablation parameters: consequences for the evolution through the last climatic cycle. Climate Dynamics 13, 11–23.

Ritz C, Rommelaere V, Dumas C, 2001. Modeling the evolution of Antarctic ice sheet over the last 420,000 years: implications for altitude changes in the Vostok region. Journal of Geophysical Research 106, 31943–31964.

Robinson A, Calov R, Ganopolski A, 2010. An efficient regional energy-moisture balance model for simulation of the Greenland Ice Sheet response to climate change. The Cryosphere 4, 129–144.

Schäfer M, Zwinger T, Christoffersen P, Gillet-Chaulet F, Laakso K, Pettersson R, Pohjola V A, Strozzi T, Moore J C, 2012. Sensitivity of basal conditions in an inverse model: Vestfonna ice cap, Nordaustlandet/Svalbard. The Cryosphere 6, 771–783.

Seddik H, Greve R, Placidi L, Hamann I, Gagliardini O, 2008. Application of a continuum-mechanical model for the flow of anisotropic polar ice to the EDML core, Antarctica. Journal of Glaciology 54, 631–642.

Seddik H, Greve R, Zwinger T, Placidi L, 2011. A full Stokes ice flow model for the vicinity of Dome Fuji, Antarctica, with induced anisotropy and fabric evolution. The Cryosphere 5, 495–508.

Shapiro N M, Ritzwoller M H, 2004. Inferring surface heat flux distributions guided by a global seismic model: particular application to Antarctica. Earth and Planetary Science Letters 223, 213–224.

Stokes C R, Clark C D, 1999. Geomorphological criteria for identifying Pleistocene ice streams. Annals of Glaciology 28, 67–74.

Stone E J, Lunt D J, Rutt I C, Hanna E, 2010. Investigating the sensitivity of numerical model simulations of the modern state of the Greenland ice-sheet and its future response to climate change. The Cryosphere 4, 397–417.

Stroeven A P, Hättestrand C, Kleman J, Heyman J, Fabel D, Fredin O, Goodfellow B W, Harbor J M, Jansen J D, Olsen L, Caffee M W, Fink D, Lundqvist J, Rosqvist G C, Strömberg B, Jansson K N, 2015. Deglaciation of Fennoscandia. Quaternary Science Reviews. doi:10.1016/j.quascirev.2015.09.016

Svendsen J I, Alexanderson H, Astakhov V I, Demidov I, Dowdeswell J A, Funder S, Gataullin V, Henriksen M, Hjort C, Houmark-Nielsen M, Hubberten H W, Ingólfsson Ó, Jakobsson M, Kjær K H, Larsen E, Lokrantz H, Lunkka J P, Lyså A, Mangerud J, Matiouchkov A, Murray A, Möller P, Niessen F, Nikolskaya O, Polyak L, Saarnisto M, Siegert C, Siegert M J, Spielhagen R F, Stein R, 2004. Late Quaternary ice sheet history of northern Eurasia. Quaternary Science Reviews, Quaternary Environments of the Eurasian North (QUEEN) 23, 1229–1271.

Tarasov L, Peltier W R, 2002. Greenland glacial history and local geodynamic consequences. Geophysical Journal International 150, 198–229.

Tzedakis P C, Raynaud D, McManus J F, Berger A, Brovkin V, Kiefer T, 2009. Interglacial diversity. Nature Geoscience 2, 751–755.

Vallelonga P, Christianson K, Alley R B, Anandakrishnan S, Christian J E M, Dahl-Jensen D, Gkinis V, Holme C, Jacobel R W, Karlsson N B, Keisling B A, Kipfstuhl S, Kjær H A, Kristensen M E L, Muto A, Peters L E, Popp T, Riverman K L, Svensson A M, Tibuleac C, Vinther B M, Weng Y, Winstrup M, 2014. Initial results from geophysical surveys and shallow coring of the Northeast Greenland Ice Stream (NEGIS). The Cryosphere 8, 1275–1287.

Van de Berg W J, van den Broeke M, Ettema J, van Meijgaard E, Kaspar F, 2011. Significant contribution of insolation to Eemian melting of the Greenland ice sheet. Nature Geoscience 4, 679–683.

van Meijgaard E, van Ulft L H, van de Berg W J, Bosveld F C, van den Hurk B J J M, Lenderink G, Siebesma A P, 2008. The KNMI regional atmospheric model RACMO version 2.1. Technical Report 302, Royal Netherlands Meteorological Institute.

Voldoire A, Sanchez-Gomez E, Salas y Mélia D, Decharme B, Cassou C, Sénési S, Valcke S, Beau I, Alias A, Chevallier M, Déqué M, Deshayes J, Douville H, Fernandez E, Madec G, Maisonnave E, Moine M-P, Planton S, Saint-Martin D, Szopa S, Tyteca S, Alkama R, Belamari S, Braun A, Coquart L, Chauvin F, 2012. The CNRM-CM5.1 global climate model: description and basic evaluation. Climate Dynamics 40, 2091–2121.

Watanabe S, Hajima T, Sudo K, Nagashima T, Takemura T, Okajima H, Nozawa T, Kawase H, Abe M, Yokohata T, Ise T, Sato H, Kato E, Takata K, Emori S, Kawamiya M, 2011. MIROC-ESM 2010: model description and basic results of CMIP5-20c3m experiments. Geoscientific Model Development 4, 845–872.

Weertman J, 1957. Deformation of floating ice shelves. Journal of Glaciology 3, 38–42.

Wekerle C, Colleoni F, Näslund J-O, Brandefelt J, Masina S, 2016. Numerical reconstructions of the penultimate glacial maximum ice sheet: sensitivity to climate forcing and model parameters. Accepted for publication in Journal of Glaciology.

Yukimoto S, Adachi Y, Hosaka M, Sakami T, Yoshimura H, Hirabara M, Tanaka T Y, Shindo E, Tsujino H, Deushi M, Mizuta R, Yabu S, Obata A, Nakano H, Koshiro T, Ose T, Kitoh A, 2012. A New Global Climate Model of the Meteorological Research Institute: MRI-CGCM3, Model Description and Basic Performance. Journal of the Meteorological Society of Japan 90A, 23–64.

Zweck C, Huybrechts P, 2005. Modeling of the northern hemisphere ice sheets during the last glacial cycle and glaciological sensitivity. Journal of Geophysical Research, Atmospheres 110, 07103. doi:10.1029/2004JD005489

Appendix 1

Table A1-1. List of parameters used in the reference simulations REF_Topo1 and REF_Topo2 (Colleoni et al. 2014b).

Climate forcing		
λ_{Ann}	5 °C/km	Lapse rate for annual mean air temperature
λ_{July}	4 °C/km	Lapse rate for July air temperature
γ	0.05 $°C^{-1}$	Precipitation correction factor
PDD parameters		
C_{ice}	3 mm/d/°C	Melting factor of ice
C_{snow}	8 mm/d/°C	Melting factor of snow
σ	5 °C	Standard deviation of the daily air temperature
csi	60 %	Percentage of ice that refreezes
Ice stream areas		
c_f	2×10^{-5}	Basal drag coefficient
h^*_{sed}	150 m	Critical sediment thickness
h^*_w	250 m	Critical hydraulic head
N^*	3.5×10^7 Pa	Critical effective pressure
Ice shelf areas		
H_{calv}	200 m	Critical thickness of ice shelves at the front
b_{melt} (above / below 450 m)	0.2 / 2.45 m/yr	Melting rate below ice shelves
Solid earth		
τ_r	3000 yrs	Characteristic relaxation time

Arkitektkopia AB, Bromma, 2016

SKB is tasked with managing Swedish nuclear and radioactive waste in a safe way.

skb.se